

The role of vertical land motion in past, present, and future relative sea level changes

Julius Oelsmann

Vollständiger Abdruck der von der TUM School of Engineering and Design der Technischen Universität München zur Erlangung des akademischen Grades eines

Doktors der Ingenieurwissenschaften (Dr.-Ing.)

genehmigten Dissertation.

Vorsitz:

Prof. Dr. techn. Roland Pail

Prüfer der Dissertation:

1. Priv.-Doz. Dr.phil. Marcello Passaro
2. Prof. Dr.-Ing. Florian Seitz
3. Assistant Prof. Dr.-Ing. Sönke Dangendorf

Die Dissertation wurde am 23.02.2023 bei der Technischen Universität München eingereicht und durch die TUM School of Engineering and Design am 15.06.2023 angenommen.

Abstract

Climate-driven sea level change due to thermal expansion and land-locked ice melt represents a major threat to coastal populations, infrastructure, and habitability. Global mean sea level (GMSL) change over the last decades (3.25 mm/year) has already doubled compared to the rates of the last century (1.4 mm/year) and is expected to directly affect hundreds of millions of people throughout the upcoming century [Nicholls et al., 2021, Fox-Kemper et al., 2021]. Therefore, because it is one of the most costly consequences of climate change, understanding the drivers and impacts of sea level change on coastal populations, economies, and ecosystems, has become a central objective of ongoing research.

However, one of the great challenges in estimating future coastal sea level change is that, in addition to climate-driven effects, a large fraction of sea level changes relative to the coast results from coastal subsidence and uplift due to vertical land motion. Vertical land motion is generated by a complex superposition of processes, such as the glacial isostatic adjustment, tectonics, sediment compaction, or human-induced groundwater extraction, which shape regional to local relative sea level changes in a highly heterogeneous manner. Despite compelling evidence for the relevance of these processes, previous research has applied simplified assumptions about vertical land motion, so far neglecting its non-linear character in regional and global scale analyses, and using limited observational constraints. To overcome these limitations, I develop here a new Bayesian approach to reconstruct vertical land motion continuously in space and time, based on a variety of measurement techniques, such as the Global Navigation Satellite System, tide gauges, and satellite altimetry. Using this reconstruction, I aim to find an answer to the questions of how vertical land motion has contributed to past and present relative sea level change, and to what extent it can be projected into the upcoming century.

In light of this novel vertical land motion reconstruction, I disentangle its role in relative sea level changes over 1900-2150. Vertical land motion explains a significant proportion (34%) of the variance in present-day relative sea level change. Subsidence increases the relative sea level change especially in densely populated coastal regions, such that these areas experience a relative sea level rise (of 3.74 - 5.14 mm/year, depending on the measurement technique) that is about twice as large as the global coastal-length weighted mean sea level change. While the projected sea level change in 2150 will be dominated by absolute sea level changes, vertical land motion will account for half of the variance in the deviations of regional relative sea level changes.

In contrast to previous research, I demonstrate that regional vertical land motion should not be considered as a linear process, due to a variety of non-linear dynamics, such as tectonic activity, surface mass deformation, or human impacts. When these processes are taken into account, non-linear vertical land motion significantly increases the uncertainties in coastal sea level projections compared to current estimates such as those in the recent 6th Assessment Report of the Intergovernmental Panel on Climate Change [Fox-Kemper et al., 2021]. Accordingly, vertical land motion explains 39% of the combined relative sea level change uncertainties in global coastal sea level projections. Thus, previously neglected time-varying effects significantly increase confidence intervals in projections of relative sea level change. These results reinforce the need to incorporate

observation-based vertical land motion estimates in sea level studies to better understand and model these time-varying processes.

The vertical land motion reconstruction is essential for multidisciplinary approaches focused on future coastal impacts, for advancing coastal sea level measurements (i.e., for calibration/validation of satellite altimetry), and provides crucial information for using tide gauges as a source of absolute sea level change estimates. The latter is particularly important for understanding the causes of coastal sea level variations and the evolution of historical changes over the last century. This is underlined by this work, which shows that the provided vertical land motion estimates are suitable to constrain vertical land motion at tide gauges over the last century, as the resulting absolute sea level change estimates are highly consistent with estimates from previous sea level reconstruction approaches.

Given the partially non-linear behavior of vertical land motion, I motivate the reconsideration of its role as a dynamic component of coastal sea level change. I recommend further research to better understand how vertical land motion has changed over the past century and to develop additional probabilistic or process-based scenarios for future changes in vertical land motion. Because highly populated coasts are disproportionately exposed to subsidence-induced sea level rise, but are poorly instrumented with GNSS stations, future efforts should focus on improving the observational database in these regions.

Zusammenfassung

Der globale Meeresspiegelanstieg, der hauptsächlich durch die Erwärmung der Ozeane und die damit verbundene Ausdehnung des Wassers sowie durch Eisschmelze verursacht wird, stellt eine existentielle Bedrohung für Bevölkerungen und Infrastrukturen vieler Küstenregionen dar. Im Vergleich zum Anstieg des 20. Jahrhunderts (1.4 mm/Jahr), hat sich der globale Meeresspiegelanstieg (3.25 mm/Jahr) in den letzten Jahrzehnten bereits verdoppelt. Es wird erwartet, dass gegen Ende des 21. Jahrhunderts mehrere hundert Millionen Menschen von den damit verbundenen Folgen betroffen sein werden [Nicholls et al., 2021, Fox-Kemper et al., 2021]. Weil der Meeresspiegelanstieg zu den kostenintensivsten Konsequenzen des Klimawandels gehört, ist die Untersuchung der Ursachen und Auswirkungen dieser langfristigen Veränderungen auf Küstensysteme ein zentraler Gegenstand aktueller Forschung.

Eine der größten Herausforderungen bei der Abschätzung künftiger Veränderungen des Meeresspiegels besteht jedoch darin, dass ein großer Anteil der Meeresspiegelveränderungen relativ zur Küste neben den klimabedingten Prozessen auch durch vertikale Landbewegungen beeinflusst wird. Vertikale Landbewegungen entstehen durch eine komplexe Überlagerung von Prozessen wie der Postglazialen Landhebung, tektonischer Aktivität, Sedimentverdichtung oder durch den Menschen verursachte Grundwasserentnahme, welche regionale und lokale relative Meeresspiegeländerungen in höchst ungleichmäßiger Weise beeinflussen. Trotz der Relevanz dieser Prozesse wurden in der bisherigen Forschung oft nur vereinfachte Annahmen zu vertikalen Landbewegungen getroffen. Insbesondere der zum Teil nichtlineare Charakter der Landbewegungen wurde häufig vernachlässigt und es wurden oft nur begrenzt direkte Beobachtungsdaten verwendet. Um diese Einschränkungen zu überwinden, wird hier ein neuer Bayes'scher Ansatz zur kontinuierlichen räumlichen und zeitlichen Rekonstruktion der vertikalen Landbewegung auf der Grundlage einer Vielzahl von Messverfahren (z.B. dem globalen Navigationssatellitensystem (GNSS), Pegelmessstationen und Satellitenaltimetrie) entwickelt. Das Ziel dieser Arbeit ist zu verstehen, wie vertikale Landbewegungen zu Veränderungen des relativen Meeresspiegels beitragen und inwieweit diese für das kommende Jahrhundert prognostiziert werden können.

Mithilfe der neuartigen Rekonstruktion der vertikalen Landbewegungen untersuche ich deren Einfluss auf relative Meeresspiegelveränderungen im Zeitraum von 1900 bis 2150. Vertikale Landbewegungen haben einen erheblichen Anteil (34%) an den heutigen relativen Meeresspiegelveränderungen. Landabsenkungen verstärken relative Meeresspiegeländerungen insbesondere in stark besiedelten Küstenregionen, so dass diese Gebiete von einem weit höheren relativen Meeresspiegelanstieg (d.h. 3.74 - 5.14 mm/Jahr, je nach Messverfahren) betroffen sind, als es durch den durchschnittlichen absoluten Meeresspiegelanstieg der Fall wäre. Obwohl absolute Meeresspiegeländerungen einen Großteil der projizierten relativen Meeresspiegelveränderungen im Jahr 2150 erklären werden, wird etwa die Hälfte der Abweichungen vom globalen Mittel von vertikalen Landbewegungen verursacht sein.

Im Gegensatz zu früheren Forschungsarbeiten zeige ich, dass vertikale Landbewegung nicht als ein linearer Prozess betrachtet werden sollte, da sie durch eine Vielzahl nichtlinearer Prozesse wie tektonischer Aktivität,

Massenveränderungen oder menschlichen Ursachen beeinflusst wird. Diese nichtlinearen Prozesse erhöhen die Unsicherheiten in Meeresspiegelprojektionen an den Küsten im Vergleich zu den aktuellen Schätzungen des aktuellen IPCC (Intergovernmental Panel on Climate Change) Berichts [Fox-Kemper et al., 2021]. Demnach erklären die vertikalen Landbewegungen 39% der kombinierten Unsicherheiten der relativen Meeresspiegeländerung in globalen Projektionen. Die bisher vernachlässigten zeitvariablen Effekte wirken sich also signifikant auf die Konfidenzintervalle in Projektionen relativer Meeresspiegelveränderungen aus. Diese Ergebnisse bekräftigen die Notwendigkeit, beobachtungsbasierte vertikale Landbewegungen in Meeresspiegelstudien einzubeziehen, um diese zeitvariablen Prozesse besser zu verstehen und zu modellieren.

Die in dieser Arbeit entwickelte Rekonstruktion der vertikalen Landbewegungen ist wichtig für eine Vielzahl multidisziplinärer Untersuchungen, die sich mit zukünftigen Auswirkungen auf die globalen Küsten beschäftigen. Schätzungen vertikaler Landbewegungen sind insbesondere essentiell für die Berechnung von absoluten Meeresspiegeländerungen auf Grundlage der Daten von Pegelmessstationen. Letzteres ist wichtig, um die Ursachen der Meeresspiegelveränderungen an der Küste sowie die Entwicklung der historischen Veränderungen im letzten Jahrhundert zu verstehen. In dieser Dissertation wird gezeigt, dass die bereitgestellten Schätzungen der vertikalen Landbewegungen geeignet sind, um die vertikalen Landbewegungen an den Pegeln im letzten Jahrhundert zu bestimmen, da die daraus resultierenden Abschätzungen der absoluten Meeresspiegeländerungen in hohem Maße mit den Schätzungen bestehender Arbeiten übereinstimmen.

In Anbetracht des zum Teil nichtlinearen Verhaltens der vertikalen Landbewegung motiviert diese Arbeit dazu, dessen Rolle als dynamische Komponente der relativen Meeresspiegelveränderungen neu zu überdenken. Ich empfehle weitere Untersuchungen, um besser zu verstehen, wie sich vertikale Landbewegungen im letzten Jahrhundert verändert haben sowie zusätzliche prozessbasierte Szenarien für zukünftige Veränderungen der vertikalen Landbewegungen zu entwickeln. Da die stark besiedelten Küsten überproportional dem durch Landabsenkungen verursachten relativen Meeresspiegelanstieg ausgesetzt sind, aber kaum mit GNSS-Stationen ausgestattet sind, sollten sich künftige Bemühungen auf die Verbesserung der Verfügbarkeit der Messungen in diesen Regionen konzentrieren.

Preface

During some of the conferences I attended during my PhD program, I kept asking some of the senior scientists what they thought was the most important success factor in their career. Interestingly, the most common answer was luck. I would have expected answers like perseverance, diligence, or simply talent, but I still got the rather modest answer: luck.

Luck was often associated with seemingly random opportunities, being at the right place at the right time, or random and lucky new collaborations. However, the answer luck was still somehow a very unsatisfying answer for me, since luck is something you can't seem to actively control.

Even though I would like to have an answer to the question of success, I have to agree with my colleagues that many things are out of our control and often seem to be a product of chance. In retrospect, my journey through the doctoral studies was also a chain of fortunate external coincidences, events, conditions, and encounters that were actually not a direct product of my actions. First and foremost, I was lucky to be mentored by such supportive and motivating supervisors as Marcello and Florian, lucky to be connected to many great people like Marta or Kiko, and lucky that my project was already so well planned from the start by Marcello and Laura. Therefore, I would like to express my sincere gratitude to my supervisors and colleagues in the acknowledgements (section 5.4), without whose support this work would not have been possible. Actually, my whole decision to go to DGFI in Munich was very fortunate. Before that, I studied at the University of Hamburg and the Max-Planck Institute of Meteorology, where I could well imagine staying. Then, by chance, there was a good offer in Munich at the right time, which ultimately gave me a lot of new perspectives and opportunities.

So does that mean that ultimately everything is controlled by randomly distributed luck or can we influence the probability of experiencing luck in some way? I believe that sometimes there is indeed a possibility to influence one's luck. Here I would like to make an analogy to one of the methods I use in this thesis: Bayesian Statistics and Markov chain Monte Carlo methods. In Bayesian statistics, one usually tries to find a probability distribution of a parameter. Applied to real life, this would be, for example, the search for the next topic for a paper, for the next collaboration partner, for the most promising project proposal, or the best career decision. In Bayesian statistics, the probability distribution of a parameter is often inferred by exploratory analysis. For this purpose, Markov chain Monte Carlo (MCMC) methods are used, which generate many different samples of a variable, based on which a probability distribution of the unknown variable can be found. The Markov chain usually starts at a value associated with a prior assumption about the actual value of a parameter. Then the Markov chain iteratively jumps from state to state so that the totality of all sampled states forms a probability distribution that converges to the true probability distribution of a parameter. In our real-life example about the pursuit of luck and success, that would be us trying out a new idea or a career path that we initially believe will work. Similarly as MCMC methods, we iteratively try out new ideas or different life choices, constantly accepting or rejecting ideas or choices depending on whether they work for us. The degree of success of these ideas or decisions strongly determines how far we stray or move away from our

original convictions. In this context, I see the term 'luck' as describing a particular state that has beneficial effects for us and that we have discovered (seemingly by accident) after exploring many other states. As an example, this means that out of a dozen ideas, one idea worked really well, that out of 100 people met, one person had a really favorable impact on us, or that out of 10 missed opportunities, one had a really beneficial impact on our career path. What fundamentally matters here is our ability to reject states that don't work, accept and recognize states that work well, and finally explore enough states to find an optimal number of good states. All of these properties are also essential in MCMC methods, which can differ greatly in how well they explore a probability space and how efficient they are in that process.

Now let me give you my final thoughts on luck seen in a Bayesian framework. I do not disagree that luck is an essential factor for success and can usually be not controlled. However, I believe that our actions share similarities with these MCMC methods, that can increase the probability of encountering these lucky states. One of these characteristics that I have seen in particular in Marcello and Marta is unconditional positivity and passion: These character traits are virtually the momentum required to pull off many different attempts. Another factor is efficiency: give up an idea if it doesn't work after a certain time and don't get lost in modes with lower probability! One of the biggest mistakes might actually be to dogmatically hold on to an originally bad idea. Also in Bayesian statistics there is the term 'multimodality' that describes multiple local maxima in the probability space, which may not present the global maximum, i.e., the globally best state, or choice. These considerations underline that it is important to constantly seize opportunities and that I finally started this journey is probably my small contribution to these happy and lucky moments of the last four years.

Finally, I would like to leave you with some final words about the leitmotif of this work. In this doctoral thesis I determine the impacts of vertical land motion (VLM) on relative sea level changes. When we started the project we had a relatively clear idea of what we wanted to do. We wanted to estimate VLM as linear trends along the coasts, and then extrapolate them into the future or the past. However, in analyzing many individual time series, I often found that VLM was much more variable and often could not be well described with a purely linear trend. Although many movements are on the order of ± 10 mm/year, some processes can cause much larger movements, or even instantaneous displacements up to 1 m. These non-linear effects eventually became the central topics of my 2nd and 3rd papers, which is just another nice example of how updating one's prior beliefs can lead to very different final outcomes.

Nonlinear relationships and systems are usually much more difficult for us to understand than purely linear ones. Very likely, that is exactly what makes them so interesting. In the context of this work, nonlinearities are not only found in the variability of VLM, but also in the distribution of the regional impacts of relative sea level change. In particular through my collaboration with Robert Nicholls, I have become aware of how non-uniformly and non-linearly the population is distributed along the world's coastlines: The bulk of the coastal population (more than 90%) covers only about 1% of the total coastal length. At the same time, most of the important observations of vertical land motion and relative sea level change (GNSS and tide gauges) are usually not (publicly) available in these highly populated regions. This poses enormous challenges to estimate the impacts of relative sea level change and future damages in these regions, especially when some processes (VLM) are highly non-linear and partially unpredictable. With this work, I would like to draw attention to these difficulties and present proposed solutions and recommendations. Since I am sure that I have not yet found the 'globally optimal solutions' here, this work shall motivate further efforts to better understand and

quantify nonlinear VLM, and determine its influences in past, contemporary and future relative sea level changes.

The main results of this work are part of previous publications and studies which are still in submission or preparation. In the main body (sections 2 to 4) I mark the text content (sentences, paragraphs and figures), which are directly taken from the associated articles by the following colored symbols:

P1: > ... < Oelsmann, J., Passaro, M., Dettmering, D., Schwatke, C., Sánchez, L., and Seitz, F. (2021): *The zone of influence: matching sea level variability from coastal altimetry and tide gauges for vertical land motion estimation*, Ocean Sci., 17, 35–57, DOI: 10.5194/os-17-35-2021.

P2: > ... < Oelsmann, J., Passaro, M., Sánchez, L., Dettmering, D., Schwatke, C., and Seitz, F. (2022): *Bayesian modelling of piecewise trends and discontinuities to improve the estimation of coastal vertical land motion*. J Geod 96, 62. DOI: 10.1007/s00190-022-01645-6.

P3: > ... < Oelsmann, J., Marcos, M., Passaro, M., Sánchez, L., Dettmering, D., Dangendorf, S., and Seitz, F. (2023): *Vertical land motion reconstruction unveils non-linear effects on relative sea level*, submitted

P4: > ... < Oelsmann, J., Nicholls R., Lincke D., Marcos, M., Sánchez, L., Dettmering, D., Hinkel J., and Seitz, F. (2023): *Coastal populations experience sea level rise twice as large as the global average*, in preparation

Throughout the thesis, I also refer to other publications related to my contributions to the SL_cci project [e.g., Oelsmann and Passaro, 2022, Cazenave et al., 2022]. Parts of the data and software described in this thesis can be found at Oelsmann et al. [2022b], ZENODO, <https://doi.org/10.5281/zenodo.8308347>, <https://github.com/oelsmann/discotimes>, and <https://github.com/oelsmann/bpca>.

Contents

Abstract	iii
Zusammenfassung	v
Preface	vii
1 The role of vertical land motion for relative sea level change	1
1.1 Introduction	1
1.2 Components of regional to local relative sea level changes	3
1.3 Estimating relative sea level change	7
1.4 Challenges and research objectives	11
1.4.1 Improving the determination of vertical land motion using coastal altimetry and tide gauge data	12
1.4.2 Probabilistic reconstruction of vertical land motion	13
1.4.3 Understanding the impacts of vertical land motion on relative sea level change	14
1.5 Outline	16
2 Improving the determination of vertical land motion using coastal altimetry and tide gauge data	17
2.1 Introduction	17
2.2 Datasets and combination approaches	18
2.3 The Zone of Influence - coherent sea level variations in the coastal zone	19
2.4 Global validation of vertical land motion estimates	22
2.4.1 Trend and uncertainty estimation	23
2.4.2 Comparison of different dataset configurations	24
2.5 Discussion	28
3 Probabilistic reconstruction of vertical land motion	33
3.1 Introduction	33
3.2 Vertical land motion time series analysis	36
3.2.1 Bayesian modeling of piecewise trends and discontinuities	36
3.2.2 Sensitivity experiments with synthetic data	40
3.2.3 Discontinuity detection in multi-technique observations	45
3.2.4 Validation with external data and alternative algorithms	52
3.2.5 Discussion	54

3.3	Bayesian vertical land motion reconstruction	54
3.3.1	Pre-processing of the data	54
3.3.2	Bayesian principal component analysis	55
3.3.3	Bayesian transdimensional regression	57
3.3.4	Validation	59
3.3.5	Discussion	60
4	Understanding the impacts of vertical land motion on relative sea level change	63
4.1	Introduction	63
4.2	Non-linear vertical land motion along global coastlines	64
4.3	The contribution of vertical land motion to contemporary regional sea level change	66
4.4	Non-linear vertical land motion limits regional coastal sea level change projections	70
4.5	Exposure of coastal populations to contemporary relative sea level change	73
4.6	Discussion	77
5	Conclusions	81
5.1	Improving the determination of vertical land motion using coastal altimetry and tide gauge data	81
5.2	Probabilistic reconstruction of vertical land motion observations	82
5.3	Understanding the impacts of vertical land motion on relative sea level change	84
5.4	Recommendations	85
	Abbreviations	93
	Bibliography	95
	Acknowledgements	117
	Appendix	119
1	Model initialization	119
2	Model selection strategies	119
3	Piecewise and linear trend validation	121
4	Comparison of InSAR and GNSS VLM data	122

1 The role of vertical land motion for relative sea level change

1.1 Introduction

In 2013, the province of Bohol, Philippines got struck by a 7.2-magnitude earthquake. As a consequence, many coastal communities around Tubigon subsided by about 40 cm. Ever since then, one of the surrounding islands, Isla Batasan, experiences regular flooding during high tides, such that the island is completely inundated for 135 days a year [Jamero et al., 2016, 2017]. Despite these flooding events, most of the inhabitants are reluctant to relocate to the mainland and rely on limited adaptation measures like stiling houses or raising floors using coral stones. Isla Batasan makes a compelling case of the vulnerability of small, low-lying, and developing island states where local processes such as land subsidence exacerbate climate-change-induced sea level change. In fact, in many major coastal cities, like Tokyo, Shanghai, Bangkok, Jakarta, and New Orleans, human-induced land subsidence has exceeded contemporary rates of sea level change, with subsidence of up to 4 m in the last century [Nicholls et al., 2021]. Understanding this entanglement of vertical land motion (VLM) and absolute sea level change is thus fundamental to assessing future flood risks, planning coastal adaptation, or motivating mitigation. In this dissertation, I develop a novel approach to estimate the variability and uncertainty intervals of vertical land motion over the last 25 years based on direct observations. I use these estimates to provide projections of future relative sea level changes, which represent an important benchmark for coastal planning on a global scale.

Global sea level rise has become one of the most direct consequences of global warming. Over the 20th century, the GMSL rose at rates of 1.4 mm/year [Church and White, 2011, Hay et al., 2015, Dangendorf et al., 2019, Frederikse et al., 2020, Fox-Kemper et al., 2021]. The rate of sea level rise started to increase at about 1820-1860 and is unprecedented over the last 3000 years [Kopp et al., 2016, Gulev et al., 2021]. In the last few years, we have gained an increased understanding of the sources of these changes [e.g., Frederikse et al., 2020]. Ice melt from glaciers as well as the Greenland Ice Sheet explained 52.3% and 29.3% of the GMSL change over the last century. Ocean heat uptake and the associated thermal expansion of water accounted for 32% of sea level rise, while land-water storage changes had an overall negative contribution of -14% [Fox-Kemper et al., 2021].

Most of our knowledge of last-century sea level change stems from long-term tide gauge records, which are however unevenly distributed along the coastlines. Thanks to the introduction of satellite altimetry in 1992, which covers the complete ocean surface, we have now a much more complete picture of global sea level change (SLC). During the altimetry era, GMSL rise has further increased to 3.25 mm/year (1993-2018) [Fox-Kemper et al., 2021]. This acceleration is expected to continue further during the upcoming decades, with projected rates of 5.2-12.1 mm/year (during 2080-2100 for the lower and higher end emission scenarios [Fox-Kemper et al., 2021]). Thus, future sea level change will pose existential challenges to low-lying coastal

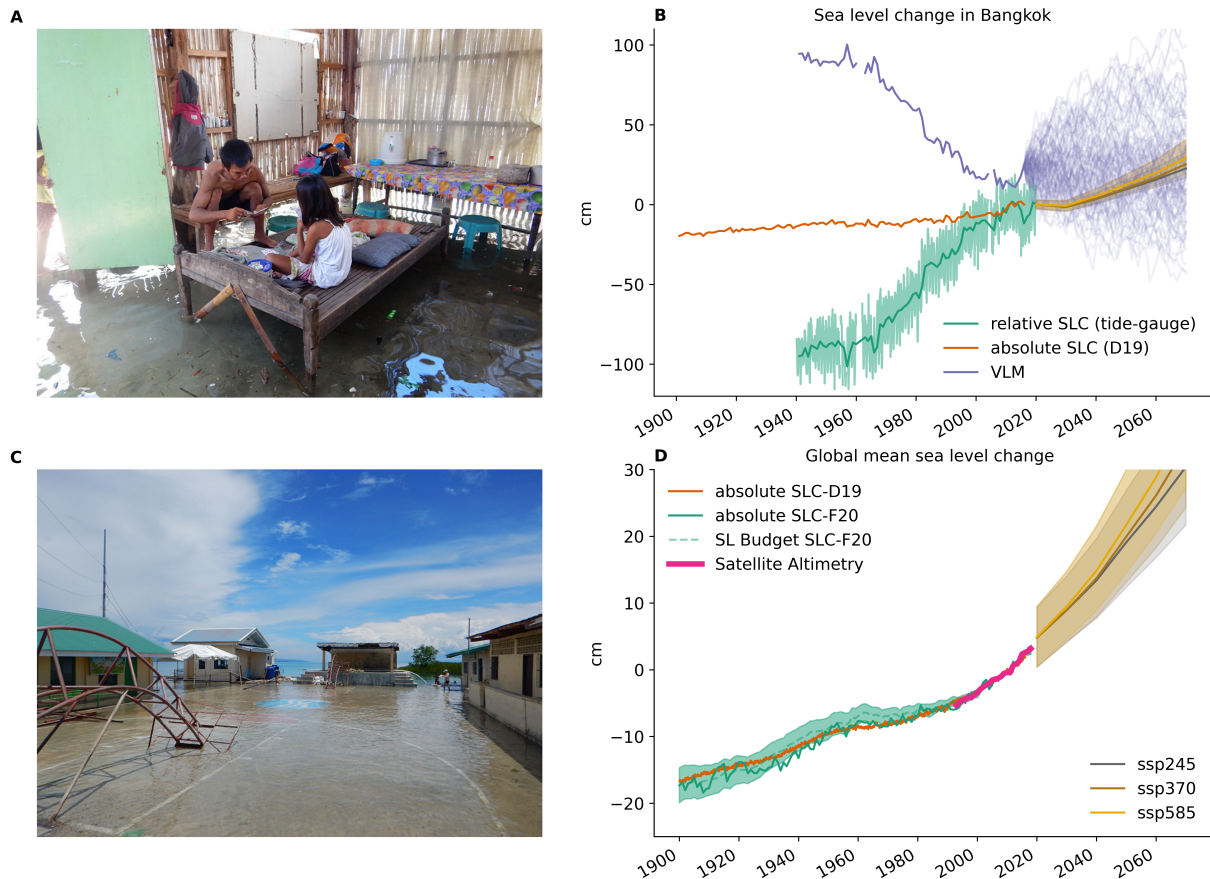


Figure 1.1 A and C show flooding of Ubay, which is one of the earthquake-affected islands near Tubigon, Bohol, Philippines (adjusted from Jamero et al. [2017]). (B) Relative sea level change (from Permanent Service for Mean Sea Level (PSMSL), green), reconstructed absolute sea level change (over the last century, Dangendorf et al. [2019], orange) and VLM (derived as the difference of the latter, purple) at the Bangkok tide gauge. Shown is also an ensemble (of many realizations) of first-order autoregressive processes, with the same noise properties as the VLM time series (and zero trend) to exemplify future VLM scenarios. Different absolute sea level projection scenarios [Garner et al., 2021b, Fox-Kemper et al., 2021] are shown in yellow, brown and grey. D shows historic Global Mean Sea Level (GMSL) reconstructions (from Dangendorf et al. [2019], orange, and Frederikse et al. [2020], green line), as well as the estimated sum of contributors (such as mass, or thermosteric effects) of the sea level budget and uncertainties (green, dashed line). The GMSL curve from satellite altimetry (green) is obtained from Frederikse et al. [2020] and based on the MEaSUREs gridded sea surface height anomalies version 1812 dataset [Zlotnicki et al., 2019]. GMSL scenarios are provided as in B.

populations. It is estimated that more than 300 million people will be directly affected by sea level change in 2050 [Nicholls et al., 2021], and estimated investments costs of coastal adaptation range in the order of several hundreds of billions of USD per year globally [Oppenheimer et al., 2019]. Therefore, understanding the components and processes of past sea level change is fundamental to bolster estimations of the trajectories of future sea level change and its consequences.

To assess future sea level change impacts, for two decades the world climate research program dedicates efforts to generate sea level projections based on the Coupled Model Intercomparison Project (CMIP) [Eyring et al., 2016]. Estimates of future contributions to sea level change from, for example, ice melt or the thermal expansion of the ocean rely on different underlying future emission scenarios, so-called shared socioeconomic pathways (SSPs, e.g., see Fig. 1.1D). These simulations, together with observations of satellite altimetry, pro-

vide crucial information on *absolute* sea level change (i.e., the change with respect to a reference ellipsoid see also Fig. 1.4), which approximates the *geocentric* sea level change, i.e., the change with respect to the center of mass of the earth [Stammer and Cazenave, 2017]. However, as exemplified by the subsiding Isla Batasan, for coastal populations, *relative sea level change* is the most important quantity. Relative sea level changes depict sea level changes relative to the land (or sea floor) and are thus influenced by both vertical land motion and absolute sea level rise. This concept can be easily explained using the case of the city of Bangkok (Fig. 1.1B). Shown are the relative sea level change measurements of a tide gauge, as well as an estimate of absolute sea level rise (together with effects from earth gravity, earth rotation and solid-earth deformation (GRD)) over the last century at the coast [Dangendorf et al., 2019]. The relative sea level change significantly exceeded the climate-induced absolute sea level change by a factor of four to five during the last century, which was mainly caused by strong land subsidence of about 80 cm. Thus, at this coastal location vertical land motion represents the dominant contributor to the coastal relative sea level budget.

As in many other large coastal cities, land subsidence due to human-related groundwater extraction has played the main role in relative sea level changes over the last century and is expected to do so in future [Raucoles et al., 2013, Wöppelmann and Marcos, 2016, Nicholls et al., 2021, Tay et al., 2022]. Because many highly urbanized coastal areas are affected by land subsidence, relative sea level changes can be up to four times faster than the contemporary global average rates [Liu et al., 2020, Nicholls et al., 2021]. Thus, regional-scale coastal subsidence and uplift can either amplify or alleviate the regional impacts of sea level rise [Wöppelmann and Marcos, 2016, Pfeffer et al., 2017, Hawkins et al., 2019b, Hammond et al., 2021]. A central challenge to regional-scale sea level change impact assessment is, that neither vertical land motion nor absolute sea level change affects coasts in a uniform manner. Therefore, future planning relies on accurate estimates of the rates and variability of vertical land motion, which can be assessed using a variety of observational techniques [Santamaría-Gómez et al., 2014, Kleinherenbrink et al., 2018, Frederikse et al., 2019, Buzzanga et al., 2020, Hammond et al., 2021], or geodynamic process models of the solid earth [Peltier, 2004].

Depending on the location, vertical land motion will significantly contribute to the projected changes and uncertainties, as exemplified by the different trajectories of vertical land motion and absolute sea level change in Fig. 1.1B. To make assumptions about these future changes, we need to learn from observations of the past and present behavior of vertical land motion. The major objective of this work is to exploit a comprehensive network of observations to determine contemporary vertical land motion and its uncertainties, which are used to inform future projections of relative sea level change.

1.2 Components of regional to local relative sea level changes

Although this work focuses primarily on the contribution of vertical land motion, it is helpful to consider the full spectrum of processes that affect coastal sea level change to understand their compound impacts on relative sea level. Coastal relative sea level is influenced by a complex superposition of ocean, cryosphere, and solid-earth processes that act on manifold temporal and spatial scales. Relative sea level change is often decomposed into its contributions from absolute sea level change and vertical land motion (see also schematic in Fig. 1.4). As I will show, this separation is sometimes not straightforward, because some processes that are associated with mass redistribution in the earth system can have an impact on both, absolute sea level change and vertical land motion. In the following, I provide a brief overview of the most important concepts,

definitions, and drivers of relative sea level change. Knowledge of the spatiotemporal characteristics of these processes is fundamental to comprehending the current challenges of observing and estimating the individual components of relative sea level change.

Causes of absolute sea level change

Absolute sea level changes are driven by the thermal expansion of the ocean, i.e., the *thermosteric* sea level component, by halosteric changes (i.e., changes in seawater salinity), as well as by mass changes due to land ice melt or land water storage changes, which contribute to the *barystatic* sea-level change. Depending on the source of ice melt or land water storage changes, the barystatic effects cause large-scale sea level responses, so-called fingerprints, which are associated with changes in the ocean mass, the geoid as well as with the solid earth [e.g. Dangendorf et al., 2021]. Superimposed to these large-scale contributions are changes in ocean circulation, as well as ocean density changes generating sea level variability on a much wider range of spatial and temporal scales. Density changes (steric changes) are driven by thermosteric and halosteric effects. Ocean circulation influences sea level due to the redistribution of mass (i.e., manometric changes), heat, and freshwater, which contribute to changes in the ocean density. Atmospheric forcing like wind stress, sea level pressure changes, air-sea heat and freshwater exchange, and other natural and anthropogenic effects shape and control these changes in the ocean state. These processes generate sea level variability at a broad spectrum of timescales. Hence, long term trends or multidecadal variability are superimposed by short term, monthly to interannual changes, which are often associated with high regional variability, as can be seen for example by the mesoscale variations in the Alghulas Current or Gulf Stream region in Fig. 1.2A. For relatively short periods of observations (like the altimetry era, i.e., 1992 - present), regional sea level change can thus strongly deviate from the GMSL change by several mm/year [e.g. Stammer et al., 2013].

In the coastal zone, sea level dynamics can differ substantially from open ocean variability, mainly due to the modulation of open ocean signals by the presence of coastlines and changes in bathymetry [Hughes et al., 2019]. Coastal sea level variations are governed by many different processes associated with different amplitudes and time scales. High frequency variations (time scales of minutes to days) include processes like coastal gravity waves, seiches, surges, and tides. On longer periods (daily to interannual scales), wave setup, continental boundary waves, and river runoff dominate coastal sea level variability [e.g., Woodworth et al., 2019]. Many of these processes are, however, not yet fully understood. In particular the dynamics of wave setup, river runoff, coastally trapped waves, tides, and their impact on coastal sea level are the subject of ongoing research [e.g., Hughes et al., 2019, Hart-Davis et al., 2021, Toomey et al., 2022, Piecuch, 2022]. Because some of these processes are associated with very small spatial scales, observing coastal sea level variations has become a central objective for satellite altimetry [Passaro et al., 2014, Cazenave et al., 2022].

Causes of vertical land motion

As demonstrated by the subsiding Isla Batasan and Bangkok, vertical land motion can cause relative sea level changes to be fundamentally different from absolute sea level change. For this reason, relative sea level changes (Fig. 1.1C) measured by tide gauges, show quite a different picture from what we observe by satellite altimetry (Fig. 1.1A). Similarly, as for absolute sea level variability, different processes cause distinct spatiotemporal variability in vertical land motion, with spatial scales ranging from several thousands of km to a few km only, and temporal scales from millennia to seconds.

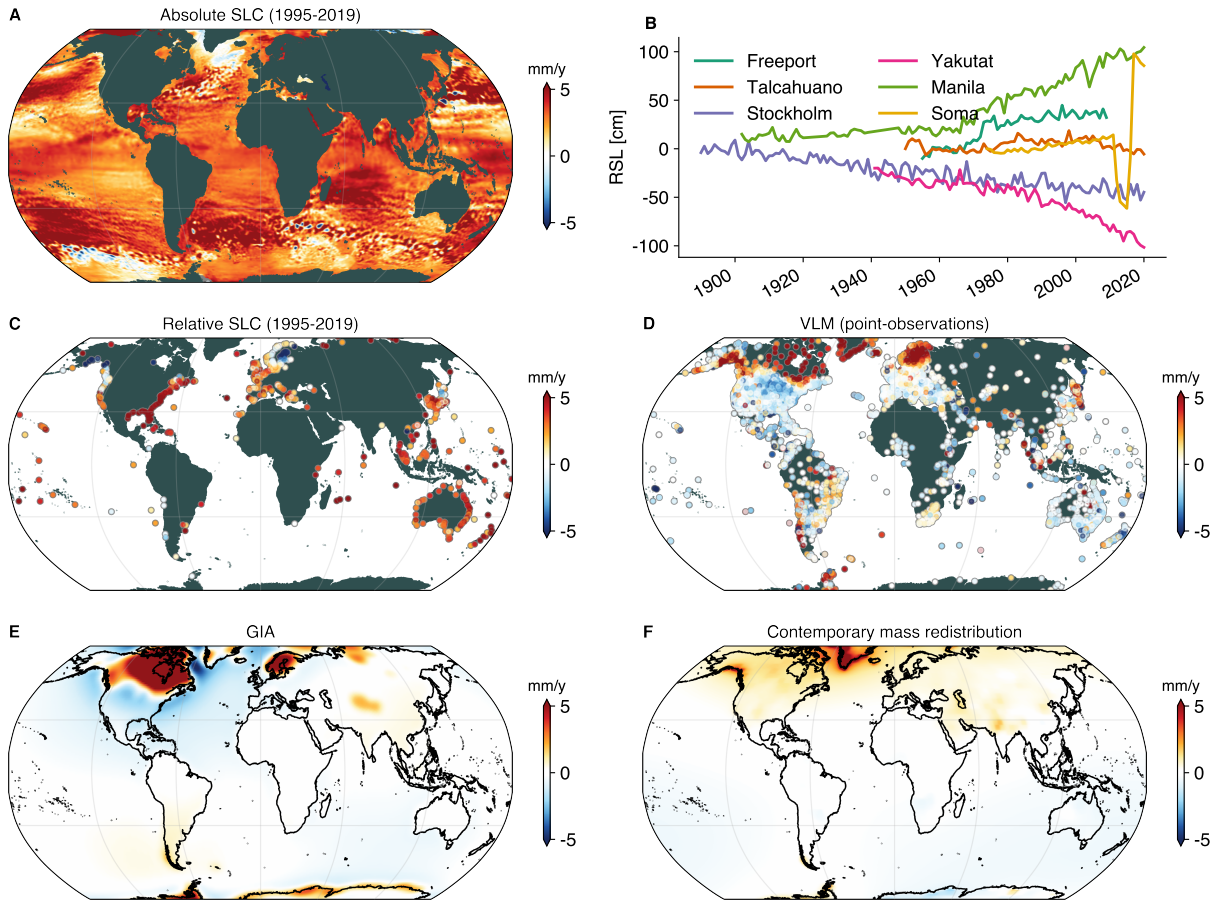


Figure 1.2 A depicts absolute sea level change over 1995-2019 based on gridded altimetry from the Copernicus Marine Environment Monitoring Service (CMEMS; <http://marine.copernicus.eu>, last access: 10 December 2020). B and C show Relative sea level (RSL) time series and trends from tide gauge observations (PSMSL). VLM from point-observations (as derived in chapter 3), from Glacial isostatic adjustment (GIA) [Caron et al., 2018] and from contemporary mass redistribution [Frederikse et al., 2019] are shown in D, E and F.

Among the most pronounced sources of global scale vertical land motion are changes in the cryosphere, i.e. changes in the land ice mass. The melting of the great ice sheets after the Last Glacial Maximum (LGM), approximately 21,000 years ago, caused a process called *glacial isostatic adjustment*, which manifests itself with ongoing changes in GRD. On decadal and centennial time scales, changes in ice mass loading generate almost instantaneous elastic responses of the lithosphere, i.e., the Earth's surface recovers approximately proportional to the change in ice mass [Pugh and Woodworth, 2014]. On much longer time scales from hundreds to thousands of years, deglaciation causes visco-elastic processes to attain isostatic equilibrium. Mantle material flows back to the centers of formerly glaciated areas. This causes ongoing uplift (also called post-glacial rebound) in areas like Fennoscandia, Canada, and other parts of North America, and subsidence in the forebulge areas of the LGM ice sheets (Fig. 1.2E). These long-term effects are now commonly described by the term *glacial isostatic adjustment* or *GIA* [e.g. Pugh and Woodworth, 2014, Peltier, 2004, Mark E. and Jerry, 2011].

Vertical land motion due to GIA has a direct effect on relative sea level and has led to falling sea levels, for example, in cities like Stockholm or Yakutat (Fig. 1.2B). Next to the GIA-induced solid-earth deformation, there are also secondary effects, i.e. changes in the Earth gravity and Earth rotation. Solid-earth mass changes

alter the geoid and cause increased gravitational attraction in areas where the mantle material accumulates, and vice versa. This in turn leads to a redistribution of water with ancillary mass loading effects [King et al., 2012]. The solid-earth deformations are also accompanied by changes in the shape of the ocean sea floor and an increase in the ocean volume, which is associated with a slight overall geocentric sea level fall on a global average [Mark E. and Jerry, 2011]. Hence, GIA is affecting relative sea level change via changes in absolute sea level as well as via vertical land motion.

While GIA is associated with visco-elastic changes in the Earth on very long time scales, contemporary mass redistribution (CMR) generates GRD responses on much shorter time scales (i.e., intraannual to decadal time scales). These surface mass loading changes are associated with changes in hydrological loading, i.e. due to terrestrial water storage changes, atmospheric and oceanic loading, as well as changes in the cryosphere (due to mass changes of ice sheets and glaciers, e.g., Slangen et al. [2014], Kopp et al. [2014], Frederikse et al. [2019]). CMR-induced vertical land motion can be non-linear, due to non-linear melting rates, and can also exhibit substantial seasonal variations with regional amplitudes of more than 1 cm, which are most pronounced in tropical regions [Ray et al., 2021]. Thanks to the Gravity Recovery And Climate Experiment (GRACE) [Tapley et al., 2004] we can infer CMR-induced changes in the gravity field and their impacts on the solid earth [e.g. Frederikse et al., 2019]. Figure 1.2F shows an estimate of linear rates of vertical land motion caused by changes in CMR, which are mainly derived from GRACE data [Frederikse et al., 2019]. Changes in the cryosphere govern trends in CMR and lead to subtle uplift signals in the order of 0.5 mm/year over Northern Europe and America, and subsidence over Australia. Even though these effects are about one order of magnitude smaller than vertical land motion from GIA, knowledge of CMR is fundamental to understanding and disentangling the different vertical land motion components observed by geodetic measurements and for extrapolating relative sea level changes into the past and the future.

Another source of vertical displacements of the solid earth is tectonic activity, acting on a large range of time scales from seconds to millions of years [Shirzaei et al., 2021]. Convergence between tectonic plates is a central cause for vertical land motion along continental margins [Mazzotti et al., 2008, Pugh and Woodworth, 2014]. Earthquakes often lead to instantaneous vertical displacements on the order of cm to m (i.e., as shown by the earthquake-affected tide gauge in SOMO, near Fukushima) and are in many cases followed by postseismic deformation [Vigny et al., 2011, Imakiire and Koarai, 2012, Gunawan et al., 2014]. Interseismic phases can be interrupted by slow-slip events, which make it particularly challenging to determine the interseismic trends [Houlié and Stern, 2017, Naish et al., 2022]. Next to these highly non-linear effects, other tectonic motions sustain for thousands to millions of years, for example, the continental collision that led to the formation of the Alpine orogeny [Serpelloni et al., 2013, Sánchez et al., 2018]. Previous studies used coastal sea-level proxies to infer these long-term tectonic rates [Pedoja et al., 2018]. However, in case of highly temporally and spatially variable tectonic VLM, its determination relies on direct observations and is particularly challenging for sea level research [Klos et al., 2019].

Several other processes like erosion [Gómez et al., 2021], subsurface fluid withdrawal [Emery and Aubrey, 1991b, Kolker et al., 2011, Liu et al., 2020], sediment loading and compaction [Ericson et al., 2006, Törnqvist et al., 2008, Syvitski et al., 2009], volcanism and mantle dynamics [Kreemer et al., 2020] further complicate the determination of vertical land motion. Processes like groundwater depletion not only affect the solid Earth, but also alter gravitational attraction and absolute sea level in the far field by a redistribution of water mass [Wada et al., 2012, Veit and Conrad, 2016]. Vertical land motion caused by the human-induced extraction

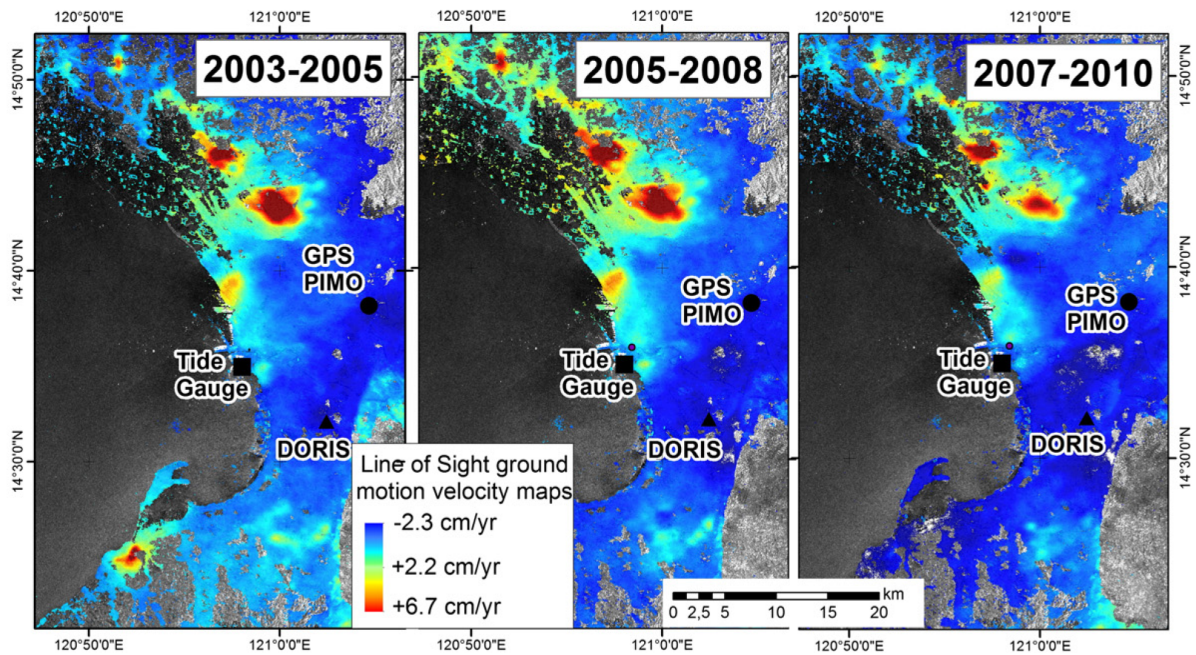


Figure 1.3 Adjusted from Fig. 4. B of Raucoules et al. [2013]: Line of Sight ground motion velocity maps in cm/yr for 2003–2005, 2005–2008, and 2007–2010 (Envisat/Advanced Synthetic Aperture Radar (ASAR) data).

of groundwater, oil, and gas has strongly contributed to the total relative sea level change in many urban areas around the world [Brooks et al., 2007, Raucoules et al., 2013, Buzzanga et al., 2020, Zanchettin et al., 2021, Nicholls et al., 2021, Tay et al., 2022]. Time-varying human-induced extraction rates can lead to highly non-linear vertical land motion on very small spatial scales in the order of a few km. Figure 1.3 shows such high spatial and temporal variability in Manila based on Interferometric Synthetic Aperture Radar (InSAR) observations. Large parts of the city are subsiding with rates up to 23 mm/year due to extensive groundwater use in the area. Note, that Fig. 1.3 also indicates the station locations of point-wise measurements of relative sea level and vertical land motion. The strong spatiotemporal vertical land motion variations hamper meaningful extrapolations of observed vertical land motion in time or space, when based on these point-wise observations. Therefore, our capability of resolving certain small-scale processes strongly depends on the type and availability of direct vertical land motion observations and the characteristics of the spatiotemporal variability of vertical land motion itself.

1.3 Estimating relative sea level change

Several strategies have been developed to estimate the contribution of the individual components of relative sea level change. Figure 1.2 summarizes the most important approaches and observing systems to assess relative sea level change on a global scale: tide gauges, satellite altimetry, Global Navigation Satellite System (GNSS), GRACE, and GIA models. Other approaches, like InSAR [Buzzanga et al., 2020, Tay et al., 2022] or geological observations [Engelhart et al., 2009] have so far been used mainly at the regional to local scale and will therefore not be explained in detail here. The methods depicted in Fig. 1.2 provide estimates of different components of relative sea level at different spatial/temporal scales, and different precision and accuracy levels. Given the individual merits and limitations of these methods, a central objective of this work is to

comprehensively synthesize and exploit these data sources, to gain a more complete picture of past, contemporary, and future relative sea level change. In the following, I provide a general overview of the different observational techniques and their applications in sea level research.

Tide gauges

Tide gauge observations represent an invaluable source of information on relative sea level. Because some of the tide gauge measurements date back until the 17th century, they represent a window into the century-long history of sea level change and thus are essential constraints for sea level reconstructions or budget analyses [e.g., Church and White, 2011, Hay et al., 2015, Dangendorf et al., 2019, Frederikse et al., 2020]. Several other research fields, like tidal estimation, extreme sea level analyses, or validation and calibration of satellite altimetry, to name a few, rely on tide gauge measurements. Given its importance, services like PSMSL, the University of Hawaii Sea Level Center (UHSLC), or the Global Extreme Sea Level Analysis (GESLA) dedicate efforts to processing and collecting tide gauge data from national databases or local authorities. As can be seen in Fig. 1.2C, the tide gauge station distribution is still relatively inhomogeneous and most of the more than 800 active tide gauges (of the PSMSL database) are located in places like Europe, North America, or Australia. Because *relative sea level* measurements by tide gauges are influenced by vertical land motion and absolute sea level change, additional information on vertical land motion at the tide gauges is required to study the local rates of absolute sea level change. Aligning external vertical land motion estimates with the rates experienced at the tide gauge can sometimes be challenging, as tide gauges often underestimate shallow subsidence (occurring in the upper 5 m) when anchored at deeper levels [Keogh and Törnqvist, 2019]. Several different approaches have been applied to estimate vertical land motion at tide gauges, which were based on using information from GNSS data, GIA models, satellite altimetry, or indirect methods like sea level reconstructions. In this thesis, I aim to densify and improve vertical land motion estimates with respect to existing approaches, which will be in part indirectly based on relative sea level data from tide gauge observations.

Satellite altimetry

Thanks to the continuous observations of satellite altimetry since three decades, and due to ongoing improvements in coastal altimetry products, measurement gaps of sea level along the global coastlines are now being closed [e.g. Cazenave et al., 2022]. Figure 1.4 summarizes some of the most important concepts to understand the principle sea level measurements by satellite altimetry. Here, the term *sea level* refers to the absolute sea level, which is the *sea surface height (SSH)* with respect to a *reference ellipsoid*, as shown in Fig. 1.4. The reference ellipsoid is a surface of an ellipsoidal volume, which is defined to approximately resemble the *geoid*, a surface with uniform geopotential [e.g. Heiskanen and Moritz, 1984, Gregory et al., 2019]. Several different reference ellipsoids exist, i.e. the TOPEX/Poseidon ellipsoid [Stammer and Cazenave, 2017], the GRS-80 (Geodetic Reference System, 1980; [Moritz, 2000]) ellipsoid, or the WGS-84 ellipsoid, which differ slightly in their parameters.

Information on SSH is derived from the satellite altitude (H) and range (D), which is the measured distance between the altimeter and the sea surface [e.g., Stammer and Cazenave, 2017]. The velocity and position of the altimeter are determined by Precise Orbit Determination (POD) using tracking systems like GNSS, Satellite Laser Ranging (SLR) systems or Doppler Orbitography and Radiopositioning Integrated by Satellite (DORIS) [e.g., Jäggi and Arnold, 2017, Rudenko et al., 2023]. The altimetric range is measured by transmitting

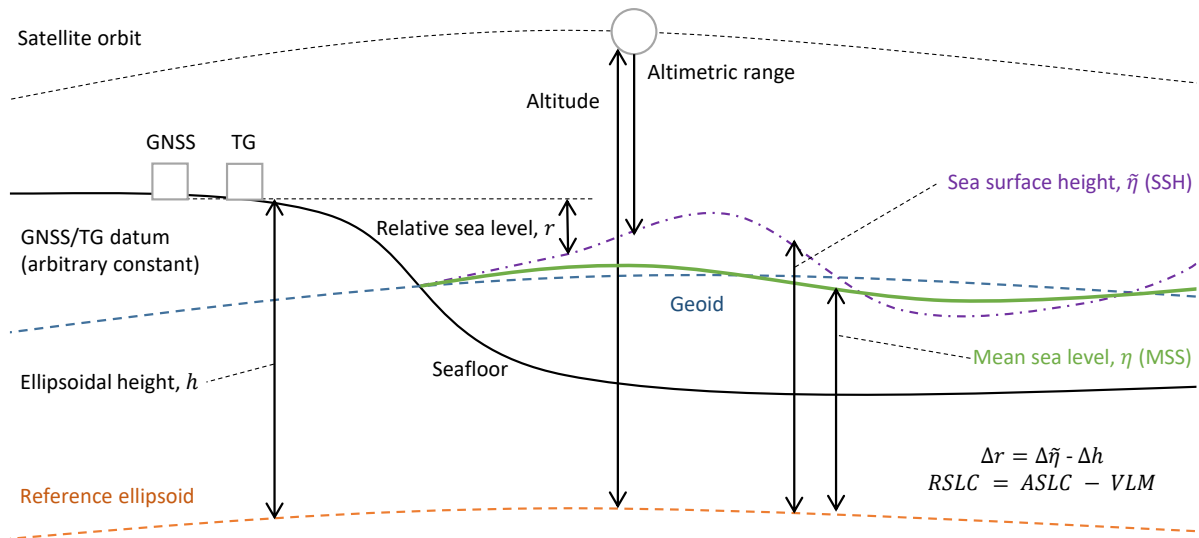


Figure 1.4 Schematic of measurement systems and surfaces relating to sea level (see also Wöppelmann and Marcos [2016] or Gregory et al. [2019]).

radar pulses, which are reflected by the sea surface and then recorded by the altimeter. The received signal can usually be mathematically described by a waveform-like function from which several quantities like the range, wave height, or surface wind speeds can be derived.

Several corrections and adjustments have to be applied to obtain accurate range estimates from these radar measurements (e.g., as summarized by Andersen and Scharroo [2011]): the instrumental errors, the effects due to the presence of the atmosphere (dry and wet tropospheric correction), and the adjustments due to the interaction of the signal with the sea surface. Such adjustments include also the possibility to remove unwanted geophysical signals. Research focused on ocean dynamics or temporal variations in sea level is usually interested in the *Sea level anomaly (SLA)* with respect to a time mean of SSH, called mean sea level or *mean sea surface*. SLAs are commonly additionally corrected for signals from other prevalent geophysical effects, which are often not of primary interest in a variety of applications. Among these geophysical corrections, the tidal correction is one of the most important ones, because tidal variability explains a large fraction of sea level variability, particularly in the coastal zone [Andersen and Scharroo, 2011]. The Dynamic atmospheric correction (DAC) removes dynamical adjustments of the ocean to changes in atmospheric pressure.

This very brief overview emphasizes the large number of factors that must be accounted for to derive accurate SLA estimates from satellite altimetry measurements. All of these adjustments and corrections represent potential error sources, which propagate into the final SLA data. Note, that there are several other error sources, stemming from altimeter drifts, mission cross-calibration, or altimeter footprint contamination in the coastal zone, which have so far not been mentioned. Hence, current efforts are dedicated to further improving geophysical and range corrections, honing coastal retracking, and decreasing radial orbit errors [e.g., Passaro et al., 2014, Cazenave et al., 2018]. As a response to these improvements, uncertainty recommendations for GMSL change have changed from 1 mm/year to 0.3 mm/year over the last decades [Ablain et al., 2019, Abdalla et al., 2021].

Global Navigation Satellite Systems

Next to relative and absolute sea level measurements by tide gauges and satellite altimetry, respectively, > for more than a decade, direct geodetic height measurements (GNSS, such as Global Positioning System (GPS), GLObal'naya Navigatsionnaya Sputnikovaya Sistema (GLONASS), or European Global Satellite Navigation System (GALILEO)) have been exploited to determine vertical motions of the solid earth [Wöppelmann et al., 2007, Snay et al., 2007, Mazzotti et al., 2008]. GNSS measurements denote the most precise source of vertical land motion and are of paramount importance in local to global scale sea level research [e.g., Bouin and Wöppelmann, 2010, Fenoglio et al., 2012, Santamaría-Gómez et al., 2017, Hammond et al., 2021]. Wöppelmann and Marcos [2016] identified comparably low formal errors of GNSS-VLM rates (0.21 mm/year) when autocorrelation was taken into account. Santamaría-Gómez et al. [2012] estimated an accuracy of 0.6 mm/year of GNSS-based vertical land motion (from at least three years of continuous data), by comparing 36 globally distributed co-located GNSS velocity estimates. Thus, because of its considerable accuracy, vertical GNSS velocities represent important benchmark estimates for many sea-level applications, e.g., for GIA-model evaluation or local VLM-corrections of tide gauge records [Sánchez and Bosch, 2009, Sanli and Blewitt, 2001].

<

Figure 1.2D shows rates from GNSS time series from the Nevada Geodetic Laboratory of the University of Nevada (NGL), a database of more than 17,000 stations (Blewitt et al. [2016], <http://geodesy.unr.edu>). As can be seen, the stations are not uniformly distributed and most of the stations are installed in places like Europe, North America, or Japan. When used to constrain vertical land motion at tide gauges, GNSS-stations should be ideally very close to the tide gauge because vertical land motion was shown to exhibit potentially high spatial variability even on small scales (tens of kilometers) [e.g., Raucoules et al., 2013, Buzanga et al., 2020]. This requirement, however, reduces the number of available co-located stations. As an example, only 130 GNSS stations are within a 1 km range of Global Sea Level Observing System (GLOSS) tide gauges [Wöppelmann et al., 2019]) and thus confine the global coastal coverage to mostly Europe, Japan, and North America.

Differences of satellite and tide gauge observations (SAT TG)

> To increase the number of vertical land motion estimates, several studies advanced the application of combining satellite altimetry (SAT) and tide gauge (TG) observations [Cazenave et al., 1999, Nerem and Mitchum, 2003, Kuo et al., 2004, Pfeffer and Allemand, 2016, Wöppelmann and Marcos, 2016, Kleinherenbrink et al., 2018]. The principle of this approach is to subtract the absolute sea level change gathered by the altimeter from relative sea level change observations at the TG. Ideally, the differenced time series (SAT minus TG) yields the vertical motion of the TG with respect to the reference of the altimeter. The accuracy of this technique depends heavily on the stability of the altimeter measurement system, among numerous other factors. Major systematic errors stem from limitations in the realization of the reference frame, as well as from limitations in the long-term stability of altimeter instruments and corrections [e.g., Couhert et al., 2015, Watson et al., 2015, Wöppelmann and Marcos, 2016]. 'Satellite altimetry minus tide gauge (SAT TG)' vertical land motion estimates can be affected by altimeter drift or errors originating from the intermission drift biases (or drifts w.r.t. the reference mission). Due to the availability of global and continuous absolute sea level measurements, this method not only provides a complementary source to GNSS measurements, but also improves the geographical distribution of the data, as virtually every valid TG can be used. <

GIA models

GIA models rely on the approximation of different parameters of the ice load history and rheology of the Earth [King et al., 2012]. However, different assumptions of these parameters can lead to discrepancies between GIA model solutions, with differences in the order of several mm/year in vertical land motion [King et al., 2010, Jevrejeva et al., 2014, Caron et al., 2018]. The present-day signal of GIA can be observed using geodetic techniques, which represent, next to relative sea level records, valuable information to further constrain GIA models [King et al., 2010, Caron et al., 2018]. Figure 1.2E shows vertical land motion from a GIA model of Caron et al. [2018]. The large-scale GIA fingerprints resemble the point estimates of direct vertical land motion observations (Fig. 1.2D). Given its strong influence on global vertical land motion and the fact that GIA is one of the few vertical land motion processes that can be modeled, previous studies of past and future sea level heavily relied on GIA models, but often neglected other sources of vertical land motion [Church and White, 2011, Slangen et al., 2014, Jackson and Jevrejeva, 2016].

› While all of these three sources of information, GIA-models, GNSS, and SATTG techniques have individual merits, their combined use is valuable to further substantiate vertical land motion estimates. GNSS observations are necessary to validate both GIA models and the SATTG approach [Santamaría-Gómez et al., 2012, Wöppelmann and Marcos, 2016, Kleinherenbrink et al., 2018]. Recent studies combined all three approaches to reconstruct GMSL [Dangendorf et al., 2017], and to densify the estimation of contemporary rates of vertical land motion [Pfeffer et al., 2017], or relative sea level change [Hawkins et al., 2019b]. Any advancement in these individual approaches, therefore, supports the mutual development and improves the global assessment of coastal vertical land motion estimates. ‹

1.4 Challenges and research objectives

In the previous sections, I highlight that vertical land motion affects coastal relative sea level change in a highly non-uniform manner and can regionally even dominate the coastal sea level budget. However, our ability to estimate vertical land motion is hampered mainly by the limited availability of observational constraints, its significant spatial and temporal variability, as well as the complexity of the superposition of processes that cannot be adequately assessed with geodynamic models. These factors pose significant challenges to ongoing sea level research. Despite the complexity of vertical land motion processes, previous work, including sea level reconstructions [Church and White, 2011, Kopp et al., 2014, Hay et al., 2015, Dangendorf et al., 2019] and sea level projections [Carson et al., 2016, Nicholls et al., 2021, Fox-Kemper et al., 2021] relied on simplified assumptions of vertical land motion. This thesis addresses these challenges to answer the following overarching research question:

⇒ **What is the impact of vertical land motion on regional-scale relative sea level change?**

To answer this research question and to improve the determination of vertical land motion, several innovations in data processing and synthesis are developed and applied to a comprehensive set of observations. I generate a vertical land motion reconstruction to assess its role in past, contemporary, and future sea level changes on a regional scale. In the next three sections, I outline the main challenges and research questions, along with the individual innovations of this work. These sections correspond to the three main chapters of this thesis (2, 3, and 4), where I present solutions to each of the research questions.

1.4.1 Improving the determination of vertical land motion using coastal altimetry and tide gauge data

This work aims to combine and improve vertical land motion data from a variety of techniques (GNSS data, tide gauges, and satellite altimetry), as presented in section 1.3. Vertical land motion estimates from differences between altimetry and tide gauge observations (VLM_{SATTG}) represent a vital complementary source for global vertical land motion information next to GNSS data. However, SATTG vertical land motion estimates are still less precise and accurate than vertical land motion measurements by GNSS. As an example, Wöppelmann and Marcos [2016] (WM16) investigated performances of different gridded and along-track altimetry products, e.g., from Archiving, Validation, and Interpretation of Satellite Oceanographic data (AVISO) or Goddard Space Flight Center (GSFC) altimetry data, and monthly-mean TG records from PSMSL. Using the gridded AVISO product, WM16 obtained vertical land motion estimates with median formal uncertainties of 0.8 mm/year and an accuracy of 1.47 mm/year based on the validation against GNSS-based trends from ULR5 (Université de La Rochelle, Institut Géographique National analysis) at 113 colocated stations. Kleinherenbrink et al. [2018] further improved the accuracy of SATTG vertical land motion data by using along-track altimetry (TOPOgraphy EXperiment (TOPEX), Jason 1 and 2, from the Radar Altimeter Database (RADS) [Scharroo et al., 2012]) to estimate vertical land motion. Their approach aimed at overcoming the spatial down-sampling/smoothing and associated loss of information in gridded products such as AVISO. They also advanced the procedure of combining altimetry and TG data. As a result, they achieved an accuracy of 1.20 mm/year (at 155 stations), which significantly improved WM16's results.

► Based on Kleinherenbrink et al. [2018] and WM16, two essential factors are identified which are vital for the quality of trend estimation by SATTG difference. Advancements with respect to both factors not only potentially led to improved vertical land motion estimates in Kleinherenbrink et al. [2018], but also motivate further innovations. The first important factor is the data quality of the altimetry measurements in the coastal zone. In coastal regions, accuracy of altimetry measurements is affected by the local departure of the radar signal from the known ocean response (due to inhomogeneities of the illuminated area) and by the inaccuracy of the standard routinely applied corrections and tidal models. As mentioned in section 1.3, developments for the solution of both issues caused rapid improvements in recent years, e.g., through the application of coastal retracking and advanced geophysical corrections [e.g., Passaro et al., 2014, Fernandes et al., 2015, Cipollini et al., 2017]. Dedicated coastal altimetry datasets (e.g., ESA development of COASTal ALTimetry (COASTALT), Adaptive Leading Edge Subwaveform (ALES), Prototype Innovant de Système de Traitement pour l'Altimétrie Côtière et l'Hydrologie (PISTACH)) might thus outperform previously applied products (e.g., AVISO) that do not yet benefit from these implementations.

Next to issues concerning data quality, the second factor is the sensitivity of VLM_{SATTG} estimates to the spatial selection of altimeter data in the vicinity of the TG. WM16 showed, that averaging SLA in a radius of 1° around the TG resulted in higher correlations than using the best correlated or the closest grid point to the TG. Kleinherenbrink et al. [2018] found a small influence of variations of absolute correlation thresholds (between altimetry and TG data) on the trend estimates. Therefore, considering the diversity of factors controlling coastal sea level variability, such as surface winds, or coastal and bathymetric characteristics, an advanced adaptation of the choice of altimetry SLA can potentially improve the representation of the signal captured by the TG.

These reasons motivate further improvements in both components, the quality of the data, and the practice of combining altimetry and TG data. To further improve SATTG vertical land motion estimates and to understand how dedicated along-track coastal altimetry can outperform standard gridded products, the following research questions need to be answered: <

⇒ **How can we use coastal altimetry observations to improve vertical land motion estimates?**

⇒ **Which factors control the accuracy and uncertainty of vertical land motion estimates from coastal altimetry and tide gauges?**

In chapter 2, I will present a new approach of combining SAT and TG observations to improve vertical land motion estimates. In contrast to previous attempts, I exploit TG and SAT data at the highest available temporal and spatial scale for globally distributed stations. Dedicated coastal along-track altimetry data is combined with high frequency TG records from GESLA. Implementation of these high frequency TG records constitutes a further innovation for vertical land motion estimation. So far, such data has only been applied in local studies [Idžanović et al., 2019] and monthly TG data were commonly exploited in this regard. I show that the precision and accuracy of the trend estimates can be optimized when using refined spatial selection criteria of altimetry sea level anomalies. With this approach, I identify coherent zones of sea level variability, which best represent the coastal in situ measurements.

1.4.2 Probabilistic reconstruction of vertical land motion

GNSS data and vertical land motion estimates based on SAT and TG differences represent essential observation-based constraints to assess the global scale impact of vertical land motion on relative sea level change. To estimate the contribution of vertical land motion in sea level reconstructions or projections, commonly, information on the linear rates of observed vertical land motion is extrapolated in time [Kopp et al., 2014, Wöppelmann and Marcos, 2016, Frederikse et al., 2020]. > However, GNSS and SATTG time series, whose records are typically shorter than three decades, are not always suitable to estimate a long-term linear trend. These time series can be affected by variable velocities at shorter timescales, which are most commonly caused by earthquakes and their associated post-seismic crustal deformations [e.g., Klos et al., 2019], but can also have other natural or human-related origins, like volcanic activity [Cazenave et al., 1999] or subsurface fluid withdrawal [Kolker et al., 2011]. As previously described, geophysical processes, such as earthquakes can also cause instantaneous displacements in the measurements (i.e., discontinuities), as can be seen in the affected tide gauge record in Soma (Japan) in Fig. 1.2B, for instance. Next to geophysical causes, Gazeaux et al. [2013] found that about one-third of discontinuities detected in GNSS time series could be attributed to instrumental issues, such as antenna changes.

These issues must be taken into account to compute unbiased linear rates of vertical land motion or to identify significant trend changes. However, while discontinuity detection has been extensively addressed for GNSS data [Blewitt et al., 2016, Klos et al., 2019], no study has yet adequately tackled the problem of directly estimating discontinuities in SATTG time series. Wöppelmann and Marcos [2016], for example, manually rejected time series, which were potentially affected by non-linearities. Klos et al. [2019], on the other hand, utilized GNSS data, to correct SATTG vertical land motion estimates that were strongly influenced by tectonic activity. Thus, an improved and independent characterization of SATTG time series is crucial, because

SATTG observations have the potential to substantially expand scarce coastal vertical land motion estimates derived from GNSS time series, which also usually cover a shorter time span than the SATTG observations [Wöppelmann and Marcos, 2016]. ◀ These knowledge gaps motivate the following research question:

⇒ **How can we detect discontinuities and trend changes in vertical land motion observations?**

Another fundamental limitation of coastal vertical land motion determination is the uneven and sometimes sparse distribution of GNSS and tide gauge stations along shorelines (see Figs. 1.2C and 1.2D). As mentioned in the previous section, only a limited number of GNSS stations are in the vicinity of tide gauges. Missing information on vertical land motion at tide gauges is a problem for coastal sea level studies in the altimetry era, as well as for sea level reconstructions. Continuous regional-scale vertical land motion estimates are also required for sea level projections, which otherwise are only constrained by GIA vertical land motion. Thus, to extrapolate GNSS-based vertical land motion at tide gauge stations and to provide global-scale vertical land motion interpolations at the regional scale several different interpolation approaches have been applied. These include methods like weighted radial averaging [Pfeffer et al., 2017, Kleinherenbrink et al., 2018, Frederikse et al., 2020], GPS Imaging [Hammond et al., 2021] or Bayesian regression methods [Bodin and Sambridge, 2009, Husson et al., 2018, Hawkins et al., 2019b]. These studies commonly relied on the assumption of strictly linear vertical land motion and are thus uninformative about the actual variations of contemporary vertical land motion. Understanding the influence of non-linear processes such as earthquakes or mass loading changes, however, is important to evaluate to what extent current rates of vertical land motion can be extrapolated in time and to determine physically-informed uncertainty estimates. Combining data from different observational techniques (i.e., GNSS and SATTG) can further improve these estimates. Thus, to derive a comprehensive global-scale vertical land motion reconstruction, the following questions need to be addressed:

⇒ **How can we align the large multi-technique networks of inhomogeneously distributed observations to reconstruct vertical land motion?**

⇒ **How can we model continuous space- and time-resolving vertical land motion?**

In chapter 3, I derive a time-resolving reconstruction of contemporary coastal vertical land motion to more realistically describe temporal variations, as opposed to simply assuming purely linear motion. First, I develop a Bayesian model to automatically and simultaneously detect change points, caused by discontinuities and trend changes, as well as other common time series features in both, GNSS and SATTG observations. Secondly, I extract common motion vertical land motion signatures of the combined set of observations using Bayesian Principal Component Analysis, to model regional scale coherent modes of variability and trends. Finally, the estimated coefficients associated with linear trends and the estimated modes will be interpolated in space to derive a global vertical land motion reconstruction.

1.4.3 Understanding the impacts of vertical land motion on relative sea level change

The increasing number of GNSS stations over the last decades and the availability of indirect vertical land motion estimates from tide gauges and satellite altimetry have facilitated the use of direct vertical land motion

observations to study their impact along the global coastlines. Previous research has utilized these geodetic constraints to shed light on subcontinental scale dynamics, such as tectonic processes, which can not be assessed with GIA models alone [Santamaría-Gómez et al., 2017, Hawkins et al., 2019b, Hammond et al., 2021]. However, despite the present abundance of vertical land motion observations, several previous investigations lacked direct geodetic constraints, relied on simplified assumptions of the spectrum of vertical land motion processes, and were often inconsistent about the applied vertical land motion correction across different studies. It is important to identify the causes and implications of these differences in the applied vertical land motion estimates because they have a direct impact on our understanding of past and future relative sea level change.

Vertical land motion is also an essential quantity in sea level reconstructions of the twentieth century, which are crucial to determine the forcing factors of sea level changes and to characterize contemporary and future sea level changes [Hay et al., 2015, Dangendorf et al., 2019]. Reconstructions of sea level changes commonly incorporate information from tide gauges and require estimates of vertical land motion to deduce the absolute and relative sea level change components. Previous work either used GIA models [Church and White, 2011], indirect GIA fingerprints [Kopp et al., 2014, Hay et al., 2015, Dangendorf et al., 2019], or direct geodetic information [Frederikse et al., 2020], to account for a linear vertical land motion component. Hence, there are inconsistencies in the applied vertical land motion data, which can lead to global and even more pronounced regional differences in relative sea level estimates over the last century [Santamaría-Gómez et al., 2017].

Such differences in the applied vertical land motion estimates exist also across sea level projection studies (e.g., see Oppenheimer et al. [2019], Table 4.5 for comparison), which so far only incorporated GIA models [Slangen et al., 2014, Jackson and Jevrejeva, 2016] or indirect vertical land motion estimates from tide gauges [Kopp et al., 2014]. The latter vertical land motion estimates were derived from a probabilistic sea level reconstruction, which statistically modeled past sea level changes as a combination of (1) a globally uniform process, (2) a regionally varying and temporally linear process, and a (3) regionally varying, temporally auto-correlated non-linear process. The second linear process was calibrated against the ICE-5G VM2-90 GIA model of Peltier [2004] and was used as the vertical land motion estimates in projections [Kopp et al., 2014]. However, in contrast to Dangendorf et al. [2019] no prior information, such as fingerprints of ocean variability (i.e., Empirical Orthogonal Functions (EOF)), ice melt, and GRD effects were included in this reconstruction, which makes an unambiguous separation of solid earth processes (vertical land motion) from other effects, such as mass changes or thermosteric changes difficult when only relying on a highly unconstrained statistical model. Hence, the vertical land motion estimates are highly influenced by the choice of the GIA model (used as a prior estimate) and the lack of direct geodetic VLM constraints. Thus, direct vertical land motion measurements, e.g., from GNSS data are vital to further constrain regional-scale, non-GIA vertical land motion, because they have been not yet included in sea level projections on a global scale. Like sea level reconstructions, current projections are also based on the working hypothesis of 'linear' vertical land motion. Considering the vertical land motion processes causing highly non-linear responses, it is, however, unclear in which regions this working hypothesis is valid, and to what extent vertical land motion can be extrapolated in time. It is expected that non-linear vertical land motion, together with other factors such as station density and formal errors in the station time series, significantly influence uncertainties in the vertical land motion estimates. Hence, a rigorous quantification of the region-dependent uncertainties is required to determine the lower

and upper confidence intervals of future relative sea level changes (together with those from climate models), which is fundamental for coastal planning.

To overcome the lack of direct geodetic constraints and imperfect information on non-linear vertical land motion in sea level reconstructions and projections, I aim at utilizing the vertical land motion reconstruction, developed in chapter 3, to dismantle the following questions:

- ⇒ **What is the contribution of vertical land motion (non-GIA and time-varying effects) on past, present, and future relative sea level change?**
- ⇒ **What are the origins of vertical land motion uncertainties and their implications for regional sea level projections?**

In chapter 4 I use the improved vertical land motion and uncertainty estimates to reassess past and contemporary sea level change, and to increase our confidence in projected regional sea level change and uncertainty estimates. I show that previously neglected time-varying effects significantly increase the uncertainty intervals in projections of relative sea level change. Investigations of how contemporary relative sea level changes affect coastal populations reveal that densely populated coasts are disproportionately exposed to subsidence-induced sea level rise and are often poorly equipped with measurement systems. Given these current limitations and uncertainties due non-linear VLM and observational gaps, future developments of coastal relative sea level observing systems in these regions are required.

1.5 Outline

In this dissertation, I determine the influence of vertical land motion on the evolution and uncertainties of relative sea level change along the global coastlines. In chapter 2, I optimize the estimation of vertical land motion based on coastal altimetry and tide gauge data. I analyze these estimates, together with a comprehensive network of vertical land motion observations in chapter 3. Here, I present a new time-series analysis technique for different types of vertical land motion observations, to estimate time-variable trends, discontinuities, and uncertainties. The pre-processed time series are used to generate a time- and space-resolving vertical land motion reconstruction over 1995-2020. The vertical land motion reconstruction allows me to estimate its contribution along the global coastlines. Estimates of the long-term motion and time-variable components are applied to reconcile past, present, and future coastal sea level change in chapter 4. I discuss the implications of physically induced vertical land motion uncertainties on our ability to robustly project regional future sea level changes. Considering these results from a socioeconomic perspective, I reassess the exposure of coastal populations to contemporary relative sea level changes. Finally, in chapter 5 I answer my research questions and provide recommendations for future activities and innovations necessary to further refine our understanding of relative sea level changes.

2 Improving the determination of vertical land motion using coastal altimetry and tide gauge data

2.1 Introduction

The objective of this chapter is the improvement of the determination of vertical land motion based on altimetry and tide gauge observations. For this purpose, I explore the sensitivity of the accuracy and precision of VLM estimates to the altimetry data type and the combination approach of altimetry and tide gauge observations. In particular, I quantify the specific value of using dedicated coastal altimetry data compared to previously applied gridded altimeter products.

Coastal along-track data is essential to enhance the spatial resolution of small-scale sea level signals in the coastal zone. Recent developments facilitate the usage of coastal altimetry data up to 3 km to the coast [Passaro et al., 2014, Fernandes et al., 2015, Cipollini et al., 2017, Cazenave et al., 2022]. It is important to understand the advantages of the application of coastal along-track altimetry compared to currently available gridded altimeter data, since they differ fundamentally in terms of spatiotemporal sampling and coastal performance. Gridded datasets provide a homogeneous sampling of sea level in space and time due to the applied different space- and time-interpolation techniques [Ducet et al., 2000, Taburet et al., 2019]. Along-track data provide discrete point-wise observations in time, with different temporal resolutions depending on the altimeter mission. It is unclear how the different space/time sampling and the coastal performance of the different altimetry datasets influence the estimation of VLM from altimetry and tide gauges. To understand these influences, I apply different datasets and test different spatial selection approaches of altimetry data.

Previous studies commonly applied monthly PSMSL tide gauge data to estimate VLM from SATTG. However, a better understanding is required, as to what extent the monthly averaged tide gauge observations agree with the altimetry data, which consist of at maximum three observations/month for missions with a 10-day repeat cycle. Therefore, to better represent the altimetry observations at the time of measurement, I use high-frequency tide gauge observations from the GESLA database, which provides measurements with a time sampling from minutes to hours. Improvements with respect to using monthly averaged PSMSL data are investigated.

While data quality is expected to have an important influence on the accuracy of VLM estimates, also the data selection approach has been shown to affect the performance of the SATTG techniques [Cazenave et al., 1999, Wöppelmann and Marcos, 2016, Kleinherenbrink et al., 2018]. Several selection approaches were applied so far, e.g., using the point of highest correlation, the closest point, or spatial averages. Hence, I explore how different selection procedures influence the comparability of tide gauge and altimetry data. The performance of the different dataset combinations is assessed using high-quality coastal GNSS data from the URL6a database. I place my findings in the context of physical mechanisms of coastal sea level variability, which are subject of ongoing investigations.

The main outcomes of the work presented in this chapter are different VLM time series datasets, derived on the SATTG technique. The derived time series represent a crucial complementary data source to the GNSS network, which are analyzed and merged in chapter 3.

2.2 Datasets and combination approaches

In this section I provide information on the altimetry and tide gauge datasets, as well as on the combination of both data sources. I use along-track (ALES) and gridded altimetry (AVISO) data, as well as monthly (PSMSL) and a high-frequency (GESLA) tide gauge observations.

› The coastal along-track data is obtained from 1 Hz multi-mission altimetry measurements processed by Deutsches Geodätisches Forschungsinstitut der Technischen Universität München (DGFI-TUM) with the Open Altimeter Database (OpenADB) (<https://openadb.dgfi.tum.de>, last access: 10 December 2020). The data cover a period of 23 years (1995-2018) and are reprocessed with the ALES retracker [Passaro et al., 2014]. This product is hereinafter called ALES. To reduce radial errors in the different missions, the tailored coastal altimetry product is cross-calibrated using the global multi-mission crossover analysis (MMXO) [Bosch and Savcenko, 2007, Bosch et al., 2014]. A comprehensive list of the geophysical adjustments and corrections can be found in Oelmann et al. [2021]. Next to the along-track data, the gridded Ssalto/Duacs altimeter (produced and distributed by the Copernicus Marine Environment Monitoring Service (CMEMS; <http://marine.copernicus.eu>, last access: 10 December 2020)) is used (hereinafter called AVISO). The data are resolved on a 0.25° Cartesian grid and cover the period from 1992–2019. ‹

I use monthly mean PSMSL tide gauge data [Holgate et al., 2013] and high-frequency data from GESLA [Woodworth et al., 2016]. The latter database collects data from a variety of different providers and the data is not quality-controlled like the PSMSL database. That means, the data can contain irregularities like station shifts or point outlier due to natural or instrumental issues. Hence, several outlier detection steps are applied to pre-process the data (see Oelmann et al. [2021]). A 40-h loess filter is applied to suppress tidal variability. This filtering approach most effectively reduces tidal variance at periods lower than 2 days (e.g. reduction by more than two orders of magnitudes at daily periods). However, tidal variability at periods larger than 2 days is not significantly attenuated by the filter. Therefore, one caveat of this approach is that there remains residual tidal variance at longer periods between TGs and altimetry, given that the latter features a model-based adjustment for longer tides. I do, however, not apply the same tidal model to the TGs, due to known issues related to decreased model performance in shallow water [Piccioni et al., 2018]. Both data-sets are corrected for the dynamic atmospheric correction (DAC)[Carrère and Lyard, 2003].

I analyze four different data combination approaches to understand the sensitivity of the VLM estimations to the (1) quality and resolution of the data and (2) the selection procedure: ALES–PSMSL-250 km, ALES–GESLA-250 km, AVISO–PSMSL-250 km and ALES–GESLA–ZOI. These dataset combinations differ in terms of temporal and spatial sampling and hence facilitate the identification of the factors that influence the quality of VLM estimates. Estimates can either be influenced by the altimetry data (ALES, AVISO), the temporal sampling (PSMSL, GESLA), or the spatial selection. Table 2.1 provides an overview of the different datasets used:

› To produce the ALES-GESLA-250km dataset, I compute differences of the merged, non-uniformly sampled SLAs and the hourly-sampled GESLA TG records by cubic interpolation of the latter with a maximum

Table 2.1 Altimetry and tide gauge combinations

Dataset name	Description
ALES-PSMSL-250km	Monthly averaged, coastal along-track altimetry coupled with PSMSL tide gauge data. Altimetry data are averaged within a 250 km radius around the tide gauge.
ALES-GESLA-250km	High-frequency, coastal along-track altimetry coupled with GESLA tide gauge data. Altimetry data are averaged within a 250 km radius around the tide gauge.
AVISO-PSMSL-250km	Monthly gridded altimetry coupled with PSMSL tide gauge data. Altimetry data are averaged within a 250 km radius around the tide gauge.
ALES-GESLA-ZOI	High-frequency, coastal along-track altimetry coupled with GESLA tide gauge data. Altimetry data are averaged based on comparability (e.g., correlation) of altimetry and tide gauge data.

allowed time-lag of 3 hours between the measurements. I down-sample these high-rate differenced time series to monthly means. For ALES-PSMSL-250km on the other hand, I first compute monthly-means from SLAs from which the monthly-sampled relative SLAs from PSMSL are subtracted. Finally, I directly compute the differenced SATTG time series from the averaged monthly AVISO and the PSMSL data, which yields the AVISO-PSMSL-250km dataset. The dataset ALES-GESLA-ZOI is based on an optimized selection of along-track data in the coastal zone as described in the following section. <

2.3 The Zone of Influence - coherent sea level variations in the coastal zone

To optimize the combination of along-track data and tide gauge data, I develop a new SLA selection scheme, which aims to maximize the consistency of observed altimetry-based SLAs with tide gauge observations. This approach is motivated by previous research, which used the highest correlated altimetry data [Cazenave et al., 1999, Santamaría-Gómez et al., 2014, Wöppelmann and Marcos, 2016].

> The presence of the coast and sloping bathymetry give rise to a variety of coastal sea level dynamics which can be quite different from the open ocean [Hughes et al., 2019]. Many of the driving factors and mechanisms are still poorly understood and subject of ongoing research [Hughes et al., 2019, Marcos et al., 2019]. Previous studies reported that sea level variations can be correlated over thousand of kilometers along the continental slopes [Hughes and Meredith, 2006, Calafat et al., 2018]. It was shown that these coherent sea level variations were tightly bound to the continental shelf and often differed in terms of spectral features from the open ocean. This so called 'de-coupling' of coastal and open ocean sea level variability was discussed to be associated with coastally trapped waves, a mechanism which is unique to the coast [Hughes and Meredith, 2006, Hughes et al., 2019]. While such signals generate high spatial coherence, other local features, such as the presence of a coastal current, can significantly modify the sea level variability within a few kilometers of the coast, as shown in the case of the seasonal signal of the Norwegian Coastal Current in Passaro et al. [2015]. Accordingly, the capability to compare TG-based sea level variability and trends with altimetry depends on which timescales and length scales are resolved by the data, as well as on the accuracy of sea level measurements in the coastal zone. <

To improve the comparability of coastal altimetry measurements and the in situ TG observations, I extend the methodology proposed by Santamaría-Gómez et al. [2014], who looked for the altimetry grid point most

correlated with the TG, and Kleinherenbrink et al. [2018], who considered a larger set of points based on absolute thresholds of correlation. In contrast to these previous studies, I assess the influence of using relative thresholds of comparability on both the accuracy and the uncertainty of the trends. I examine different metrics S defining the consistency of altimetry and tide gauge data. These include: correlation, Root Mean Square (RMS) and residual annual cycle. Using these criteria, I aim to identify regions where altimetry data show maximum consistency with TG observations. This region is hereinafter called the Zone of Influence (ZOI). This approach is intended decrease noise of the differenced, high-frequency VLM SATTG time series and thus improve the accuracy and precision of the VLM estimates.

I derive the statistics S based on detrended altimetry and TG data. Thus, all the metrics may be influenced by the similarity of the annual cycle. Note, that by repeating this analysis using detrended and deseasoned data (not shown), no significant differences are identified. A comparison of the results based on deseasoned and deseasoned data can be found in the online discussion section of the published study [Oelsmann et al., 2021].

► I identify coherent zones of sea-level variability represented by different selection-criteria in Fig. 2.1. The statistics S are computed based on individual along-track SLA time series and GESLA TGs. I show different maps of these along-track statistics for (a) the Australian Coast, (b) Californian Coast and (c) Chichijima island (Japan). The contour in the first column exemplifies the extent of a ZOI, which represents a sub-set of the 20% best correlated data.

The obtained coherent structures reveal notable dependencies on the local bathymetric and coastal properties. Figure 2.1a), for instance, shows far-reaching alongshore correlations, a coherent structure that supported by all of the analyzed selection criteria. In this example, the correlation structure indicates a separation of coastal shelf-sea and offshore dynamics as supported by the underlying bathymetric gradients. Kurapov et al. [2016] found similarly pronounced coherent SLAs along the Californian coast, as shown in Fig. 2.1b). Based on model data and TG observations, they explained the large-scale along-shore correlation pattern in part with the propagation of coastal trapped waves. In other locations such as in Chichijima island (see Fig. 2.1c), coastal and bathymetric control of sea level (SL) is reduced and different structures of coherency evolve. Consequently, the ZOI can strongly vary in shape depending on the local coastal features and drivers of coastal variability.

Comparing these three examples, I also observe that absolute values of the statistics differ from site to site. Correlations of along-track data near the Australian coastline, for instance, outperform those in example Fig. 2.1b). The same holds for the $\text{RMS}_{\text{SATTG}}$ values. These differences not only indicate different degrees of coherency, but can also stem from regional deviations in the quality of data, i.e. quality of TG records or error sources in the altimetric product, such as tidal adjustments or coastal corrections. Differences can also be caused by coastal properties, e.g., when the TGs are located in sheltered areas, which separates the in-situ variability from those measured at distant altimeter tracks. Therefore, I analyze the use of relative thresholds to select SLAs, since setting absolute thresholds as in Kleinherenbrink et al. [2018] might not be applicable in all cases. Figure 2.1c) also shows that different statistics can lead to different extents of the ZOI, considering that rather poorly correlated areas are partially characterized by low residual annual cycle amplitudes.

Selecting altimetry observations in the ZOI based on a sub-set of highly consistent SLAs can significantly reduce the SATTG residuals as exemplified in Fig. 2.2. Here, I show three time series of SATTG differences for the Australian site (as shown in Fig. 2.1a). The first series (Fig. 2.2a) indicates much lower residual noise, when

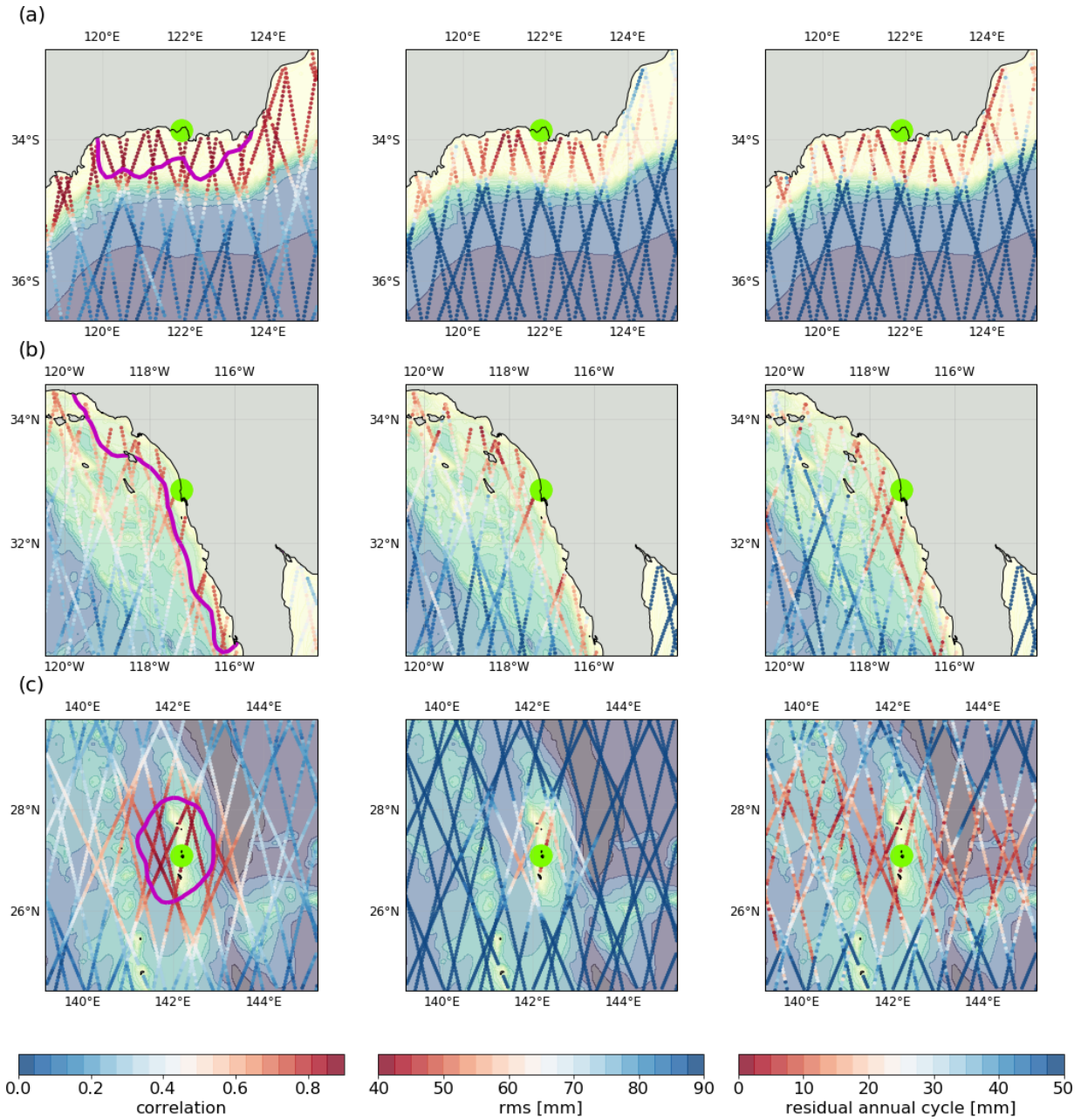


Figure 2.1 Zone of Influence: Different coherent zones of sea level variability are identified by different statistical criteria S . The columns show correlations, RMS_{SATTG} and the residual annual cycle from left to right. The metrics are computed on every point of the 1 Hz along-track product, comparing the performance of altimetry measurements with the TGs, highlighted in green (center). (a) shows the South-Coast of Western Australia, (b) the western coast of North America (TG in San Diego) and (c) Chichijima island (Japan). The 'color' contour in the first column indicates a Zone of Influence based on 20% of the best-correlated SLAs within a 300 km radius. The filled contours denote the underlying bathymetry.

the time series is constructed from the 20% best SLAs (according to the RMS_{SATTG}). Here, the ALES-GESLA-ZOI residuals outperform those of the other combinations ALES-PSMSL-250km and AVISO-PSMSL-250km, which are still affected by a pronounced annual cycle not related to VLM. <

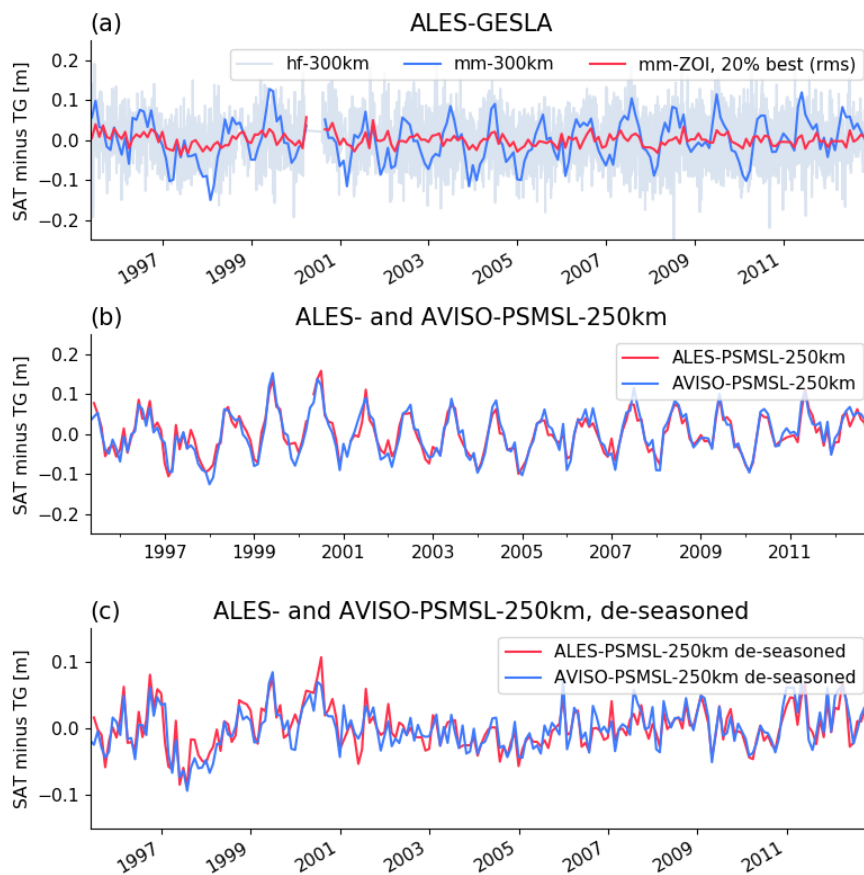


Figure 2.2 Shown are SATTG time series for different datasets and configurations for the TG in Fig. 2.1a). (a) Monthly mean (mm) time series for ALES-GESLA, when all SLAs are averaged in a 300 km radius (blue) and when SLAs are comprised of the 20% most representative anomalies based on the $RMS_{SAT TG}$ between altimetry and TG (red). The grey line denotes the underlying high-frequency time series. (b) Monthly mean differenced time series for ALES-PSMSL and AVISO-PSMSL, which are based on a 250km-radius selection of SLAs. (c) Same as (b) but with the annual and semi-annual signals removed.

2.4 Global validation of vertical land motion estimates

Figure 2.2 shows that using a RMS-based altimetry selection can reduce the noise of $VLM_{SAT TG}$ time series for individual stations. To identify a globally optimal ZOI selection I vary the relative thresholds X between 0.0 and 0.975 (with a stepsize of 0.025), which refers to using 100% and 2.5% of the best performing SLAs according to each criteria. For each threshold and criterion I compute an individual global $VLM_{SAT TG}$ trend and uncertainty dataset.

› The performance of the trend estimates for a specific ZOI definition is evaluated in terms of accuracy and uncertainty of the VLM estimates. The accuracy is obtained by validating the $VLM_{SAT TG}$ with the VLM_{GNSS} data. Note, that I validate the data based on the working hypothesis that VLM can be assumed as a strictly linear process [Wöppelmann and Marcos, 2016]. In the next chapter I will revise this simplified assumption on the linearity of VLM and define a more advanced time series model. I use the ULR6a GPS solution Santamaría-Gómez et al. [2016] provided by the GNSS data assembly centre Systeme d’Observation du Niveau des Eaux Littorales (SONEL). The reanalysis covers 19 years of GNSS data from 1995 to 2014, which are processed within the ITRF2008 reference frame, consistent with the reference frame of the altimetry data. I take into account

GNSS stations which are closer than 1 km to a TG. With this constraint I aim to avoid potential differential vertical motions between the TG and the GNSS-antenna [Wöppelmann and Marcos, 2016].

The TG locations and record lengths differ among the presented experimental datasets. Therefore, I define several requirements for the validation of those experimental-datasets, to obtain a consistent set of TG and GNSS validation pairs. In contrast to PSMSL records, GESLA-TG observations only last until 2015 (at the time of writing). Even when PSMSL TG records are truncated to before 2015, they still contain more months of valid data than GESLA. Hence, I align the time period covered by the PSMSL-TGs to the corresponding GESLA-TGs for all following experimental datasets. Generally, I only take into account SATTG time series, when they cover at least 120 months of valid data. Note, that the outlier analysis or coupling of high frequency TG data in the ZOI can reduce the length of the SATTG time series for GESLA TGs. Taking into account all these requirements, I obtain 52 common GESLA and PSMSL TGs, which provide a neighboring GNSS station within 1 km distance. These pairs are validated for ALES-PSMSL-250km, ALES-GESLA-250km and AVISO-PSMSL-250km. The ALES-GESLA-ZOI combination includes six more stations. ◀

2.4.1 Trend and uncertainty estimation

► I fit the differenced time series to a combination of a deterministic model and a stochastic noise model with the Maximum Likelihood Estimation (MLE) method. Parameters of the deterministic model are comprised of a constant offset A and a linear trend B . The annual and semi-annual signals are expressed by harmonic functions with the annual and semi-annual frequencies $\omega_{1,2}$ and amplitudes $C_{1,2}$ and $D_{1,2}$.

$$y(t) = A + Bt + \sum_{i=1}^2 C_i \cos(2\pi t \omega_i) + D_i \sin(2\pi t \omega_i) \quad (2.1)$$

When combining altimetry and TGs for VLM estimation, several sources can contaminate the differenced time series and inflate the actual 'red'-noise (low-frequency) content in the residuals, which generates auto-correlated signals in the data. The SLA computation is affected by the instrumental errors of the range estimation and of each of the geophysical corrections [Ablain et al., 2009]. Such errors, as well as the measurement error of the TG itself, show up as residuals in the differenced time series. Moreover, sea level dynamics that are not common between the TG and altimeter observation locations will also contribute to the SATTG differences. Therefore, to avoid underestimation of the uncertainty of the parameters, I take into account auto-correlation in the residuals of the detrended and deseasoned time series. I describe the power spectral density of the noise with a combination of a power-law and a white noise model (using the Hector software [Bos and Fernandes, 2019]). The power-law process assumes that time-correlated noise power is proportional to f^κ , which for negative spectral indices κ describes increasing power at lower frequencies f and a white-noise process when $\kappa = 0$ [Agnew, 1992]. The covariance matrix C of the time series residuals is comprised of the contributions of the white-noise and power-law noise:

$$C = \sigma^2(\sin^2(\phi)I + \cos^2(\phi)E(\kappa)) \quad (2.2)$$

Here, σ represents the driving-noise, which scales the amplitudes of the noise components. The fractions of the noise components are estimated using the ϕ parameter. I represents the unit matrix, which is the

covariance matrix of the white noise, E is the unit covariance matrix of the power-law noise, which depends on the spectral index κ [Bos et al., 2013a, 2019].

Santamaría-Gómez et al. [2011] showed that this combination (of power-law and white noise model) represents the best approximation of the noise content for 275 GNSS station position time series. This combination was also implemented in studies concerned with VLM_{SATTG} estimation (WM16, Kleinherenbrink et al. [2018], Ballu et al. [2019]). In particular, the spectral index κ can contribute to detect the intrusion of low-frequency signals in the differenced time series. Next to the spectral index κ , I estimate the individual fractions of the power-law and white noise models, as well as the total variance σ^2 which scales the amplitude of the noise. I emphasize that for individual regions other noise models could be more appropriate than the implemented power-law plus white noise mode model and would thus yield more realistic uncertainty estimates. Hence, a more advanced noise analysis of SATTG residual time series is applied in section 3.2.2 based on a more comprehensive dataset.

I compute the $RMS_{\Delta VLM}$ and the median of the differences (ΔVLM) of VLM_{SATTG} and VLM_{GNSS} for a given dataset combination. To take into account the derived formal errors (U) of the estimate I compute the weighted RMS_w as follows:

$$RMS_w = \sqrt{\sum_{i=1}^n (w_i (VLM_{GNSS_i} - VLM_{SATTG_i})^2)} \quad (2.3)$$

with weights

$$w_i = \frac{\sqrt{(U_{GNSS_i}^2 + U_{SATTG_i}^2)^{-1}}}{\sum_{i=1}^n (\sqrt{(U_{GNSS_i}^2 + U_{SATTG_i}^2)^{-1}})} \quad (2.4)$$

2.4.2 Comparison of different dataset configurations

Table 2.2 summarizes the performances of the different dataset combinations. Validation against GNSS vertical velocities reveals that the gridded combination AVISO-PSMSL-250km slightly outperforms ALES-PSMSL-250km in terms of accuracy. Both the $RMS_{\Delta VLM}$ and the median of absolute trend differences are 9% lower for AVISO-PSMSL-250km. This confirms that, if all the available altimetry data within a wide region are compared against monthly values of TGs, the use of a gridded product outperforms the along-track performances (WM16). Kleinherenbrink et al. [2018] similarly compared an along-track combination of 250-km-SLA averages (from RADS) and PSMSL TG data with the AVISO-PSMSL combination from WM16. They found a small $RMS_{\Delta VLM}$ reduction of 0.1 mm/year when using the along-track product without any correlation thresholds applied. Note, that WM16's trends were, however, based on 1° radius-averages of SLAs (in contrast to the 250 km selection), and record lengths were not equalized as in this study.

For both combinations, the median of the VLM differences (ALES-PSMSL-250km: -0.87 mm/year; AVISO-PSMSL-250km: 0.56 mm/year) show strong deviations with respect to each other, as well as previous studies (WM16: -0.25 mm/year and, Kleinherenbrink et al. [2018]: -0.06 mm/year). In contrast to these previous estimates, I use different spatial selection scales of SLAs, smaller numbers of TG-GNSS pairs, and deviating record lengths, which hampers a direct comparison. Moreover, the altimetry datasets might be affected by instrumental drifts. In this respect, differences among the datasets may be caused not only by different techniques

applied to reduce intermission biases (e.g., the MMXO approach for ALES), but also by different missions incorporated in the records. Note that in contrast to ALES, AVISO contains TOPEX, which has also been shown to be affected by a strong drift [Watson et al., 2015]. Other possible factors (i.e., adjustments and corrections), which can cause trends biases in the altimetry measurements, are discussed in section 2.5.

Despite the larger median bias, the observed $\text{RMS}_{\Delta\text{VLM}}$ of AVISO-PSMSL-250km (1.50 mm/year) is comparable to WM16 result (1.47 mm/year). In contrast to trend accuracies, the uncertainties are 5% lower for ALES-PSMSL-250km than for AVISO-PSMSL-250km. As in WM16's, the spectral index κ of the interpolated gridded product is lower than for the along-track data. Both κ indices (-0.56 and -0.39) are in the order of magnitude as found by WM16 for AVISO (-0.5) and the along-track product (-0.4, GSFC). The larger spectral index (-0.39) is associated with reduced power of the noise at low frequencies and thus indicates reduced contamination of the SLA signal by sea-level variations that do not represent those measured at the TG. This enhanced comparability is also reflected in the lower trend uncertainties of ALES-PSMSL-250km (0.69 mm/year) compared to AVISO-PSMSL-250km (0.73 mm/year). The differences between the characteristics of the residuals of the datasets can partially be explained by the resolution of the data: Due to the spatial filtering of the data, the gridded solution AVISO incorporates information on SLAs beyond the 250 km radius and thus contains time-correlated SL-signals with stronger deviations from the TG records.

In comparison with the low-frequency datasets (ALES-PSMSL-250km and AVISO-PSMSL-250km), the high-rate set-up ALES-GESLA-250km improves the $\text{RMS}_{\Delta\text{VLM}}$. The magnitude of the bias of trend differences decreases more substantially to 0.39 mm/year (compared to 0.87 mm/year for ALES-PSMSL-250km). Compared to ALES-PSMSL-250km, I find increased trend uncertainties for ALES-GESLA-250km, which can be partially explained by higher power-law variance (i.e., the driving-noise see eq. 2.2) of this GESLA-based configuration. Although trend uncertainties are higher for the ALES-GESLA-250km configuration, I choose this set-up to investigate the impact of the ZOI. This dataset provides better results concerning trend accuracy (weighted or unweighted RMS) and has a lower median bias. Moreover, using the high-frequency data, I am able to couple SAT and TG observations at much higher temporal resolution than it would be possible when using monthly PSMSL data. Therefore the ALES-GESLA coupling is further developed based on a better definition of the ZOI in the next section.

As addressed in section 2.2, I build the ZOI upon different criteria of comparability: $\text{RMS}_{\text{SATTG}}$, correlation, and the residual annual cycle. First, I focus on the results of using the $\text{RMS}_{\text{SATTG}}$ of the detrended differenced time series (Table 2.2 and Fig. 2.3, ALES-GESLA-ZOI). I observe that the $\text{RMS}_{\Delta\text{VLM}}$, the median of absolute and total differences (ΔVLM), as well as trend uncertainties decrease towards higher relative thresholds. The statistics converge to a minimum when the ZOI is restricted to the 30-20% best data. To compare ALES-GESLA-ZOI with the other dataset combinations, I compute the statistics for the same 52 TGs used in these configurations (note that the shown statistic in Table 2.2 refer to a larger set of 58 stations). At the 20% thresholds, I obtain similar performances with a $\text{RMS}_{\Delta\text{VLM}}$ of 1.29 mm/year, median uncertainty of 0.51 mm/year, and a median of absolute differences ($|\Delta\text{VLM}|$) of 0.86 mm/year. Thus, the improvements in $\text{RMS}_{\Delta\text{VLM}}$ compared to the plain 250 km-radius selection (ALES-GESLA-250km) is 15% and 35% for uncertainties. Therefore, I find more substantial, nearly linear reductions of trend uncertainty with increasing relative thresholds compared to trend accuracy ($\text{RMS}_{\Delta\text{VLM}}$, Table 2.2, ALES-GESLA-ZOI). As demonstrated for different time series in Fig. 2.2, selecting SLAs with a low $\text{RMS}_{\text{SATTG}}$ efficiently reduces the noise of the residuals. Correspondingly,

Table 2.2 Statistics of different SATTG combinations. ΔVLM refers to the differences of $\text{VLM}_{\text{SATTG}}$ and VLM_{GNSS} trends. X denotes the fraction of the best data used, based on the $\text{RMS}_{\text{SATTG}}$ criterion.

X	$\text{RMS}_{\Delta\text{VLM}}$ mm/year	weighted $\text{RMS}_{\Delta\text{VLM}}$ mm/year	med. $ \Delta\text{VLM} $ mm/year	med. ΔVLM mm/year	med. uncertainty	spectral index κ
ALES-PSMSL-250km (52 stations)						
	1.68	1.57	1.28	-0.87	0.69	-0.39
AVISO-PSMSL-250km (52 stations)						
	1.50	1.48	1.12	0.56	0.73	-0.56
ALES-GESLA-250km (52 stations)						
	1.51	1.47	1.14	-0.39	0.79	-0.39
ALES-GESLA-ZOI (best $\text{RMS}_{\text{SATTG}}$, 58 stations)						
0	1.54	1.45	0.98	-0.46	0.86	-0.45
0.1	1.39	1.36	0.9	-0.27	0.86	-0.44
0.2	1.34	1.33	0.88	-0.36	0.83	-0.47
0.3	1.32	1.36	0.83	-0.44	0.78	-0.46
0.4	1.3	1.38	0.87	-0.37	0.76	-0.45
0.5	1.29	1.4	0.86	-0.26	0.73	-0.47
0.6	1.3	1.43	0.87	-0.31	0.71	-0.47
0.7	1.28	1.39	0.82	-0.41	0.66	-0.48
0.8	1.28	1.37	0.86	-0.41	0.58	-0.43
0.9	1.53	1.58	0.97	-0.43	0.61	-0.46

at higher levels of comparability, the variance, which scales the amplitudes of the considered noise models, decreases (not shown).

Because the spectral index (for ALES-GESLA-ZOI) is slightly lower (-0.43 at 20% level) than for ALES-GESLA-250km (-0.39) it cannot account for the uncertainty improvements. Here, the lower κ index reveals a relative increase of power at low frequency (i.e. time scales longer than months). Thus the bulk of improvements I see in uncertainty (comparing ALES-GESLA-ZOI and ALES-GESLA-250km) stems from the reduction of the power law and white noise amplitudes in the residuals. This is in turn caused by improvements in the comparability of TG and altimetry measurements at high-frequency (i.e. days).

The $\text{RMS}_{\Delta\text{VLM}}$ and trend uncertainty level off at very high thresholds and ultimately increase when only 5% of the data is used (Fig. 2.3a and 2.3c). I argue that this is mainly related to a decrease in the sampling-density of the time series included in the selection: At the 95th percentile, the median sample size (i.e. the number of monthly averages in a time series) is 20% smaller than the sample size at the 80th percentile (which corresponds here to a relative threshold of $X=0.8$). Robust trend estimates require a minimum of samples, hence, using a reduced number of along-track data time series, even if they have a maximum degree of comparability, results in a reduced trend accuracy ($\text{RMS}_{\Delta\text{VLM}}$) on global average. Thus, I argue that the optimal threshold identified at about the 80th percentile (of the data sorted by RMS) represents a compromise between data-comparability and sampling-density of altimetry data. I emphasize that there are numerous factors, other than the time period covered, that may contribute to a lack of comparability between SATTG and GNSS trends. I further elaborate on these in the following discussion section 2.5.

When setting this optimal threshold to 20%, the ALES-GESLA-ZOI set-up outperforms the other investigated configurations. These results underpin that a refined selection procedure (ZOI) represents the dominant advancement, as this approach outstrips the improvements (in terms of trend accuracy and uncertainty) which are obtained from using different altimeter or TG data combinations.

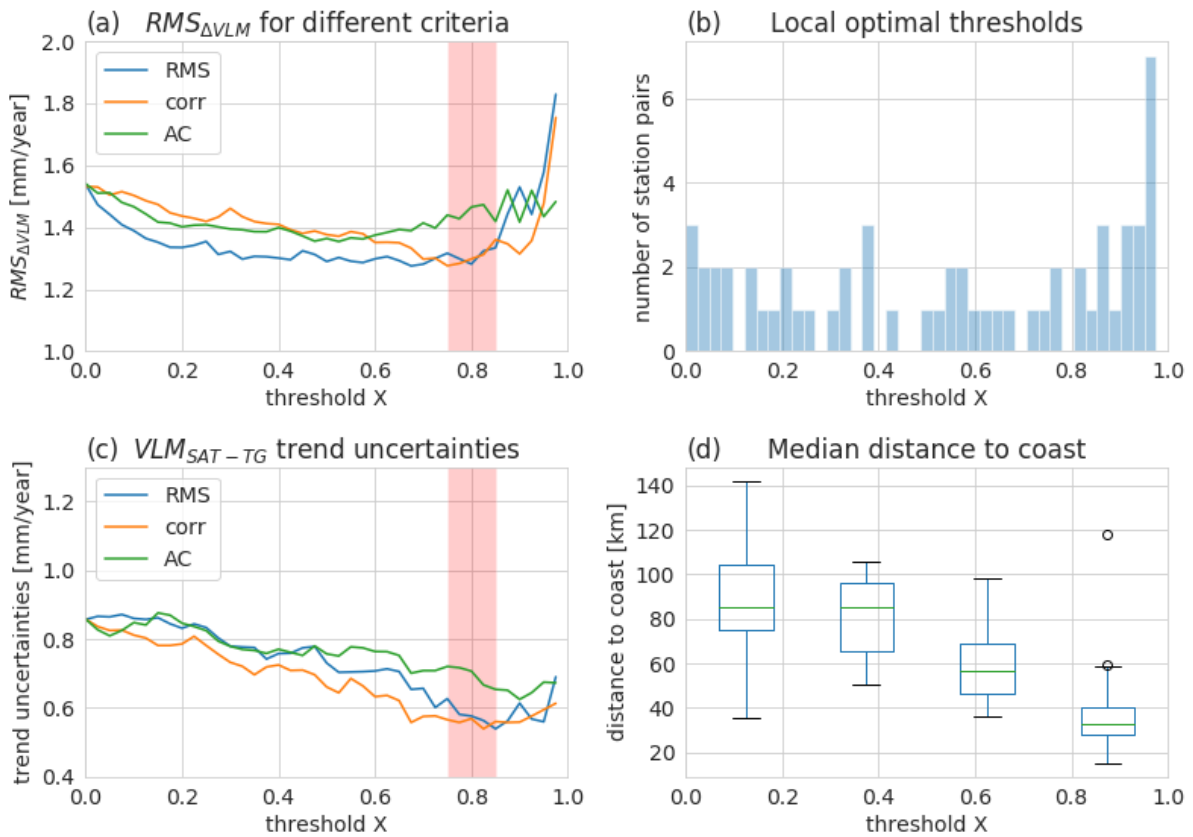


Figure 2.3 Performance of VLM_{SATTG} trend estimates for ALES-GESLA-ZOI. a) RMS_{ΔVLM} for different relative thresholds (step size 2.5%) and different selection criteria: RMS_{SATTG} (blue), correlation (red) and residual annual cycle (AC, green); c) same as (a) but for median uncertainty. b) Distribution of best performing relative thresholds for individual stations. The local optimal threshold is defined at the minimum of the absolute difference of VLM_{SATTG} and GNSS trends. d) Boxplot shows the distribution of the mean distances to coast for the individual optimum ZOI's as denoted in b). The distances refer to the distributions within the 0-25%, 25-50%, etc., levels, respectively.

Figures 2.3a and 2.3c illustrate the influence of applying different data selection criteria on the performance of estimated trends. In general, increasing relative RMS_{SATTG} or correlation thresholds yields similar optimal ranges ($\sim 20\%$) for both RMS_{ΔVLM} or uncertainty of VLM_{SATTG} trends and can thus be interchangeably used. At lower relative threshold levels (20-60%), however, the selection by the RMS-criterion yields slightly reduced RMS_{ΔVLM} values compared to the correlation-based selection. Hence, for this set of TGs a SLA-selection based on the minimum RMS_{SATTG} generally provides more accurate trend estimates (in terms of RMS_{ΔVLM}). The residual annual cycle criterion only weakly reproduces the improvements provided by the other criteria and is less suited to confine the ZOI. This finding emphasizes the need of matching the data according to the high-frequency (monthly to daily time scales) comparability, because selecting the data based on the residual annual cycle (i.e. intraannual or low frequency comparability), limits the performance of the estimates (Fig. 2.3c). Considering improvements in the bias of trend differences, I find no significant differences in using different thresholds. In contrast to the improvements in accuracy (as shown in Fig. 2.3), the median Δ VLM does not converge to a global optimum. Therefore, I discuss the contribution of other factors affecting the comparability of VLM_{SATTG} and VLM_{GNSS} in section 2.5. <

2.5 Discussion

This chapter demonstrates that selecting multiple along-track altimetry observations, which are associated with a high comparability with TGs, improves accuracy and uncertainty of VLM estimates. The results also indicate, that using only a very small set of data causes a reduction in the performance of VLM estimates, despite the enhanced coastal performance of the ALES altimetry data. This underlines the important role of the sampling-density, which is achieved by averaging the data within the ZOI. > I also find that the integration of the ZOI primarily reduces the uncertainty of $VLM_{SAT\&TG}$ trend estimates. Over a considerable range of thresholds (80 - 20% of best performing data) trend accuracies do not improve as strongly as the uncertainties decrease. This is in line with Kleinherenbrink et al. [2018], who showed that for a highly correlated sub-set of TGs, increasing absolute correlation thresholds would not significantly reduce the $RMS_{\Delta VLM}$.

Here, I discuss these findings, to better understand why trend estimates do not always improve when selecting highly comparable (w.r.t. TG) or closely located absolute SLA measurements. This question ultimately leads to the discussion of space- and time scales of the of observed coastal sea-level variability. To better understand these relationships, I incorporate results of related analyses I performed within the framework of the SL_cci initiative [Oelmann and Passaro, 2022].

The results presented in Fig. 2.3 and Table 2.2 denote metrics and performances derived from the global TG-GNSS dataset for ALES-GESLA-ZOI and support an optimal threshold at 20%. It remains to be investigated, whether the described optimum global threshold also reflects the best choice at every coastal site considered. Therefore, I investigate at which relative levels individual $VLM_{SAT\&TG}$ and VLM_{GNSS} trends estimates yield the smallest absolute deviations ΔVLM . Postulating that the actual VLM at the TG location is linear and perfectly detected by the GNSS station, these thresholds denote the 'local' optimal levels. With this analysis, I aim to better understand the spread of individual optimal ZOIs and what would be the best theoretically achievable $RMS_{\Delta VLM}$. This analysis also provides a basis to motivate future investigations, in particular, to identify factors, which may lead to locally different extents of the ZOI and to improve the accuracy of trend estimates.

Figure 2.3b displays the distribution of local optimal thresholds for TG-GNSS stations for the ALES-GESLA-ZOI dataset. Overall, the optimal levels X are broadly distributed from 0 to 0.975. I find highest concentrations between 0.8-0.975, which slightly exceeds the range of the global optimum. At the global optimum itself (0.8, based on correlations), the median distance to coast (of all SLA measurements in a ZOI) is 39.4 km. Here, 25% of the altimeter observations are within a range of 20 km to the coast, i.e. the region with the most pronounced coastal advancements of the along-track dataset [Passaro et al., 2015].

In contrast to these examples, I also find some very low local optima (Fig. 2.3b). Here, the local $VLM_{SAT\&TG}$ and GNSS trend differences do not converge to a minimum as the comparability of SAT and TG observations increases. Accordingly, in these cases, vertical land motion estimates do not necessarily benefit from the high coastal resolution of the data, because a low relative threshold is simultaneously associated with a larger-scale selection of SLAs (Fig. 2.3d). At the lower level ranges, e.g., 0-0.2, the SLAs have an average distance of 95 km to the coast. Assuming that the sources of these larger scales of coherency of coastal SL trends were known, a more advanced adaption to these additional factors would further increase accuracy of VLM estimates. An associated ideal selection of trends, based on optimal individual levels shown in Fig. 2.3d would largely reduce to $RMS_{\Delta VLM}$ to 0.89 mm/year. I emphasize that this constitutes the best $RMS_{\Delta VLM}$, which could theoretically be achieved with our dataset combination, if all of the local optimal levels could be systematically explained.

This demonstrates that, albeit there might be room for minor improvements, there is still a strong limit to bringing the $\text{RMS}_{\Delta\text{VLM}}$ below 1 mm/year.

Bathymetric and coastal properties can cause large discrepancies in responses of coastal sea level variability as they modify the character of the impact of large-scale atmospheric forcing or remote variability from the deeper ocean [Woodworth et al., 2019]. Hence, an advanced analysis of SL coherency and the role of bathymetry and its impact on sea level variability might facilitate further enhancements of trend accuracy based on SAT and TG. However, I note that physical origins may not necessarily cause the spread of individual optimal thresholds (Fig. 2.3b). If my assumption, that GNSS-trend estimates perfectly represent the linear trend over the time span of the altimetry/TG records was not met, the shown individual thresholds would erroneously reflect local optima. Ruling out these sources of error is thus a prerequisite to further study physical explanations for different extents of the ZOI.

In addition to site-dependent factors, the spatial-scales of trend coherency might also depend on the time span covered by the observations. That means, modes of sea level variability on monthly, interannual or decadal time scales, might be associated with different spatial scales than the dynamics that drive long term trends in sea level (i.e., the effect of ice melt). Coastal sea level trends that are computed in the ZOI are affected by local interannual sea level variability on top of the secular trend. Therefore, the importance to adopt the concept of the ZOI for improving trend accuracy might also be influenced by the actual time span covered by the record.

To investigate this space- and time-scale-dependency, I truncate the $\text{VLM}_{\text{SATTG}}$ time series such that I obtain different experimental ALES-GESLA-ZOI sets with maximum record lengths from 10 to 18 years. I repeat the same validation analysis against GNSS trends as in section 2.4. Figure 2.4a) encompasses anomalies of the $\text{RMS}_{\Delta\text{VLM}}$ with respect to the mean $\text{RMS}_{\Delta\text{VLM}}$ for a dataset of a specific time scale that is given in Fig. 2.4b (red). The same evolution is shown for trend uncertainties in Fig. 2.4c) and 2.4d).

The mean $\text{RMS}_{\Delta\text{VLM}}$ as well as the mean uncertainties (which are averaged over all relative thresholds for a specific maximum record length) substantially decrease with increasing record length (Figures 2.4a and 2.4c). Both statistics approximately follow the theoretical proportionality of uncertainty and sample size n of $1/\sqrt{n}$ (assuming no serial correlation). The evolution of the $\text{RMS}_{\Delta\text{VLM}}$ anomaly shows that selecting SLAs in a ZOI at high relative thresholds more substantially reduces the $\text{RMS}_{\Delta\text{VLM}}$ on shorter time scales (e.g., 10 years) than on longer time scales (Fig. 2.4a, e.g., at 18 years). At longer time scales (>16 years), the $\text{RMS}_{\Delta\text{VLM}}$ anomalies do not improve significantly between the 80% and 20% thresholds, which I also observe in the previous analysis in Fig. 2.3a. I argue that the transition time scale where the improvements in $\text{RMS}_{\Delta\text{VLM}}$ flatten out (14-16 years) marks the point at which the high frequency coastal sea level dynamical variability is superseded by dynamics producing sea level trends that are coherent on larger spatial scales. At this time scale coastal sea level trends start to merge with the offshore trends for this data-set configuration. The tendency for increasing spatial scales with time is also reflected by the increasing distances from the coast of the measurements for an optimal ZOI at a specific time scale (Fig. 2.4b). The time-scale-dependency could explain the mismatch between the relative improvements of accuracy and uncertainty when using higher levels of comparability. This is also supported by Kleinherenbrink et al. [2018], who found little sensitivity of accuracy to changing correlation thresholds (at high correlations) for SATTG combinations with a minimum length of 15 years.

The same evaluation for the dependency of uncertainty on time and level of comparability X demonstrates that using the ZOI nearly constantly improves trend uncertainties at any time scale. Hence, even though

spatial scales of trend coherency might increase with time, an ideal match of altimetry and TGs should be based on a ZOI. <

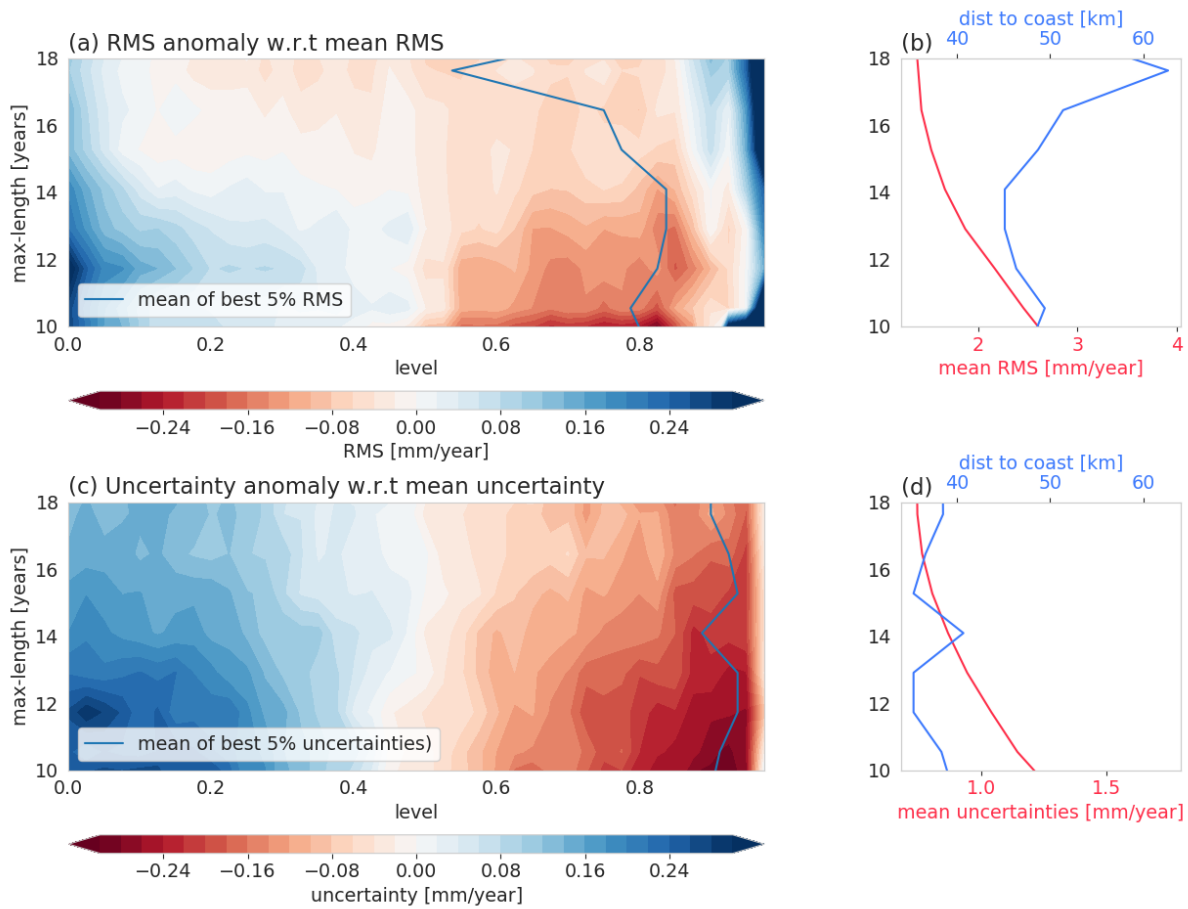


Figure 2.4 Time and space dependencies of trend uncertainty and accuracies: a) Evolution of the $RMS_{\Delta VLM}$ anomaly (SATTG vs. GNSS trend) for subsets of ALES-GESLA-ZOI, depending on a relative threshold X (x-axis) and a maximum record length (y-axis). $RMS_{\Delta VLM}$ anomaly is defined as the departure from the mean $RMS_{\Delta VLM}$ (shown in b) averaged over all thresholds X for a specific maximum record length. In b) I also show in blue the mean distance to coast of the measurements, associated with the average of the best 5% ZOI-levels per time scale, shown in a). c,d) Same as a,b) but for uncertainties.

Given that the spatial scales over which trends appear to be coherent increase with increasing time scales, the use of gridded altimetry can still provide valuable information on coastal sea level trends, despite the coarse resolution of the data. This is also supported by the relatively modest improvement of the $RMS_{\Delta VLM}$ between AVISO-PSMSL-250km and ALES-GESLA-ZOI. Investigations within the framework of the SL_cci initiative, comparing the ALES, AVISO and the XTRACK (SL_cci) datasets, demonstrated that similar performances (in terms of trend accuracy) could be achieved for the gridded dataset (AVISO) as for the optimized coastal datasets [Oelmann and Passaro, 2022]. Here, a larger number of TG-GNSS pairs (based on GNSS stations from the NGL database [Blewitt et al., 2016]) was used and gridded SLA data were selected based on the highest correlated point. The analyses also revealed a significant influence of trend biases in the altimetry products on the overall accuracy of the SATTG VLM estimates. Therefore, I discuss here some of the potential systematic errors in the different altimetry datasets.

› The previous analyses show, that VLM estimates from different datasets (e.g., AVISO-PSMSL-250km and ALES-GESLA-ZOI) are biased compared to trends inferred from GNSS observations. Based on the empirical probability distributions of the means (derived from Monte-Carlo simulations, see appendix in Oelmann et al. [2021]), I argue that these biases are significant for most of the dataset combinations (ALES-PSMSL-250km and AVISO-PSMSL-250km, ALES-GESLA-ZOI).

Several different systematic errors sources can potentially affect the accuracy of the SATTG technique with strong effects on the trend differences with respect to GNSS VLM trends. Limiting factors for VLM determination from both SATTG and GNSS observations are the accuracy and uncertainty of origin and scale of the reference frame (see WM16, Collilieux and Woppelmann [2009], Santamaría-Gómez et al. [2012]), which cannot be realized yet at the required accuracy level [Bloßfeld et al., 2019]. Moreover, as mentioned before, the multi-mission calibration applied (MMXO) reduces intermission biases as well as regionally coherent systematic errors, but does not feature a calibration against TG. The median bias identified for ALES-GESLA-ZOI could be affected by a drift of the mission used as reference. In contrast, the AVISO dataset does not include time-dependent intermission biases and might therefore be additionally influenced by systematic effects of, e.g., Environmental Satellite (Envisat) or Sentinel-3a [Dettmering and Schwatke, 2019].

Next to altimeter bias drift, non-linear VLM from contemporary mass redistribution (CMR) changes were shown to cause differences between VLM_{SATTG} and VLM_{GPS} , due to the different time periods covered [e.g. Kleinherenbrink et al., 2018]. Using GRACE observations, Frederikse et al. [2019] demonstrated that associated deformations can cause VLM on the order of 1 mm/year. Therefore, extending the validation platform, not only by using other homogeneous GNSS observations, but also GRACE estimates could help to identify and mitigate such systematic errors. ‹

Extended analyses (in the SL_cci framework, Oelmann and Passaro [2022]) further provide evidence of systematic biases in the trend estimates of the ALES, AVISO and the XTRACK (SL_cci) datasets. Among these datasets, the AVISO data was associated with the lowest trend bias. Note that for this comparison, up to 198 TG-GNSS pairs were analyzed to investigate the trend differences. Therefore, further research is crucial to systematically identify the sources (i.e., in the geophysical adjustments, corrections, orbits, missions and cross-calibration) of biases in the altimetry systems.

In this chapter, I presented an approach to improve the accuracy and uncertainty of VLM based on coastal along-track altimetry and tide gauges. I emphasize that these SATTG estimates can be affected by a wide range of error sources discussed. Another important factor is the possible non-linearity of VLM itself, which strongly affects the comparability of measurements from different geodetic techniques, when recorded over different time spans. Therefore, addressing this issue in SATTG time series is crucial for the application and our general understanding of the evolution and uncertainties of VLM.

3 Probabilistic reconstruction of vertical land motion

3.1 Introduction

In the previous chapter, I enhance VLM estimates based on the SATTG technique, which presents a valuable complementary source for coastal GNSS VLM data. Despite the improvements, SATTG VLM estimates cannot yet provide the same level of accuracy as provided by GNSS data (e.g., of 0.6 mm/year as reported by Santamaría-Gómez et al. [2014]). The combined application of GNSS data and SATTG estimates is thus fundamental to studying and understanding the regional contribution of VLM on relative sea level on a global scale. Therefore, in this chapter, I exploit a comprehensive multi-technique database consisting of GNSS, tide gauge, and altimetry data, to develop an observation-based vertical land motion reconstruction. The results of these analyses lay the foundation to study the impact of VLM in past, contemporary, and projected relative sea level change estimates in chapter 4.

In section 1.4 I identify three major challenges that hamper the precise estimation of VLM along the world's coastlines: First, GNSS or SATTG time series can be affected by discontinuities, which can be caused either by geophysical origins or instrumental issues and significantly reduce the accuracy of trend estimates [Gazeaux et al., 2013, Blewitt et al., 2016]. The need to correct time series for discontinuities in a large amount of data motivated the development of several different automated discontinuity detection solutions for GNSS data [Gazeaux et al., 2013]. However, the extent to which discontinuities are present and detectable in SATTG time series is so far unclear. The second challenge in estimating VLM is non-linear effects. Previous global scale analyses relied on the working hypothesis of strictly linear VLM [e.g., Wöppelmann and Marcos, 2016, Kleinherenbrink et al., 2018, Hawkins et al., 2019b, Hammond et al., 2021]), despite evidence of non-linear effects due to natural (i.e., tectonics, mass loading changes effects) and human-induced effects (i.e., ground-water pumping). The determination and description of these non-linear effects is essential to understand the present-day variability of VLM and its impact on relative sea level change and uncertainties. Thirdly, the inhomogeneous distribution of observations and regionally sparse availability of data hamper the analysis of VLM continuously along the coastlines. Hence, advanced interpolation techniques are required that take into account the data-density, the formal uncertainties, as well as the regional variance of VLM.

In this chapter I develop and apply several methods, to tackle the challenges of discontinuities, temporal non-linearities, and the sparse spatial distribution of the data. In the following, I present and discuss existing approaches, aimed at dealing with the aforementioned challenges.

Detecting discontinuities in geodetic time series

➤ To detect and mitigate discontinuities for accurate position and velocity estimates from GNSS data a wide range of semi- to fully automatic discontinuity detection tools [e.g., Vitti [2012], Gallagher et al. [2013], Goudarzi et al. [2013], Kowalczyk and Rapinski [2018], or Klos et al. [2019]] have been developed. Some discontinuity detection approaches feature deterministic models including, e.g., rate, annual cycle and noise

formulations, as well as step functions to model discontinuities in time series [He et al., 2017, Klos et al., 2019]. Montillet et al. [2015], for instance, investigated different approaches to detect single discontinuities at prescribed epochs using linear-least squares. Another approach of discontinuity detection is Hector [Bos et al., 2013a, Montillet and Bos, 2020], which utilizes Maximum Likelihood Estimation (MLE) to determine trends and noise parameters. Discontinuities are identified in an iterative manner until the Bayesian Information Criterion (BIC, Schwarz [1978]) reaches a predefined threshold [Bos and Fernandes, 2016]. As an alternative to explicitly modeling trends and discontinuities, Wang et al. [2016] presented a state-space model and singular spectrum analysis, which provides a better approximation of time-varying nonsecular trends or annual cycle amplitudes than the MLE method. Another non-parametric method is the Median Interannual Difference Adjusted for Skewness (MIDAS) method, Blewitt et al. [2016]), which is a variant of a Theil-Sen trend estimator and is capable to robustly mitigate discontinuities in the data for linear trend estimation. Many other solutions for discontinuity detection exists, which are more thoroughly described in, e.g., Gazeaux et al. [2013] or He et al. [2017].

In a comparative research study, Gazeaux et al. [2013] analyzed the capability of 25 different algorithms to detect discontinuities in synthetically generated data. However, they found that manual screening still outperformed the best candidate among the solutions. Trends derived from semi-/automated approaches were shown to still be biased on the order of ± 0.4 mm/year due to undetected discontinuities in the data. Given this accuracy limitation, the improvement of automatic discontinuity detection is thus subject of ongoing research and leads to the steady development of the algorithms, see, e.g., He et al. [2017].

The discontinuity detection with standard approaches like linear least-squares becomes particularly difficult for an increasing number of discontinuities with unknown epochs. In addition, as highlighted by Wang et al. [2016], site-movements are not necessarily strictly linear and can be affected by time-varying movements. Thus, it is critical to also detect discontinuities in form of the onset of trend changes or post seismic deformation to evaluate the validity of a strictly linear motion. Commonly applied algorithms, such as MIDAS, for instance, do not yet account for such time series features. Another central challenge for discontinuity and trend change detection is the appropriate identification of the stochastic properties of the time series. This is especially problematic for SATTG time series, as their associated noise amplitudes are usually one order of magnitude larger than in GNSS data.

None of the existing methods have been applied or tested to detect an arbitrary number of discontinuities and/or trend changes in SATTG time series. More generally, it is currently unknown to what extent variable velocities caused by dynamics such as seismic events can be (automatically) detected in GNSS or SATTG time series, given the high noise levels in the data. To fill this gap, I develop a new algorithm called Discontinuities in Time Series (DiscoTimeS), which simultaneously estimates the number of discontinuities, the associated magnitudes of discontinuities, and piecewise linear trends together with other time series features, such as the annual cycle and noise properties. The model implementation is presented in section 3.2 and is tested based on synthetic and real GNSS and SATTG data. ◀

Interpolating VLM in space and time

To extrapolate VLM to areas where no direct VLM observations are available, several different techniques were applied to interpolate data from existing networks of GNSS stations, tide gauges, and altimetry data [Bodin and Sambridge, 2009, Husson et al., 2018, Hawkins et al., 2019b, Pfeffer et al., 2017, Hammond et al., 2021]. One

limitation of previous interpolation techniques like spline interpolation [Serpelloni et al., 2013], least square collocation [Sánchez et al., 2018], or weighted averages of neighboring points [Pfeffer et al., 2017], is that the solutions depend on a user-defined length-scale parameter that is not dynamically adapted to the wavelength of the actually observed signal. This length scale can be variable due to different underlying VLM processes, which can be associated with very different spatial scales (see section 1.2), and due to the spatial distribution of point observations, which determines how well a process can be resolved. Therefore, previous approaches developed and applied the Bayesian transdimensional regression method [e.g., Bodin and Sambridge, 2009, Husson et al., 2018, Hawkins et al., 2019b], which dynamically adapts the complexity (spatial resolution) of the interpolated surface by parametrizing the surface with a set of variable mobile nodes (grid points). Thus, the number of nodes, which determines the complexity of the grid is an unknown parameter of the inversion and is itself estimated.

As emphasized in section 1.4.2, all of the abovementioned studies only interpolated linear trends in space but did not provide information on the actual temporal variations of VLM. To resolve VLM continuously in space and in time, I will fit a Bayesian model to the data, consisting of a trend component and a set of common modes of variability. I will use a Bayesian Principal Component Analysis (BPCA) [e.g., Wudong et al. [2020]] to estimate the modes of variability, because classical Empirical Orthogonal Function (EOF) analysis relies on the completeness of the data, which is not given in our case, due to the irregular temporal sampling and gaps in the observations. In this chapter, I will implement the method developed by Hawkins et al. [2019b], to interpolate spatial coefficients, which allows me to assess the full posterior probability distributions of the parameters.

Workflow

➤ I reconstruct coastal VLM based on the joint probabilistic analysis of a comprehensive network of GNSS stations, tide gauges, and satellite altimetry over the period of 1995-2020, resulting in a continuous time- and space-resolving VLM dataset along the global coastlines (see methods in section 3.3). The estimated patterns represent a superposition of large-scale VLM fingerprints, including linear motion signatures, e.g., the GIA and non-GIA effects, as well as regional patterns of responses to earthquakes or terrestrial water storage changes of inter-annual to decadal variability. I bolster my findings using a suite of external VLM information on GIA [Caron et al., 2018] and contemporary mass redistribution [Frederikse et al., 2020].

I apply a 3-step procedure to reconstruct the spatially and temporally varying VLM. First (1), the input data (GNSS, SATTG) are pre-processed, meaning that the time series are adjusted/corrected for offsets, single-point outliers, and the annual cycle in a semi-automated manner. The development of the associated methods is described in section 3.2.1. Second (2), in section 3.3, I perform a dimensionality reduction of the spatiotemporal variability of the data by estimating long-term linear trends and common modes of variability using Bayesian principal component analysis (BPCA). Finally (3), I spatially interpolate the approximated linear trends and the spatial coefficients of the common modes of variability and their associated uncertainties using the adaptive Bayesian transdimensional regression approach. The continuous 3D (in space and time) VLM reconstruction is obtained from the sum of the recombined principal components (PCs) and interpolated spatial coefficients, and the linear trend estimates. Accordingly, I apply an uncertainty propagation of the different components to derive the space/time-dependent uncertainties. Figure 3.1 illustrates the corresponding processing chain of the data. Details the individual steps are provided in the following sections. ◀

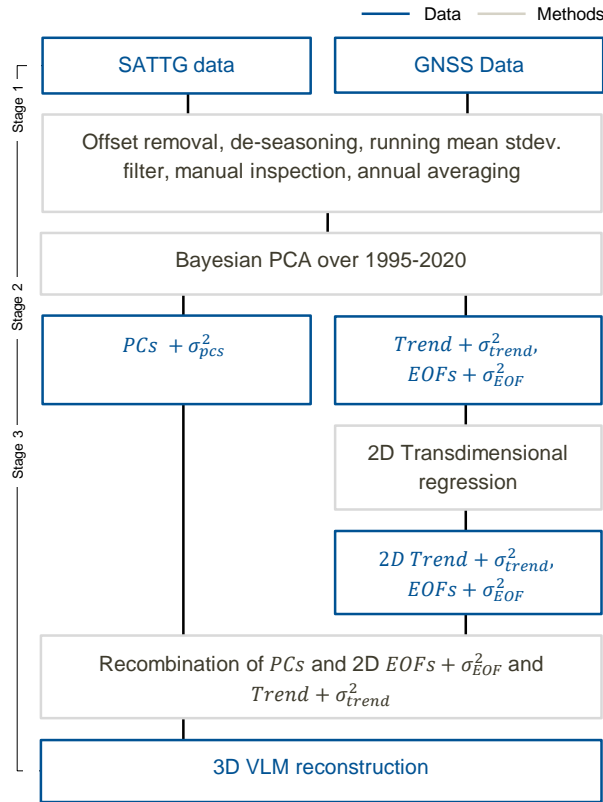


Figure 3.1 Workflow describing the processing steps of generation of the VLM reconstruction dataset.

3.2 Vertical land motion time series analysis

In this section I develop a novel approach to detect discontinuities and trend changes in SATTG and GNSS data. \blacktriangleright To cope with the extensive number of parameters, I use a Bayesian framework and generate inferences with Markov chain Monte Carlo (MCMC) methods. MCMC methods are capable to deal with highly complex models and were already successfully applied by Olivares and Teferle [2013] to estimate noise model components in GNSS data. Although not yet tested, these methods could also be adapted to SATTG time series. The framework allows me to assess the empirical probability distribution of a set of multiple unknown parameters such as the epoch and the number of change points in the data.

3.2.1 Bayesian modeling of piecewise trends and discontinuities

The overarching goal is to detect the most common time series features in GNSS and SATTG data using a single comprehensive model. The major components considered here are discontinuities $o(t)$ (abrupt changes in height), trends $g(t)$, a seasonal term $seas$, and a noise term η , which can also be identified in Fig. 3.2:

$$y(t) = o(t) + g(t) + seas + \eta \quad (3.1)$$

Here, $y(t)$ denote either GNSS or SATTG observations at time t and are described with a set of unknown parameters Θ , which define the motion components (see section 3.2.1 and Table 3.1 for a full description of Θ). The discontinuities $o(t)$ and trend components $g(t)$ are assumed to change with time. Disruptions can

occur in form of abrupt jumps, changes in trends, the onset of post-seismic deformation or a combination of such events. Thus, the time dependent components are piecewise estimated over individual segments of the time series. These segments depend on the number of change points and the time (epoch) when they occur (hereafter called change point position), which are unknown parameters Θ of the model, as well. I aim to simultaneously estimate the most likely number n and position of change points s_j , together with the other terms describing the motion signatures.

Deterministic and stochastic model components

In the following, I summarize how the deterministic components, discontinuities, trend changes, and the seasonal cycle, are defined. Suppose that the linear motion at the beginning of the time series is defined by a base trend k . The time series is divided by n change points at positions s_j (with $j = 1, \dots, n$). After every change point the base trend is updated by an incremental trend change h_j . This can be described as a cumulative sum of all trend adjustments over time $k + \sum_{j:t>s_j} h_j$. Taylor and Letham [2018] used $k + \vec{a}(t)^T \vec{h}$ ($= k + \sum_{j=1}^n a(t)_j h_j$) as an alternative representation using the Heaviside step function $\vec{a}(t) \in 0, 1$.

Thus, a segmented step function is obtained for the trend component. Multiplication of this trend function with time would, however, introduce discontinuities at the change point positions, which are proportional to the trend change: $\gamma = s_j h_j$. Hence, the full representation of the trend component must be corrected for these discontinuities as follows:

$$g(t) = (k + \vec{a}(t)^T \vec{h})t - \vec{a}(t)^T \vec{\gamma}. \quad (3.2)$$

In agreement with trend changes, arbitrary discontinuities (i.e., offsets) can occur after every change point. Such 'segment discontinuities' are parameterized in a similar way as in eq. (3.2):

$$o(t) = o + \vec{a}(t)^T \vec{p}. \quad (3.3)$$

Here, o is again the base offset and \vec{p} is a vector of length n , which comprises the discontinuity adjustments after every s_j .

For simplicity, I implement a time-invariant seasonal component (i.e., without interannual variations), which describes the seasonal cycle as monthly multi-year averages. The twelve multi-year monthly means are contained in the vector \vec{m} . Thus the seasonal component is:

$$seas = \vec{x}(t)^T \vec{m}, \quad (3.4)$$

with $\vec{x}(t) \in 0, 1$:

$$x_i(t) = \begin{cases} 1, & \text{if } month(t) = i \\ 0, & \text{otherwise} \end{cases} \quad (3.5)$$

Finally, the noise η in eq. (3.1) is approximated as a first-order autoregressive process (AR(1)). I emphasize that the presented model setup explicitly allows for trend changes, which are, however, usually constrained in other applications. These include, for example, the computation of reference frames (ITRF2014 [Altamimi et al., 2016] and DTRF2014 [Seitz et al., 2021]), or existing trend-estimators like MIDAS. In section 3.2.3, I

discuss several geophysical processes, which generate trend changes and hamper the determination of purely linear trends over the full observation period. These examples underline the advantages of detecting trend changes, which can otherwise lead to misinterpretations of estimated secular rates.

Bayesian parameter estimation

The resulting model contains a multitude of unknown model parameters, which are particularly influenced by the arbitrary number of change points and related properties (e.g., epoch, magnitude of discontinuity). Thus, given the high complexity of this problem, I use Bayesian MCMC methods [e.g., Brooks et al., 2011] to approximate the full posterior probability distribution of the model parameters $P(\theta|y)$.

For every parameter in Θ , I formulate prior beliefs of their probability distributions $P(\Theta)$, which are then updated during the sampling process. Such an assignment of $P(\Theta)$ is exemplified using the two most influential parameters in the model, which are the number n and the position s_j of change points. Note that n sets the size of the parameter vectors, e.g., of the vector containing the trend increments. Thus, for $n = 0$, no trend or discontinuity change is estimated, for instance. The number of change points is approximated with multiple (n_{max}) discrete Bernoulli distributions, which generate samples between 1 (change point detected, with probability q) and 0 (no change point detected, probability $1-q$) for every possible change point. A change point is switched on when the probability q exceeds 0.5. The probability of the positions of the change points \vec{s} is assumed to be normally distributed. Their mean values $\vec{\mu}_s$ are drawn from a random uniform distribution $U(t)$ (hyperprior, i.e. a probability distribution of the hyperparameters $\vec{\mu}_s$ of the prior distribution) spanning the full time period of observations:

$$\vec{s} \sim \mathcal{N}(\vec{\mu}_s, \sigma_s^2) \text{ with } \vec{\mu}_s \sim U(t) \text{ and } t \in [t_1, T] \quad (3.6)$$

The positive autocorrelation coefficient ϕ and the white noise amplitude σ_w^2 are both drawn from halfnormal distributions with σ_ϕ and $\hat{\sigma}_w$, respectively. Finally, I approximate all the other parameters, the trend and discontinuities o, \vec{p}, k, \vec{h} and the monthly means \vec{m} with normal distributions. Hence, the following set of unknown parameters of the model is obtained: $\Theta = (\vec{q}, \vec{\mu}_s, \mu_o, \vec{\mu}_p, \mu_k, \vec{\mu}_h, \vec{\mu}_m, \vec{\sigma}_s, \sigma_o, \vec{\sigma}_p, \sigma_k, \vec{\sigma}_h, \sigma_\phi, \hat{\sigma}_w, \vec{\sigma}_m)$. As can be seen, the complexity of the model is set by the number of change points. For example, if two change points are detected, there are $2 (\mu_o, \mu_k) + 12 (\vec{\mu}_m) + 2^*4 (\vec{q}, \vec{\mu}_s, \vec{\mu}_p, \vec{\mu}_h) + 2 \hat{\sigma}_w = 24$ different parameters to be estimated.

In addition to the type of probability distribution $P(\Theta)$, I also assign initial values of the associated parameters of the distributions. Here, I make use of prior knowledge of common GNSS and SATTG time series characteristics, to improve the parameter estimation. As an example, I implement the underlying hypothesis that VLM is generally linear in form of prior belief of the expected number of change points: I set $\vec{q}_0 = 0.1$ as the initial values for the probability (i.e., 10%) of a change point to occur (at the beginning of initialization). Thus, I define a so called informative prior for \vec{q}_0 , which expresses specific knowledge of the expectation of a change point to occur. I also define other initial values settings, which are more thoroughly explained in the appendix 1. Table 3.1 summarizes the complete model setup and initial assumptions. Note, that these initial values are set for the normalized time series.

I use different MCMC samplers to generate inferences about the desired target distribution $P(\theta|y)$. For all continuous variables I use the state-of-the-art No-U-Turn sampler (NUTS) [Hoffman and Gelman, 2014].

Table 3.1 Overview of model components, parameters and prior distributions

$y(t) = o + \vec{a}(t)^T \vec{p} + (k + \vec{a}(t)^T \vec{h})t - \vec{a}(t)^T \vec{\gamma} + x(t)^T \vec{m} + \eta$			
Name	Parameter	Prior distribution	Hyperparameter Prior distribution
CP (change point) prob.	\vec{q}	$Ber(\vec{q}), \vec{q}=0.1$	-
CP position	\vec{s}	$\sim \mathcal{N}(\vec{\mu}_s, 5^2)$	$\vec{\mu}_s \sim U(t)$ and $t \in [t_1, T]$
Discontinuities	o, \vec{p}	$\sim \mathcal{N}(\vec{0}, 2\vec{0}^2)$	-
Trends	k, \vec{h}	$\sim \mathcal{N}(\vec{0}, \vec{1}^2)$	-
Monthly means	\vec{m}	$\sim \mathcal{N}(\vec{0}, \vec{1}^2)$	-
AR1-coeff.*	ϕ	$\sim HalfNorm(0.4^2)$	-
White noise	σ_w	$\sim HalfNorm(1^2)$	-

*Lag-one autocorrelation coefficient

For the binary variables \vec{q} , which control the occurrence of change points, the Metropolis-within-Gibbs step method is used [e.g., van Ravenzwaaij et al., 2018]. In order to enhance the robustness of the parameter estimates, I generate an ensemble consisting of eight independent Markov Chains, whose initial conditions are perturbed within the limits of the aforementioned described prior distributions. Every chain features 8000 iterations, which is found to be sufficient for individual chains to achieve convergence of the parameters (according to the convergence diagnostic by Geweke [1992]). As an example, fitting a 20 year long weekly-sampled GNSS time series, takes on average four hours, which requires four cores with two hyperthreads per core.

Figure 3.2 shows independent model fits of SATTG and GNSS time series. Next to the observations (red), I show randomly selected draws from the eight different Markov chains (green), as well as the posterior mean of trends and discontinuities from the ensemble (blue), which is identified as the best chain. Vertical dashed lines indicate detected change points.

The example shows that the Markov chains may behave very differently depending on the characteristics of the time series. While there is almost no spread (green line) in the model estimates for SATTG data, the spread is much larger for the GNSS model estimates (green background shading). The latter is an example of 'multimodality', a central problem when using discrete variables [Brooks et al., 2011]. I utilize different Bayesian model selection criteria (see appendix 2), which provide a measure of model fit and complexity, to select a single best-performing chain among the ensemble members. The successful approximation of the observations by the depicted chain selection in Fig. 3.2(b), underpins that exploiting several independent chains is of paramount importance for parameter estimation. <

The discontinuity detection algorithm is applied to synthetic and observed vertical land motion time series. Several different sensitivity experiments are designed to investigate the detection-limits for different time series types (see section 3.2.2). In section 3.2.3 I analyze GNSS and SATTG observations, to generate a more realistic description of the frequencies and magnitudes of discontinuities or trend changes in VLM data. I use 381 GNSS time series from the NGL database [Blewitt et al., 2016]. The 606 SATTG time series are based on the Zone of Influence as developed in section 2.2 (see Oelsmann et al. [2022a] for more details). I compare and validate DiscoTimeS against MIDAS [Blewitt et al., 2016] and a GIA model [Caron et al., 2018] in section 3.2.4.

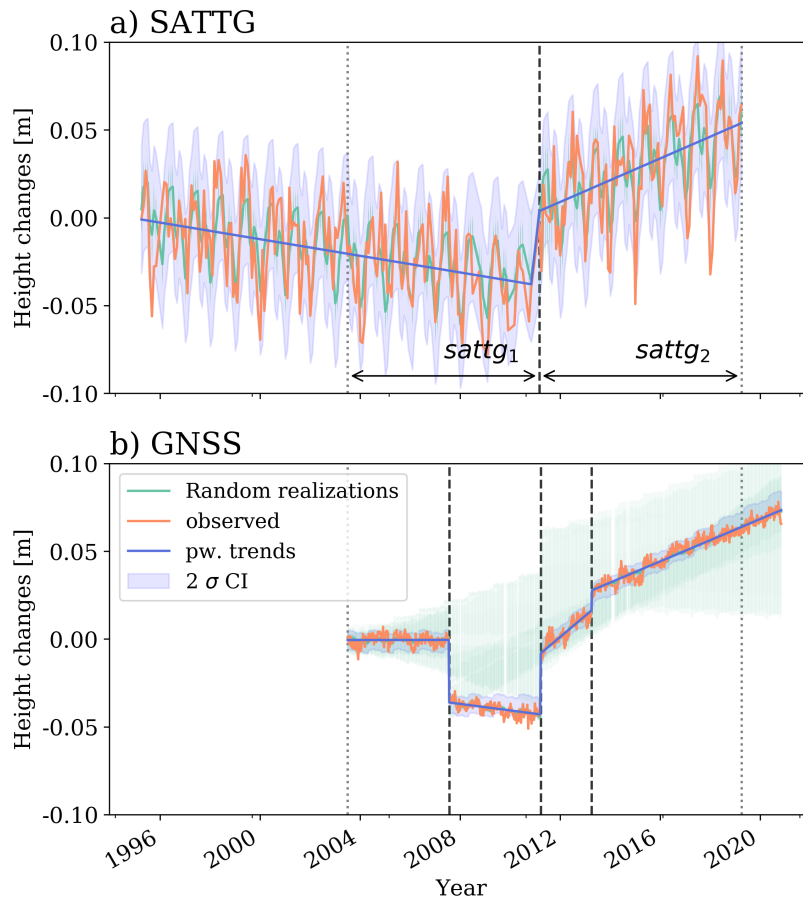


Figure 3.2 Bayesian model fit for (a) SATTG time series and (b) GNSS time series observed at co-located stations in Kujiranami (Japan). The discontinuity and trend change in 2011 is similarly detected in SATTG and GNSS data. Observed height changes [m] are shown in red together with 1000 randomly drawn realisations from different chains in green (shading in the background). The blue lines illustrate the posterior means of the selected best chain (see Appendix 2). The blue shading denotes the 2σ confidence intervals (CI) of this model. Detected change points are marked by the dashed vertical lines. The grey dotted lines confine the segments of the time series ($sattg_1$, $sattg_2$), which are compared with the GNSS piecewise trends.

3.2.2 Sensitivity experiments with synthetic data

Synthetic data of sensitivity experiments

➤ To evaluate the performance of the discontinuity detection, I apply DiscoTimeS to synthetic data that mimic the properties of real SATTG and GNSS time series and include discontinuities and trend changes. The modeled time series feature are a trend, a harmonic annual cycle and a noise term. All time series have a duration of 20 years and 5% missing values. I define the time series properties (i.e., annual cycle and noise amplitudes) according to the properties of the 606 SATTG time series and 381 GNSS time series, which are analyzed using the Bayesian model DiscoTimeS and Maximum Likelihood Estimation [Bos et al., 2013a].

Table 3.2 Synthetic time series features.

Component	SATTG	GNSS-AR1	GNSS-PLWN
Base trend k [mm/year]	0	0	0
Annual cycle amp. [mm]	20	2.5	2.5
White noise ϵ [mm]	20	3.2	2
PL noise ϵ_{pl} [$mm/year^{-k/4}$]	-	-	6
AR1. coeff. ϕ	0.3	0.45	-
Duration [years]	20	20	20
Temporal Resolution	Monthly	Weekly	Weekly
Gaps	5% (random)	5% (random)	5% (random)

I apply a seasonal term to model geophysical seasonal surface mass loading variations affecting VLM, such as tidal loading or hydrological loading [e.g., Ray et al., 2021]. In contrast to the GNSS data, seasonal variations in SATTG data can also stem from discrepancies in the observations of the different techniques (TGs and SAT). As shown in the following, these non-geophysical variations can have much larger amplitudes than those obtained from GNSS data and thus influence the noise characteristics.

Several studies affirmed that a combination of white noise (WN) and power law (PL) noise is most appropriate to describe stochastic properties of GNSS time series [e.g., Williams, 2008, Langbein, 2012]. Therefore, for the synthetic GNSS time series I create PL + WN noise, using similar noise properties as found for 275 GNSS vertical position time series by Santamaría-Gómez et al. [2011]. I use a spectral index of -0.9, which is close to flicker noise process, and amplitudes of 2 mm/year and 6 mm/year^{-k/4} for white and coloured noise, respectively. To study the impact of the noise type on the change point detection, I also analyze synthetic GNSS data with less realistic AR1 noise.

Although several studies [Bos et al., 2013b, Royston et al., 2018] investigated noise properties of sea level time series from altimetry and TG observations, there is no consensus on which noise model is most appropriate for SATTG time series. Thus, I determine the noise characteristics of the 606 observation time series using an autoregressive process AR1 and a PL + WN noise model (with the Hector Software, Bos et al. [2013a]). I find that the Bayesian Information Criterion (BIC, Schwarz [1978]) is slightly more in favor of the AR1 noise model (compared to the PL + WN process). Therefore, I apply the AR1 noise model to simulate SATTG data.

I adopt the different magnitudes of the annual cycle, the AR1 coefficient and the white noise amplitude according to median values, which are estimated from SATTG and GNSS time series (derived from fitting them with DiscoTimes), as defined in Table 3.2. The noise and annual cycle amplitudes are 6-7 times larger for SATTG than for GNSS time series. This behavior is expected to strongly influence the range of magnitudes of discontinuities and trend changes that the algorithm can detect. Therefore, in the sensitivity experiments, I take these different noise properties into account by testing the detectability of different discontinuity-to-noise ratios, instead of absolute magnitudes of discontinuities.

I perform three experiments in which I change (1) only the discontinuity-to-noise-ratio, (2) the magnitude of the trend change and (3) the number of change points, together with discontinuities and trend changes. The complete setup is described in Table 3.3. Fig. 3.3a) exemplifies time series of the experimental setups for different parameters.

The change point for the first two experiments is set in the center of the time series. These experiments are conducted to assess the sensitivity of the algorithm to detect single discontinuities and trend changes for

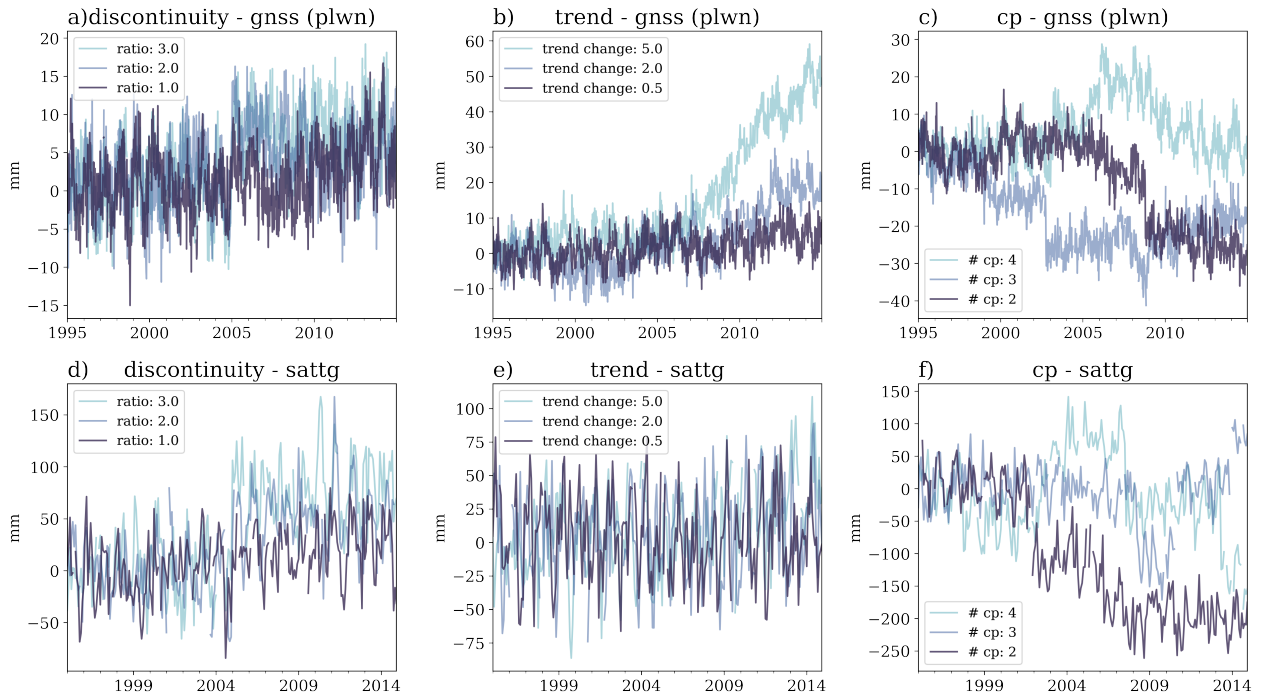


Figure 3.3 Examples of synthetic height time series (mm) generated for the sensitivity experiments. The upper (lower) row show time series which imitate VLM observations from GNSS-PLWN (and SATTG). The different lines exemplify variations of the discontinuity-to-noise ratio (a,d), the trend change magnitudes in mm/year (b,e), as well as variations in the number of change points and the magnitudes of the discontinuities and trend changes (c,f). In the discontinuity- (a,d) and the trend change experiments (b,e) the change point is located in the center of the time series. In (c) and (f) change points are randomly distributed.

different noise amplitudes in the data. The third experiment aims to reveal how different numbers of change points might affect the detection rates.

I vary the discontinuity-to-noise ratio and the trend change with a stepsize of 0.5 mm/year. For every step and every tested number of change point (in the change point experiment), I generate 10 different synthetic series and model fits.

Results: Sensitivity experiments with synthetic data

The sensitivity experiments are performed to investigate (1) the accuracy of the trend estimation (in presence of discontinuities and trend changes) as well as (2) the accuracy of the discontinuity epoch estimation. Figure 3.4 summarizes the results for the synthetic GNSS data with PL + WN and AR1 noise (first and second row),

Table 3.3 Setup of the sensitivity experiments.

Property	1. Discontinuity-exp.	2. Trend change exp.	3. Change point exp.
Number of Discontinuities	1	1	2-4
Discontinuity positions	center	center	$\sim U(t)$ with $t \in [t_1, T]$
Discontinuity-to-noise ratio	0.5, 1.0, 1.5, ...5	0	$\sim U(d)$ with $d \in [2, 5]$
Trend change	no	yes	yes
Δ Trend change	-	0.5, 1.0, 1.5, ...5 [mm/year]	$\sim \mathcal{N}(\vec{0}, \vec{1}^2)$ [mm/year]

and for the SATTG time series (last row). In columns 1-3, I illustrate the accuracy of trend estimation expressed by the absolute deviations of the estimated trends (of the individual ensembles) from the known (prescribed) linear trends (see appendix 3 for more information of this validation); column 4 shows the change point detection-rate.

I compare the absolute deviations of the estimated piecewise trends ΔPW (in green), with the deviations of trends, computed without accounting for any discontinuities in the data, i.e. the deviations of single linear trends (ΔLIN , in red). As expected, Fig. 3.4 shows that these deviations are linearly dependent on the magnitude of the discontinuity or the trend change. These statistics are compared to the deviations of trends, which are obtained, when piecewise trends are computed over the known individual time series segments (ΔLIN (discontinuity known), blue line). The latter represents the theoretical best trend estimate, given the noise of the data.

I observe that the Bayesian ΔPW estimates in the discontinuity- and the trend experiments (Fig. 3.4 first and second column) generally outperform the linear trend estimates ΔLIN . With increasing discontinuity or trend change magnitude, the accuracy of the Bayesian estimates remains almost constant, while the linear trend deviations ΔLIN are naturally increasing, in particular with increasing discontinuity magnitude. There is however a notable dependency of the ΔPW deviations on the noise type and noise amplitudes. The accuracy of trend estimates is much lower for GNSS data with PL noise, than for the data with AR1 noise. In the latter case (AR1 model, Fig. 3.4(e) and 3.4(f)), the ΔPW deviations are practically identical to the theoretically best achievable deviations, while for the GNSS-PLWN experiments deviations between 0.25 - 0.5 mm/year are found (Fig. 3.4(a) and 3.4(b)). Therefore, the higher low-frequency variability in the GNSS-PLWN data strongly influences the overall accuracy level of trend estimation and has a greater impact than the magnitude of the discontinuity.

Consistent with the differences induced by the noise model type, the noise amplitudes also affect the accuracy of trend estimates. The ΔPW trend deviations of the simulated SATTG time series (Fig. 3.4i and 3.4j), which have much higher noise amplitudes than the GNSS-AR1 data, range in the order of 0.5 - 1.5 mm/year. Nevertheless, the estimated piecewise trends are only slightly worse than the theoretical best achievable trend estimates and consistently better than the ΔLIN deviations. This underpins that the model can significantly improve the accuracy of trend estimation (ΔPW) by mitigating unknown discontinuities or trend changes.

In the change point experiments (Fig. 3.4(c), 3.4(g) and 3.4(k)) different numbers of change points with random epoch and magnitudes of discontinuities and trend changes are simulated. The experiments confirm the dependence of the accuracy of trend estimates on noise model type and amplitudes, similar to that found in the single discontinuity- and trend experiments. Here, higher trend deviations are found for the experiment with synthetic GNSS data and PL noise compared to the data with AR1 noise.

I simulate up to four change points and find that the model performances slightly deteriorate as the number of change points increases (Fig. 3.4(c), 3.4(g) and 3.4(k)). Accordingly, performances are expected to further decrease with a much larger number of change points, if the length of the time series remains the same. This is likely due to the reduced length of the remaining time series segments. For example, with four equally distributed change points, each segment would only have a length of 4 years (for a 20-year-long time series). At the given noise levels of the time series, a 4-year-long SATTG time series would, however, have a trend uncertainty of more than 5 mm/year (even without accounting for autocorrelated noise). The large noise amplitudes and their effect on trend uncertainty therefore set a natural lower bound for the accuracy of trend

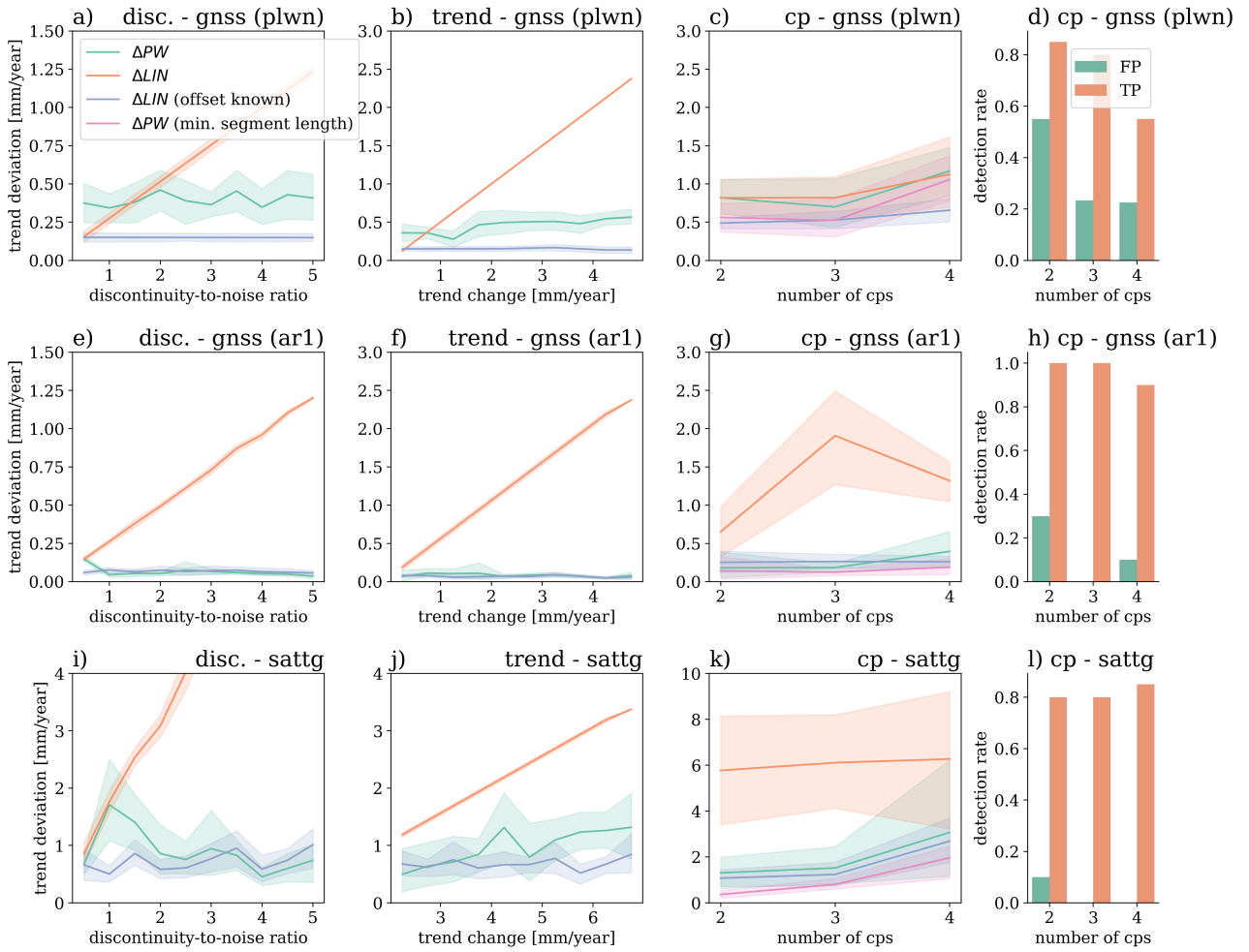


Figure 3.4 Accuracy of trend estimates and detection rates based on the sensitivity experiments with synthetic data. Results are provided for the discontinuity- (first column), trend (second column) and change point (third and fourth column) sensitivity experiments. Each row shows statistics for different time series types: GNSS-PLWN (first row), GNSS-AR1 (second row) and SATTG time series (last row). In columns 1-3 I show absolute (weighted) deviations of piecewise (ΔPW , green) and linear trend (ΔLIN , red) estimates with respect to the piecewise simulated (known) trends of the synthetic time series. The linear trends are computed with least-squares without accounting for discontinuities. The blue lines (ΔLIN) correspond to linear trend estimates that are computed over the known time series segments, i.e., here I assume the discontinuities are known. Solid lines and shadings indicate the mean and 95% confidence bounds of the different fits per tested parameter. In (c), (g) and (k) the magenta lines show ΔPW deviations when only SATTG (GNSS) segments with a length over 8 (3) years are used. A discontinuity-to-noise ratio of 1 is equivalent to 3.2 mm (GNSS) and 20 mm (SATTG). In the change point experiments, the magnitudes of the discontinuities are randomly drawn from an uniform distribution covering values within 2-5 times the white noise amplitudes. In the last column, I show True Positive (TP) and False Positive (FP) detection rates for the change point sensitivity experiment.

estimation when using short segments of SATTG or GNSS time series. Lower trend accuracy is thus less a sign of poor model performance, but rather caused by the large uncertainties of the piecewise trends. The magenta curves in Fig. 3.4(c), 3.4(g) and 3.4(k) illustrate how the ΔPW trend deviations are influenced when only longer time series are used. Here, I set the minimum required length of the SATTG (GNSS) time series to 8 (3) years, which corresponds to trend uncertainties of ~ 2 mm/year. For both time series types, SATTG and GNSS, this entails better accuracy and a reduction in the number of extreme deviations as shown by

the narrower uncertainty bands (of the ΔPW deviations), which represent the spread of the different fits per parameter. Therefore, I apply these criteria of minimum segment lengths (i.e. 8 years for SATTG and 3 years for GNSS) also for the real data applications.

The performance of the discontinuity detection is also evaluated by means of the False Positive (FP) and True Positive (TP) detection rates for the different experimental setups (see Fig. 3.4d, 3.4h and 3.4l). A change point is correctly (TP) detected when the prescribed change point position is within the (95%) confidence bounds of the 2σ uncertainties of the estimated change point position. The TP detection rate is defined as the proportion of change points that are correctly detected (with respect to the number of prescribed change points). Detected change points that do not correspond to the prescribed ones are accounted for in the False Positive (FP) detection rate, which is used to detect over/misfitting of the data.

The TP detection (FP detection) rate for the GNSS-PLWN time series are lower (higher) than for the associated GNSS-AR1 time series (Fig. 3.4(d) and 3.4(h)). These results reflect the differences in the performances with regards to the accuracy of the trend estimates. In particular, the increased FP rate for GNSS-PLWN time series consolidates that simultaneously estimating discontinuities and trend changes in the presence of PL-noise remains a key challenge for discontinuity detection. Interannual variations (in GNSS-PLWN series) are likely to be overfitted or misinterpreted as discontinuities or trend changes. This can explain the better performance for GNSS-AR1 time series, which feature little low-frequency variability. Also the generally high TP detection rate for SATTG shows that differences in the noise amplitude are less influential than the type of the noise itself.

Overall, I obtain relatively high TP detection rates (50% - 100%), compared to previously reported statistics by Gazeaux et al. [2013], where the highest reported TP rate was in the order of 40%. On average, 223 out of 270 prescribed change points are correctly detected in the cp-experiments. Differences in the experimental setups, as well as in the definition of the TP detection rate, can explain these disparities. For example, in the change point experiments performed in this work, the discontinuities have a minimum size of two times the white noise amplitude. In Gazeaux et al. [2013], the magnitudes of the discontinuities were drawn from a Pareto-distribution containing smaller discontinuities than those applied in the presented experiments. Also the definition of the detection-rate differs across the studies, considering that in this study the estimated epoch uncertainties are used as a temporal tolerance and Gazeaux et al. [2013] set a constant 5-day tolerance window around a change point. There exist also general differences in the time series noise-amplitudes and temporal resolutions. With the focus on discontinuity detection in SATTG time series, it should be noted that the accuracy of epoch estimation in SATTG data strongly decreases compared to GNSS data, given the low monthly resolution as well as the high noise levels in the data.

In summary, the synthetic experiments verify that DiscoTimeS improves the accuracy of those trend estimates that are impaired by unknown discontinuities. Hence, in the following sections I apply the algorithm to real data and test to what extent DiscoTimeS can be utilized as an unsupervised discontinuity-detector. ◀

3.2.3 Discontinuity detection in multi-technique observations

DiscoTimeS is applied to GNSS and SATTG VLM time series. I use GNSS time series from the Nevada Geodetic Laboratory (NGL) of the University of Nevada (Blewitt et al. [2016], <http://geodesy.unr.edu>) with minimum lengths of 6 years and at least 3 years of valid data. Time series with formal uncertainties larger than 2 mm/year (based on the MIDAS [Blewitt et al., 2016] estimates) are rejected from the analysis. The GNSS time

series are downsampled to weekly averages (as in Olivares et al. [2020]). SATTG time series are analyzed independently from the GNSS data. I use the same coastal altimetry dataset as described in section 2.2 and combine TG and altimetry data based on the Zone of Influence approach. I use monthly PSMSL TGs, to increase the time series length, because at the time of writing GESLA contains only data until 2015. Please refer to the discussion in Oelsmann et al. [2021], for a comparison of the performances based on PSMSL or GESLA TG data. I only use SATTG time series with at least 150 months of valid data within the period from 1995-2020.

Physical origins of trend changes in VLM data

One important premise of the development of DiscoTimeS is that VLM cannot only be disturbed by discontinuities, but can also exhibit trend changes on decadal time scales, which hamper an unbiased assessment of secular trends. The detection of significant trend changes can provide valuable information about the reliability of extrapolating the VLM at the considered station. To further substantiate the existence and physical justification of such nonsecular VLM, I show GNSS observations together with piecewise trend estimates, as well as the single linear trend estimates by MIDAS (which is a robust estimator of a single trend).

Figure 3.5 depicts three physical mechanisms that can influence the linearity of VLM. The majority of trend changes in VLM observations can be attributed to earthquakes, see Fig. 3.5(a-d). These examples are useful to understand the limitations of established methods (like MIDAS), which do not incorporate possible trend changes. In such cases, an estimation of trend changes can be applied as a pre-processing step before fitting the data with adequate models including terms of post-seismic deformation, for instance.

Next to earthquakes, VLM can also be affected by more localized processes as highlighted by the time series in the second row (e-h) of Fig. 3.5. The associated GNSS stations are all located in the Gulf of Mexico, near Houston. In this region, VLM exhibits a relatively large spatial and temporal variability (0 - 10 mm/year subsidence), which is influenced by extraction of hydrocarbons, groundwater withdrawal, land reclamation and sedimentation [Kolker et al., 2011, Letetrel et al., 2015]. Such processes likely also affect the selected GNSS stations. The station velocities in Fig. 3.5(e) and 3.5(f) indicate that averaged linear trends might not be entirely representative of a secular trend, given the detected variability in trends over different periods of time. The closely located stations DEN1 and DEN3 (with a distance of 2 km) also show a trend change around the end of year 2015, which is also not reported in the station metadata. Hence, it is assumed that local VLM explains the consistency of the signal in both stations. As in the previous examples, it is not straightforward to derive a secular trend in such cases.

The third mechanism which contributes to potential trend changes is non-linear surface deformation due to mass loading changes. In the last row of Fig. 3.5, I show stations located at high northerly latitudes (AKUR in Iceland and JNU1 in Alaska) that are most likely affected by present day ice mass changes (in addition to secular GIA VLM). In Fig. 3.5(i) and 3.5(k) I show the GNSS observations and the model estimates of piecewise trends. Next to them I show the surface deformation time series due to CMR from Frederikse et al. [2020] in panels Fig. 3.5(j) and 3.5(l), with the same GNSS time series in the background. The CMR data indicate subtle trend changes on subdecadal time scales, which are qualitatively also reflected by the GNSS data. Frederikse et al. [2019] provided evidence that decadal VLM variations due to CMR changes can significantly influence GNSS station velocities on the order of millimeters per year. This is particularly critical when VLM is derived from short time series.

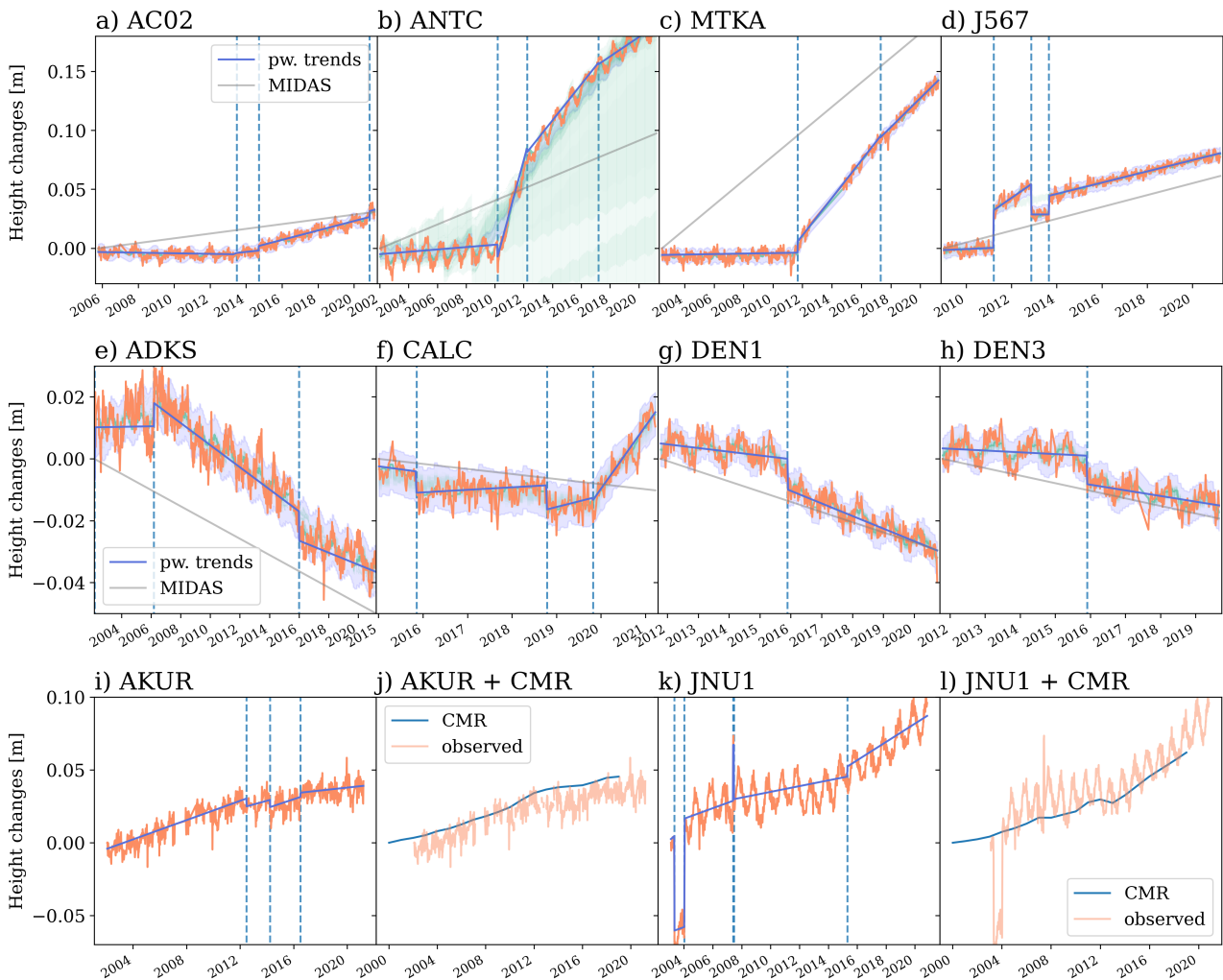


Figure 3.5 Vertical land motion time series from GNSS observations and contemporary mass redistribution (CMR). The first row depicts earthquake-affected stations from Alaska (a), Chile (b) and Japan (c and d). The second row illustrates time series from stations near or at the coast of the Gulf of Mexico, influenced by local processes causing variable velocities. The last row shows station time series in Iceland (i and j) and Alaska (k and l), which correlate on decadal time scales with CMR (j and l, blue lines). Note that a trend of 13 mm/year was subtracted from the JNU1 station. I show observations in orange, the model estimate of piecewise trends in blue (with 2σ confidence intervals and dashed lines for detected change points) and the trend estimate from MIDAS in grey (a-h).

These evident physical origins motivate the identification of trend changes in GNSS and SATTG data. Therefore, in the following section I investigate whether accounting for trend changes can improve the agreement of trends over individual periods between independent techniques.

Comparison of piecewise and linear SATTG trends with piecewise GNSS trends

I compare piecewise trends from SATTG and GNSS data at 339 globally distributed station pairs with a maximum distance of 50 km. The trends are computed with the same model settings (of the deterministic and noise components) for both time series. Fig. 3.6 displays time series at three stations that exemplify the increased consistency of the estimations in SATTG and GNSS time series when using the DiscoTimes approach.

Figure 3.6(a) (corresponding to a station located in Japan) and 3.6(b) (corresponding to a station located in Mossel Bay, South Africa) show an almost coincident epoch of the largest detected discontinuity. In the first case, the discontinuity is caused by the Tōhoku Earthquake in 2011. Due to the associated crustal deformation, the northern parts of the Tōhoku region were affected by land uplift [Imakiire and Koarai, 2012], as can also be seen from the instantaneous ~ 4 cm uplift in both time series shown in Fig. 3.6(a). The subsequent post-seismic deformation is approximated by a range of piecewise trend segments in the GNSS time series. In the SATTG time series, these subtle post-seismic signals are below the detection limits due to the larger noise amplitude of the data (see upper panel in Fig. 3.6(a)), so a single trend is estimated. Due to the strong instantaneous earthquake-induced land uplift, most of the concurrent change points (in GNSS and SATTG data) are found in Japan. Fig. 3.6(b) shows a change in the zero position of the TG (in Mossel Bay), which is in agreement with a height change in the GNSS time series. The origin of the shift in the SATTG time series (or accordingly the TG) is unclear, because it is not documented in the station metadata. The automated detection of the discontinuity is thus crucial to estimate accurate VLM trends and can facilitate and support the manual inspection of discontinuities.

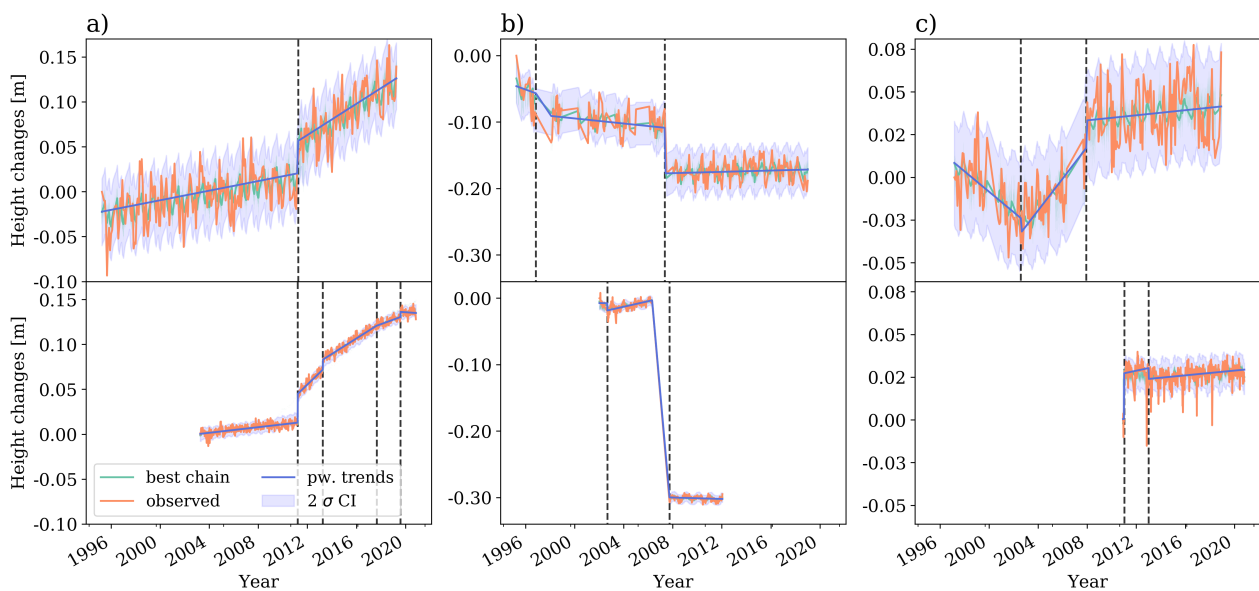


Figure 3.6 Vertical land motion time series from SATTG (top row) and GNSS (bottom row) pairs. (a) Station in Sakamoto Asamushi, Aomori, Japan, (b) station in Mossel Bay, South Africa, (c) station in La Palma, Spain. Next to the observations (orange line) I show the model mean fit in green (in the background), the model mean without the annual cycle in blue lines and finally the 2σ confidence intervals of the fit with blue shadings. The positions of the change points are marked by the vertical dashed lines. The time series show pronounced discontinuities in the SATTG observations, which are partially also observed in the GNSS time series.

Figure 3.6(c) shows height changes in time series of La Palma, a region that is affected by volcanic activity. I observe high variability in the SATTG time series over the period 1997-2008. The trend in the latter segment of SATTG aligns much better with the GNSS data over the same period than the SATTG variations before that period. Identification of such variability can be a very useful information for investigations focussing on SL-trends based on TG observations. This example also underpins the importance of analyzing such effects in SATTG time series directly, considering that often limited information is available from GNSS over the full observation period, as is the case at this particular site.

Despite the abundance of time series, which are affected by both, discontinuities and trend changes, in the majority of cases discontinuities are not necessarily associated with a trend change (such as in Fig. 3.6(b) or in the GNSS time series in Fig. 3.6(c)). In order to mitigate such inappropriate trend changes, a significance test is applied. At every detected discontinuity, I test whether the trend differences between consecutive time series segments are significant, given the combined trend uncertainties of the segments. Trend uncertainties of every time segments are recomputed, while the estimated discontinuity epochs and magnitudes are held constant. Otherwise, trend uncertainties would be influenced by the estimated epoch and discontinuity uncertainties. The recalculation of the trend uncertainties is performed with DiscoTimeS, without estimating change points and with appropriate noise models for the respective time series types. I use an AR1 model for SATTG and a PLWN model for GNSS data, assuming a constant spectral index of -0.9. Note, that in the model configuration, which incorporates the estimation of discontinuities, a AR1 noise model is used for both time series types. I iterate the test over all time series segments, which also allows me to identify multiple non-significant trend changes. Finally, for all neighboring segments with no significant trend changes, I remove the detected discontinuities and recompute the trends over the combined segments. I apply this significance test for the following statistical comparison of SATTG and GNSS trends.

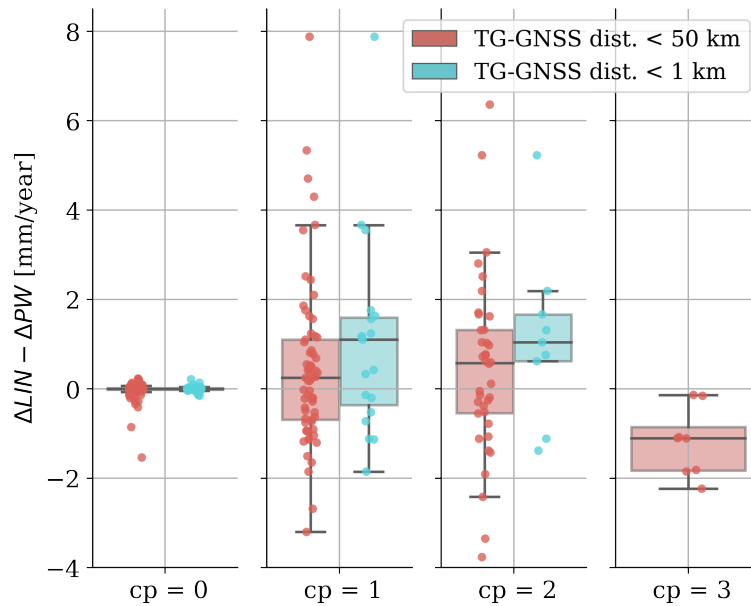


Figure 3.7 Comparison of the piecewise trend deviations ΔPW with the single linear trend deviations ΔLIN . The trend deviations are the absolute weighted deviations from the piecewise GNSS trends as described in the appendix section 3. I subtract the ΔPW from the ΔLIN deviations at every individual station pair. Therefore, a positive difference indicates an improvement by using the Bayesian model over estimating a single linear trend from a SATTG time series, and vice versa. The differences are grouped by the number of detected change points in the SATTG time series, as well as by the maximum allowed distance between GNSS and TG stations.

The extent to which the Bayesian piecewise trend estimation improves trend estimates from SATTG (w.r.t. GNSS data) is depicted by Fig. 3.7 and Table 3.4. Here, positive values of the differences of the trend deviations ΔLIN and ΔPW indicate an improvement when using the Bayesian change point detection, i.e. a better consistency between GNSS and SATTG trends is ensured. The differences are grouped by the number of detected

Table 3.4 Comparison of the absolute piecewise trend deviations ΔPW with single linear trend deviations ΔLIN (as deviations from the piecewise GNSS trends). Improvement is given as the mean of the differences of ΔLIN and ΔPW in mm/year (and %). Positive values indicate an improvement obtained after applying DiscoTimeS. The data is sorted by the number of detected change points in SATTG time series.

cp	ΔLIN mm/year	ΔPW mm/year	improvement mm/year	improvement %	# station pairs
0	1.48	1.50	-0.02	-1.1	227
1	2.20	1.72	0.48	21.7	65
2	2.61	2.16	0.46	17.5	38
3	1.62	2.80	-1.19	-73.4	8
4	5.81	5.09	0.72	12.4	1

change points in the SATTG time series. I additionally sort the data by the maximum allowed distance of a TG-GNSS pair.

In 227 of the cases, the model detects no change points in the data. Here, the deviations of trend estimates are equal for both ΔLIN and ΔPW . This means purely linear motions are assumed over the full period in both cases. When one or two change points are detected, the piecewise trend estimation outperforms the linear trend estimation with a mean improvement of 0.48 mm/year (21.7 %) for one detected change point and an improvement of 0.46 mm/year (17.5 %) for two detected change points. The percentage of improvements refers to the absolute deviations of trends, which are also listed in Table 3.4.

There are only nine cases where more than two change points are detected. Here, the scatter of trend differences using the piecewise estimation decreases compared to the linear estimates. This could be due to the increased fragmentation of the data and shortness of the time series segments. However, the small number of samples (9) hinders a robust assessment of the significance of the improvement/deterioration. In general, the lower consistency achieved in such cases suggests a cautious treatment of SATTG piecewise trends with more than two detected change points for the given record lengths.

To test the significance of the improvement when at least one change point is detected (i.e. $n > 0$), I apply ordinary bootstrapping (see, e.g., Storch and Zwiers [1999]). Based on the given differences of $\Delta LIN - \Delta PW$ (with $n > 0$), I generate 10,000 random sets with replacements, using the same sample size for each set (i.e., 112 VLM differences). I compute the mean of these bootstrapped sets, which yields an empirical probability distribution of the mean and its 95% confidence intervals (i.e. the 2.5% and 97.5% percentiles). The obtained mean of +0.36 [0.02, 0.7] mm/year shows that in general the improvement by fitting piecewise trends is significant.

The geographical distribution of the differences (mm/year) between ΔLIN and ΔPW is illustrated in Fig. 3.8. Improvement (deterioration) with respect to a linear trend estimation is indicated with red (blue) and the circles sizes are scaled by their absolute values. The largest improvement occurs in regions with pronounced tectonic activity, in particular in Japan (Fig. 3.8(c)).

I also observe improvements (in the order of ~ 1 -2 mm/year) in regions with less tectonic activity, which are nearly randomly distributed over the globe. This indicates that a non-negligible part of the stations are also affected by other (local) phenomena, which are potentially more difficult to detect and less likely to be known than those related to earthquakes. Another area where improvements are more frequent is the East Australian coast. Frederikse et al. [2019] showed that this region is affected by variable velocities due to CMR. Vertical solid Earth crustal deformation rates were shown to vary from ~ 0.5 mm/year in 2002 - 2009 to -1.5

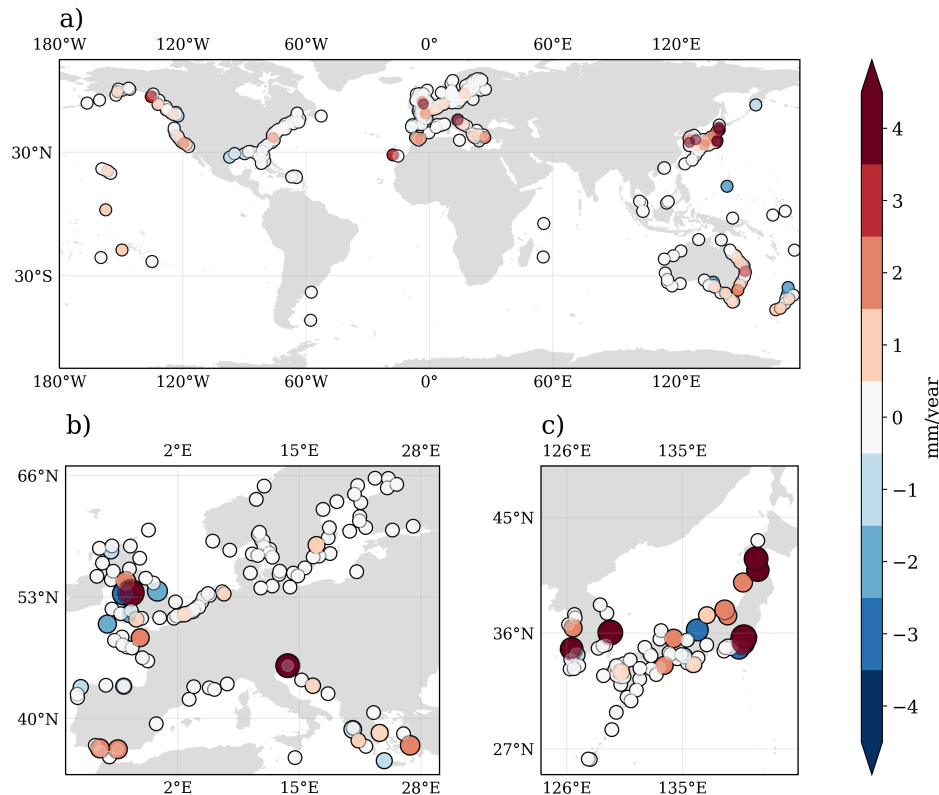


Figure 3.8 Geographical distribution of trend differences (between ΔLIN and ΔPW). Positive values indicate an improvement (in mm/year) in the agreement of SATTG and GNSS VLM after applying DiscoTimeS. (a) shows the global distribution; (b) shows Europe and (c) Japan and South Korea. In the regional maps the scatter points of absolute values larger than 0.5 mm/year are scaled by the square root of their absolute magnitudes.

mm/year in 2009 - 2017. This could be an explanation for a better agreement of the piecewise SATTG and GNSS trends in this area. For this comparison, SATTG and GNSS data are intentionally not corrected for CMR to test how associated variable velocities can be detected by DiscoTimeS.

In some cases the DiscoTimeS trend estimates are less accurate than the single linear trend estimates. Some of these cases are located in Great Britain (Fig. 3.8(b)) and Japan (Fig. 3.8(c)). There are various possible reasons which might explain such a degradation. One factor could be the relatively large allowed maximum distance of 50 km between the GNSS and TG stations. The comparability of piecewise trend estimates with GNSS could be severely reduced, when the VLM dynamics are caused by very localized events. In such cases, a smooth long term linear trend may fit better to a distant GNSS estimate. Indeed, when only allowing for a maximum distance of 1 km, some of those cases can be mitigated and the improvements by using piecewise trend estimates increases further (Fig. 3.7).

Next to differential VLM at GNSS and TG stations caused by highly localized VLM, it should be emphasized that errors in the altimetry data or mismatches between SAT and TG sea level observations still represent the largest error sources. This is also controlled by the accuracy of altimetry SL observations in the coastal zone, which is influenced by a large variety of factors, for example, the applied corrections and adjustments

(e.g., tidal corrections), but also local conditions such as complex coastlines or islands, which can perturb the backscattered radar signal. Next to deviations in the observed oceanic sea level signals, the associated nonphysical noise in SATTG VLM time series can thus lead to an erroneous detection of discontinuities, which should therefore be carefully inspected. <

3.2.4 Validation with external data and alternative algorithms

> One important contribution of DiscoTimeS is its ability for qualitatively labelling the vertical land motion as 'constant' or 'variable'. While trend uncertainty is a good statistical measure to quantify a possible range of trend changes, it is, however, less suited as a measure to resolve a possible time-dependent variable velocities. Therefore, I also investigate how the information on the segmentation and trend changes in the SATTG and GNSS time series can be exploited to increase their agreement with large-scale VLM signals such as GIA (and CMR). I use the estimated number of change points to detect potentially non-linear motion in SATTG time series. For GNSS data, where more discontinuities ($n > 0$ in 92% of the cases, i.e. 688 in total) are detected, I allow for a possible small rate of change in the trends (< 0.4 mm/year), such that the overall motion is still labelled as 'constant'. This threshold corresponds to the median weighted standard deviation of piecewise trends within a times series, $std(pw_gnss)$, based on all analyzed GNSS data. To substantiate the results, I complement the analysis by comparing estimated GNSS trends with those computed with MIDAS [Blewitt et al., 2016].

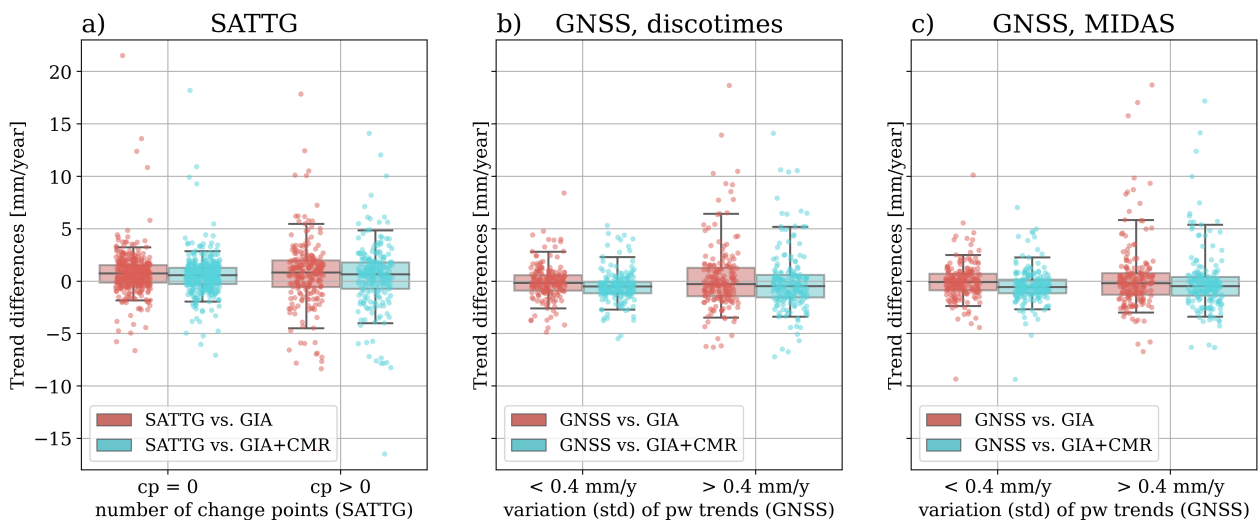


Figure 3.9 Trend differences between (a) single linear SATTG estimates, (b) time-averaged piecewise GNSS trend estimates and (c) MIDAS trend estimates and VLM from GIA (red) and GIA+CMR (blue). The 606 single linear SATTG trend estimates are grouped into a set where no change point was detected ($n=0$, 380 cases) and another set where at least one change point was detected ($n > 1$, 226 cases). The GNSS data are grouped into sets in which the weighted standard deviation of the trend changes in a single time series is below or above 0.4 mm/year. This value represents the median of all standard deviations for the 381 GNSS stations. Trend differences are up to twice as large for SATTG and GNSS VLM observations which are characterized as 'variable' VLM.

Figure 3.9 and Table 3.5 show the differences of single linear SATTG trends with respect to GIA and GIA+CMR estimates. The linear SATTG trends are grouped according to whether or not the model detects change points. Linear SATTG trends agree much better with the large scale VLM, when the model detects

Table 3.5 Statistics of trend differences of linear SATTG trends (computed with least-squares without accounting for change points) and GNSS with respect to GIA/GIA+CMR VLM estimates. SATTG estimates are grouped depending on whether or not change points are detected. GNSS estimates are instead grouped by the standard deviation of piecewise trends as estimated by DiscoTimeS. I also provide the statistics for MIDAS linear trend estimates, which are grouped according to the criterium estimated with DiscoTimeS. Shown are the standard deviation and the median of the differences, as well as the number of estimates.

VLM estimate	condition number of change points	STD [mm/year]	median Δ Trends [mm/year]	count
SATTG-GIA	n = 0	2.13	0.76	380
	n > 0	3.35	0.85	226
SATTG-GIA+CMR	n = 0	1.95	0.59	380
	n > 0	3.17	0.68	226
DiscoTimeS	trend standard deviation			
GNSS-GIA	< 0.4 mm/year	1.66	-0.15	191
	> 0.4 mm/year	3.25	-0.27	190
GNSS-GIA+CMR	< 0.4 mm/year	1.53	-0.49	191
	> 0.4 mm/year	2.93	-0.48	190
MIDAS	trend standard deviation			
GNSS-GIA	< 0.4 mm/year	1.81	-0.06	191
	> 0.4 mm/year	3.33	-0.18	190
GNSS-GIA+CMR	< 0.4 mm/year	1.68	-0.55	191
	> 0.4 mm/year	2.99	-0.45	190

no change points, i.e. when it characterises the motion over the full period as 'linear'. The agreement with GIA+CMR VLM, which is quantified by the standard deviation of the differences, is almost 40% (1.22 mm/year) better in the case of no detected change points. I obtain the best agreement when also including the CMR correction compared to using the GIA estimate only.

Nevertheless, the standard deviation of the differences between the SATTG trends and the combined GIA+CMR effect (1.95 mm/year) as well as the median bias of trends (0.59) are relatively large. Such high discrepancies can be caused by local VLM, which is linear but not represented by either the GIA model nor the CMR effect. There is, for example, a strong outlier with a deviation from GIA+CMR of almost 18.2 mm/year when no change point is detected (Fig. 3.9(a)). The derived SATTG time series (from a TG in Elfin Cove, Alaska) is associated with a very steady uplift motion (of 21 mm/year), which is not captured by the combined GIA+CMR effect. Overall, despite these cases of local but highly linear VLM, excluding the SATTG estimates associated with variable velocities strongly improves the agreement of SATTG and GIA+CMR VLM on a global scale.

I obtain similar results from the analogous analysis comparing GNSS and GIA+CMR effects. Here, I compare the weighted averaged piecewise trends (estimated with DiscoTimeS), as well as the MIDAS trends with GIA+CMR VLM data. The trend differences are sorted according to the standard deviation of trend changes within a time series as detected by DiscoTimeS. Trend differences with respect to large scale GIA+CMR VLM are strongly reduced for time series where a low standard deviation of trend changes is detected ($std < 0.4$ mm/year) compared to time series where a high standard deviation in trend changes is detected (see Fig. 3.9b and Table 3.5 second section). As for SATTG VLM estimates, the combined GIA+CMR effect improves the comparability compared to the GIA VLM correction alone.

These findings are also supported by the analysis of MIDAS trends, which are grouped according to the same criteria as the piecewise DiscoTimeS estimates. The standard deviation (STD) of the differences between the MIDAS trend estimates versus GIA (or GIA+CMR) trends is consistent with the statistics obtained by the DiscoTimeS estimates (Table 3.5). Based on these statistics, the performances of DiscoTimeS in terms of trend estimation are at the same level of MIDAS, also when a significant non-linear behavior is detected. The results not only underline the benefit of detecting trend changes to spot significant variable velocities, but also substantiate the validity of DiscoTimeS for mitigating discontinuities. In essence, the significantly improved consistency with GIA+CMR data demonstrates the successful detection and characterization of variable velocities in both GNSS and SATTG time series.

3.2.5 Discussion

DiscoTimeS is a new approach to automatically and simultaneously estimate discontinuities, trend changes, seasonality and noise properties in geophysical time series. However there are some caveats that should be considered when using DiscoTimeS as an unsupervised discontinuity-detector.

The results of the sensitivity experiments show that PL noise has a significant impact on the accuracy of trend estimates, as well as on the detection rates of change points. This implies that PL noise can represent an ambiguity to the model, which causes difficulties to discriminate between noise and discontinuities or trend changes, and can potentially lead to overfitting of the data. The discussion on the role of PL-noise for discontinuity detection was also raised by Gazeaux et al. [2013]. They highlighted that Hector [Bos and Fernandes, 2016], as the only algorithm to take into account PL-noise, yielded a lower FP rate (i.e. was less likely to overfit the data), but also had a reduced TP detection rate. Thus, further developments are required to better disentangle discontinuities in the presence of low-frequency noise and to find a compromise between over- and underfitting of the data, which ultimately depends on the user requirements. Because I analyze time series with an unknown number of discontinuities and additionally trend changes (and PL-noise), which substantially increases the complexity of the problem and thus the uncertainties of the estimates, the model estimates should be carefully revised and interpreted by the user.

Next to the complications associated with time series noise estimation, the estimation and interpretation of change points in SATTG data can be particularly challenging. Differences between SAT and TG data, which can either be caused by physical or instrumental issues, can compromise the discontinuity detection. Such time series should therefore be carefully inspected by the user.

Finally, a remaining caveat is that the parametrization of post-seismic relaxation with piecewise incremental trends is a simplification of the process and can be better described by using a relaxation model [e.g., Montillet and Bos [2020]]. These limitations should be considered, when applying the presented method as an unsupervised discontinuity and trend change detection tool for pre-processing data. In section 5.4 I provide several recommendations to further improve the presented approach. <

3.3 Bayesian vertical land motion reconstruction

3.3.1 Pre-processing of the data

The previous section 3.2 describes the development and validation of the discontinuity-detector, which is now applied on a global scale. DiscoTimeS is applied to detect discontinuities in 10957 GNSS and 713 SATTG time

series. The GNSS data stem from the NGL database ([Blewitt et al., 2016], <http://geodesy.unr.edu>, accessed on 1 December, 2021). Only GNSS time series covering at least 5 years (with a minimum of 2 years of valid data) are used. Time series with an absolute trend greater than 20 mm/year and a trend uncertainty greater than 3 mm/year (based on MIDAS [Blewitt et al., 2016] trend and uncertainty estimates) are omitted to remove single extremes or noisy data. For example, less than 1% of the station rates are larger (in absolute terms) than 20 mm/year with an uncertainty lower than 3mm/year. The SATTG time series are constructed based on PSMSL tide gauges [Holgate et al., 2013] and 0.25° gridded satellite altimetry data from the Copernicus Marine Service (CMEMS) (https://resources.marine.copernicus.eu/product-detail/SEALEVEL_GLO_PHY_L4_MY_008_047/INFORMATION, last access 24.03.2022). Due to systematic trend differences in the along-track altimetry data, the gridded dataset (hereinafter called CMEMS) is used (see also the discussion in 2.5 and the extended validation in Oelsmann and Passaro [2022]). Following the approach of selecting altimetry data in the Zone of Influence (presented in section 2), the combination of SATTG data is optimized by using the highest correlated grid point with respect to monthly tide gauge observations (based on detrended and de-seasoned data) [e.g., Cazenave et al., 1999, Wöppelmann and Marcos, 2016, Kleinherenbrink et al., 2018, Oelsmann et al., 2021]. Only SATTG time series with at least 120 months of valid data are used for the VLM reconstruction.

‣ To reconstruct smoothly varying height changes, the detected discontinuities are removed from the weekly averaged GNSS time series and monthly SATTG data. After the unsupervised discontinuity detection the time series are manually reviewed. Estimated discontinuities are rejected in case of misfitting or oversegmentation of the data. Since some of the discontinuities are caused by physical processes, this might reduce the actual VLM variability in the model. Therefore, in section 5.4, I provide recommendations to further improve the treatment of discontinuous events. I also reject stations after visual screening of the time series (as is common practice, see, e.g., Wöppelmann and Marcos [2016], Gruszczynski et al. [2018]) and apply an outlier analysis based on the regional variability of trends. Any remaining outliers, e.g., caused by local effects, like settling of the installation platform or building, are further reduced with the spatial interpolation of neighboring data. Problematic stations that are located on ice, for instance, are excluded according to the selection by Husson et al. [2018]. A complete list of rejected stations can be found in the supplementary information of the associated study of this section [Oelsmann et al., 2023].

The time series are corrected for discontinuities and the annual cycle. Remaining single-point outliers (in the time series) are rejected by removing values which exceed a running mean standard-deviation outlier test. For this purpose, I first compute the median of the 12-month running standard-deviation (σ_{12m}), which provides a measure of variability that is not influenced by potential remaining outliers in the data. Next, I reject values whose difference with respect to the 12-month running mean is three times larger than σ_{12m} . Finally, since I focus on interannual to decadal VLM variations, I compute annual averages to obtain a homogeneous temporal sampling. To align the station-dependent absolute height differences I compute height changes with respect to the value in 2014.

3.3.2 Bayesian principal component analysis

The aim of my approach is to capture common modes of spatiotemporal variability of VLM on interannual to decadal time scales, together with underlying long-term trends. The main drivers of interannual/decadal variability are tectonic activity, surface mass loading changes (for example, from terrestrial water storage

changes), or local effects such as groundwater depletion. Previous studies [Klos et al., 2019, Frederikse et al., 2019] demonstrated that these processes can exhibit spatially coherent variations in the order of several 100 km. Thus, in order to disentangle and describe these modes, I use the Principal Component Analysis (PCA).

PCA was previously applied to GNSS data to identify a Common Mode Error in order to reduce its associated effect on networks of GNSS data [Gruszczynski et al., 2018, Riddell et al., 2020, Wudong et al., 2020]. To overcome the problem of missing values in time series, previous studies employed probabilistic PCA (PPCA), which allows approximating the principal components for discontinuous data [Gruszczynski et al., 2018]. Here, I utilize PPCA, more precisely Bayesian PCA (BPCA), as it has the advantage of estimating a full empirical probability distribution of the parameters [Wudong et al., 2020] in contrast to maximum likelihood estimation [Gruszczynski et al., 2018].

I estimate heights $U(\mathbf{x}, \mathbf{t})$ at every station, represented by the space-dimension \mathbf{x} and time \mathbf{t} as described by the following model:

$$U(\mathbf{x}, \mathbf{t}) = \mathbf{g}(\mathbf{x}) \otimes \mathbf{t} + \sum_{k=1}^n \mathbf{W}_k(\mathbf{x}) \otimes \mathbf{p}_k(\mathbf{t}) \quad (3.7)$$

Here, $\mathbf{p}_k(\mathbf{t})$ are t -dimensional latent variables, or principal components, which are mapped onto the observations by the transformation matrix $\mathbf{W}_k(\mathbf{x})$. $\mathbf{W}_k(\mathbf{x})$ represent the spatial pattern of the common modes of variability (hereinafter called the EOF (empirical orthogonal functions) pattern). The principal components $\mathbf{p}_k(\mathbf{t})$ modulate the evolution of these pattern over time. The vector \mathbf{g} accounts for constant linear trends in the time series. The technique-dependent variance $\epsilon(\mathbf{x})$ is estimated individually for the two different techniques (GNSS and SATTG), considering that noise amplitudes differ by one order of magnitude. Hence, the likelihood of the unknown parameters Φ_b given the observations \mathbf{d} is:

$$P(\Phi_b | \mathbf{d}) \sim \mathcal{N}(U - \mathbf{d}, \epsilon(\mathbf{x})^2) \quad (3.8)$$

I define prior distributions for each parameter. I assign Gaussian distributions to \mathbf{g} and $\mathbf{W}_k(\mathbf{x})$, and a half-normal distribution to the estimated variance $\epsilon(\mathbf{x})$:

$$P(\mathbf{g}) \sim \mathcal{N}(\mu_g, \sigma_g^2) \quad (3.9)$$

$$P(\mathbf{W}) \sim \mathcal{N}(\mu_W, \sigma_W^2) \quad (3.10)$$

$$P(\epsilon) \sim \text{Half-normal}(\sigma_\epsilon^2) \quad (3.11)$$

The principal components are modeled as Gaussian Random Walks to simulate smoothly varying behavior of the VLM. In doing so, the principal components represent auto-correlated time series. With this constraint, I avoid that spurious high frequency signals are absorbed by the principal components. Note that discontinuities are removed from the data prior to applying the BPCA, which otherwise would lead to an overestimation of the variance of the principal components. In this case, the principal component \mathbf{p}_k at time step t is obtained by adding the random normally distributed innovation \mathbf{h}_k at time step $t - 1$, as summarized by the following formula:

$$\mathbf{p}_{k,t} = \mathbf{p}_{k,t-1} + \mathbf{h}_{k,t}, P(\mathbf{h}_k) \sim \mathcal{N}(\mu_{h_k}, \sigma_{h_k}^2) \quad (3.12)$$

Different prior assumptions are assigned to the parameters. I initialize the point-wise trends μ_g with linear trend estimates derived with ordinary least squares analysis, and set σ_g^2 to 10 mm/year. μ_w is set to zero, and σ_w^2 is set to 15 cm. $\sigma_{h_k}^2$ is set to 0.001 for the first component ($k = 1$) and $\sigma_{h_k}^2 = \sigma_{h_{k-1}}^2 / 2$ for every subsequent component, such that the prescribed amplitudes of the Gaussian Random Walks decay with increasing number of components. Finally, I assign σ_ϵ^2 to 40 cm.

I perform the BPCA for several continental subregions. These include North America, Europe, Oceania (Australia, New Zealand and Southeast Asia), Japan, Africa, South/Central Asia, and South America. I apply this regional separation to maximize the explained temporal VLM variability depending on the given regional processes. Distinct differences between the modes of variability are particularly caused by tectonic activity. I determine the maximum number of used PCs n by repeatedly applying different numbers of PCs. If the weighted explained variance EV of the data \mathbf{U}_{obs} by the model \mathbf{U}_{model} does not improve significantly (i.e., when the improvement is below 1-2%) by adding new PCs, I stop the iteration. The explained variance is computed by taking into account weights w associated with the regional distribution of the data (i.e., the station density s) and the technique-dependent estimated variance parameter (see eq. 3.13). This avoids an over-representation of variability in regions with high station coverage or very noisy SATTG data.

$$EV = 1 - \frac{\sum Var(\mathbf{U}_{obs} - \mathbf{U}_{model})\mathbf{w}}{\sum Var(\mathbf{U}_{obs})\mathbf{w}}, \mathbf{w} = \frac{1}{\epsilon s} \quad (3.13)$$

3.3.3 Bayesian transdimensional regression

The BPCA method yields a reconstruction of the evolution of VLM in time at every point-wise station. In order to obtain continuous estimates of VLM in space, I interpolate the estimated parameters Φ_b of trend and EOF pattern (μ_w) using a Bayesian transdimensional regression approach [Bodin et al., 2012, Husson et al., 2018, Hawkins et al., 2019a] as developed by Hawkins et al. [2019b]. A major advantage of this Bayesian framework is that an explicit regularization of the model parameters, in particular the definition of the spatial resolution, is not required and it is performed automatically by the algorithm [Bodin and Sambridge, 2009]. This is advantageous compared to interpolation methods, which rely on a fixed number of model parameters or user-defined interpolation length-scales.

As in Hawkins et al. [2019b], I apply a Delaunay linear interpolation to recover smooth surfaces. I use the posterior averages Φ_b and standard deviations $\sigma_{b,x}$ of the BPCA as input parameters of the Bayesian regression. The Bayesian regression estimates the parameter values and statistical uncertainties, while dynamically adapting the complexity, i.e., the spatial resolution of the grid or the number of mobile nodes, which depends on the spatial distribution (density of the data). The posterior probability distributions $P(\Phi, \Phi_b)$ of the unknown parameters (trend and EOF surfaces) are approximated using a hybrid of Markov chain Monte Carlo (MCMC) and Hamilton Monte Carlo techniques. The interpolated parameters (and their uncertainties) are directly estimated from the model ensemble (and spread), which consists of many different grid-realizations.

I run 56 independent Markov chains. I start from randomized initial conditions, drawn from the prior distribution of the parameters. As an example for the interpolation of trends, I use a uniform prior of VLM rates between ± 15 mm/year. Every chain is run for 1,000,000 iterations where only the last 500,000 iterations

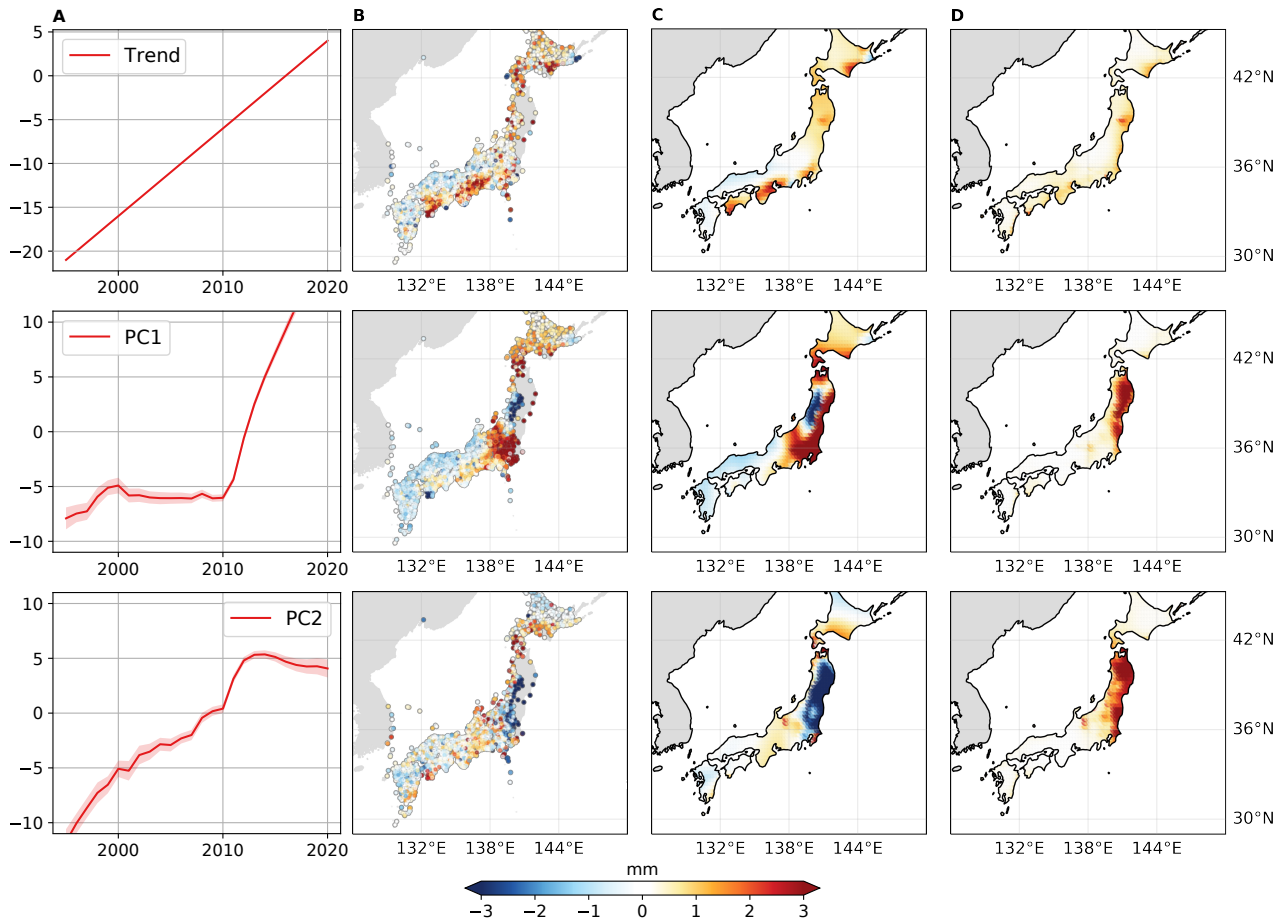


Figure 3.10 The first column (A) shows the trend coefficient (top), and the first (middle) and second (bottom) principal components (and uncertainties) estimated for Japan. B shows the corresponding point-wise spatial trend and EOF pattern. C displays the interpolated estimates of the pattern; the associated uncertainties are provided by D.

are retained and averaged. At every iteration of the Markov chain, the model state is perturbed, which involves the variation of the number and distribution of the grid nodes. Thus, every Markov chain consists of a large ensemble of model states, which form the basis to compute the full posterior distribution. From this distribution, parameter uncertainties are derived. The final interpolated 2D map is projected onto a regularly spaced coastal profile of 0.25° resolution. Finally, I calculate the uncertainty propagation by incorporating the estimated errors of the interpolated trend and EOF pattern, as well as the time-dependent errors of the PCs.

Figure 3.10 gives an overview of the different intermediate results obtained after the BPCA and the 2D interpolation in Japan, which is prone to seismic activity. Illustrated are the estimated PCs (Fig. 3.10A), together with the point-wise (Fig. 3.10B) and interpolated EOFs and trends (Fig. 3.10C), as well as their uncertainties (Fig. 3.10D). The spatial uncertainty estimates are influenced by the station density, the spatial scatter of the data, and their formal uncertainties. As an example, lower station density particularly contributes to increased uncertainties of the EOF pattern in the Tōhoku region.

Table 3.6 Explained weighted variance of estimated VLM and number of estimated PCs.

Region	Expl. Variance [%]	Number of PCs used
North America	96.2	2
Europe	94.0	2
South America	89.6	3
Japan	98.5	3
Oceania	87.1	2
Africa	94.6	2
South/Central Asia	87.5	3

3.3.4 Validation

The point-wise BPCA VLM estimates capture most of the variance. Explained regional variances of the observational database (GNSS and SATTG time series) range from 87.1% to 98.5%, as shown in Table 3.6.

I compare coastal linear trend estimates from the interpolated VLM reconstruction with GIA estimates [Caron et al., 2018] and VLM inferences from the SL reconstruction [Kopp et al., 2014], which were applied in the 6th Assessment Report of the Intergovernmental Panel on Climate Change (AR6) [Fox-Kemper et al., 2021]. The different VLM estimates are compared with GNSS trends [Blewitt et al., 2016] at 775 tide gauges in Fig. 3.11G. I compute the significance ratio of the trend differences with respect to the combined uncertainties $SR = \Delta VLM_{model-GNSS} / \sqrt{\sigma_{model}^2 + \sigma_{GNSS}^2}$. A significance ratio of $SR < 1$ indicates that the trend differences are within the estimated limits of uncertainties and thus they are not significant. This ratio is a useful statistic to evaluate the accuracy of both the estimated trends and uncertainties. Figure 3.11G displays the distributions of the SR s for the different datasets. The standard deviations of SR are 1.2, 2.1, and 2.2 for the VLM reconstruction of this study, Caron et al. [2018] and Kopp et al. [2014]. Here, a higher SR points to either higher trend differences or underestimated uncertainties in Caron et al. [2018] and Kopp et al. [2014]. The standard deviations of the trend differences $\Delta VLM_{model-GNSS}$ (irrespective of the uncertainties) are 1.9, 2.5, and 2.5 mm/year for the VLM reconstruction, Caron et al. [2018] and Kopp et al. [2014]. Therefore, the VLM reconstruction based on BPCA and Bayesian transdimensional regression computed in this study provides more realistic estimates of both VLM trends and uncertainties. Since a portion of the validation data is included in the VLM reconstruction, this comparison validates the statistical approach of the VLM reconstruction rather than the underlying database, which contains much more and higher quality VLM data than the other VLM datasets. Hence, with this analysis I aim to emphasize the discrepancies between contemporary VLM and previously applied estimates [Kopp et al., 2014, Caron et al., 2018], which do not include any GNSS data, and which do not account for non-linear effects.

Regional differences between the VLM reconstruction and estimates from Dangendorf et al. [2019] and Kopp et al. [2014] are shown in Fig. 3.11A and 3.11B. Here, the VLM estimate of Dangendorf et al. [2019] was derived from the difference of the provided absolute and relative SL trends and thus complies with the VLM fingerprint of GIA [Hay et al., 2015]. Note, that the absolute sea level data in Dangendorf et al. [2019] contain the deformational component of CMR. Fig. 3.11D shows differences between the estimated long-term trend uncertainties of the VLM reconstruction and those provided by Kopp et al. [2014] at tide gauges. In addition, I show a comparison of regional averages of VLM and uncertainty estimates in Fig. 3.11E and 3.11F. These patterns highlight that there are substantial regional differences exist between independent VLM estimates due to differences in underlying datasets and methods. In the next chapter I evaluate the impact of VLM on

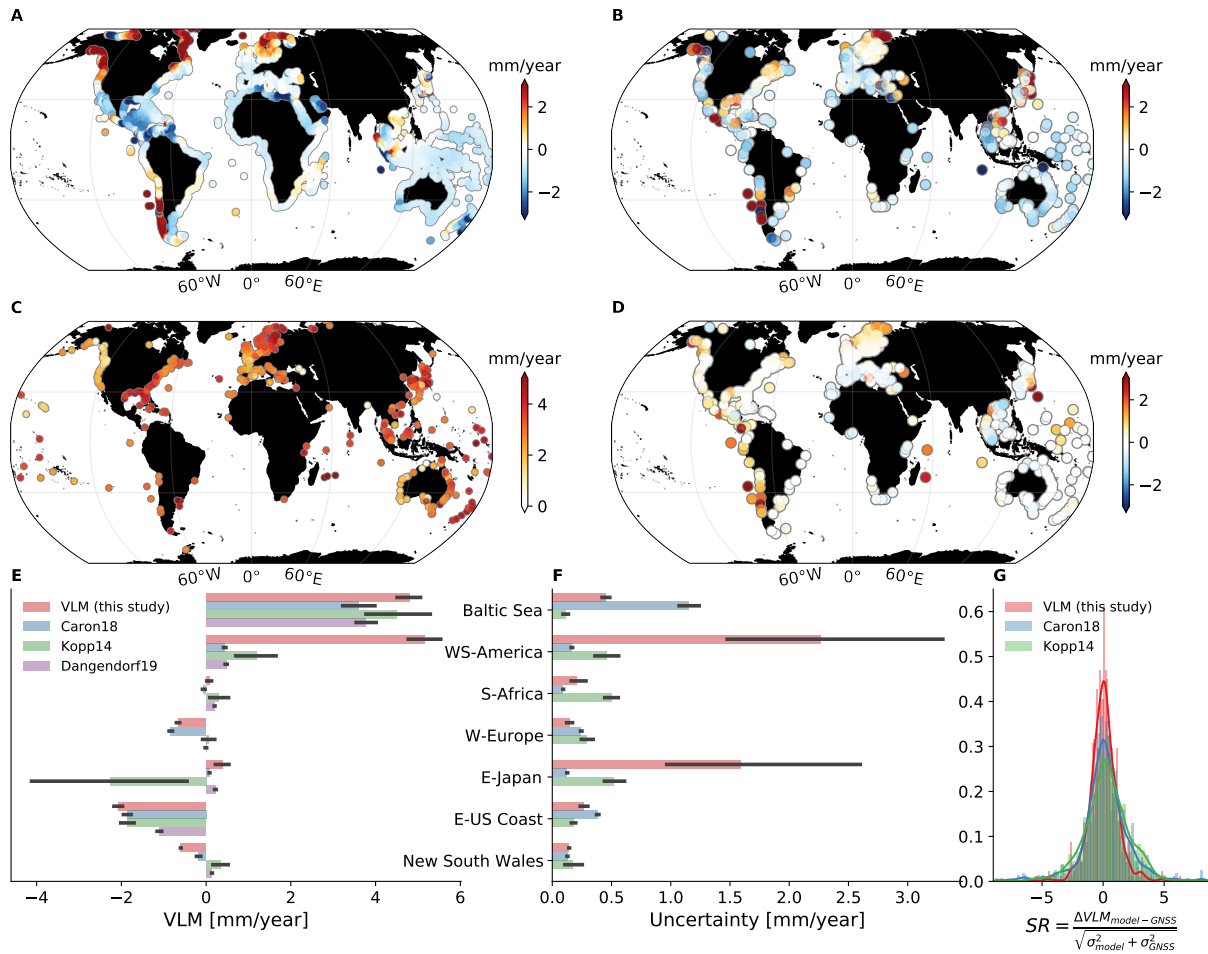


Figure 3.11 A and B show trend differences of VLM of this study and the VLM estimates of recent SL reconstructions [Dangendorf et al., 2019, Kopp et al., 2014]. Note, that the estimate of Dangendorf et al. [2019] complies here with the GIA fingerprint of their SL reconstruction, which is hence consistent with the estimate derived by Hay et al. [2015]. (C) Absolute SL trends from altimetry (CMEMS) over 1995-2020. D shows differences in the estimated uncertainties of the VLM reconstruction and those applied at tide gauges in the Intergovernmental Panel on Climate Change (IPCC) AR6 report [Kopp et al., 2014, Fox-Kemper et al., 2021]. E and F compare trend and uncertainty estimates from different solutions. G shows the significance ratio of the trend differences $SR = \Delta VLM_{model-GNSS} / \sqrt{\sigma_{model}^2 + \sigma_{GNSS}^2}$ of different model estimates w.r.t. to 775 GNSS trends and uncertainties estimated with MIDAS [Blewitt et al., 2016]. The standard deviation of are 1.2, 2.1 and 2.2 for the VLM reconstruction, Caron et al. [2018] and Kopp et al. [2014].

relative sea level change based of the VLM reconstruction and investigate potential differences with respect to VLM data from the GIA model [Caron et al., 2018], as well as the indirect VLM estimates from the sea level reconstruction [Dangendorf et al., 2019].

3.3.5 Discussion

I present here a mostly automated processing chain to generate a spatiotemporally interpolated VLM estimate based on single-point observations from different measurement techniques. One main advantage of this approach is that it involves a rigorous uncertainty quantification. I explicitly describe different white noise classes for the different techniques (GNSS, or SATTG) and quantify the uncertainties of all parameters, such as trends, PCs, or white noise amplitudes, individually. The Bayesian transdimensional regression provides

interpolated parameters and uncertainties by integrating the point estimates and uncertainties, the spatial distribution, and the spatial variability of the data. Overall, I applied minimal manual manipulation of the data and included as little prior information as possible, to maximize the objectivity of this reconstruction. However, there are still some limitations to this mostly unsupervised approach. First of all, the results may be still influenced by undetected discontinuities (either by DiscoTimeS or by visual inspection), which is an ongoing problem in geodetic time series analysis [Gazeaux et al., 2013]. While it is expected that large discontinuities are more likely to be detected (see section 3.2.2), multiple small discontinuities (with a magnitude below the white noise amplitude) can still lead to trend biases. It should also be mentioned that, when correcting for the discontinuities (i.e., by subtracting a step function), the effective degrees of freedom are reduced in the data, which is currently not accounted for in the model. Hence, I assume here that the epoch and magnitude of the discontinuities are perfectly known, which is of course an oversimplified assumption. Note also that the discontinuities are available for the single time series but not estimated in the global interpolated model. To overcome this simplification, and as suggested by Matt King (personal communication, July 14, 2022), the discontinuities could be explicitly estimated within the BPCA model, which however would also drastically increase its complexity and computing time.

In general, the BPCA approach has similarities with previously applied EOF-based approaches to reconstruct SL variations [e.g., Church and White, 2011]. This is advantageous, as it presents a completely independent VLM estimation that requires no prior knowledge of VLM, such as a GIA background model or information on spatiotemporal variations. However, it is worth discussing if including external information, such as a GIA fingerprint, or spatiotemporal variations from mass loading changes (i.e., as done by Frederikse et al. [2020] using GRACE data), might increase the robustness of the model estimates. As an example, the model could include a temporally invariant component initialized with a GIA model, a set of spatiotemporal correlated regional components, describing variations associated with mass loading changes (as informed by GRACE observations), spatiotemporal regional components describing non-GIA and non-mass related changes (such as earthquakes), as well as components describing local residual motions. As an alternative to constraining the model by these external estimates, future efforts could also investigate, if the model would benefit from implementing a spatial covariance function in the spatial weighting functions $\mathbf{W}_k(\mathbf{x})$ of the independent modes of variability. This would facilitate the estimation of the spatial length scales of the signals and simultaneously enforce spatially continuous behavior. However, one limitation to this approach could be spatial discontinuous VLM responses, which cannot be described by such smooth spatial patterns.

4 Understanding the impacts of vertical land motion on relative sea level change

4.1 Introduction

In the previous section, I derive a three-dimensional coastal VLM reconstruction, which facilitates the assessment of linear motions together with the contemporary (1995-2020) non-linear variability of VLM. I identify a significant proportion of stations, that are affected by variable trends. Such variations can be coherent on a regional scale due to a variety of reasons, e.g., earthquakes or surface mass deformation due to mass loading changes. In this chapter, I aim to shed light on how VLM has contributed to sea level changes over the last century, during the altimetry era, and how VLM will affect future sea level change on a regional scale. The sources of VLM and its variability will be discussed by comparison with external VLM estimates from GIA models and GRACE observations.

In section 3.2.4, I show that previous VLM estimates incorporated in SL reconstructions [Dangendorf et al., 2019] can differ from the linear VLM estimates of the VLM reconstruction. VLM in the SL-reconstruction [Dangendorf et al., 2019] is only indirectly constrained by tide gauges. Hence, in this section, I investigate differences in absolute sea level change estimates over the last century, depending on the applied VLM adjustment. For this purpose, I correct tide gauges by the VLM reconstruction which benefits from a large network of direct observational constraints.

In section 3.2.4, I also compare the VLM reconstruction with point-estimates of VLM from a probabilistic SL analysis [Kopp et al., 2014], which is likewise solely based on tide gauge observations, and is incorporated in regional relative sea level projections of the latest 6th Assessment Report of the Intergovernmental Panel on Climate Change (IPCC) [Fox-Kemper et al., 2021]. The latter estimates lack direct geodetic constraints from GNSS data and do not account for temporal variability. It is unclear how the potential misrepresentation of the prior information on GIA-fingerprints, the abundance of non-GIA VLM processes, and non-linear VLM effects influence these estimates of projected coastal SL change. Therefore, using the VLM reconstruction, I will reconcile the role of VLM in SL projections by increasing the number of underlying observations by more than a 10-fold, by using direct geodetic data, and by taking into consideration the influences of non-linear VLM. The results shall particularly clarify the uncertainty contribution of VLM to relative sea level projections, which is a central limitation to the assessment of future changes.

Finally, to assess the societal implications of my findings, I will examine how VLM affects the exposure of coastal populations to contemporary RSL change. Understanding the future risks and coastal exposure to natural and anthropogenic sea level change is essential for estimating costs of future loss and coastal adaptation planning [e.g. Nicholls et al., 2021]. Flood risk and vulnerability assessment require a comprehensive analysis of the interaction of coastal hazards (e.g., storm surges, wave hazards, mean absolute sea level (ASL) change and VLM), socio-economic factors (e.g., coastal population density and assets) as well as coastal prop-

erties (e.g., land elevation) [Hinkel and Klein, 2009, Oppenheimer et al., 2019]. However, existing global-scale analyses of coastal exposure have not yet exploited comprehensive databases of direct VLM observations, as provided in this study [e.g. Ericson et al., 2006, Syvitski et al., 2009, Nicholls et al., 2021]. Most of the previous VLM estimates relied on GIA models only, were taken from literature values, or were based on expert judgments. Therefore, in section 4.5 I will utilize the VLM reconstruction to bridge these knowledge gaps and to derive more realistic RSL rates.

4.2 Non-linear vertical land motion along global coastlines

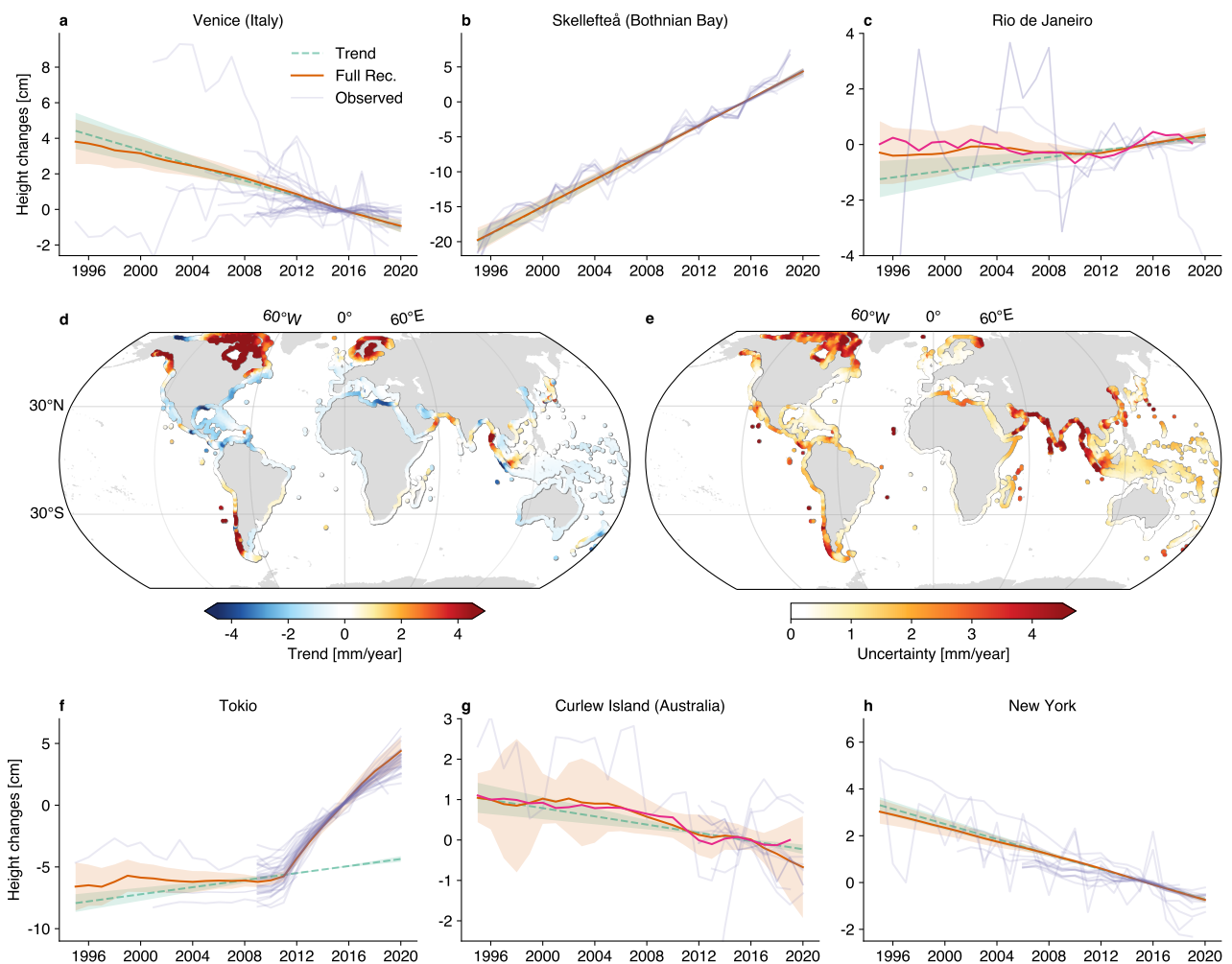


Figure 4.1 Bayesian VLM reconstruction from 1995-2020 based on observations. A-C and F-H show time series of observed VLM at different locations, together with the full VLM reconstruction (red) and the estimated trend component (green). Translucent purple time series indicate observed VLM in close vicinity to the depicted location to illustrate the spatiotemporal variability in the observations. The effect of contemporary mass redistribution [Frederikse et al., 2020] on VLM is shown by the pink line (C, G). D-E illustrate Bayesian estimates of interpolated linear trends and uncertainties.

›The reconstructed coastal VLM is compared to point-wise observations at selected sites in Figure 4.1. Six sites (Fig. 4.1 A, B, C, F, G, H) are chosen to illustrate the performance of the full reconstruction (red lines) compared to observations in their vicinity (purple lines). The estimated linear trends and uncertainties are represented by the green lines. The geographical pattern of the linear trends and the corresponding uncertainties are mapped along the global coastlines in panels 4.1D and 4.1E.

When focusing only on the linear trends from reconstructed VLM (Fig. 4.1D), the spatial patterns reflect to a large extent the characteristic GIA signatures, most visible in North America and Fennoscandia. These patterns are superimposed on regional non-GIA related effects, due to natural or anthropogenic causes. Linear trends in VLM are routinely used to identify regions with significant rates of land subsidence and thus enhanced relative SL change. Using the reconstruction, VLM trends computed for the period 1995-2020 show negative values along the coasts of the Gulf of Mexico (-1 to -7 mm/yr), in agreement with previous research [Emery and Aubrey, 1991b, Letetrel et al., 2015, Liu et al., 2020]. Likewise, the Australian coastlines subside with average rates of -0.82 mm/year. This estimate aligns well with recent works [Riddell et al., 2020, Hammond et al., 2021] and confirms systematic differences between the observed subsidence rates and GIA model estimates. Even at the city-scale, the reconstruction is able to resolve VLM. One clear example is the iconic case of the city of Venice (Fig. 4.1A), in whose vicinity subsidence rates of -1 to -3 mm/year are detected. I find that non-linear VLM increases estimated trend uncertainties, particularly in subduction zones (e.g., in South America, Indonesia, and Japan, see Fig. 4.1E). Lower uncertainties (< 1 mm/year) are estimated for central Europe and the US East coast, which is in accordance with a reduced estimated variance of non-linear processes (see Fig. 4.7).

Changes in coastal VLM are non-linear at many locations, as evidenced in Fig. 4.1. In Venice, for example, the area is affected by a complex superposition of GIA, sedimentary and tectonic processes as well as human activities (fluid extraction) [Zanchettin et al., 2021]. While the subsidence rates are relatively stable over the observed period, high interannual and decadal VLM variability has been reported before 1995 [Zanchettin et al., 2021]. At the coasts of Japan, earthquakes and the associated seismic deformation generate highly non-linear VLM responses. One of the advantages of the BPCA is that the secular background trend can be separated from the earthquake-related dynamics, in contrast to previous global-scale analyses [Wöppelmann and Marcos, 2016, Hawkins et al., 2019b, Hammond et al., 2021]. Knowledge of the secular background trends will be essential to extrapolate VLM beyond the observational period, in such a way that it is unbiased by present-day variability.

Pronounced tectonic effects and also the subtleties of surface mass loading changes are attainable with the Bayesian VLM reconstruction. Predominantly hydrologically-forced interannual VLM variations are visible in the VLM time series (of the full reconstruction) of Rio de Janeiro and Curlew Island, which correlate with the independently derived estimate of contemporary mass redistribution (CMR) effects [Frederikse et al., 2020] (with correlation coefficients of 0.5 and 0.9). The identification of these regional non-linear processes is crucial to estimate the contribution of VLM to contemporary relative sea level change and its uncertainties.

4.3 The contribution of vertical land motion to contemporary regional sea level change

I examine the evolution of contemporary absolute SL changes (1900-2020) using the VLM reconstruction in combination with century-long tide gauges. The results are compared to independent absolute SL change estimates from a recent SL reconstruction [Dangendorf et al., 2019] and satellite altimetry observations.

To exemplify how non-linear and non-GIA VLM impacts the calculation of SL change, I show the results for three different tide gauges in Fig. 4.2. First, Fig. 4.2A addresses the effect of non-linear VLM (blue line) on relative SL change measured by the tide gauge (dark green line) subjected to tectonic activity. Here, the combined effect of inferred VLM and relative SL change shows high agreement with the absolute SL observations from altimetry. To extrapolate VLM back in time, I use the estimated linear trend component (and associated uncertainties) from the BPCA analysis. The adjusted absolute SL (1965-1995) estimate of the tide gauge (Fig. 4.2A) is consistent with the sea level reconstruction [Dangendorf et al., 2019]. This corroborates that the separation of the time-varying present-day VLM and a secular background trend provides valuable information on past SL changes, provided that the tide gauge is not affected by additional non-linear VLM, when no direct VLM observations are available (see also section 5.4).

Second, Fig. 4.2B is a notable example of VLM controlled by plate-tectonic processes and GIA [James et al., 2009, Newton et al., 2021]. The tide gauge in Seattle shows a subsidence of the order of 1 mm/year, which deviates strongly from the predicted uplift by the GIA model (see Fig. 4.2B and Fig. 4.3). This deviation is partly caused by the mismatch of the amplitude and the spatial structure of the North-South gradient of observed VLM and GIA model estimates [Newton et al., 2021]. The high agreement of the VLM-adjusted tide gauge observations and reconstructed sea level suggests constant VLM rates over the last century at this location. This is also supported by geological data, which indicate steady subsidence rates over the last 5 thousand years [Engelhart et al., 2015, Yousefi et al., 2018].

The third case displays the Freeport tide gauge located at the Gulf of Mexico (Fig. 4.2C), which is affected by non-linear VLM due to withdrawal of hydrocarbons and groundwater [Emery and Aubrey, 1991a, Liu et al., 2020]. While tide gauge relative SL change and observed VLM both display a constant pace after 1970, the relative SL change before that period indicates either substantially increased subsidence rates or even instantaneous vertical displacement of the tide gauge. Similar non-linear rates were observed at the Galveston tide gauge [Kolker et al., 2011], which is relatively close (64 km) to Freeport. Thus, on regional to local scales, unobserved effects of non-linear VLM (mainly due to tectonic processes and human activities) introduce large uncertainties in SL reconstructions and can significantly exceed the estimated Bayesian model uncertainty intervals (which are added to the re-estimated absolute SL in Fig. 4.2C). This confirms the importance of identifying present-day VLM variability, which is paramount for aligning tide gauge and altimetry observations and alleviating the propagation of non-linear effects into extrapolated observed VLM signatures back in time.

To understand the contribution of VLM to SL change over the last century from regional to global scales, I adjust tide gauges for VLM and derive the absolute coastal sea level change from 1995 to 2020 (Fig. 4.4A and Fig. 3.11C) and from 1900 to 2000 (Fig. 4.4B). I find high consistency between absolute SL trends from 1995-2020 inferred from 542 tide gauges and the regional coastal altimetry-based trends (which are interpolated onto the tide gauge location, see Fig. 4.4B). The average of absolute SL trends of all globally distributed tide

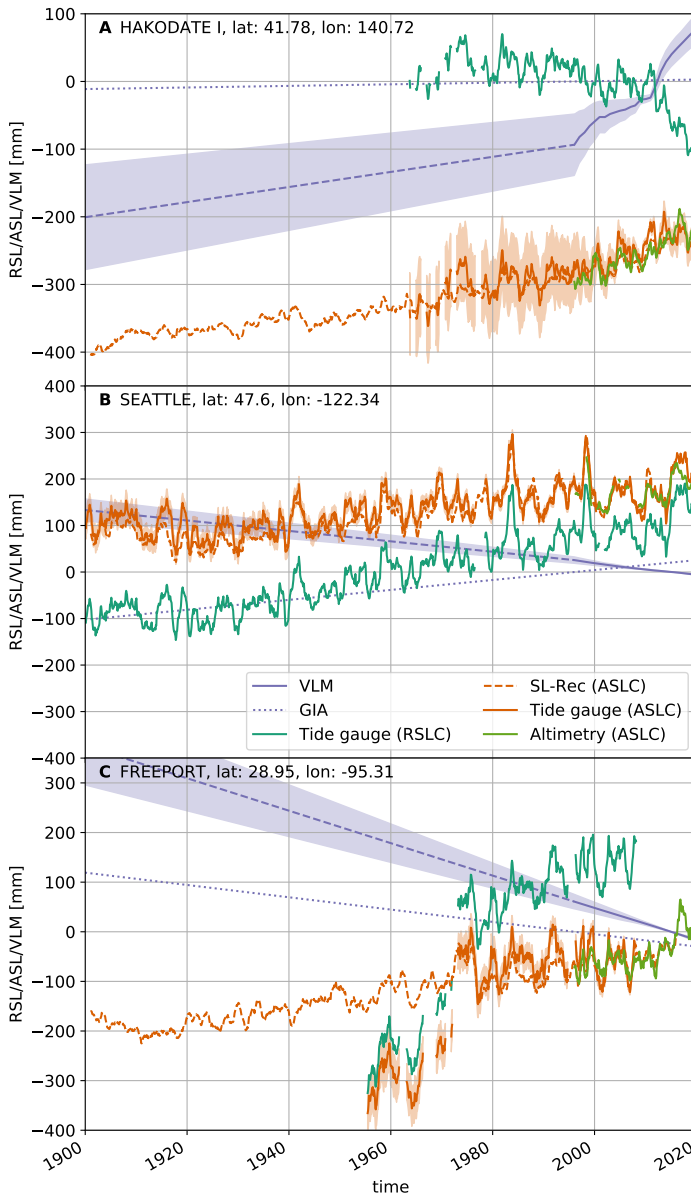


Figure 4.2 Time series of relative SL change (dark green line) and VLM-adjusted absolute SL change from tide gauges (orange solid line) in (A) Hokodate (Japan), (B) Seattle (USA), and (C) Freeport (USA). The present-day VLM estimate is shown by the blue solid line, the linear trend estimate (dashed line) represents the extrapolation of VLM back in time, and the dotted line indicates the GIA model [Caron et al., 2018] estimate at the tide gauge. For comparison, the altimetry observations (green) and SL-reconstruction estimates [Dangendorf et al., 2019] (orange dashed lines) over the last century are included.

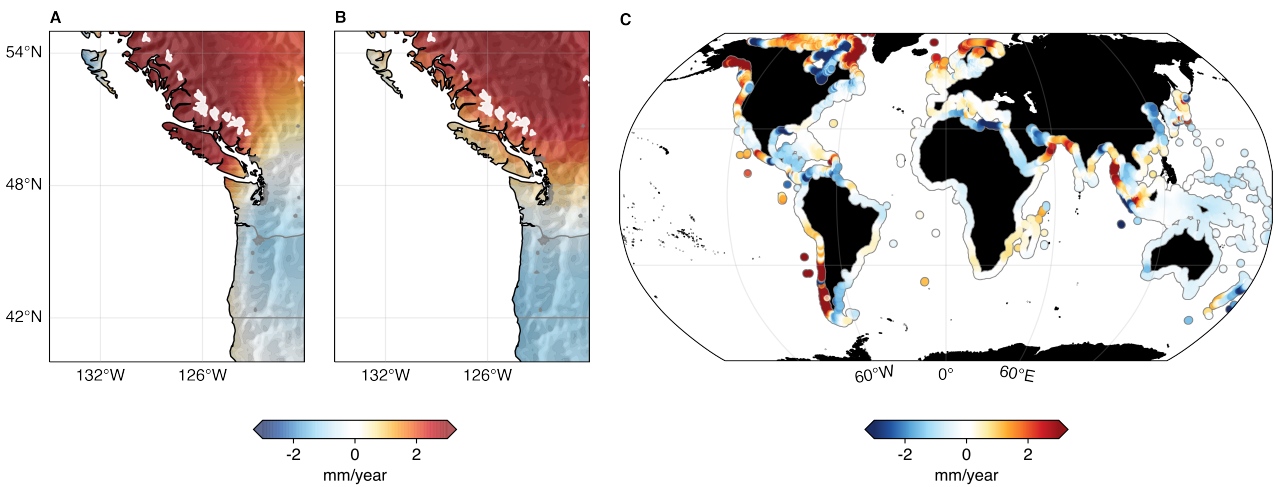


Figure 4.3 Shown are linear trends of (A) the VLM reconstruction, (B) the GIA estimate [Caron et al., 2018], and (C) differences between the VLM reconstruction and the GIA estimate.

gauges is 3.09 mm/year (median: 3.18) using the closest altimetry point and 3.20 mm/year (median: 2.92) using VLM-adjusted tide gauges records for the period 1995-2020.

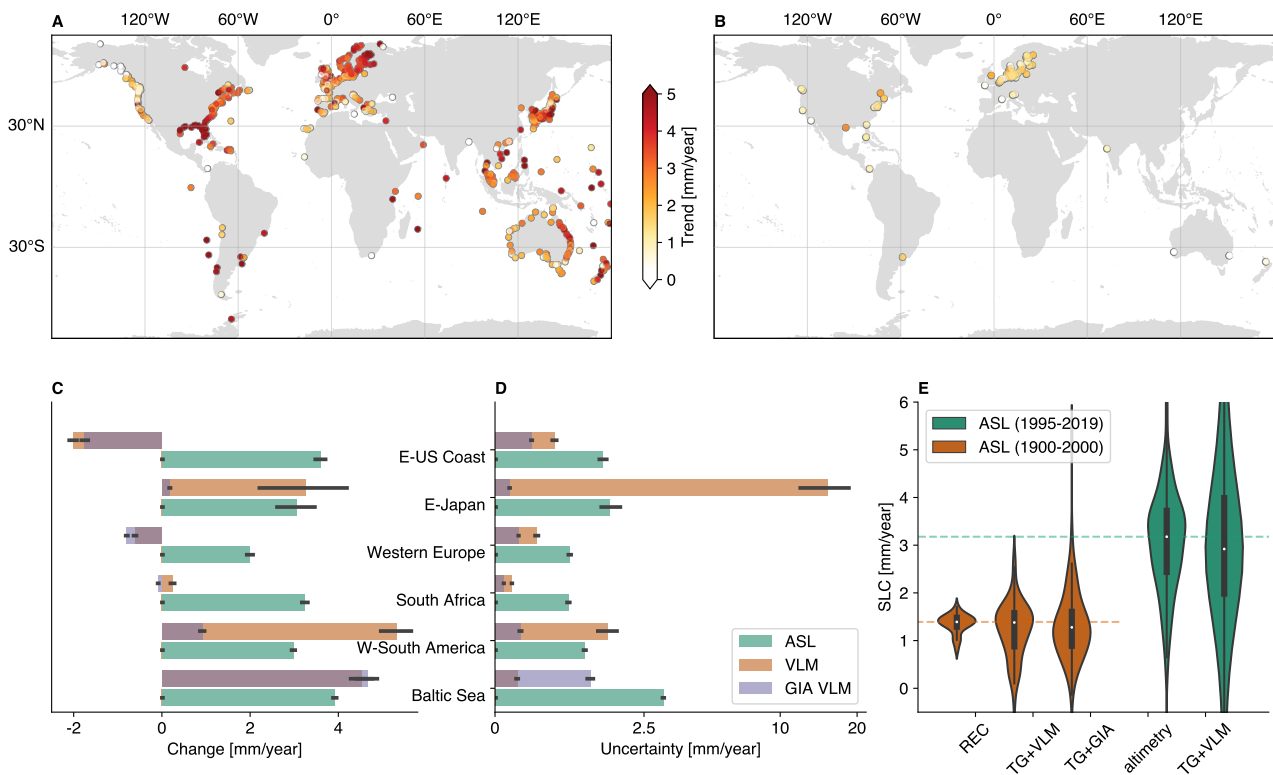


Figure 4.4 (A) Absolute SL trends from VLM-adjusted tide gauges from 1995-2020. Here, VLM is computed from the present-day VLM reconstruction, which includes the full effect of inferred interannual variability. B shows absolute SL trends computed over the last century (1900-2000) at 64 tide gauges (with at least 80 years of data), which are adjusted for the linear trend component of the reconstruction excluding the present-day variability. C and D illustrate the absolute SL and VLM uncertainties and trends for different macroregions, together with the averaged GIA model estimate along the coastlines for the period 1995-2020 (note the non-linear scale for the uncertainty components). Here, the 95% confidence intervals of the estimates within a region is indicated by the black lines. E provides the distributions of contemporary absolute SL observations/estimates (from 1900-2000 and 1995-2020) for SL reconstructions (REC), VLM-adjusted tide gauges (using both the VLM reconstruction and the GIA model estimate) as well as for altimetry observations (each for the same set of tide gauges). The dashed lines indicate the median estimates of the SL reconstruction (brown) and the altimetry observations (green).

To quantify the different components of relative SL change on a regional scale, I compute coastal averages of absolute SL trends, VLM, and their uncertainties from 1995-2020 at six different coastal macroregions (Fig. 4.4C and 4.4D). Note that the linear rates of VLM are computed from the full Bayesian reconstruction including the present-day VLM variability. Regional differences in relative SL change that are linked to VLM are on a similar order of magnitude as those associated to ocean dynamical processes (see, for example, the contrast between East and West US coasts in Fig. 4.4A or Wang et al. [2021]). Subsidence in both Western Europe and the Eastern US coast adds to the absolute SL change and yields relative SL trends from 2.6 ± 1.0 mm/year and 5.6 ± 1.6 mm/year, respectively, for the period 1995-2020 (Fig. 4.4C). A large share of the subsidence in Western Europe and the Eastern US Coast (between 31°N and 41°N) can be associated with the GIA forebulge collapse [Piecuch et al., 2018, Karegar et al., 2017, Hammond et al., 2021]. Compared to late Holocene geological rates

[Karegar et al., 2016], both the GIA model and the VLM reconstruction predict stronger subsidence south of 40°N along the US East coast (see also Fig. 4.5), which was also reported in previous work [Karegar et al., 2017] and discussed to be caused by ongoing groundwater extraction in these areas. When taking into account its combined uncertainties, the inferred VLM does not significantly deviate from the GIA model [Caron et al., 2018], averaged along the same coastal profiles (see also Fig. 4.3). There is low temporal variability in Western Europe and the Eastern US Coast (see Fig. 4.7B), leading to similar uncertainty estimates as provided by the GIA model. Other regions, however, are subject to tectonic processes that can inflate uncertainties of VLM almost exponentially (note the non-linear scale in Fig. 4.4D). This is particularly evident for Eastern Japan and Western South America, where tectonic uplift completely offsets the present absolute SL change.

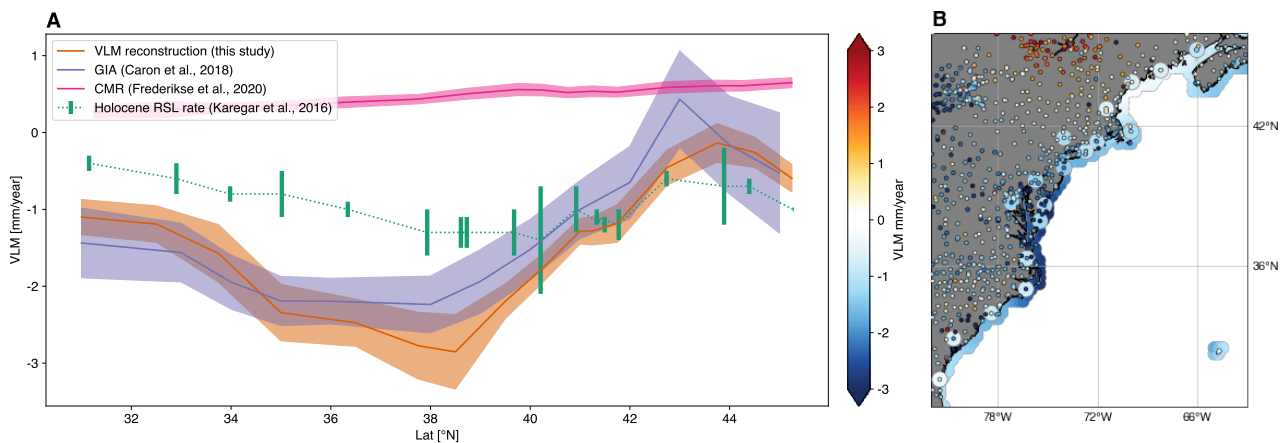


Figure 4.5 (A) comparison of VLM (and its uncertainty) from GIA (purple, Caron et al. [2018]), CMR (pink, Frederikse et al. [2020]), late Holocene records from the last 4000 years (green, Karegar et al. [2016]), and the VLM reconstruction (orange) as a function of latitude along the US East coast (as in Karegar et al. [2017]). (B) indicates the GNSS and SATTG rates used in this study as small circles, the geological rates as large circles [Karegar et al., 2016], as well as the coastal profile of the VLM reconstruction along the coastline.

Averaged along the global coastal profile shown in Fig. 4.1D, VLM explains a significant fraction of the variance of relative SL change (34%) and its uncertainties (26%) over the altimetry era. Overall, the estimated uncertainties of the VLM reconstruction, which takes into account non-linear processes, are higher than the uncertainties provided by the GIA model [Caron et al., 2018] (explaining 19% of the relative SL trend uncertainties).

The VLM reconstruction represents a crucial observation-based constraint to SL estimates over the last century. Hence, I explore the impact of VLM on relative SL change over the period 1900-2000 using 64 tide gauges with at least 80 years of data (Fig. 4.4B). Relative SL change at tide gauges is corrected for VLM in two ways: using the VLM reconstruction of this study and a GIA model. The effect of CMR (from Frederikse et al. [2020]) is subtracted from the ASL sea level reconstruction [Dangendorf et al., 2019], as well as from both VLM datasets. I compare the outputs with absolute SL change from the global SL reconstruction from Dangendorf et al. [2019], for which I extract the same tide gauge locations. I recall here that the SL reconstruction incorporates GIA and estimates of local residual VLM [Dangendorf et al., 2019]. Most of the long-term tide gauges are located in well-instrumented regions like Europe and the US, as shown by the distribution of VLM-adjusted absolute SL trends of tide gauges in Fig. 4.4B. Because these regions are dominated by GIA-related uplift and subsidence, they are specifically sensitive to the accuracy of the applied GIA fingerprint estimate.

The median absolute SL change estimates (from 1900-2000) for the SL reconstruction [Dangendorf et al., 2019] are 1.39 mm/year, 1.38 mm/year for the VLM-adjusted tide gauges, and 1.27 mm/year for the GIA-adjusted tide gauges (see Fig. 4.4E). Using bootstrapped confidence intervals, I find that none of these averages are significantly different from each other (at the 95% confidence level). This high agreement indicates that the linear rates of the VLM reconstruction derived in this study are suitable to be extrapolated back into the last century (at the location of the tide gauges), to constrain the VLM at tide gauges and to derive absolute sea level estimates. It also supports the validity of indirectly inferring VLM rates from long tide gauge records in sea level reconstructions. However, it should be noted, that these results are based on a relatively small subset of tide gauges, which are mostly located in northern Europe and the USA. These regions are found to be associated with relatively stable VLM in time (after removing the effect of CMR), which facilitates the extrapolation of the rates back in time. Regions, which are affected by larger temporal variations in the VLM rates, such as the Gulf of Mexico, or regions affected by tectonic activity, may be less suited to extrapolate VLM back in time, if VLM is derived only from a limited observational period (1995-2020). At some locations, like at tide gauges in the Gulf of Mexico and Australia (Fig. 4.4B), for instance, I find differences (on the order of mm/year) in the absolute SL rates of the reconstruction from Dangendorf et al. [2019] and the trends from the VLM-adjusted tide gauges (based on the VLM derived in this study). Thus, assuming that the absolute SL rates of the reconstruction [Dangendorf et al., 2019] represent the ground truth, these differences could be caused by variations in the VLM over the last century. Thus, there is an urgent need to investigate the extent to which non-linear VLM effects are also present in century-long TG records (see also discussion in section 5.4).

4.4 Non-linear vertical land motion limits regional coastal sea level change projections

To estimate the different contributions of absolute SL change and VLM to projected coastal relative sea level, I utilize the outputs of the Coupled Model Intercomparison Project Phase 6 (CMIP6) [Eyring et al., 2016]. I explore different scenarios (SSP2-4.5, SSP3-7.0 and SSP5-8.5 [O'Neill et al., 2016]), each relying on different emission scenarios. I particularly focus on the SSP2-4.5 scenario, which represents the medium pathway of future emissions in which CO₂ levels are assumed to decline mid-century, causing a temperature increase of 2.7° in 2100. Higher greenhouse gas emissions are assumed for SSP3-7.0 and SSP5-8.5 scenarios, which are associated with a radiative forcing of 7 Wm^{-2} and 8.5 Wm^{-2} or global CO₂ concentrations of more than 800 or 1100 ppm by the year 2100 [O'Neill et al., 2016]. I consider the ensemble median and the likely range (one-sigma confidence intervals) of the integrated contributions from ice sheets, glaciers, land water storage, and ocean dynamics [Garner et al., 2021b,a]. The projected absolute coastal sea level change (of the SSP2-4.5 scenario) is combined with the long-term linear trends of the VLM reconstruction. To project the VLM uncertainties, I generate a 1000-member ensemble of possible future trajectories of natural or anthropogenic VLM variability. These trajectories are modeled by Gaussian Random Walks starting from 2020 until 2150, and are informed by the parameters estimated (in section 3.3) to determine the present-day variability. To derive the final VLM uncertainties compute the square root of the sum of the squares of the standard deviation of the ensemble spread and the trend uncertainties estimated in the Bayesian model.

Figures 4.6A-C and 4.6F-H provide an overview of different projected local relative SL change estimates based on both the VLM reconstruction and the GIA model at six different locations. GIA-induced uplift and subsidence strongly contribute to future sea level in the Bothnian Bay (Skellefteå) and the Eastern US Coast (New York), which is consistent with the VLM reconstruction. Discrepancies between relative SL projections can be found in areas affected by localized subsidence (e.g., in Venice, the Gulf of Mexico, or the Nile Delta) or in regions impacted by high tectonic activity (Western South America and Japan). As shown in the previous analyses (e.g., Fig. 4.2), unresolved processes in GIA models inevitably contribute to regional deviations of relative SL change projections.

In Fig. 4.6E, I illustrate the regional future relative SL change in absolute terms and as the deviation from the global median SL rise (0.93 m in 2150), obtained as the median of the ensemble model outputs and for the same aforementioned macroregions. The bars depicting the VLM components indicate its contribution to relative SL change. With respect to the altimetry era, the absolute explained spatial variance of coastal relative SL change by VLM is projected to decrease to about 22% in 2150 along the world's coastlines, where coastal SL change is by implication more strongly dominated by the increased mean absolute SL rise. However, on a regional scale, VLM plays a predominant role in future SL change as shown in Fig. 4.6E. I estimate that VLM will explain 51% of the variance of the relative SL deviations from the global mean in 2150. The regional impact of VLM is thus at the same magnitude as the combined responses to ocean dynamics and mass change fingerprints. The bulk of the contribution of VLM is attributable to GIA [Caron et al., 2018], which accounts for 41%. The contribution of VLM remains of comparable importance when considering other radiative forcing scenarios. Here, 49% (for SSP3-7.0) and 47% (for SSP5-8.5) of the variances of relative SL change deviations from the global mean are explained by VLM (with a global mean projected absolute SL change of 1.03 m and 1.17 m in 2150, respectively).

In addition to these absolute contributions to relative SL change, I find that VLM uncertainties explain a substantial proportion of the combined relative SL change uncertainties (39%). Here, the relative SL uncertainties are computed based on the combined uncertainties of the VLM projections and the 17th to 83rd percentiles of the absolute SL projections. Note, that this uncertainty contribution cannot be unequivocally compared to the results obtained for the altimetry era, where absolute SL uncertainties are computed based on the observed SL variability in contrast to the absolute SL uncertainties of the projections, which are derived from the ensemble spread of different model components [e.g., Slangen et al. [2023], Kopp et al. [2023]]. Particularly large uncertainties are introduced in areas where non-linear VLM is dominant (see Fig. 4.7B). Regionally, non-linear VLM hampers significant projections of relative SL change, as exemplified in Fig. 4.6C. The uncertainty estimates in tectonically active regions (South America, Alaska, Japan) of the VLM reconstruction are systematically higher (by a factor of 2-5) than the coastal VLM uncertainty estimates estimated at tide gauges by the IPCC AR6 report [Kopp et al., 2014, Fox-Kemper et al., 2021] (see Fig. 3.11D). I provide evidence that the reconstructed VLM and uncertainty estimates more realistically reflect direct observations than alternative estimates [Kopp et al., 2014, Caron et al., 2018], because I explicitly take non-linear effects into account (see Fig. 3.11H).

By comparing different independent estimates of coastal VLM, I find that large discrepancies between these estimates (> 10 mm/year) are associated with high temporal variability of VLM, as derived from the VLM reconstruction (see Fig. 4.7A and 4.7B). Therefore, non-linear VLM not only inflates coastal relative SL change uncertainties, but also directly affects the VLM estimates when they are estimated over different observation

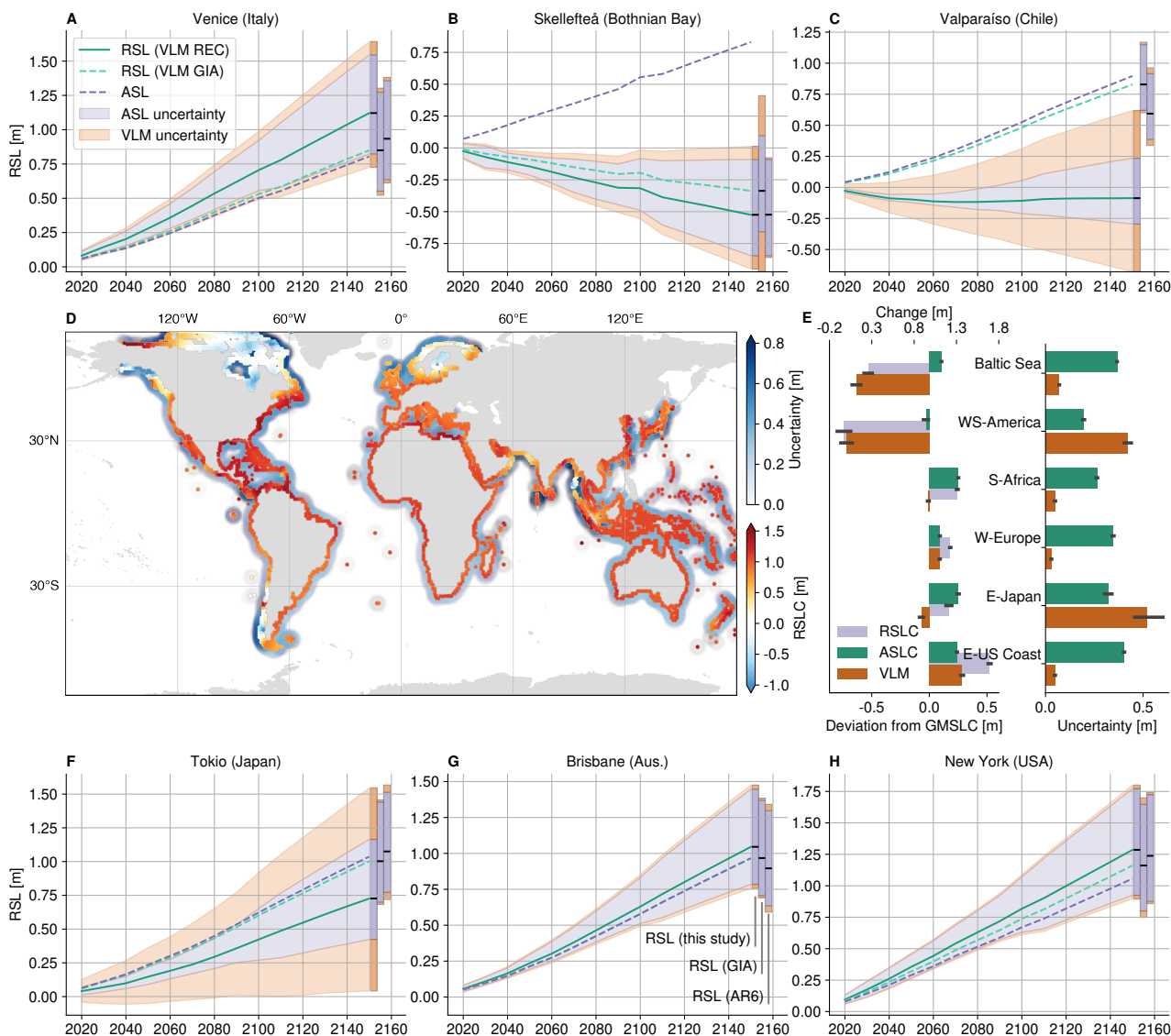


Figure 4.6 Overview of global and regional projected relative sea level change based on IPCC AR6 projections [Fox-Kemper et al., 2021, Garner et al., 2021b,a] (SSP2-4.5 scenario [O’Neill et al., 2016]), the VLM reconstruction, and GIA model estimates [Caron et al., 2018]. A-C and F-H show time series of the evolution of the estimated relative SL change, either based on the VLM-reconstruction (solid teal line) or GIA model [Caron et al., 2018] (dashed teal line) from 2020-2150. The absolute projected SL change is depicted by the blue dashed line and consists of the contributions of ice sheets, glaciers, land water storage, and ocean dynamics [Garner et al., 2021b,a]. Uncertainty contributions of the absolute SL change and VLM (blue and orange shading) add up to the combined relative SL change uncertainties. D shows the coastal projected relative SL change, as well as the combined uncertainties (blue shading) of the absolute SL projections and the VLM reconstruction. E separates the different contributors of relative SL change and uncertainties for different regions. The relative SL change and absolute SL change are given in absolute terms as well as the deviation from the global mean sea level rise in 2150.

periods and are approximated with purely linear motion. Such differences between different VLM solutions translate into differences of up to 1 m in RSL change in 100 years. Inevitably, these regional errors due to large VLM variability must be compensated by large uncertainty ranges in the RSL projections, which is ensured by the presented approach.

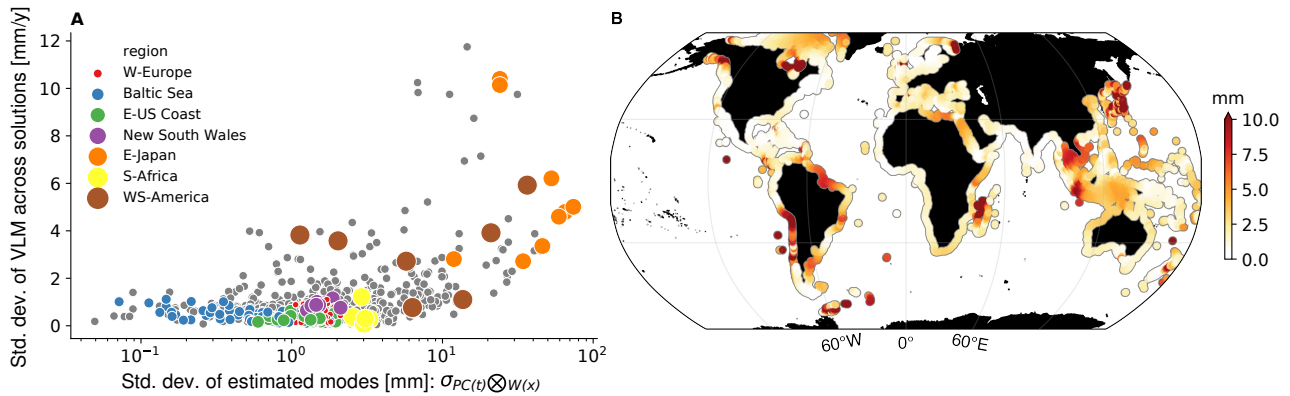


Figure 4.7 (A) illustrates how time-variable VLM relates to differences in VLM estimates across different solutions. Here, the y-axis shows the standard deviations of different VLM estimates (i.e., the VLM reconstruction, [Kopp et al., 2014, Caron et al., 2018, Dangendorf et al., 2019] and GNSS trends) computed at 755 different coastal GNSS stations [mm/year]. The x-axis (note the logarithmic scale) sorts the data according to the estimated standard deviation (in time) of the present-day VLM variability of the reconstruction $\sigma_{PC} \otimes_{EOF}$ (i.e., the variability estimated by the EOFs in mm). Time-variable VLM increases the probability of discrepancies between different VLM estimates. (B) depicts the estimated coastal present-day VLM variability $\sigma_{PC} \otimes_{EOF}$.

These findings highlight the importance of the proposed approach aimed at the determination of non-linear VLM processes using comprehensive databases of VLM observations. Unpredictable processes such as earthquakes or the lack of human-induced VLM projections [Zanchettin et al., 2021] remain key challenges, because they reduce the confidence in projected pathways of regional sea level change (see also discussion in section 4.6). <

4.5 Exposure of coastal populations to contemporary relative sea level change

In the previous sections, I corroborate that VLM shapes a significant fraction of the observed variability of RSL change on regional scale and that high uncertainties in these trends can complicate the assessment of future coastal impacts. Regional variations in RSL changes will hence affect coastal population and ecosystems in a highly non-uniform manner. In this section, I reconcile how coastal population is exposed to the contemporary compound effects of ASL change and VLM.

> Previous studies dealing with the societal implications of RSL changes have incorporated effects from VLM sources like GIA, delta and city subsidence [e.g. Ericson et al., 2006, Syvitski et al., 2009, Nicholls et al., 2021], together with estimates of contemporary and projected ASL change. Nicholls et al. [2021] highlighted that human-induced subsidence in cities (mainly due to subsurface fluid withdrawal), as well as subsidence caused by changes in sediment supply in deltas due to human constructions (like flood defenses) significantly increase the actual RSL experienced in densely populated coastal areas. They showed that, when ASL trends (from 1993 to 2015) are combined with the contributions of GIA and city and delta VLM, the global coastal-population weighted RSL rise (7.8 - 9.9 mm/year) strongly exceeds the global average (2.6 mm/year). This is mainly due to the fact that highly urbanized areas are more frequently affected by enhanced human-induced subsidence, which is qualitatively also supported by a recent study estimating VLM in major coastal cities based on InSAR data [Tay et al., 2022].

A major limitation of the study performed by Nicholls et al. [2021] is that the city and delta subsidence estimates were partially taken from literature values [Ericson et al., 2006], expert judgements, and were sometimes manually set to 1 mm/year, in case no data was available. In addition, no other observational information on regional-scale effects like plate tectonics was included. All these data are, however, critical for the conclusions drawn, that highly populated areas are exposed to higher-than-average sea level rise. Therefore, I reassess here these results in light of actual VLM observations, as provided in this work. For this purpose, I investigate the exposure of the coastal population to contemporary rates of relative sea level change using observations only.

To refine the resolution of VLM in major coastal cities, I exploit the recently published InSAR VLM data provided (computed from Sentinel-1 SAR images from October 2014 to April 2020) by Tay et al. [2022]. Due to the low precision of this technique, the rates usually have a higher uncertainty (i.e., mean uncertainty of 2.7 mm/year) than the trends of the interpolated VLM map. Still, these data are valuable to resolve subsidence at very small scales and in cities where no GNSS (or tide gauge) station data are installed or publicly available. This allows me to fill in observational gaps, in particular, in large cities in India and China. The InSAR VLM is combined with the linear rates of the VLM reconstruction (hereinafter called OE23), which serves here as a background model for global to regional scale processes. This means that the values of the VLM map are replaced by the InSAR data wherever they are available. I also incorporate GIA estimates, wherever OE23 has missing data. The combined dataset (OE23 + InSAR + GIA) is mapped onto the 12,148 coastal segments of the DIVA model [Vafeidis et al., 2008], which share similar coastal characteristics [Nicholls et al., 2021]. Note, that in the following analyses, some of the very northerly regions and Antarctica are masked out, mainly due to missing altimetry data. In addition to the information on the location and extent of the coastal segments (including the length of the coastline), I use the population data from the DIVA model as applied in [Nicholls et al., 2021]. Here I consider the population living below 10 m elevation in 2015, which is 768 million people in total. The digital elevation model data are obtained from Shuttle Radar Topography Mission (SRTM) elevation data [Rabus et al., 2003, Jarvis et al., 2008] is combined with Global Rural–Urban Mapping Project population data using resampling methods [Merkens et al., 2018], and provided at the same segments of the DIVA model.

Figure 4.8 D shows the coastal population (below 10 m above sea level, as used in Nicholls et al. [2021]), as well as (B) contemporary RSL rates from (A) ASL change (CMEMS) and the combined (C) VLM estimates. As can be seen, most of the densely populated areas are situated in Southeast Asia and tend to be more frequent in tropical to subtropical regions. In these areas, the ASL change is higher than the GMSL change, due to GRD effects and changes in the ocean circulation [e.g. Hinkel et al., 2014]. Tropical regions are also usually not affected by uplift due to GIA, which in other areas offsets some of the contemporary ASL change. As a result, from a socio-economic perspective, GIA only plays a minor role in affecting coastal RSL change. Hence, direct observations of VLM are even more essential in areas where non-GIA processes dominate.

Estimates of contemporary relative sea level change differ substantially depending on whether the GIA VLM effect alone or the combined VLM estimates (OE23 + InSAR + GIA), which incorporate VLM observations, are taken into account (Fig. 4.9). The integration of the variety of VLM processes of the combined VLM product (e.g., from GIA, tectonics, local subsidence, etc.) significantly increases the scatter of RSL trend estimates compared to the RSL change, when only ASL + GIA, or the ASL change alone is considered. The coastal-length weighted standard deviation of RSL changes (3.33 mm/year; with all effects included) is about twice as large as the standard variation of the ASL changes (1.71 mm/year). This is partially also caused by single

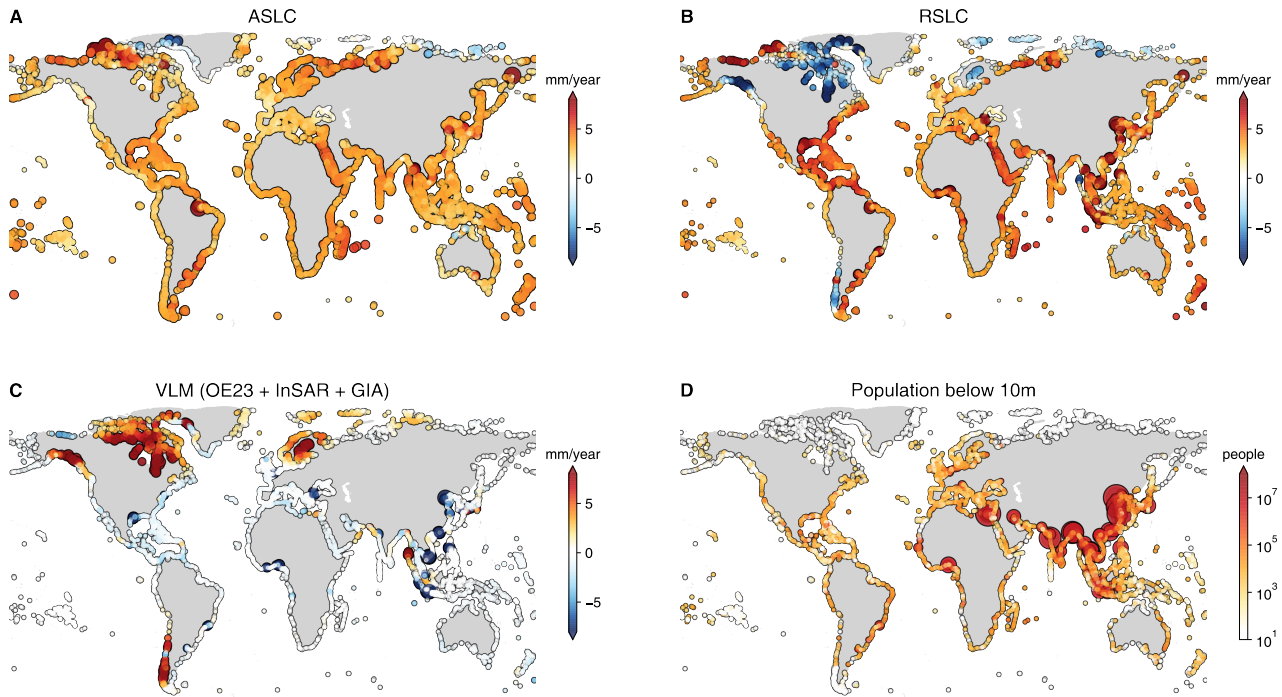


Figure 4.8 A) ASL change from CMEMS over 1995-2019. B) RSL change as the combination of ASL change and VLM (based on the VLM reconstruction (OE23), GIA (Caron et al. [2018], where OE23 has missing data) and InSAR from Tay et al. [2022]). The latter VLM data are illustrated in C. D) shows the number of people living below 10 m in elevation on a logarithmic scale. The sizes of the data points are scaled by their absolute value.

extremes in regional or local subsidence or uplift, leading to much longer tails in the distribution of RSL change. Therefore, VLM (with a standard deviation of 2.65 mm/year) is here a dominant driver of the regional variability in RSL changes (see also Table 4.1).

The distribution of the RSL trends in Figure 4.9A also indicates that higher-than-average RSL changes are statistically more frequent in regions with higher population. This effects becomes more apparent when comparing the coastal-length versus the population weighted RSL trends, as in Table 4.1. Here, I use different VLM data combinations to generate different estimates of global coastal RSL changes. When only using the VLM reconstruction (together with GIA estimates at locations with missing data) the population weighted average RSL change (3.74 mm/year) is almost twice as large as the coastal-length-weighted average (1.99 mm/year). This is mainly caused by VLM, with a minor contribution of ASL change (see first and second row in Table 4.1). Including InSAR estimates at large cities further increases this discrepancy, such that the population weighted RSL change of 5.14 mm/year becomes more than twice as large as the coastal-length weighted RSL change (of 2.09 mm/year). When I replace the InSAR data in these estimates (OE23 + InSAR + GIA) with the delta and city subsidence data from Nicholls [2011], I find an even higher population weighted RSL change (8.79 mm/year). This can be explained by differences in the VLM estimates of these datasets, i.e. the subsidence rates are higher in the city and delta data from Nicholls [2011] than in the InSAR data from Tay et al. [2022]. Here, it should be noted that Nicholls [2011] provides much more city and delta VLM data compared to the InSAR data (which is provided at the 50 largest coastal cities). Hence, I also show the RSL and VLM estimates only at the locations where both datasets contain estimates (in the last two rows of Table

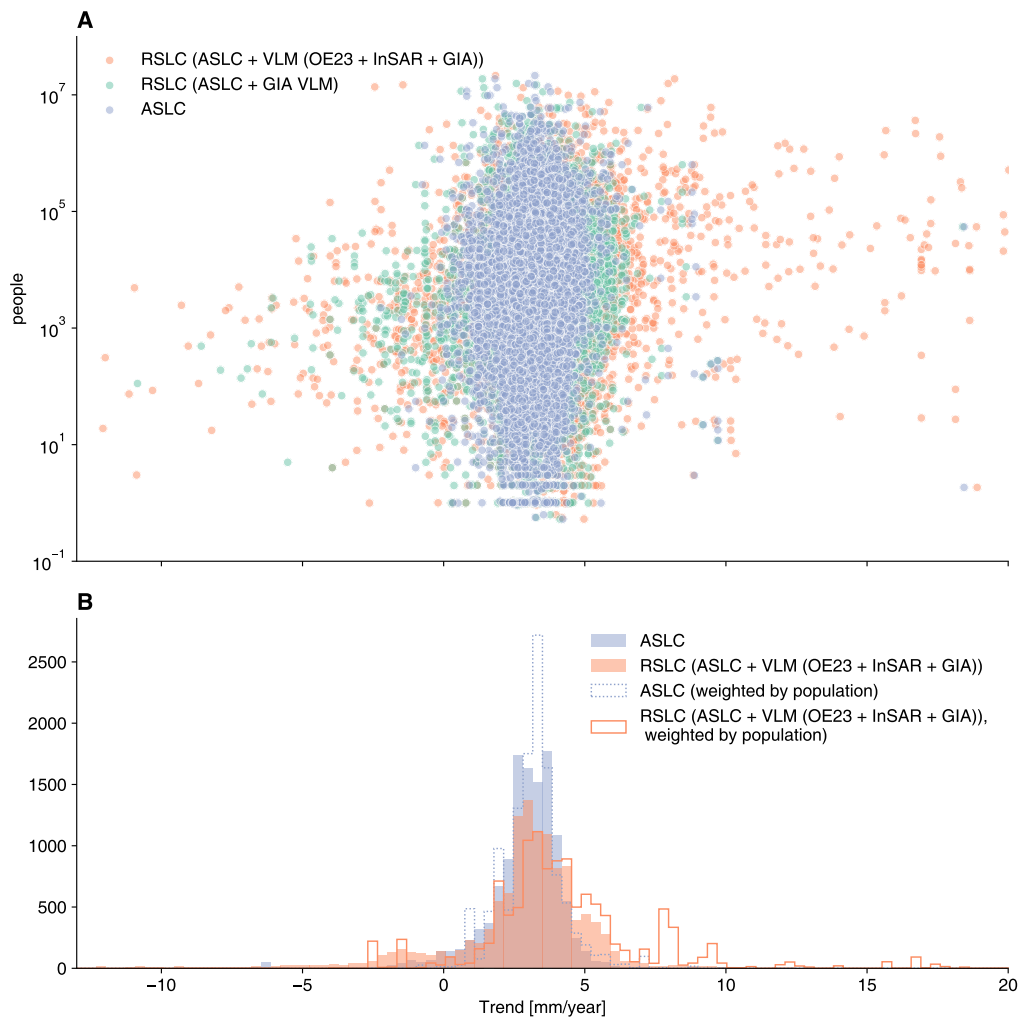


Figure 4.9 A) number of people living below 10 m in elevation versus ASL change and RSL change based on different VLM estimates (GIA or OE23 + InSAR + GIA). B) shows the unweighted distributions of the data, as well as the population weighted distributions (filled and unfilled contour lines).

4.1). This comparison confirms that the city VLM estimates from Nicholls [2011] are generally lower than the VLM estimates from InSAR observations [Tay et al., 2022].

Although there are large differences between these datasets, these results reinforce that highly populated areas are affected by higher-than-average RSL change, which is mainly due to the contribution of subsidence [Nicholls et al., 2021, Tay et al., 2022]. However, it should be emphasized that this relationship is highly non-linear and clearly dominated by a few extreme cases, where very large cities are affected by strong subsidence and thus increased RSL change. This finding is also supported by Figure 4.10A, which shows global averages of the individual VLM contributions to RSL change based on the different datasets (GIA, OE23, InSAR and city + delta VLM). Here, I set the coastal VLM to zero where no data are provided. As can be seen, the global population weighted averages based on InSAR or city and delta VLM show relatively high subsidence and thus large contributions to RSL changes, even though these estimates are only available for a small fraction of the world's coastlines. This is due to the power-law distribution of the coastal population, i.e. 90% of the global coastal population (in the most densely populated regions) lives in an area that extends along only 1% of the global coastline. The data indicate that these densely populated regions more likely to coincide with

Table 4.1 VLM, ASL and RSL change in [mm/year]. Provided are mean and standard-deviation of coastal-length (coastal l.) and population weighted data. RSL change and VLM data are given for different VLM dataset combinations (columns 2-6). In the last two columns (5-6), I compare two different VLM data combinations, in which the InSAR [Tay et al., 2022] and city VLM data [Nicholls, 2011] are only used at locations where both datasets provide estimates.

		OE23 + GIA		OE23 + GIA + InSAR		OE23 + GIA + delta + city		OE23 + GIA + InSAR (comp.)		OE23 + GIA + city (comp.)	
	ASL	RSL	VLM	RSL	VLM	RSL	VLM	RSL	VLM	RSL	VLM
mean (coastal l.)	2.85	1.99	0.86	2.09	0.76	2.15	0.70	2.00	0.85	2.03	0.83
1 σ (coastal l.)	1.71	3.33	2.65	3.55	2.91	3.92	3.38	3.36	2.69	3.55	2.92
mean (population)	3.19	3.74	-0.55	5.14	-1.95	8.79	-5.60	4.42	-1.23	6.88	-3.70
1 σ (population)	1.12	1.36	1.24	5.11	5.08	13.77	13.77	4.08	4.11	13.01	12.96

higher-than-average subsidence, which explains why humans experience RSL changes much higher than the spatially averaged rates.

Not only the RSL rates, but also the global averages of the formal uncertainties are affected by the applied weighting factors 4.10C. As can be seen, the population weighted uncertainties of the combined RSL trends are significantly larger than the coastal-length weighted RSL uncertainties. This is mainly caused by the distribution of VLM uncertainties, which are increased in highly populated areas. The increase in the VLM uncertainties can be partially explained by the low precision of the InSAR approach and the relative shortness of the InSAR time series (6 years). Note, that the InSAR data are provided at the 50 largest coastal cities and thus have a strong impact on the population weighted averages. Another factor could also be the low GNSS station density in Southeast-Asia on which the VLM reconstruction is based, as discussed in more detail in the next section 4.6 and Figure 4.12. In general, the high RSL rates in highly populated areas are additionally exacerbated by high uncertainties in these estimates, which should be taken into account in coastal planning.

<

4.6 Discussion

In this chapter, I incorporate observational VLM constraints to complete our picture of the spatiotemporal patterns of coastal VLM and improve our understanding of contemporary and future coastal SL change. The continuous and time-resolving VLM reconstruction represents a key contribution to the multi-technique coastal observing system and facilitates the alignment of tide gauges and altimetry, which is particularly important to improve the impact-assessment of coastal sea level change. I separate present-day VLM changes from long-term VLM trends, which can be applied to further reduce the spread of reconstructed global mean SL trends over the last century (see [Frederikse et al., 2020] for an overview). My results highlight the evident impact of VLM in shaping the regional patterns of future projected relative SL, which is comparable to the combined contributions from projected changes of the ocean circulation and mass changes. Neglecting the effect of VLM in sea level projections, could lead to an underestimation of RSL in 2150 by up to 50 cm at the regional scale (see Fig. 4.11). I determine effects of non-linear VLM that, so far, have been underestimated and that significantly raise the uncertainties of projected coastal relative SL change above previously

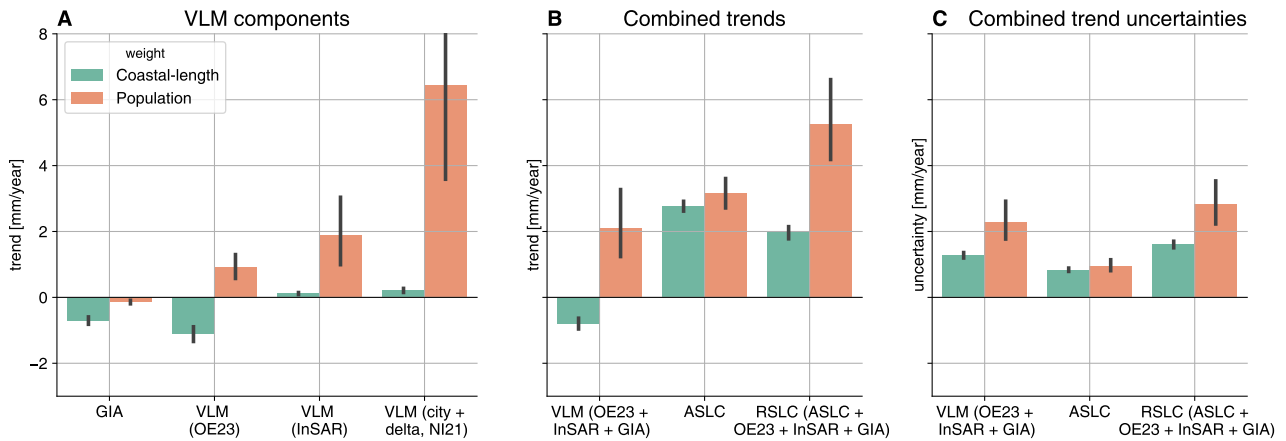


Figure 4.10 A) Global averages of different VLM estimates using different weightings. The VLM data are shown in terms of their contribution to RSL change (i.e., positive sign for subsidence, and vice versa). I set zero VLM at every coastal segment where an individual VLM dataset does not provide any data. B) and C) show the trends and 1σ -uncertainties of different dataset combinations. For the VLM dataset OE23 + InSAR + GIA I substitute uncertainties of the VLM reconstruction (OE23) with InSAR-based uncertainties in cities (wherever such data is available).

reported levels [Kopp et al., 2014]. \triangleright Regional RSL change uncertainties can be as large as 100 cm in 2150, which must be taken into account in coastal planning (Fig. 4.11B). However, I emphasize that these results themselves have an uncertainty, because it is assumed here that all contributing uncertainties (from VLM, ice sheets, thermal expansion, etc.) are captured with equal accuracy. Currently this cannot be guaranteed because of the different methodologies applied here, which also differ for the estimation of the individual ASL components (emulators, process models, Atmosphere-Ocean General Circulation Model ensembles, etc., see Fox-Kemper et al. [2021], Slangen et al. [2023]) and because of the structural uncertainty in ASL projections [Kopp et al., 2023]. \triangleleft

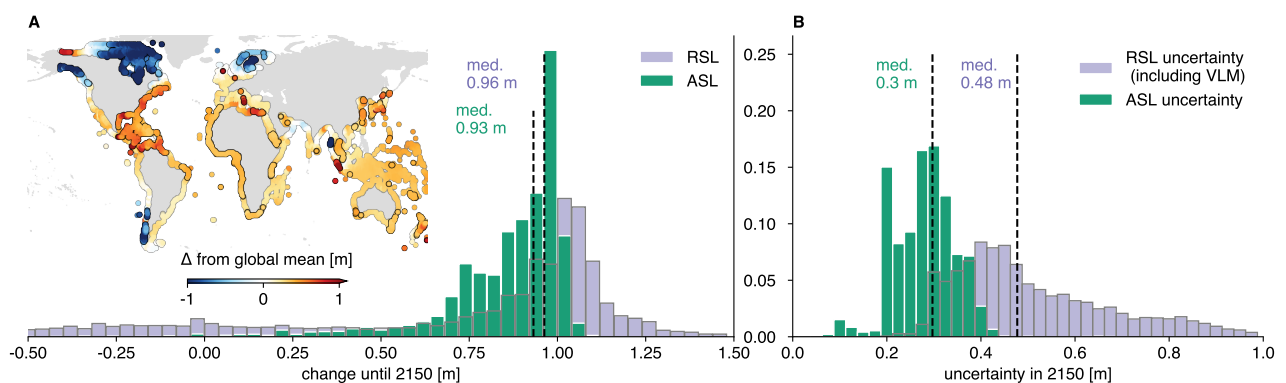


Figure 4.11 (A) Histogram of projected coastal ASL (SSP2-4.5 scenario, Fox-Kemper et al. [2021], Garner et al. [2021b,a]) and RSL changes until 2150 [m]. The map indicates deviations of RSL changes from the global coastal mean RSL change. The black circles highlight where these differences are significant (based on the combined 1σ uncertainties). The dashed lines display the median values of the distributions. (B) Same as in (A) but for the estimated RSL and ASL change uncertainties in 2150.

My results show that resolving non-linear vertical land movements represents an additional challenge for SL reconstructions or future projections. Since the accurate determination of VLM variations ultimately relies

on a network of high-quality observations (usually GNSS data), it is difficult to extend this analysis further back into the last century, as this would again solely rely on tide gauge observations. Nevertheless, future efforts are recommended to reassess differences in SL reconstructions due to non-linear VLM, as found in this work (for more details see also section 5.4).

Parts of the uncertainties in the VLM reconstruction arise from limited data availability, especially in densely populated areas such as India, China, Indonesia or Africa as illustrated in Figure 4.12A. This is a major particular problem for the largest coastal cities, where millions of people live at a low elevations (Figure 4.12B). Therefore, as requested by many previous studies, the maintenance and extension of the existing GNSS network, in particular at tide gauges and along highly urbanized coastlines, are of fundamental importance to monitor the trajectories of coastal VLM. To complement the sparse VLM database, very recent studies [Tay et al., 2022, Naish et al., 2022] have exploited InSAR at unprecedented scales. Therefore, it is expected that data derived with this technique will become increasingly available on a global scale and will help to further refine VLM reconstructions and future projections (see also section 5.4).

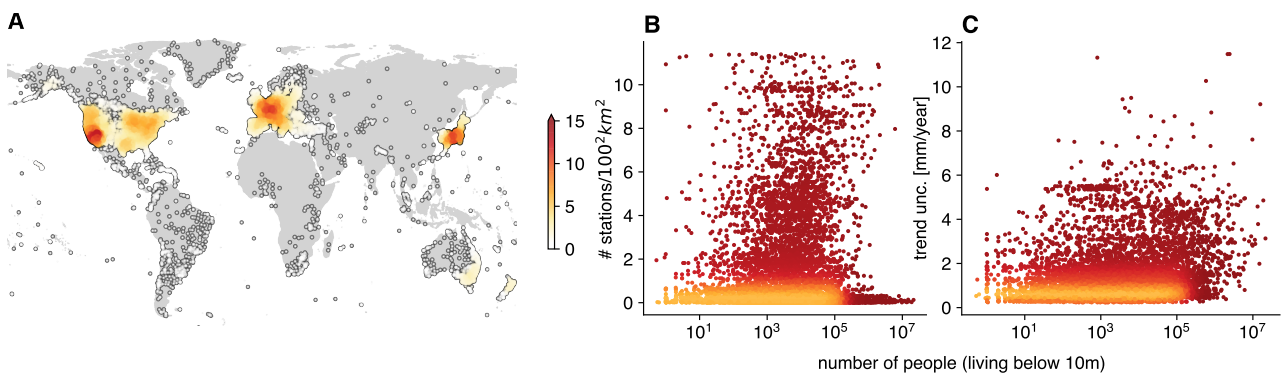


Figure 4.12 A) shows the station density in terms of number of stations per 100² km². The station density was computed based on the number of stations within a 500 km search radius around an individual station, divided by the area covered by this circle. B) and C) show the station density and the trend uncertainties (of the contemporary RSL changes as estimated in section 4.5) versus the number of people living below 10 m in elevation (on a logarithmic scale). The values of the station density and the population (defined at the coastlines) are coupled by nearest neighbor interpolation.

› In section 4.5 I reassess the exposure of coastal populations to contemporary RSL change using VLM observations. My results reconfirm previous work [Nicholls et al., 2021], that RSL rise is on average higher in highly populated areas. However, the relative increase between the population-density and the coastal-length weighted RSL rise is not as large as previously reported [Nicholls et al., 2021]. These differences could be either caused by overestimated subsidence rates in cities and deltas by Nicholls et al. [2021], which were mostly not based on actual geodetic measurements, or by missing observations (in the applied VLM observation data) due to their partially sparse spatial distribution. Another finding is that also the RSL change uncertainty estimates are higher in densely populated areas (see also Figure 4.12C), which can be caused by a variety of factors, such as the low precision of the InSAR technique, or the low data availability in these regions.

One of the limitations of the InSAR approach is that a geodetic tie, i.e. data from a GNSS station, is required to convert the VLM rates into a global reference system. As noted by Tay et al. [2022], such a reference point was not always available, which can thus lead to discrepancies between the InSAR VLM estimates and the GNSS trends. To better understand these differences and the extent to which InSAR VLM data might be biased with respect to the GNSS data, I compare both measurements in Fig. 1 (provided in the appendix). I

identify substantial differences between these trend estimates (with a standard deviation of about 5 mm/year). I also find that the trend differences vary little depending on the allowed maximum distance (5 km (245 pairs) and 1 km (176 pairs)) between the GNSS station and the InSAR data point. Nevertheless, the InSAR data are overall not systematically biased when considering the median of trend differences. Based on the significance ratio (SR, i.e. the trend differences divided by the combined errors), I find that more than half of the trend differences are significant (i.e., when the absolute SR is greater than one). I find more frequent significant differences when the InSAR approach predicts lower VLM than the GNSS-based estimates. These analyses indicate that the InSAR data are still associated with a relatively low accuracy and should be treated with caution. Thus, to further increase the confidence in these results and to facilitate the assessment of the future sea level change impacts, it is vital to extend direct VLM measurements in time and space, in particular in highly vulnerable areas. <

5 Conclusions

In this dissertation I explore the contribution of vertical land motion to past, present, and future relative sea level changes, using a large database of observations. Throughout my investigations, I tackle a variety of questions, which lead to different methodological innovations and improved estimates of vertical land motion. In the following, I provide conclusions answering each of my research questions and give recommendations to overcome unsolved challenges.

5.1 Improving the determination of vertical land motion using coastal altimetry and tide gauge data

Previous studies showed, that using altimetry and tide gauge data to estimate coastal vertical land motion, can be a crucial complementary data source next to direct geodetic measurements by GNSS [Wöppelmann and Marcos, 2016, Pfeffer et al., 2017, Kleinherenbrink et al., 2018]. The accuracy and precision of these VLM estimates are influenced by the applied altimetry dataset, as well as by the selection of the altimetry data in the coastal zone. Previous advances in coastal retracking have further improved the quality of along-track data near the coast [Passaro et al., 2014]. However, because these dedicated coastal products have so far not been applied to derive vertical land motion from altimetry and tide gauge differences, I answer the following research question:

⇒ **How can we use coastal altimetry observations to improve vertical land motion estimates?**

Selecting dedicated coastal along-track altimetry data based on the agreement (in terms of correlation or RMS) with tide gauge observations improves vertical land motion estimates. Coherent zones of variability (i.e., the Zone of Influence) are identified based on different metrics, e.g., correlation or RMS between the along-track data and tide gauge observations. The selection of altimetry data, which are highly consistent with tide gauge data, leads to significant improvements in the VLM estimates in contrast to using a fixed radius. Validation against GNSS velocity estimates (at 58 stations) yields an $\text{RMS}_{\Delta\text{VLM}}$ of VLM_{SATG} and VLM_{GNSS} differences of 1.28 mm/year with a median formal uncertainty of VLM_{SATG} trends of 0.58 mm/year. This refined selection method improves trend accuracy by 15% and uncertainty by 35% compared to the 250 km-average selection.

⇒ **Which factors control the accuracy and uncertainty of vertical land motion estimates from coastal altimetry and tide gauges?**

The performance of vertical land motion estimates is mainly influenced by the consistency of altimetry data with tide gauge observations and the sampling density of the along-track data. I show that a trade-off must be made between the consistency (e.g., correlation) of altimetry data and tide gauges, and

the sampling density of the merged altimetry time series. Using only a very few altimetry time series, which are associated with the highest correlation with tide gauges (or even the single highest correlated time series), leads to reduced accuracy and increased uncertainty of the resulting VLM estimates. Therefore, it is crucial to combine multiple tracks of multimission altimetry datasets, to densify the averaged time series. **Systematic biases in the altimetry data deteriorate the accuracy of associated vertical land motion estimates.** These biases can be caused by various factors such as the applied corrections, altimeter drifts, or the accuracy and uncertainty of the origin and scale of the reference frame. My analyses highlight the presence of such biases in different along-track products, which can even lead to an overall decreased accuracy in vertical land motion estimates based on coastal altimetry products compared to gridded altimetry. Further minimization of such biases is important, because coastal altimetry generally has a higher correlation with tide gauges than gridded data, which leads to lower uncertainties in the associated VLM estimates. **With increasing time series length, the accuracy of VLM data becomes less sensitive to the spatial selection, due to increasing space scales of absolute sea level signals.** I show, that the relative improvement in the accuracy of VLM obtained by selecting very highly correlated altimetry data (in the vicinity of the coast) compared to selecting data in a larger radius, decreases sharply with increasing VLM time series length. One hypothesis is that this is caused by long term absolute sea level changes (associated with large spatial scales) that begin to emerge from the shorter term coastal variability as the time scale increases. This finding has implications for the use of gridded data versus along-track data at long time scales, as it is expected that the benefits of observing sea level trends very close to the coast decrease with increasing lengths of the observation period. However, it should be noted that these results are based on global averages, and different results may be obtained depending on local coastal characteristics and forcings, e.g., for coastal zones affected by long term changes in river runoff or wind stress. Thus, further investigations are required to draw more site-specific conclusions in this regard.

5.2 Probabilistic reconstruction of vertical land motion observations

A major challenge to understanding the role of VLM in relative sea level change is that the global coastlines are only inhomogeneously covered with GNSS stations or TGs from which VLM can be inferred indirectly. Therefore, extensive research has been conducted to interpolate linear trends of VLM along the coastlines [Pfeffer et al., 2017, Husson et al., 2018, Hawkins et al., 2019b, Hammond et al., 2021]. In chapter 3, I highlight that VLM is not strictly linear in every region due to a variety of processes. Changes in the rates or discontinuities in the time series represent significant complications for the determination of VLM. To tackle these issues, I developed an unsupervised trend change and discontinuity detector (DiscoTimeS) to answer the following research question:

⇒ **How can we detect discontinuities and trend changes in vertical land motion observations?**

Discontinuities and trend changes can be automatically detected by explicitly modeling these individual components in a single model. In section 3.2 I develop a new approach, which enables the simultaneous estimation of discontinuities, trend changes, seasonalities, and time series noise properties using Bayesian methods. Based on synthetic experiments, I show that trends can be estimated with an accuracy of 0.3-0.5 (0.5-1.5) mm/year for GNSS (SATTG) time series, which are affected by both trend changes and

discontinuities. Discontinuities of the order of 3–4 mm and 1 mm/year trend changes can be detected in synthetic GNSS time series (with white noise amplitudes of 3.2 mm and a duration of 20 years). The detection limit for discontinuities for much noisier SATTG-type time series (20 mm white noise amplitudes) is an order of magnitude larger, at about 4 cm. The lower limit at which discontinuities and trend changes can be detected, thus strongly depends on the noise properties of the time series. **Accounting for trend changes and discontinuities is essential to improve the consistency between VLM observations from different techniques, as well as between VLM observations and GIA models.** I show that processes like tectonic activity, non-linear surface mass deformation, and local effects induce trend changes in a significant number of GNSS and SATTG time series. When trend changes are explicitly modeled, the agreement of VLM between GNSS and SATTG data is improved by 0.36 mm/year, compared to when only strictly linear trends are estimated. The ability to detect change points in VLM time series also supports a more objective selection of VLM observations necessary to constrain GIA models. That means, information on the presence of possible time-variable trends in time series can be used to reject VLM data that is affected by such nonlinearities.

Low frequency noise impairs the unbiased detection of trend changes. Low frequency power law noise has a significant impact on the accuracy of the estimation of trend, as well as on the detection rates of change points. Power law noise can represent an ambiguity to the model, such that part of the noise can be erroneously parameterized by discontinuities and/or trend changes. This difficulty to separate low frequency noise from signals like discontinuities or trend changes increases the tendency of overfitting. Further innovations, e.g., the simultaneous change point detection in all three time series components (North, East, Up), or multiple neighboring stations (i.e., network-based approach) should be pursued to mitigate these issues (see recommendations in section 5.4).

⇒ **How can we align the large multi-technique networks of inhomogeneously distributed observations to reconstruct vertical land motion?**

⇒ **How can we model continuous space- and time-resolving vertical land motion?**

The VLM reconstruction is derived by estimating trends and common modes of variability to describe spatial and temporal variations. In section 3.3, I use a three-step procedure to reconstruct VLM: First, I remove discontinuities from the GNSS and SATTG data, using my unsupervised approach. Secondly, I apply a Bayesian Principal Component Analysis to fit a model to the data, that consists of a trend component and a set of independent modes of variability. In doing so, I account for the different noise properties of the different underlying VLM time series types. This model is applied to different regions in order to maximize the variability explained at the regional scale. In the third step, the obtained spatial parameters are then interpolated in space using Bayesian transdimensional regression, which dynamically adapts the smoothness of the interpolation based on properties of the underlying data distribution. **The VLM reconstruction provides more realistic trend and uncertainty estimates than previous approaches.** I show that the assumption of strictly 'linear VLM' is inadequate in some regions, in particular in those affected by tectonic activity or local processes. Hence, explicit modeling of time-varying effects more realistically reflects these non-linear motions. The Bayesian approach also provides realistic uncertainties that are influenced by the formal uncertainties of the observations, the variations in space and time, as well as by the density of the observations. Based on the significance ratio computed from the VLM derived in this study and GNSS data (in section 3.3.4), I show that the VLM reconstruction captures contemporary coastal VLM processes almost twice as accurately

as GIA models [Caron et al., 2018] or estimates used in current sea level projections [Kopp et al., 2014]. One remaining caveat is that the validation data (NGL-GNSS trends) is also incorporated in the VLM reconstruction itself. Thus, this comparison primarily confirms the validity of the spatiotemporal reconstruction approach developed in this work. In general, the results suggest that it is essential to incorporate currently available direct geodetic constraints, because they significantly improve the resolution of VLM in space and time.

5.3 Understanding the impacts of vertical land motion on relative sea level change

Extensive research has been conducted to assess the manifold imprints of VLM on relative sea level change (e.g., Peltier [2004], Wöppelmann and Marcos [2016], Pfeffer et al. [2017], Santamaría-Gómez et al. [2017]). The determination of the contribution of VLM on coastal sea level change is fundamental to understanding the historic sea level change over the last century and to providing projections for the upcoming centuries, together with estimates of their uncertainties. While more recent studies have utilized large networks of VLM data to interpolate VLM along the coastlines [Hawkins et al., 2019b, Hammond et al., 2021], the data have not yet been applied to systematically address the role of VLM in sea level reconstructions and projections. In my dissertation, I develop a VLM dataset, which provides time-resolving VLM estimates along the global coastlines. I use these estimates to answer the following research question:

⇒ **What is the contribution of vertical land motion (non-GIA and time-varying effects) on past, present, and future relative sea level change?**

Vertical land motion explains one-third of the contemporary coastal relative sea level change on a global scale. Relative sea level change is regionally strongly modulated by the influence on VLM. Regions such as the Gulf of Mexico, Venice, Australia, or the Nile Delta are subsiding at rates of 1-7 mm/year. Other regions, such as the west coast of South America and parts of Japan, are affected by tectonic uplift. I provide evidence of non-linear VLM, which is caused by different processes such as earthquakes, non-linear surface deformation due to mass loading changes, or local effects associated with human activities. Non-linear VLM has also affected historical tide gauges records, which, so far has not been taken into account in sea level reconstructions. Therefore, in order to extrapolate the VLM into the past or the future, it is necessary to separate the long-term linear motions from the present-day variability. **The VLM reconstruction is suitable for constraining long TG records needed to estimate sea level changes over the last century.** The comparison of a recent sea level reconstruction with VLM corrected tide gauges indicates high agreement in the ASL rates over the last century (1.39 mm/year and 1.38 mm/year). Hence, the linear trends provided by the VLM reconstruction are broadly representative of the long term VLM at the selected tide gauges and consistent with the indirectly derived VLM from the hybrid sea level reconstruction by Dangendorf et al. [2019]. However, although most of these long term tide gauges are located in regions of low variability in the observed VLM rates, other stations are potentially affected by non-linear effects that should be considered in future efforts to reconstruct global absolute sea level changes. **A significant proportion of VLM cannot be explained by the effects associated with GIA.** VLM based on a GIA model is highly consistent with the observed signal (as modeled in the VLM reconstruction) in regions like Western Europe or the Northeast US coast. Discrepancies are partially caused by differences in the amplitude and spatial extent of the modeled

and observed GIA signal itself, however, most of the differences stem from processes unrelated to GIA. These deviations are most pronounced in areas affected by tectonic activity (South America, Japan, Alaska) or in areas that are affected by regional subsidence (e.g., the Gulf of Mexico and Australia). Also, the observed VLM uncertainties are up to an order of magnitude higher than those estimated in a GIA model in such areas. Therefore, these observation-based VLM estimates are essential to complement GIA models to account for regional-scale contemporary VLM effects in SL reconstructions and projections.

The results reinforce previous research that **humans experience a higher relative sea level rise than the spatially averaged coastal sea level change**. Previous studies [Nicholls et al., 2021, Tay et al., 2022] put the focus on examining RSL change in areas of high population density. However, the VLM datasets employed were either not fully based on actual observations, or were only confined to selected coastal regions. Therefore, using the VLM reconstruction together with InSAR estimates in large coastal cities [Tay et al., 2022], I provide a more comprehensive, observation-based dataset on a global scale. I reconfirm recent findings [Nicholls et al., 2021], that subsidence increases the RSL change experienced in highly populated areas. The contemporary population-density weighted RSL change of 5.14 mm/year is more than twice as large as the coastal-length weighted RSL change (2.09 mm/year). These results suggest that **current estimates of damages and costs of future sea level change should be reevaluated in light of these novel VLM data**.

⇒ **What are the origins of vertical land motion uncertainties and their implications for regional sea level projections?**

VLM uncertainties are inflated by non-linear variability and low (TG and GNSS) station density. Explicit modeling of non-linear VLM processes shows that high VLM variability increases the uncertainty contribution of VLM to RSL change uncertainties and also explains differences between different independent VLM estimates from previous studies. Low station density, particularly in highly populated areas, often limits the ability to resolve highly localized changes, which additionally enhances uncertainties in the estimates. **Uncertainties in relative sea level change projections have been so far underestimated.** I show that VLM uncertainties explain 39% of the combined relative sea level change uncertainties in global relative sea level projections in 2150. Both, the rates and the uncertainties of VLM provided in this work more realistically describe contemporary VLM than the data currently used in sea level projections [Kopp et al., 2014]. These results demonstrate the importance of incorporating geodetic constraints and determining non-linear VLM to estimate future trajectories and confidence intervals of VLM. Given the high uncertainty associated with the frequency of occurrence of earthquakes or future subsidence due to changes in subsurface fluid rates, sea level projections could be further refined using probabilistic or processed-based VLM scenarios.

5.4 Recommendations

Understanding differences in coastal and open ocean sea level trends

The coastal sea level trend analyses have shown that data from satellite altimetry and tide gauges can be optimally combined using a subset of coastal altimetry data that are highly consistent (e.g., correlated) with the tide gauge observations. The investigations reveal coherent structures of coastal sea level variability, which are characterized by regionally varying along- and across-shore length scales, which appear to be partially influenced by the underlying bathymetric and coastal properties. By selecting highly correlated altimetry data,

the differences between altimetry and tide gauge data, and thus the trend uncertainties from the resulting SATTG VLM estimates, can be significantly reduced. In contrast to shorter time scales (i.e. < 10 years), at longer time scales, the agreement of altimetry and tide gauge trends becomes less dependent on the degree of correlation between altimetry and tide gauges, or the distance to the coast. Hence, these results do not support the assumption that altimetry-based sea level trends very close to the coast generally agree better with trends observed at tide gauges. However, it should be noted that this result can be influenced by a variety of factors that are unrelated to actual geophysical processes or conditions. These include, for example, the data quality and sampling frequency of the altimetry data very close to the coast, as well as potential mismatches between the applied GNSS-VLM correction and the actual VLM experienced at the TG. Another caveat of this analysis is that it reflects averaged results for a set of globally distributed tide gauges. The coastal sea level processes can, however, strongly differ across these coastal locations. Different factors, like bathymetric properties (e.g., the width of the continental shelf), local wind forcing, river runoff, or latitude-dependent ocean dynamics, etc., can cause differences in the spatial structures of coherency of sea level variability. How these factors affect coastal sea levels and how they control differences between coastal and open ocean changes is still under investigation. Hence, given these differences between local characteristics of sea level variability, my results can not be unequivocally extrapolated to every coastal site, as they refer to global averages. In this context, it is important to note that recent work [Cazenave et al., 2022] has detected significant differences between coastal sea level trends within the last 5 km and further offshore from the coast (10-15 km). However, it is still not fully understood, whether these effects are caused by the data processing (i.e., applied corrections) or by actual physical processes, e.g., by river runoff. Hence, further research is required to better understand the drivers and the spatial scales of coherent sea level variability in the coastal zone. Thus, a systematic analysis of the correlation length scales and their dependencies on local factors, like river runoff, or shelf width is recommended.

Overcoming systematic satellite altimetry trend biases

Several studies show that some of the applied altimetry datasets (e.g., the XTRACK data from SL_cci) are affected by significant trend biases [Oelsmann et al., 2021, Dettmering et al., 2021, Peng et al., 2022, Oelsmann and Passaro, 2022]. In section 2.5, I discuss the various factors which can contribute to such systematic biases, but do not identify their sources. Depending on the number and distribution of validation stations (i.e., VLM-corrected tide gauges), these biases can be as large as ± 1 mm/year globally with even higher values at the regional scale [Oelsmann and Passaro, 2022, Peng et al., 2022]. These biases are particularly problematic because they offset improvements made in terms of the accuracy of altimetry observations in the coastal zone and limit the usability of satellite altimetry for sea level trend or VLM analysis. The identification of the sources of these biases is thus fundamental to improving the accuracy of regional trends provided by the different datasets. These issues motivate a systematic comparison of applied altimetry corrections, adjustments, the reference frames, orbits, and intermission calibration approaches in different currently available datasets, e.g., CMEMS (formerly called AVISO), OpenADB, or SL_cci. This analysis also requires the definition of a common validation platform, which could be the station network of GLOSS, for instance.

Advancing geodetic time series analysis

Undetected discontinuities in VLM time series significantly deteriorate the accuracy of VLM estimates. In my thesis, I show that, next to discontinuities, also trend changes should be identified, to more realistically describe height variations in time. Hence, I developed an automatic approach (DiscoTimeS) to detect these time series features and analyzed more than 10,000 VLM time series from different geodetic techniques. However, some remaining limitations of DiscoTimeS motivate further improvements. First of all, any non-linearity is parameterized by segmented trend changes, which could be improved by using exponential/logarithmic functions, as commonly done to model post-seismic deformation [e.g., see Montillet and Bos [2020]]. Another innovation could feature the simultaneous detection of change points in all three components (North, East, Up), as some discontinuities might be more obvious in other components than in the usually much noisier vertical component. In 'The Detection of Offsets in GPS Experiment (DOGEx)' experiment [Gazeaux et al., 2013], the best automated solutions simultaneously estimated discontinuities either in all three components (i.e., the 'find outliers and discontinuities in time series (FODITS)' solution), or in the horizontal components (Jet Propulsion Laboratory (JPL) solution). This implementation could decrease under/overfitting of the number of change points and improve the lower discontinuity detection limit. Another major limitation of the Bayesian change point estimation is that sampling from the Markov chains is computationally very expensive and much slower than most of the discontinuity detectors [Gazeaux et al., 2013]. Therefore, to reduce computation time, the priors of the Bayesian model could be initialized by the detected discontinuities from currently best-performing automated solutions, like the one of Tehranchi et al. [2020], or from time series meta-information. Finally, a comprehensive database containing meta-information on reported and automated or manually detected discontinuities for available GNSS and tide gauge time series, would be a major contribution to the field. Services such as SONEL offer solutions from different providers for GNSS data near tide gauges and also recently published information on manually selected discontinuities [Métivier et al., 2014, Gravelle et al., 2023]. However, more comprehensive GNSS datasets (e.g., as hosted by NGL) do not yet feature such comprehensive information on manually or automatically detected discontinuities, as they only provide station metadata.

Influence of (non-linear) vertical land motion on sea level reconstructions

The determination of the evolution of GMSL change over the last century depends heavily on appropriate vertical land motion estimates at tide gauges. In chapter 4 I discussed several different approaches to define VLM in sea level reconstructions. VLM has been either indirectly estimated from the residual trends at TGs [Kopp et al., 2014, Dangendorf et al., 2019], from GIA models [Church et al., 2013] or actual geodetic observations [Frederikse et al., 2020]. There are still open questions left about how direct geodetic constraints or indirect estimates from the sea level reconstruction itself should be ideally applied to reconstruct GMSL. A major challenge is, that it is sometimes not clear to what extent trends from direct geodetic constraints can be extrapolated back in time. While the assumption of linear VLM is indeed true for most of the time series, particularly for processes like GIA, the extrapolation of trends at stations affected by local non-linear processes is much more delicate. In my analyses, I discuss some of the sources and implications of non-linear VLM and suggest that some historical TG records might also be affected by non-linear VLM. Therefore, I recommend re-examining sea level reconstructions by accounting for non-linear VLM. As an example, Fig. 5.1 shows RSL observations from long tide gauge observations. The stations are selected to highlight evidence of non-linear

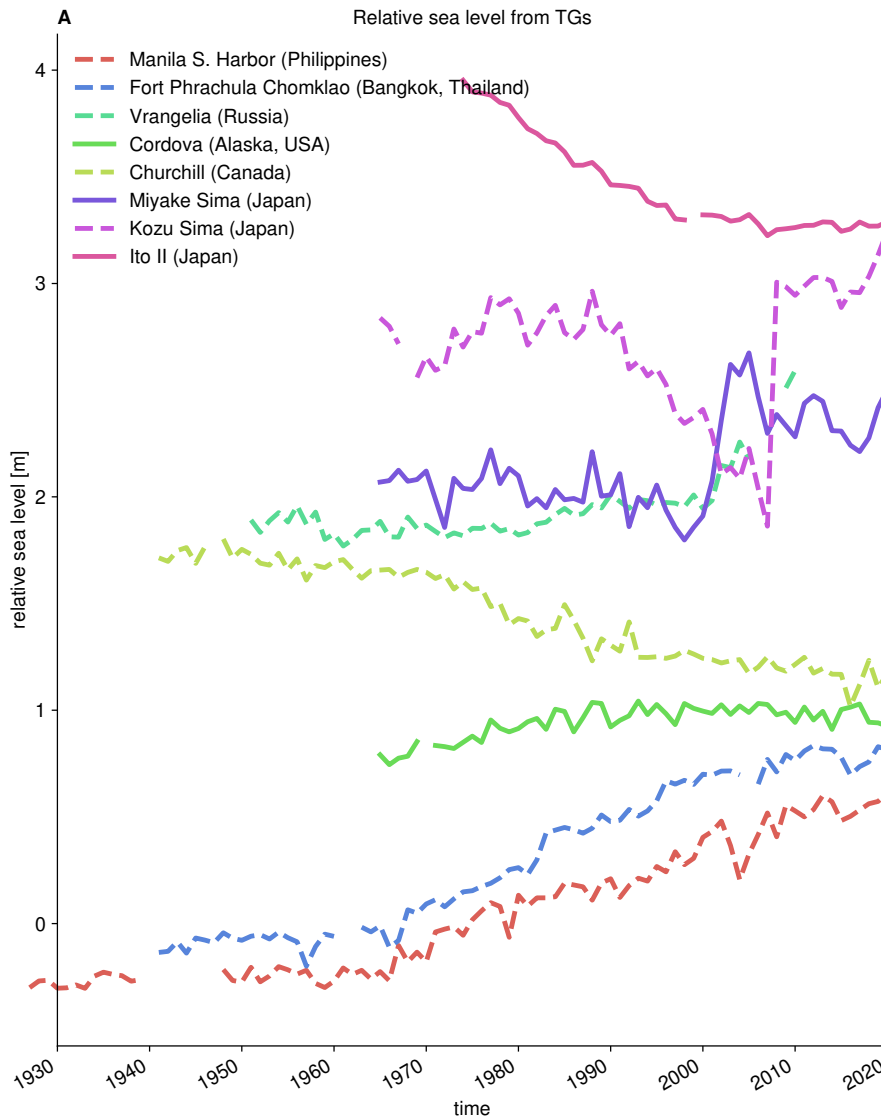


Figure 5.1 RSL observations from annually averaged PSMSL TG data with an arbitrary offset applied.

VLM in the residual time series. For example, at the TGs in Manila and Bangkok, RSL rise started to accelerate around 1960. Since the beginning of the records, RSL has risen by about 75 cm, which is likely caused by local human activities, and is four times as large as the GMSL change over the same period. Other tide gauges also indicate an effect of non-linear VLM prior to the altimetry era, either caused by earthquakes or volcanic activity (e.g., at Kozu Sima and Miyake Sima).

To improve sea level reconstructions, such non-linear variations could be explicitly described, e.g., by using stochastic processes that adequately fit the time series spectral properties of the residuals (i.e., unexplained variance at the tide gauges after accounting for density changes, GRD, and ocean-mass driven processes). This would, however, increase the degree of freedom in the reconstructions, which might require further constraints of VLM. Hence, another important implementation would be the inclusion of GNSS observations as additional constraints in the sea level reconstruction. Spatiotemporally coherent VLM dynamics could be described as a set of independent modes (or fingerprints) similarly as done in chapter 4. These modes could be extrapolated back in time using the TG residuals as constraints when no GNSS data are available. This approach would merge indirect estimates from the sea level reconstruction with direct geodetic constraints,

and could resolve some of the differences when only one of these data sources of VLM is used. Dangendorf et al. [2021] also discussed this issue, arguing that the indirect VLM estimates of the reconstruction should be used, since they show a higher correlation with residual trends from tide gauges (derived from over the last century) than when using direct VLM observations [Frederikse et al., 2020]. Hence, how these long term VLM estimates from SL reconstructions can be aligned with contemporary (GNSS-based) estimates in light of potentially non-linear VLM requires further investigations.

Spatial resolution and distribution of vertical land motion and relative sea level observations

A central limitation for sea level studies of the past, present, and future, is the lack of continuous VLM and relative sea level observations in time and space. Tide gauges and GNSS stations are highly inhomogeneously distributed, with a much higher abundance in, e.g., Europe, North America, and Japan. The scarcity of long term tide gauges observations, in particular in South America and Africa, is a central problem for our understanding of the historic changes and drivers of sea level at the global, basin, and regional scale (e.g., see discussions in Piecuch [2022] or Frederikse et al. [2021]). Likewise, missing VLM observations from GNSS stations hinder the assessment of subsidence and uplift rates continuously along the coastlines and are mostly confined to the last few decades. In my thesis, I show that interpolating data from the existing network of tide gauges and GNSS stations usually resolves VLM at scales larger than 100 km, mainly due to the sparsity of stations. However, many previous studies underlined the importance to resolve VLM at the local scale (i.e., a resolution from m to kms), because VLM rates can strongly vary in space, in particular in urbanized areas affected by human activities [Raucoules et al., 2013, Wöppelmann et al., 2013, Jones et al., 2016]. Hence, observations from the three techniques used in this work, satellite altimetry, tide gauges, and GNSS data, could be further complemented and densified by VLM estimates from InSAR.

InSAR could theoretically fill gaps in VLM observations along the coastlines worldwide at a resolution in the order of 10-100 m [Buzzanga et al., 2020]. However, due to atmospheric and surface scattering effects, this technique is less precise than GNSS, with uncertainties at the mm/year scale [Buzzanga et al., 2020, Hamling et al., 2022, Tay et al., 2022]. Another disadvantage is that the data processing is highly computationally demanding and that the determination of the rates in a reference frame requires geodetic ties (GNSS stations). While most investigations applied InSAR in local case studies [Wöppelmann et al., 2013, Raucoules et al., 2013, Poitevin et al., 2019, Buzzanga et al., 2020], more recent studies applied InSAR at scales of several 100 km. Tay et al. [2022], for instance, determined VLM rates at all large coastal cities with a population greater than 5 Million people, accounting for 22% of the world's population. This is particularly vital for many large Southeast Asian cities, which are poorly equipped with tide gauges or GNSS stations. As another example, Hamling et al. [2022] determined InSAR-based VLM for the complete land surface of New Zealand. These estimates are crucial, as they enable local sea level projections at an unprecedented resolution [Tay et al., 2022, Naish et al., 2022]. It is expected that InSAR will be increasingly applied to bridge the observational gaps on ever larger scales. As an example, it is planned to generate InSAR-based VLM data for the entire US coast [Sweet et al., 2022]. Therefore, InSAR has the potential to become a central component of the relative sea level observing system, together with altimetry, tide gauges, and GNSS data.

Vertical land motion projections

This work corroborated that VLM cannot be considered as a linear background process at every coastal region, due to a variety of anthropogenic and natural factors. Despite these findings, to extrapolate VLM back in time and into the future, I still utilized the linear rates derived from the Bayesian reconstruction, assuming that current rates most likely represent long term changes, as commonly done [Kopp et al., 2014, Wöppelmann and Marcos, 2016, Fox-Kemper et al., 2021]. However, given the variability detected over the last decades, it is not clear that VLM will continue to be linear everywhere. Thus, regionally, projecting linear VLM rates into the future may not adequately capture the individual trajectories of future relative sea level change. While the uncertainties derived in my work can be very informative about the upper and lower bounds of future sea levels, they may not be very useful in cases where VLM changes rapidly and differs from the observed present-day variability. Some processes, such as earthquakes, which can cause nearly instantaneous vertical displacements on the order of m, or changes in human-induced subsurface fluid withdrawal rates, make it difficult or even impossible to generate meaningful future predictions [Geller, 1997, Kanamori, 2003]. It is therefore possible that current sea level projections [Fox-Kemper et al., 2021], including those provided in this work, still underestimate the uncertainty introduced by unpredictable VLM processes.

I propose here several ideas for designing more realistic projections. (1) The approach of statistically simulating future trajectories of VLM changes could be further improved. As described in section 4.4, I approximate projected VLM uncertainties based on an ensemble of Gaussian Random Walks, which are modeled according to the parameters estimated to determine the present-day variability. This is illustrated, for example, in the introduction in Fig. 1.2, where I show an ensemble of randomized first-order autoregressive processes that have the same time series properties as the variations of the VLM observed at the Bangkok tide gauge. However, using autoregressive processes to model these trajectories is a very simplistic approach as it assumes smooth and continuous VLM variations. This could be further developed by incorporating discontinuous effects, e.g., by simulating VLM responses to earthquakes in regions of high tectonic activity (see, e.g., Newton et al. [2021]). These natural events could be statistically modeled based on their observed probability distributions of magnitude and frequency. It should be noted, however, that it is heavily debated if long term (10-30 years) earthquake predictions are possible, given the high uncertainty in the location, the timing, and the magnitude of the events [Geller, 1997, Kanamori, 2003]. (2) Another recommendation is to develop process-based VLM scenarios for locations where human behavior is expected to play a dominant role for VLM. Previous work has emphasized the importance of focusing on highly urbanized coastal regions, as these locations are often affected by human-induced subsidence and thus higher-than-average sea level rise [Nicholls et al., 2021]. In these areas, future human behavior will directly affect future exposure to sea level rise. Thus, recent work has introduced different scenarios of subsidence control for Chinese coastlines [Fang et al., 2022]. These VLM scenarios are not only important for the understanding of future sea level rise, but can also motivate human actions to mitigate reaching the upper limits of currently projected relative sea level rise. These process-based scenarios could be coupled with the observed fingerprints of GIA, tectonics, and other regional effects that are not influenced by human activities.

Abbreviations

Abbreviation	Description	Page Number
ALES	Adaptive Leading Edge Subwaveform	12, 18, 25, 28, 30, 31
AR(1)	first-order autoregressive process	37
AR6	6th Assessment Report of the Intergovernmental Panel on Climate Change	59, 60, 71, 72
ASAR	Advanced Synthetic Aperture Radar	7
ASL	absolute sea level	63, 73–75, 84
AVISO	Archiving, Validation, and Interpretation of Satellite Oceanographic data	12, 18, 19, 25, 30, 31, 86
BPCA	Bayesian Principal Component Analysis	35, 56–59, 65, 66
CMEMS	Copernicus Marine Service	55, 74, 75, 86
CMIP	Coupled Model Intercomparison Project	2
CMIP6	Coupled Model Intercomparison Project Phase 6	70
CMR	contemporary mass redistribution	6, 31, 46, 47, 50–53, 65
COASTALT	ESA development of COASTal ALTimetry	12
DAC	dynamic atmospheric correction	9, 18
DGFI-TUM	Deutsches Geodätisches Forschungsinstitut der Technischen Universität München	18
DIC	deviance information criterion	120
DiscoTimeS	Discontinuities in Time Series	34, 39–41, 45–47, 49–54, 87
DOGEx	The Detection of Offsets in GPS Experiment	87
DORIS	Doppler Orbitography and Radiopositioning Integrated by Satellite	8
Envisat	Environmental Satellite	31
EOF	Empirical Orthogonal Functions	15, 35, 56–58
FODITS	find outliers and discontinuities in time series	87
FP	False Positive	44, 45, 54
GALILEO	European Global Satellite Navigation System	10

Abbreviation	Description	Page Number
GESLA	Global Extreme Sea Level Analysis	8, 13, 17–20, 23, 46
GIA	glacial isostatic adjustment	5–8, 11, 14, 15, 35, 39, 46, 52–54, 59, 60, 63–69, 71–74, 83–85, 87, 90
GLONASS	GLObal'naya Navigaionnaya Sputnikovaya Sistema	10
GLOSS	Global Sea Level Observing System	10, 86
GMSL	Global Mean Sea Level	1, 2, 4, 9, 11, 74, 87, 88
GNSS	Global Navigation Satellite System	7, 8, 10–15, 17, 18, 22–24, 26–31, 33–36, 38–56, 59, 60, 63, 73, 74, 79, 81–84, 87–89
GPS	Global Positioning System	10, 14, 22
GRACE	Gravity Recovery And Climate Experiment	6, 7, 31, 63
GRD	earth gravity, earth rotation and solid-earth deformation	3, 5, 6, 74, 88
GSFC	Goddard Space Flight Center	12, 25
InSAR	Interferometric Synthetic Aperture Radar	7, 73–75, 79, 85, 89
IPCC	Intergovernmental Panel on Climate Change	60, 63, 71, 72
JPL	Jet Propulsion Laboratory	87
LGM	Last Glacial Maximum	5
MCMC	Markov chain Monte Carlo	36, 38, 57
MIDAS	Median Interannual Difference Adjusted for Skewness	34, 37, 39, 45–47, 52–55, 60
MLE	Maximum Likelihood Estimation	23, 34
MMXO	multi-mission crossover analysis	18, 25, 31
NGL	Nevada Geodetic Laboratory of the University of Nevada	10, 30, 39, 45, 55, 84, 87
NUTS	No-U-Turn sampler	38
OpenADB	Open Altimeter Database	18, 86
PCA	Principal Component Analysis	56
PISTACH	Prototype Innovant de Système de Traitement pour l'Altimétrie Côtière et l'Hydrologie	12
PL	power law	41–43, 54
POD	Precise Orbit Determination	8

Abbreviation	Description	Page Number
PSIS-LOO	Pareto-smoothed importance sampling leave-one-out cross-validation	119
PSMSL	Permanent Service for Mean Sea Level	2, 5, 8, 12, 17–19, 23–25, 46, 55
RADS	Radar Altimeter Database	12, 24
RMS	Root Mean Square	20, 25, 26, 81
RSL	relative sea level	5, 63, 64, 73–77, 79, 85, 87, 88
SAT	satellite altimetry	10, 13, 25, 28, 29, 41, 51, 54
SATTG	satellite altimetry minus tide gauge	10, 11, 14
SL	sea level	20, 28, 29, 51, 59, 60, 63, 65–72, 77–79, 85
SLA	sea level anomaly	9, 12, 19, 20, 23, 25, 28, 30
SLC	sea level change	1
SLR	Satellite Laser Ranging	8
SONEL	Systeme d’Observation du Niveau des Eaux Littorales	22, 87
SSH	sea surface height	8, 9
TG	tide gauge	10, 12, 13, 18–26, 28, 29, 31, 41, 46, 48, 49, 51, 53, 54, 87, 88
TOPEX	TOPOgraphy EXperiment	12, 25
TP	True Positive	44, 45, 54
UHSLC	University of Hawaii Sea Level Center	8
VLM	vertical land motion	1, 2, 5, 16–18, 20–24, 28, 30, 31, 33–36, 38, 39, 41, 42, 45, 46, 48, 50–53, 55–57, 59, 60, 63–75, 77–90
WAIC	widely applicable information criterion	120
WM16	Wöppelmann and Marcos [2016]	12, 24, 25, 31
WN	white noise	41, 42
ZOI	Zone of Influence	20, 22, 23, 25–30

Bibliography

Abdalla S., Abdeh Kolahchi A., Ablain M., Adusumilli S., Aich Bhowmick S., Alou-Font E., Amarouche L., Andersen O. B., Antich H., Aouf L., Arbic B., Armitage T., Arnault S., Artana C., Aulicino G., Ayoub N., Badulin S., Baker S., Banks C., Bao L., Barbetta S., Barceló-Llull B., Barlier F., Basu S., Bauer-Gottwein P., Becker M., Beckley B., Bellefond N., Belonenko T., Benkiran M., Benkouider T., Bennartz R., Benveniste J., Bercher N., Berge-Nguyen M., Bettencourt J., Blarel F., Blazquez A., Blumstein D., Bonnefond P., Borde F., Bouffard J., Boy F., Boy J.-P., Brachet C., Brasseur P., Braun A., Brocca L., Brockley D., Brodeau L., Brown S., Bruinsma S., Bulczak A., Buzzard S., Cahill M., Calmant S., Calzas M., Camici S., Cancet M., Capdeville H., Carabajal C. C., Carrere L., Cazenave A., Chassignet E. P., Chauhan P., Cherchali S., Chereskin T., Cheymol C., Ciani D., Cipollini P., Cirillo F., Cosme E., Coss S., Cotroneo Y., Cotton D., Couhert A., Coutin-Faye S., Crétaux J.-F., Cyr F., d'Ovidio F., Darrozes J., David C., Dayoub N., De Staerke D., Deng X., Desai S., Desjonqueres J.-D., Dettmering D., Di Bella A., Díaz-Barroso L., Dibarboure G., Dieng H. B., Dinardo S., Dobslaw H., Dodet G., Doglioli A., Domeneghetti A., Donahue D., Dong S., Donlon C., Dorandeu J., Drezen C., Drinkwater M., Du Penhoat Y., Dushaw B., Egido A., Erofeeva S., Escudier P., Esselborn S., Exertier P., Fablet R., Falco C., Farrell S. L., Faugere Y., Femenias P., Fenoglio L., Fernandes J., Fernández J. G., Ferrage P., Ferrari R., Fichen L., Filippucci P., Flampouris S., Fleury S., Fornari M., Forsberg R., Frappart F., laure Frery M., Garcia P., Garcia-Mondejar A., Gaudelli J., Gaultier L., Getirana A., Gibert F., Gil A., Gilbert L., Gille S., Giulicchi L., Gómez-Enri J., Gómez-Navarro L., Gommenginger C., Gourdeau L., Griffin D., Groh A., Guerin A., Guerrero R., Guinle T., Gupta P., Gutknecht B. D., Hamon M., Han G., Hauser D., Helm V., Hendricks S., Hernandez F., Hogg A., Horwath M., Idžanović M., Janssen P., Jeansou E., Jia Y., Jia Y., Jiang L., Johannessen J. A., Kamachi M., Karimova S., Kelly K., Kim S. Y., King R., Kittel C. M., Klein P., Klos A., Knudsen P., Koenig R., Kostianoy A., Kouraev A., Kumar R., Labroue S., Lago L. S., Lambin J., Lasson L., Laurain O., Laxenaire R., Lázaro C., Le Gac S., Le Sommer J., Le Traon P.-Y., Lebedev S., Léger F., Legresy B., Lemoine F., Lenain L., Leuliette E., Levy M., Lillibridge J., Liu J., Llovel W., Lyard F., Macintosh C., Makhoul Varona E., Manfredi C., Marin F., Mason E., Massari C., Mavrocordatos C., Maximenko N., McMillan M., Medina T., Melet A., Meloni M., Mertikas S., Metref S., Meyssignac B., Minster J.-F., Moreau T., Moreira D., Morel Y., Morrow R., Moyard J., Mulet S., Naeije M., Nerem R. S., Ngodock H., Nielsen K., Øie Nilsen J. E., Niño F., Nogueira Loddo C., Noûs C., Obligis E., Otosaka I., Otten M., Oztunali Ozbahceci B., P. Raj R., Paiva R., Paniagua G., Paolo F., Paris A., Pascual A., Passaro M., Paul S., Pavelsky T., Pearson C., Penduff T., Peng F., Perosanz F., Picot N., Piras F., Poggiali V., Étienne Poirier, Ponce de León S., Prants S., Prigent C., Provost C., Pujol M.-I., Qiu B., Quilfen Y., Rami A., Raney R. K., Raynal M., Remy E., Rémy F., Restano M., Richardson A., Richardson D., Ricker R., Ricko M., Rinne E., Rose S. K., Rosmorduc V., Rudenko S., Ruiz S., Ryan B. J., Salaün C., Sanchez-Roman A., Sandberg Sørensen L., Sandwell D., Saraceno M., Scagliola M., Schaeffer P., Scharffenberg M. G., Scharroo R., Schiller A., Schneider R., Schwatke C., Scozzari A., Ser-giacomi E., Seyler F., Shah R., Sharma R., Shaw A., Shepherd A., Shriver J., Shum C., Simons W., Simonsen S. B., Slater T., Smith W., Soares S., Sokolovskiy M., Soudarin L., Spatar C., Speich S., Srinivasan M., Srokosz M., Stanev E., Staneva J., Steunou

- N., Stroeve J., Su B., Sulistioadi Y. B., Swain D., Sylvestre-baron A., Taburet N., Tailleux R., Takayama K., Tapley B., Tarpanelli A., Tavernier G., Testut L., Thakur P. K., Thibaut P., Thompson L., Tintoré J., Tison C., Tourain C., Tournadre J., Townsend B., Tran N., Trilles S., Tsamados M., Tseng K.-H., Ubelmann C., Uebbing B., Vergara O., Verron J., Vieira T., Vignudelli S., Vinogradova Shiffer N., Visser P., Vivier F., Volkov D., von Schuckmann K., Vuglinskii V., Vuilleumier P., Walter B., Wang J., Wang C., Watson C., Wilkin J., Willis J., Wilson H., Woodworth P., Yang K., Yao F., Zaharia R., Zakharova E., Zaron E. D., Zhang Y., Zhao Z., Zinchenko V., and Zlotnicki V. (2021). *Altimetry for the future: Building on 25 years of progress*. *Advances in Space Research*, 68(2):319–363, ISSN: 0273-1177, DOI: 10.1016/j.asr.2021.01.022, <https://www.sciencedirect.com/science/article/pii/S0273117721000594>. 25 Years of Progress in Radar Altimetry.
- Ablain M., Cazenave A., Valladeau G., and Guinehut S. (2009). *A new assessment of the error budget of global mean sea level rate estimated by satellite altimetry over 1993–2008*. *Ocean Science*, 5(2):193–201, DOI: 10.5194/os-5-193-2009, <https://os.copernicus.org/articles/5/193/2009/>.
- Ablain M., Meyssignac B., Zawadzki L., Jugier R., Ribes A., Spada G., Benveniste J., Cazenave A., and Picot N. (2019). *Uncertainty in satellite estimates of global mean sea-level changes, trend and acceleration*. *Earth System Science Data*, 11(3):1189–1202, DOI: 10.5194/essd-11-1189-2019, <https://essd.copernicus.org/articles/11/1189/2019/>.
- Agnew D. C. (1992). *The time-domain behavior of power-law noises*. *Geophysical Research Letters*, 19(4):333–336, DOI: 10.1029/91GL02832, <https://agupubs.onlinelibrary.wiley.com/doi/abs/10.1029/91GL02832>.
- Altamimi Z., Rebischung P., Métivier L., and Collilieux X. (2016). *ITRF2014: A new release of the International Terrestrial Reference Frame modeling nonlinear station motions*. *Journal of Geophysical Research: Solid Earth*, ISSN: 21699356, DOI: 10.1002/2016JB013098.
- Andersen O. B. and Scharroo R. (2011). *Range and Geophysical Corrections in Coastal Regions: And Implications for Mean Sea Surface Determination*, pages 103–145. Springer Berlin Heidelberg, Berlin, Heidelberg, ISBN: 978-3-642-12796-0, DOI: 10.1007/978-3-642-12796-0_5, https://doi.org/10.1007/978-3-642-12796-0_5.
- Ballu V., Gravelle M., Wöppelmann G., de Viron O., Rebischung P., Becker M., and Sakic P. (2019). *Vertical land motion in the Southwest and Central Pacific from available GNSS solutions and implications for relative sea levels*. *Geophysical Journal International*, 218(3):1537–1551, ISSN: 0956-540X, DOI: 10.1093/gji/ggz247, <https://doi.org/10.1093/gji/ggz247>.
- Blewitt G., Kreemer C., Hammond W. C., and Gazeaux J. (2016). *MIDAS robust trend estimator for accurate GPS station velocities without step detection*. *Journal of Geophysical Research: Solid Earth*, 121(3):2054–2068, DOI: 10.1002/2015JB012552.
- Bloßfeld M., Angermann D., and Seitz M. (2019). *DGFI-TUM Analysis and Scale Investigations of the Latest Terrestrial Reference Frame Realizations*. In Freymueller J. T. and Sánchez L. (Eds.), *International Symposium on Advancing Geodesy in a Changing World*, pages 3–9, Cham. Springer International Publishing, ISBN: 978-3-030-12915-6.

- Bodin T., Salmon M., Kennett B. L. N., and Sambridge M. (2012). *Probabilistic surface reconstruction from multiple data sets: An example for the Australian Moho*. Journal of Geophysical Research: Solid Earth, 117(B10), DOI: 10.1029/2012JB009547, <https://agupubs.onlinelibrary.wiley.com/doi/abs/10.1029/2012JB009547>.
- Bodin T. and Sambridge M. (2009). *Seismic tomography with the reversible jump algorithm*. Geophysical Journal International, 178(3):1411–1436, ISSN: 0956-540X, DOI: 10.1111/j.1365-246X.2009.04226.x, <https://doi.org/10.1111/j.1365-246X.2009.04226.x>.
- Bos M. and Fernandes R. (2019). *Hector user manual, available online at http://segal.ubi.pt/hector/manual_1.7.2.pdf, last accessed on November 02, 2020*.
- Bos M. S. and Fernandes R. M. S. (2016). *Applied automatic offset detection using HECTOR within EPOS-IP*. Ponta Delgada (Azores, Portugal). 18th General Assembly of WEGENER.
- Bos M. S., Fernandes R. M. S., Williams S. D. P., and Bastos L. (2013a). *Fast error analysis of continuous GNSS observations with missing data*. Journal of Geodesy, 87(4):351–360, DOI: 10.1007/s00190-012-0605-0, <http://nora.nerc.ac.uk/id/eprint/501636/>.
- Bos M. S., Montillet J.-P., Williams S. D. P., and Fernandes R. M. S. (2019). *Introduction to Geodetic Time Series Analysis*. Springer Geophysics, page 29–52, ISBN: 9783030217181, ISSN: 2364-9127, DOI: 10.1007/978-3-030-21718-1_2, http://dx.doi.org/10.1007/978-3-030-21718-1_2.
- Bos M. S., Williams S. D. P., Araújo I. B., and Bastos L. (2013b). *The effect of temporal correlated noise on the sea level rate and acceleration uncertainty*. Geophysical Journal International, 196(3):1423–1430, ISSN: 0956-540X, DOI: 10.1093/gji/ggt481, <https://doi.org/10.1093/gji/ggt481>.
- Bosch W., Dettmering D., and Schwatke C. (2014). *Multi-Mission Cross-Calibration of Satellite Altimeters: Constructing a Long-Term Data Record for Global and Regional Sea Level Change Studies*. Remote Sensing, 6(3):2255–2281, DOI: 10.3390/rs6032255.
- Bosch W. and Savcenko R. (2007). *Satellite altimetry: Multi-mission cross calibration*. In *International Association of Geodesy Symposia*. ISBN: 9783540493495, ISSN: 09399585, DOI: 10.1007/978-3-540-49350-1_8.
- Bouin M. N. and Wöppelmann G. (2010). *Land motion estimates from GPS at tide gauges: a geophysical evaluation*. Geophysical Journal International, 180(1):193–209, ISSN: 0956-540X, DOI: 10.1111/j.1365-246X.2009.04411.x, <https://doi.org/10.1111/j.1365-246X.2009.04411.x>.
- Brooks B. A., Merrifield M. A., Foster J., Werner C. L., Gomez F., Bevis M., and Gill S. (2007). *Space geodetic determination of spatial variability in relative sea level change, Los Angeles basin*. Geophys. Res. Lett., 34(1):L01611, ISSN: 0094-8276, DOI: 10.1029/2006GL028171, <http://doi.wiley.com/10.1029/2006GL028171>.
- Brooks S., Gelman A., Jones G., and Meng X.-L. (2011). *Handbook of Markov Chain Monte Carlo*. Chapman Hall/CRC press, ISBN: 978-1-4200-7941-8.

- Buzzanga B., Bekaert D. P. S., Hamlington B. D., and Sangha S. S. (2020). *Toward Sustained Monitoring of Subsidence at the Coast Using InSAR and GPS: An Application in Hampton Roads, Virginia*. *Geophysical Research Letters*, 47(18):e2020GL090013, DOI: 10.1029/2020GL090013, <https://agupubs.onlinelibrary.wiley.com/doi/abs/10.1029/2020GL090013>.
- Calafat F. M., Wahl T., Lindsten F., Williams J., and Frajka-Williams E. (2018). *Coherent modulation of the sea-level annual cycle in the United States by Atlantic Rossby waves*. *Nature Communications*, 9(1), ISSN: 20411723, DOI: 10.1038/s41467-018-04898-y.
- Caron L., Ivins E. R., Larour E., Adhikari S., Nilsson J., and Blewitt G. (2018). *GIA Model Statistics for GRACE Hydrology, Cryosphere, and Ocean Science*. *Geophysical Research Letters*, 45(5):2203–2212, DOI: 10.1002/2017GL076644.
- Carrère L. and Lyard F. (2003). *Modeling the barotropic response of the global ocean to atmospheric wind and pressure forcing - comparisons with observations*. *Geophysical Research Letters*, 30(6), DOI: 10.1029/2002GL016473, <https://agupubs.onlinelibrary.wiley.com/doi/abs/10.1029/2002GL016473>.
- Carson M., Köhl A., Stammer D., Slangen A., Katsman C., Wal R., Church J., and White N. (2016). *Coastal Sea Level Changes, Observed and Projected during the 20th and 21st Century*. *Climatic Change*, 134:269–281, DOI: 10.1007/s10584-015-1520-1.
- Cazenave A., Dominh K., Ponchaut F., Soudarin L., Cretaux J. F., and Le Provost C. (1999). *Sea level changes from Topex-Poseidon altimetry and tide gauges, and vertical crustal motions from DORIS*. *Geophysical Research Letters*, ISSN: 00948276, DOI: 10.1029/1999GL900472.
- Cazenave A., Gouzenes Y., Birol F., Leger F., Passaro M., Calafat F. M., Shaw A., Nino F., Legeais J. F., Oelsmann J., Restano M., and Benveniste J. (2022). *Sea level along the world's coastlines can be measured by a network of virtual altimetry stations*. *Communications Earth & Environment*, 3(1):117, ISSN: 2662-4435, DOI: 10.1038/s43247-022-00448-z, <https://doi.org/10.1038/s43247-022-00448-z>.
- Cazenave A., Palanisamy H., and Ablain M. (2018). *Contemporary sea level changes from satellite altimetry: What have we learned? What are the new challenges?* *Advances in Space Research*, 62(7):1639 – 1653, ISSN: 0273-1177, DOI: 10.1016/j.asr.2018.07.017, <http://www.sciencedirect.com/science/article/pii/S0273117718305799>.
- Church J., Clark P., Cazenave A., Gregory J., Jevrejeva S., Levermann A., Merrifield M., Milne G., Nerem R., Nunn P., Payne A., Pfeffer W., Stammer D., and Unnikrishnan A. (2013). *2013: Sea level change*. *Climate Change 2013: The Physical Science Basis. Contribution of Working Group I to the Fifth Assessment Report of the Intergovernmental Panel on Climate Change*, pages 1137–1216, ISBN: ISBN 978-1-107-66182-0, ISSN: 0074-6142, DOI: 10.1017/CB09781107415315.026.
- Church J. and White N. (2011). *Sea-Level Rise from the Late 19th to the Early 21st Century*. *Surveys in Geophysics*, 32:585–602, DOI: 10.1007/s10712-011-9119-1.
- Cipollini P., Calafat F. M., Jevrejeva S., Melet A., and Prandi P. (2017). *Monitoring Sea Level in the Coastal Zone with Satellite Altimetry and Tide Gauges*. ISSN: 15730956, DOI: 10.1007/s10712-016-9392-0.

- Collilieux X. and Woppelmann G. (2009). *Global sea-level rise and its relation to the terrestrial reference frame*. Journal of Geodesy, 85:9–22, DOI: 10.1007/s00190-010-0412-4.
- Couhert A., Cerri L., Legeais J.-F., Michaël A., Zelensky N., Haines B., Lemoine F., Bertiger W., Desai S., and Otten M. (2015). *Towards the 1 mm/y stability of the radial orbit error at regional scales*. Advances in Space Research, 55, DOI: 10.1016/j.asr.2014.06.041.
- Dangendorf S., Frederikse T., Chafik L., Klinck J. M., Ezer T., and Hamlington B. D. (2021). *Data-driven reconstruction reveals large-scale ocean circulation control on coastal sea level*. Nat. Clim. Chang., 11(6):514–520, ISSN: 1758-678X, 1758-6798, DOI: 10.1038/s41558-021-01046-1, <http://www.nature.com/articles/s41558-021-01046-1>.
- Dangendorf S., Hay C., Calafat F. M., Marcos M., Piecuch C. G., Berk K., and Jensen J. (2019). *Persistent acceleration in global sea-level rise since the 1960s*. Nat. Clim. Chang., 9(9):705–710, ISSN: 1758-678X, 1758-6798, DOI: 10.1038/s41558-019-0531-8, <http://www.nature.com/articles/s41558-019-0531-8>.
- Dangendorf S., Marcos M., Wöppelmann G., Conrad C. P., Frederikse T., and Riva R. (2017). *Reassessment of 20th century global mean sea level rise*. Proceedings of the National Academy of Sciences, ISSN: 0027-8424, DOI: 10.1073/pnas.1616007114, <https://www.pnas.org/content/early/2017/05/16/1616007114>.
- Dettmering D., Müller F. L., Oelmann J., Passaro M., Schwatke C., Restano M., Benveniste J., and Seitz F. (2021). *North SEAL: a new dataset of sea level changes in the North Sea from satellite altimetry*. Earth System Science Data, 13(8):3733–3753, DOI: 10.5194/essd-13-3733-2021, <https://essd.copernicus.org/articles/13/3733/2021/>.
- Dettmering D. and Schwatke C. (2019). *Multi-Mission Cross-Calibration of Satellite Altimeters: Systematic Differences Between Sentinel-3A and Jason-3*. International Association of Geodesy Symposia, DOI: 10.1007/1345_2019_58.
- Ducet N., Le Traon P. Y., and Reverdin G. (2000). *Global high-resolution mapping of ocean circulation from TOPEX/Poseidon and ERS-1 and -2*. Journal of Geophysical Research: Oceans, 105(C8):19477–19498, DOI: 10.1029/2000JC900063, <https://agupubs.onlinelibrary.wiley.com/doi/abs/10.1029/2000JC900063>.
- Emery K. O. and Aubrey D. G. (1991a). *Causes of Relative Sea-Level Change*. In *Sea Levels, Land Levels, and Tide Gauges*, pages 23–52. Springer New York, New York, NY, ISBN: 978-1-4613-9103-6 978-1-4613-9101-2, DOI: 10.1007/978-1-4613-9101-2_2, http://link.springer.com/10.1007/978-1-4613-9101-2_2.
- Emery K. O. and Aubrey D. G. (1991b). *Sea Levels, Land Levels, and Tide Gauges*. Springer New York, New York, NY, ISBN: 978-1-4613-9103-6 978-1-4613-9101-2, DOI: 10.1007/978-1-4613-9101-2, <http://link.springer.com/10.1007/978-1-4613-9101-2>.
- Engelhart S. E., Horton B. P., Douglas B. C., Peltier W. R., and Tornqvist T. E. (2009). *Spatial variability of late Holocene and 20th century sea-level rise along the Atlantic coast of the United States*. Geol-

- ogy, 37(12):1115–1118, ISSN: 0091-7613, 1943-2682, DOI: 10.1130/G30360A.1, <https://pubs.geoscienceworld.org/geology/article/37/12/1115-1118/103884>.
- Engelhart S. E., Vacchi M., Horton B. P., Nelson A. R., and Kopp R. E. (2015). *A sea-level database for the Pacific coast of central North America*. *Quaternary Science Reviews*, 113:78–92, ISSN: 0277-3791, DOI: 10.1016/j.quascirev.2014.12.001, <https://www.sciencedirect.com/science/article/pii/S0277379114004843>.
- Ericson J., Vorosmarty C., Dingman S., Ward L., and Meybeck M. (2006). *Effective sea-level rise and deltas: Causes of change and human dimension implications*. *Global and Planetary Change*, 50(1-2):63–82, ISSN: 09218181, DOI: 10.1016/j.gloplacha.2005.07.004, <https://linkinghub.elsevier.com/retrieve/pii/S0921818105001827>.
- Eyring V., Bony S., Meehl G. A., Senior C. A., Stevens B., Stouffer R. J., and Taylor K. E. (2016). *Overview of the Coupled Model Intercomparison Project Phase 6 (CMIP6) experimental design and organization*. *Geosci. Model Dev.*, 9(5):1937–1958, ISSN: 1991-9603, DOI: 10.5194/gmd-9-1937-2016, <https://gmd.copernicus.org/articles/9/1937/2016/>.
- Fang J., Nicholls R. J., Brown S., Lincke D., Hinkel J., Vafeidis A. T., Du S., Zhao Q., Liu M., and Shi P. (2022). *Benefits of subsidence control for coastal flooding in China*. *Nature Communications*, 13(1):6946, DOI: 10.1038/s41467-022-34525-w.
- Fenoglio L., Schöne T., Illigner J., Becker M., Manurung P., and Khafid (2012). *Sea Level Change and Vertical Motion from Satellite Altimetry, Tide Gauges and GPS in the Indonesian Region*. *Marine Geodesy*, 35, DOI: 10.1080/01490419.2012.718682.
- Fernandes M. J., Lázaro C., Ablain M., and Pires N. (2015). *Remote Sensing of Environment Improved wet path delays for all ESA and reference altimetric missions*. *Remote Sensing of Environment*, 169:50–74, ISSN: 0034-4257, DOI: 10.1016/j.rse.2015.07.023, <http://dx.doi.org/10.1016/j.rse.2015.07.023>.
- Fox-Kemper B., Hewitt H. T., Xiao C., Aðalgeirsdóttir G., Drijfhout S. S., Edwards T. L., Golledge N. R., Hemer M., Kopp R. E., Krinner G., Mix A., Notz D., Nowicki S., Nurhati I. S., Ruiz L., Sallée J.-B., Slangen A. B. A., and Yu Y. (2021). *Ocean, Cryosphere and Sea Level Change*. *Climate Change 2021: The Physical Science Basis. Contribution of Working Group I to the Sixth Assessment Report of the Intergovernmental Panel on Climate Change*, [MassonDelmotte, V., P. Zhai, A. Pirani, S. L. Connors, C. Péan, S. Berger, N. Caud, Y. Chen, L. Goldfarb, M. I. Gomis, M. Huang, K. Leitzell, E. Lonnoy, J. B. R. Matthews, T. K. Maycock, T. Waterfield, O. Yelekçi, R. Yu and B. Zhou (eds.)], Cambridge University Press. In Press., DOI: 10.1017/9781009157896.011.
- Frederikse T., Adhikari S., Daley T. J., Dangendorf S., Gehrels R., Landerer F., Marcos M., Newton T. L., Rush G., Slangen A. B. A., and Wöppelmann G. (2021). *Constraining 20th-Century Sea-Level Rise in the South Atlantic Ocean*. *Journal of Geophysical Research: Oceans*, 126(3):e2020JC016970, DOI: 10.1029/2020JC016970, <https://agupubs.onlinelibrary.wiley.com/doi/abs/10.1029/2020JC016970>. e2020JC016970 2020JC016970.

- Frederikse T., Landerer F., Caron L., Adhikari S., Parkes D., Humphrey V. W., Dangendorf S., Hogarth P., Zanna L., Cheng L., and Wu Y.-H. (2020). *The causes of sea-level rise since 1900*. *Nature*, 584(7821):393–397, ISSN: 0028-0836, 1476-4687, DOI: 10.1038/s41586-020-2591-3, <https://www.nature.com/articles/s41586-020-2591-3>.
- Frederikse T., Landerer F. W., and Caron L. (2019). *The imprints of contemporary mass redistribution on local sea level and vertical land motion observations*. *Solid Earth*, 10(6):1971–1987, DOI: 10.5194/se-10-1971-2019, <https://se.copernicus.org/articles/10/1971/2019/>.
- Gallagher C., Lund R., and Robbins M. (2013). *Changepoint Detection in Climate Time Series with Long-Term Trends*. *Journal of Climate*, 26:4994–5006, DOI: 10.1175/JCLI-D-12-00704.1.
- Garner G. G., Hermans T., Kopp R. E., Slangen A. B. A., Edwards T. L., Levermann A., Nowicki S., Palmer M. D., Smith C., Fox-Kemper B., Hewitt H. T., Xiao C., Aðalgeirsdóttir G., Drijfhout S. S., Golledge N. R., Hemer M., Krinner G., Mix A., Notz D., Nowicki S., Nurhati I. S., Ruiz L., Sallee J.-B., Yu Y., Hua L., Palmer T., and Pearso B. (2021a). *IPCC AR6 Sea-Level Rise Projections. Version 20210809. PO.DAAC, CA, USA. Dataset accessed 2022-02-15 at <https://podaac.jpl.nasa.gov/announcements/2021-08-09-Sea-level-projections-from-the-IPCC-6th-Assessment-Report>*.
- Garner G. G., Kopp R. E., Hermans T., Slangen A. B. A., Koubbe G., Turilli M., Jha S., Edwards T. L., Levermann A., Nowicki S., Palmer M. D., and Smith C. (2021b). *Framework for Assessing Changes To Sea-level (FACTS)*. Geoscientific Model Development., in prep.
- Gazeaux J., Williams S., King M., Bos M., Dach R., Deo M., Moore A. W., Ostini L., Petrie E., Roggero M., Teferle F. N., Olivares G., and Webb F. H. (2013). *Detecting offsets in GPS time series: First results from the detection of offsets in GPS experiment*. *Journal of Geophysical Research: Solid Earth*, 118(5):2397–2407, DOI: 10.1002/jgrb.50152, <https://agupubs.onlinelibrary.wiley.com/doi/abs/10.1002/jgrb.50152>.
- Geller R. J. (1997). *Earthquake prediction: a critical review*. *Geophysical Journal International*, 131(3):425–450, ISSN: 0956-540X, DOI: 10.1111/j.1365-246X.1997.tb06588.x, <https://doi.org/10.1111/j.1365-246X.1997.tb06588.x>.
- Gelman A., Hwang J., and Vehtari A. (2013). *Understanding predictive information criteria for Bayesian models*. *Statistics and Computing*, 24, DOI: 10.1007/s11222-013-9416-2.
- Geweke J. (1992). *Evaluating the Accuracy of Sampling-Based Approaches to the Calculation of Posterior Moments*. In *BAYESIAN STATISTICS*, pages 169–193. University Press, DOI: 10.21034/sr.148.
- Gómez J. F., Kwoil E., Walker I. J., and Shirzaei M. (2021). *Vertical Land Motion as a Driver of Coastline Changes on a Deltaic System in the Colombian Caribbean*. *Geosciences*, 11(7):300, ISSN: 2076-3263, DOI: 10.3390/geosciences11070300, <https://www.mdpi.com/2076-3263/11/7/300>.
- Goudarzi M., Cocard M., Santerre R., and Woldai T. (2013). *GPS interactive time series analysis software*. *GPS solutions*, 17(4):595–603, ISSN: 1080-5370, DOI: 10.1007/s10291-012-0296-2.

- Gravelle M., Wöppelmann G., Gobron K., Altamimi Z., Guichard M., Herring T., and Rebeschung P. (2023). *The ULR-repro3 GPS data reanalysis and its estimates of vertical land motion at tide gauges for sea level science*. Earth System Science Data, 15(1):497–509, DOI: 10.5194/essd-15-497-2023, <https://essd.copernicus.org/articles/15/497/2023/>.
- Gregory J. M., Griffies S. M., Hughes C. W., Lowe J. A., Church J. A., Fukimori I., Gomez N., and Tamisiea M. E. (2019). *Concepts and Terminology for Sea Level: Mean, Variability and Change, Both Local and Global*, volume 0123456789. ISBN: 0123456789, DOI: 10.1007/s10712-019-09525-z.
- Gruszczynski M., Klos A., and Bogusz J. (2018). *A Filtering of Incomplete GNSS Position Time Series with Probabilistic Principal Component Analysis*. Pure and Applied Geophysics, 175(5):1841–1867, ISSN: 0033-4553, 1420-9136, DOI: 10.1007/s00024-018-1856-3, <http://link.springer.com/10.1007/s00024-018-1856-3>.
- Gulev S., Thorne P., Ahn J., Dentener F., Domingues C., Gerland S., Gong D., Kaufman D., Nnamchi H., Quaas J., Rivera J., Sathyendranath S., Smith S., Trewin B., von Schuckmann K., and Vose R. (2021). *Changing State of the Climate System*. In Masson-Delmotte V., Zhai P., Pirani A., Connors S., Péan C., Berger S., Caud N., Chen Y., Goldfarb L., Gomis M., Huang M., Leitzell K., Lonnoy E., Matthews J., Maycock T., Waterfield T., Yelekçi O., Yu R., and Zhou B. (Eds.), *Climate Change 2021: The Physical Science Basis. Contribution of Working Group I to the Sixth Assessment Report of the Intergovernmental Panel on Climate Change*, chapter 2. Cambridge University Press, Cambridge, UK and New York, NY, USA, DOI: 10.1017/9781009157896.004.
- Gunawan E., Sagiya T., Ito T., Kimata F., Tabei T., Ohta Y., Meilano I., Abidin H. Z., Agustan, Nurdin I., and Sugiyanto D. (2014). *A comprehensive model of postseismic deformation of the 2004 Sumatra–Andaman earthquake deduced from GPS observations in northern Sumatra*. Journal of Asian Earth Sciences, 88:218–229, ISSN: 13679120, DOI: 10.1016/j.jseaes.2014.03.016, <https://linkinghub.elsevier.com/retrieve/pii/S1367912014001485>.
- Hamling I. J., Wright T. J., Hreinsdóttir S., and Wallace L. M. (2022). *A Snapshot of New Zealand’s Dynamic Deformation Field From Envisat InSAR and GNSS Observations Between 2003 and 2011*. Geophysical Research Letters, 49(2):e2021GL096465, DOI: 10.1029/2021GL096465, <https://agupubs.onlinelibrary.wiley.com/doi/abs/10.1029/2021GL096465>. e2021GL096465 2021GL096465.
- Hammond W. C., Blewitt G., Kreemer C., and Nerem R. S. (2021). *GPS Imaging of Global Vertical Land Motion for Studies of Sea Level Rise*. Journal of Geophysical Research: Solid Earth, 126(7):e2021JB022355, DOI: 10.1029/2021JB022355, <https://agupubs.onlinelibrary.wiley.com/doi/abs/10.1029/2021JB022355>. e2021JB022355 2021JB022355.
- Hart-Davis M. G., Piccioni G., Dettmering D., Schwatke C., Passaro M., and Seitz F. (2021). *EOT20: a global ocean tide model from multi-mission satellite altimetry*. Earth System Science Data, 13(8):3869–3884, DOI: 10.5194/essd-13-3869-2021, <https://essd.copernicus.org/articles/13/3869/2021/>.
- Hawkins R., Bodin T., Sambridge M., Choblet G., and Husson L. (2019a). *Trans-Dimensional Surface Reconstruction With Different Classes of Parameterization*. Geochemistry, Geophysics, Geosystems, 20(1):505–529, DOI: 10.1029/2018GC008022, <https://agupubs.onlinelibrary.wiley.com/doi/abs/10.1029/2018GC008022>.

- Hawkins R., Husson L., Choblet G., Bodin T., and Pfeffer J. (2019b). *Virtual Tide Gauges for Predicting Relative Sea Level Rise*. Journal of Geophysical Research: Solid Earth, 124(12):13367–13391, DOI: 10.1029/2019JB017943, <https://agupubs.onlinelibrary.wiley.com/doi/abs/10.1029/2019JB017943>.
- Hay C. C., Morrow E., Kopp R. E., and Mitrovica J. X. (2015). *Probabilistic reanalysis of twentieth-century sea-level rise*. Nature, ISSN: 0028-0836, DOI: 10.1038/nature14093.
- He X., Montillet J.-P., Fernandes R., Bos M., Yu K., Hua X., and Jiang W. (2017). *Review of current GPS methodologies for producing accurate time series and their error sources*. Journal of Geodynamics, 106:12–29, ISSN: 0264-3707, DOI: 10.1016/j.jog.2017.01.004, <https://www.sciencedirect.com/science/article/pii/S0264370716301168>.
- Heiskanen W. A. and Moritz H. (1984). *Physical Geodesy*. Springer Vienna, ISBN: 978-3-211-27467-5, DOI: 10.1007/b139113.
- Hinkel J. and Klein R. J. (2009). *Integrating knowledge to assess coastal vulnerability to sea-level rise: The development of the DIVA tool*. Global Environmental Change, 19(3):384–395, ISSN: 0959-3780, DOI: 10.1016/j.gloenvcha.2009.03.002, <https://www.sciencedirect.com/science/article/pii/S0959378009000247>.
- Hinkel J., Lincke D., Vafeidis A., Perrette M., Nicholls R., Tol R., Marzeion B., Fettweis X., Ionescu C., and Levermann A. (2014). *Coastal flood damage and adaptation cost under 21st century sea-level rise*. Proceedings of the National Academy of Sciences of the United States of America, 111:3292–7, DOI: 10.1073/pnas.1222469111.
- Hoffman M. D. and Gelman A. (2014). *The No-U-Turn Sampler: Adaptively Setting Path Lengths in Hamiltonian Monte Carlo*. Journal of Machine Learning Research, 15(47):1593–1623, DOI: 10.48550/arXiv.1111.4246, <http://jmlr.org/papers/v15/hoffman14a.html>.
- Holgate S. J., Matthews A., Woodworth P. L., Rickards L. J., Tamisiea M. E., Bradshaw E., Foden P. R., Gordon K. M., Jevrejeva S., and Pugh J. (2013). *New Data Systems and Products at the Permanent Service for Mean Sea Level*. Journal of Coastal Research, pages 493–504, DOI: 10.2112/JCOASTRES-D-12-00175.1, <https://doi.org/10.2112/JCOASTRES-D-12-00175.1>.
- Houlié N. and Stern T. (2017). *Vertical tectonics at an active continental margin*. Earth and Planetary Science Letters, 457:292–301, ISSN: 0012821X, DOI: 10.1016/j.epsl.2016.10.018, <https://linkinghub.elsevier.com/retrieve/pii/S0012821X16305751>.
- Hughes C., Fukumori I., Griffies S. M., and Huthnance J. M. (2019). *Sea Level and the Role of Coastal Trapped Waves in Mediating the Influence of the Open Ocean on the Coast*. Surveys in Geophysics, 40(6):1467–1492, ISBN: 0123456789, ISSN: 1573-0956, DOI: 10.1007/s10712-019-09535-x, <https://doi.org/10.1007/s10712-019-09535-x>.
- Hughes C. and Meredith M. (2006). *Coherent sea-level fluctuations along the global continental slope*. Philosophical transactions. Series A, Mathematical, physical, and engineering sciences, 364:885–901, DOI: 10.1098/rsta.2006.1744.

- Husson L., Bodin T., Spada G., Choblet G., and Kreemer C. (2018). *Bayesian surface reconstruction of geodetic uplift rates: Mapping the global fingerprint of Glacial Isostatic Adjustment*. *Journal of Geodynamics*, 122:25–40, DOI: 10.1016/j.jog.2018.10.002, <https://hal-univ-lyon1.archives-ouvertes.fr/hal-02327157>.
- Idžanović M., Gerlach C., Breili K., and Andersen O. (2019). *An Attempt to Observe Vertical Land Motion along the Norwegian Coast by CryoSat-2 and Tide Gauges*. *Remote Sensing*, 11:744, DOI: 10.3390/rs11070744.
- Imakiire T. and Koarai M. (2012). *Wide-area land subsidence caused by “the 2011 Off the Pacific Coast of Tohoku Earthquake”*. *Soils and Foundations*, 52(5):842–855, ISSN: 0038-0806, DOI: 10.1016/j.sandf.2012.11.007, <https://www.sciencedirect.com/science/article/pii/S0038080612000984>. Special Issue on Geotechnical Aspects of the 2011 off the Pacific Coast of Tohoku Earthquake.
- Jackson L. P. and Jevrejeva S. (2016). *A probabilistic approach to 21st century regional sea-level projections using RCP and High-end scenarios*. *Global and Planetary Change*, 146:179–189, ISSN: 0921-8181, DOI: 10.1016/j.gloplacha.2016.10.006, <https://www.sciencedirect.com/science/article/pii/S0921818116300686>.
- Jamero M. L., Esteban M., and Onuki M. (2016). *Potential in-Situ Adaptation Strategies for Climate-Related Sea-Level Rise: Insights from a Small Island in The Philippines Experiencing Earthquake-Induced Land Subsidence*. *J-Sustain*, 4(2):44–53, ISSN: 21874506, DOI: 10.24910/jsustain/4.2/4453, http://www.j-sustain.com/files/pub/file/2016/Vol%204%20No%202/J-Sustain_Vol4_No2_44-53%20DM-015-10153.pdf.
- Jamero M. L., Onuki M., Esteban M., Billones-Sensano X. K., Tan N., Nellas A., Takagi H., Thao N. D., and Valenzuela V. P. (2017). *Small-island communities in the Philippines prefer local measures to relocation in response to sea-level rise*. *Nature Clim Change*, 7(8):581–586, ISSN: 1758-678X, 1758-6798, DOI: 10.1038/nclimate3344, <http://www.nature.com/articles/nclimate3344>.
- James T. S., Gowan E. J., Wada I., and Wang K. (2009). *Viscosity of the asthenosphere from glacial isostatic adjustment and subduction dynamics at the northern Cascadia subduction zone, British Columbia, Canada*. *J. Geophys. Res.*, 114(B4):B04405, ISSN: 0148-0227, DOI: 10.1029/2008JB006077, <http://doi.wiley.com/10.1029/2008JB006077>.
- Jarvis A., Guevara E., Reuter H., and Nelson A. (2008). *Hole-filled SRTM for the globe : version 4 : data grid*. Published by CGIAR-CSI on 19 August 2008.
- Jevrejeva S., Moore J. C., Grinsted A., Matthews A. P., and Spada G. (2014). *Trends and acceleration in global and regional sea levels since 1807*. *Global and Planetary Change*, ISSN: 09218181, DOI: 10.1016/j.gloplacha.2013.12.004.
- Jones C. E., An K., Blom R. G., Kent J. D., Ivins E. R., and Bekaert D. (2016). *Anthropogenic and geologic influences on subsidence in the vicinity of New Orleans, Louisiana*. *Journal of Geophysical Research: Solid Earth*, 121(5):3867–3887, DOI: 10.1002/2015JB012636, <https://agupubs.onlinelibrary.wiley.com/doi/abs/10.1002/2015JB012636>.

- Jäggi A. and Arnold D. (2017). *Precise Orbit Determination*, pages 35–80. ISBN: 978-3-319-49940-6, DOI: 10.1007/978-3-319-49941-3_2.
- Kanamori H. (2003). 72 - *Earthquake Prediction: An Overview*. In Lee W. H., Kanamori H., Jennings P. C., and Kisslinger C. (Eds.), *International Handbook of Earthquake and Engineering Seismology, Part B*, volume 81 of *International Geophysics*, pages 1205–1216. Academic Press, ISSN: 0074-6142, DOI: 10.1016/S0074-6142(03)80186-9, <https://www.sciencedirect.com/science/article/pii/S0074614203801869>.
- Karegar M. A., Dixon T. H., and Engelhart S. E. (2016). *Subsidence along the Atlantic Coast of North America: Insights from GPS and late Holocene relative sea level data*. *Geophysical Research Letters*, 43(7):3126–3133, DOI: 10.1002/2016GL068015, <https://agupubs.onlinelibrary.wiley.com/doi/abs/10.1002/2016GL068015>.
- Karegar M. A., Dixon T. H., Malservisi R., Kusche J., and Engelhart S. E. (2017). *Nuisance Flooding and Relative Sea-Level Rise: the Importance of Present-Day Land Motion*. *Scientific Reports*, 7(1):11197, ISSN: 2045-2322, DOI: 10.1038/s41598-017-11544-y, <https://doi.org/10.1038/s41598-017-11544-y>.
- Keogh M. E. and Törnqvist T. E. (2019). *Measuring rates of present-day relative sea-level rise in low-elevation coastal zones: a critical evaluation*. *Ocean Science*, 15(1):61–73, DOI: 10.5194/os-15-61-2019, <https://os.copernicus.org/articles/15/61/2019/>.
- King M. A., Altamimi Z., Boehm J., Bos M., Dach R., Elosegui P., Fund F., Hernandez-Pajares M., Lavallee D., Cervera P. J. M., Penna N., Riva R. E. M., Steigenberger P., van Dam T., Vittuari L., Williams S., and Willis P. (2010). *Improved constraints on models of glacial isostatic adjustment: a review of the contribution of ground-based geodetic observations*. *Surveys in Geophysics*, 31(5):465–507, DOI: 10.1007/s10712-010-9100-4, <http://nora.nerc.ac.uk/id/eprint/13774/>.
- King M. A., Keshin M., Whitehouse P. L., Thomas I. D., Milne G., and Riva R. E. M. (2012). *Regional biases in absolute sea-level estimates from tide gauge data due to residual unmodeled vertical land movement*. *Geophysical Research Letters*, 39(14), DOI: 10.1029/2012GL052348, <https://agupubs.onlinelibrary.wiley.com/doi/abs/10.1029/2012GL052348>.
- Kleinherenbrink M., Riva R., and Frederikse T. (2018). *A comparison of methods to estimate vertical land motion trends from GNSS and altimetry at tide gauge stations*. *Ocean Science*, 14(2):187–204, DOI: 10.5194/os-14-187-2018, <https://os.copernicus.org/articles/14/187/2018/>.
- Klos A., Kusche J., Fenoglio-Marc L., Bos M. S., and Bogusz J. (2019). *Introducing a Vertical Land Motion Model for Improving Estimates of Sea Level Rates Derived from Tide Gauge Records Affected by Earthquakes*. *GPS Solut.*, 23(4):1–12, ISSN: 1080-5370, DOI: 10.1007/s10291-019-0896-1, <https://doi.org/10.1007/s10291-019-0896-1>.
- Kolker A. S., Allison M. A., and Hameed S. (2011). *An evaluation of subsidence rates and sea-level variability in the northern Gulf of Mexico*. *Geophysical Research Letters*, 38(21), DOI: 10.1029/2011GL049458, <https://agupubs.onlinelibrary.wiley.com/doi/abs/10.1029/2011GL049458>.

- Kopp R. E., Garner G. G., Hermans T. H. J., Jha S., Kumar P., Slangen A. B. A., Turilli M., Edwards T. L., Gregory J. M., Koubbe G., Levermann A., Merzky A., Nowicki S., Palmer M. D., and Smith C. (2023). *The Framework for Assessing Changes To Sea-level (FACTS) v1.0-rc: A platform for characterizing parametric and structural uncertainty in future global, relative, and extreme sea-level change*. EGU-sphere, 2023:1–34, DOI: 10.5194/egusphere-2023-14, <https://egusphere.copernicus.org/preprints/egusphere-2023-14/>.
- Kopp R. E., Horton R. M., Little C. M., Mitrovica J. X., Oppenheimer M., Rasmussen D. J., Strauss B. H., and Tebaldi C. (2014). *Probabilistic 21st and 22nd century sea-level projections at a global network of tide-gauge sites*. Earth's Future, 2(8):383–406, ISSN: 2328-4277, 2328-4277, DOI: 10.1002/2014EF000239, <https://onlinelibrary.wiley.com/doi/10.1002/2014EF000239>.
- Kopp R. E., Kemp A. C., Bittermann K., Horton B. P., Donnelly J. P., Gehrels W. R., Hay C. C., Mitrovica J. X., Morrow E. D., and Rahmstorf S. (2016). *Temperature-driven global sea-level variability in the Common Era*. Proc. Natl. Acad. Sci. U.S.A., 113(11), ISSN: 0027-8424, 1091-6490, DOI: 10.1073/pnas.1517056113, <https://pnas.org/doi/full/10.1073/pnas.1517056113>.
- Kowalczyk K. and Rapinski J. (2018). *Verification of a GNSS Time Series Discontinuity Detection Approach in Support of the Estimation of Vertical Crustal Movements*. ISPRS International Journal of Geo-Information, 7:149, DOI: 10.3390/ijgi7040149.
- Kreemer C., Blewitt G., and Davis P. M. (2020). *Geodetic evidence for a buoyant mantle plume beneath the Eifel volcanic area, NW Europe*. Geophysical Journal International, 222(2):1316–1332, ISSN: 0956-540X, 1365-246X, DOI: 10.1093/gji/ggaa227, <https://academic.oup.com/gji/article/222/2/1316/5835686>.
- Kuo C. Y., Shum C. K., Braun A., and Mitrovica J. X. (2004). *Vertical crustal motion determined by satellite altimetry and tide gauge data in Fennoscandia*. Geophysical Research Letters, 31(1), DOI: 10.1029/2003GL019106, <https://agupubs.onlinelibrary.wiley.com/doi/abs/10.1029/2003GL019106>.
- Kurapov A., Erofeeva S., and Myers E. (2016). *Coastal sea level variability in the US West Coast Ocean Forecast System (WCOFS)*. Ocean Dynamics, 67, DOI: 10.1007/s10236-016-1013-4.
- Langbein J. (2012). *Estimating rate uncertainty with maximum likelihood: differences between power-law and flicker – random-walk models*. pages 775–783, DOI: 10.1007/s00190-012-0556-5.
- Letetrel C., Karpytchev M., Bouin M.-N., Marcos M., Santamaría-Gómez A., and Wöppelmann G. (2015). *Estimation of vertical land movement rates along the coasts of the Gulf of Mexico over the past decades*. Continental Shelf Research, 111:42–51, ISSN: 0278-4343, DOI: 10.1016/j.csr.2015.10.018, <https://www.sciencedirect.com/science/article/pii/S0278434315300935>.
- Liu Y., Li J., Fasullo J., and Galloway D. L. (2020). *Land subsidence contributions to relative sea level rise at tide gauge Galveston Pier 21, Texas*. Sci Rep, 10(1):17905, ISSN: 2045-2322, DOI: 10.1038/s41598-020-74696-4, <https://www.nature.com/articles/s41598-020-74696-4>.

- Marcos M., Wöppelmann G., Matthews A., Ponte R. M., Birol F., Arduin F., Coco G., Santamaría-Gómez A., Ballu V., Testut L., Chambers D., and Stopa J. E. (2019). *Coastal Sea Level and Related Fields from Existing Observing Systems*. *Surveys in Geophysics*, 40(6):1293–1317, ISSN: 1573–0956, DOI: 10.1007/s10712-019-09513-3, <https://doi.org/10.1007/s10712-019-09513-3>.
- Mark E. T. and Jerry X. M. (2011). *The Moving Boundaries of Sea Level Change: Understanding the Origins of Geographic Variability*. *Oceanography*, 24(2):144 – 157, DOI: 10.5670/oceanog.2011.25, <https://doi.org/10.5670/oceanog.2011.25>.
- Mazzotti S., Jones C., and Thomson R. E. (2008). *Relative and absolute sea level rise in western Canada and northwestern United States from a combined tide gauge-GPS analysis*. *Journal of Geophysical Research: Oceans*, 113(C11), DOI: 10.1029/2008JC004835, <https://agupubs.onlinelibrary.wiley.com/doi/abs/10.1029/2008JC004835>.
- Merkens J.-L., Lincke D., Hinkel J., Brown S., and Vafeidis A. T. (2018). *Regionalisation of population growth projections in coastal exposure analysis*. *Climatic Change*, 151(3):413–426, DOI: 10.1007/s10584-018-2334-8, https://ideas.repec.org/a/spr/climat/v151y2018i3d10.1007_s10584-018-2334-8.html.
- Montillet J.-P. and Bos M. S. (Eds.) (2020). *Geodetic Time Series Analysis in Earth Sciences*. Springer Geophysics. Springer International Publishing, Cham, ISBN: 978-3-030-21717-4 978-3-030-21718-1, DOI: 10.1007/978-3-030-21718-1, <http://link.springer.com/10.1007/978-3-030-21718-1>.
- Montillet J.-P., Williams S. D. P., Koulali A., and McClusky S. C. (2015). *Estimation of offsets in GPS time-series and application to the detection of earthquake deformation in the far-field*. *Geophysical Journal International*, 200(2):1207–1221, ISSN: 0956–540X, DOI: 10.1093/gji/ggu473, <https://doi.org/10.1093/gji/ggu473>.
- Moritz H. (2000). *Geodetic Reference System 1980*. *Journal of Geodesy*, 74(1):128–133, ISSN: 1432–1394, DOI: 10.1007/s001900050278.
- Métivier L., Collilieux X., Lercier D., Altamimi Z., and Beauducel F. (2014). *Global coseismic deformations, GNSS time series analysis, and earthquake scaling laws*. *Journal of Geophysical Research: Solid Earth*, 119(12):9095–9109, DOI: 10.1002/2014JB011280, <https://agupubs.onlinelibrary.wiley.com/doi/abs/10.1002/2014JB011280>.
- Naish T., Levy R. H., Hamling I. J., Garner G., Hreinsdóttir S., Kopp R. E., Golledge N. R., Bell R., Paulik R., Lawrence J., and et al. (2022). *The significance of vertical land movements at convergent plate boundaries in probabilistic sea-level projections for AR6 scenarios: The New Zealand case*. *Earth and Space Science Open Archive*, page 33, DOI: 10.1002/essoar.10511878.1, <https://doi.org/10.1002/essoar.10511878.1>.
- Nerem R. S. and Mitchum G. T. (2003). *Estimates of vertical crustal motion derived from differences of TOPEX/POSEIDON and tide gauge sea level measurements*. *Geophysical Research Letters*, DOI: 10.1029/2002gl015037.

- Newton T., Weldon R., Miller I., Schmidt D., Mauger G., Morgan H., and Grossman E. (2021). *An Assessment of Vertical Land Movement to Support Coastal Hazards Planning in Washington State*. *Water*, 13(3):281, ISSN: 2073-4441, DOI: 10.3390/w13030281, <https://www.mdpi.com/2073-4441/13/3/281>.
- Nicholls R. J. (2011). *Planning for the Impacts of Sea Level Rise*. *Oceanography*, 24(2):144 – 157, DOI: 10.5670/oceanog.2011.34, <https://doi.org/10.5670/oceanog.2011.34>.
- Nicholls R. J., Lincke D., Hinkel J., Brown S., Vafeidis A. T., Meyssignac B., Hanson S. E., Merkens J.-L., and Fang J. (2021). *A global analysis of subsidence, relative sea-level change and coastal flood exposure*. *Nat. Clim. Chang.*, 11(4):338–342, ISSN: 1758-678X, 1758-6798, DOI: 10.1038/s41558-021-00993-z, <http://www.nature.com/articles/s41558-021-00993-z>.
- Oelsmann J., Marcos M., Passaro M., Sanchez L., Dettmering D., Dangendorf S., and Seitz F. (2023). *Vertical land motion reconstruction unveils nonlinear effects on relative sea level*. *Nature Geosciences*, submitted.
- Oelsmann J. and Passaro M. (2022). *ESA Sea Level CCI+, CCN2 TUM D1.1*. https://climate.esa.int/documents/1609/SLCCI_CCN2_D1.1_TUM_v2.pdf.
- Oelsmann J., Passaro M., Dettmering D., Schwatke C., Sánchez L., and Seitz F. (2021). *The zone of influence: matching sea level variability from coastal altimetry and tide gauges for vertical land motion estimation*. *Ocean Science*, 17(1):35–57, DOI: 10.5194/os-17-35-2021, <https://os.copernicus.org/articles/17/35/2021/>.
- Oelsmann J., Passaro M., Sánchez L., Dettmering D., Schwatke C., and Seitz F. (2022a). *Bayesian modelling of piecewise trends and discontinuities to improve the estimation of coastal vertical land motion*. *Journal of Geodesy*, 96(62), DOI: 10.1007/s00190-022-01645-6.
- Oelsmann J., Passaro M., Sánchez L., Dettmering D., Schwatke C., and Seitz F. (2022b). *Piecewise trends and discontinuities in GNSS and SATTG time series*. *SEANOE*, DOI: 10.17882/90028.
- Olivares G., Teferle F. N., and Hunegnaw A. (2020). *Markov Chain Monte Carlo and the Application to Geodetic Time Series Analysis*. In Montillet J.-P. and Bos M. S. (Eds.), *Geodetic Time Series Analysis in Earth Sciences*, pages 53–138. Springer International Publishing, Cham, ISBN: 978-3-030-21717-4 978-3-030-21718-1, DOI: 10.1007/978-3-030-21718-1_3, http://link.springer.com/10.1007/978-3-030-21718-1_3. Series Title: Springer Geophysics.
- Olivares G. and Teferle N. (2013). *A Bayesian Monte Carlo Markov Chain Method for Parameter Estimation of Fractional Differenced Gaussian Processes*. *IEEE Transactions on Signal Processing*, 61:2405–2412, DOI: 10.1109/TSP.2013.2245658.
- O'Neill B. C., Tebaldi C., van Vuuren D. P., Eyring V., Friedlingstein P., Hurtt G., Knutti R., Kriegler E., Lamarque J.-F., Lowe J., Meehl G. A., Moss R., Riahi K., and Sanderson B. M. (2016). *The Scenario Model Inter-comparison Project (ScenarioMIP) for CMIP6*. *Geosci. Model Dev.*, 9(9):3461–3482, ISSN: 1991-9603, DOI: 10.5194/gmd-9-3461-2016, <https://gmd.copernicus.org/articles/9/3461/2016/>.
- Oppenheimer M., Glavovic B., Hinkel J., van de Wal R., Magnan A., Abd-Elgawad A., Cai R., Cifuentes-Jara M., DeConto R., Ghosh T., Hay J., Isla F., Marzeion B., Meyssignac B., and Sebesvari Z. (2019). *Sea Level Rise and*

- Implications for Low-Lying Islands, Coasts and Communities*. In Pörtner H.-O., Roberts D., Masson-Delmotte V., Zhai P., Tignor M., Poloczanska E., Mintenbeck K., Alegría A., Nicolai M., Okem A., Petzold J., Rama B., and Weyer N. (Eds.), *IPCC Special Report on the Ocean and Cryosphere in a Changing Climate*, chapter 4. Cambridge University Press, Cambridge, UK and New York, NY, USA, DOI: 10.1017/9781009157964.006.
- Passaro M., Cipollini P., and Benveniste J. (2015). *Annual sea level variability of the coastal ocean: The Baltic Sea-North Sea transition zone*. *Journal of Geophysical Research: Oceans*, 120(4):3061–3078, ISSN: 21699291, DOI: 10.1002/2014JC010510.
- Passaro M., Cipollini P., Vignudelli S., Quartly G. D., and Snaith H. M. (2014). *ALES: A multi-mission adaptive subwaveform retracker for coastal and open ocean altimetry*. *Remote Sensing of Environment*, 145:173–189, ISSN: 00344257, DOI: 10.1016/j.rse.2014.02.008, <http://dx.doi.org/10.1016/j.rse.2014.02.008>.
- Pedaja K., Husson L., Bezos A., Pastier A.-M., Imran A. M., Arias-Ruiz C., Sarr A.-C., Elliot M., Pons-Branchu E., Nexer M., Regard V., Hafidz A., Robert X., Benoit L., Delcaillau B., Authemayou C., Dumoulin C., and Choblet G. (2018). *On the long-lasting sequences of coral reef terraces from SE Sulawesi (Indonesia): Distribution, formation, and global significance*. *Quaternary Science Reviews*, 188:37–57, ISSN: 0277-3791, DOI: 10.1016/j.quascirev.2018.03.033, <https://www.sciencedirect.com/science/article/pii/S0277379117309824>.
- Peltier W. (2004). *GLOBAL GLACIAL ISOSTASY AND THE SURFACE OF THE ICE-AGE EARTH: The ICE-5G (VM2) Model and GRACE*. *Annual Review of Earth and Planetary Sciences*, 32(1):111–149, DOI: 10.1146/annurev.earth.32.082503.144359, <https://doi.org/10.1146/annurev.earth.32.082503.144359>.
- Peng F., Deng X., and Cheng X. (2022). *Australian Coastal Sea Level Trends Over 16 yr of Reprocessed Jason Altimeter 20-Hz Data Sets*. *Journal of Geophysical Research: Oceans*, 127(3):e2021JC018145, DOI: 10.1029/2021JC018145, <https://agupubs.onlinelibrary.wiley.com/doi/abs/10.1029/2021JC018145>. e2021JC018145 2021JC018145.
- Pfeffer J. and Allemand P. (2016). *The key role of vertical land motions in coastal sea level variations: A global synthesis of multisatellite altimetry, tide gauge data and GPS measurements*. *Earth and Planetary Science Letters*, 439:39–47, ISSN: 0012821X, DOI: 10.1016/j.epsl.2016.01.027, <http://dx.doi.org/10.1016/j.epsl.2016.01.027>.
- Pfeffer J., Spada G., Mémin A., Boy J.-P., and Allemand P. (2017). *Decoding the origins of vertical land motions observed today at coasts*. *Geophysical Journal International*, 210(1):148–165, ISSN: 0956-540X, DOI: 10.1093/gji/ggx142, <https://doi.org/10.1093/gji/ggx142>.
- Piccioni G., Dettmering D., Passaro M., Schwatke C., Bosch W., and Seitz F. (2018). *Coastal Improvements for Tide Models: The Impact of ALES Retracker*. *Remote Sensing*, 10:700, DOI: 10.3390/rs10050700.
- Piecuch C. (2022). *River effects on sea-level rise in the Río de la Plata during the past century*. *EGU-sphere*, 2022:1–30, DOI: 10.5194/egusphere-2022-700, <https://egusphere.copernicus.org/preprints/egusphere-2022-700/>.

- Piecuch C., Huybers P., Hay C. C., Kemp A. C., Little C. M., Mitrovica J. X., Ponte R. M., and Tingley M. P. (2018). *Origin of spatial variation in US East Coast sea-level trends during 1900–2017*. *Nature*, 564(7736):400–404, ISSN: 0028–0836, 1476–4687, DOI: 10.1038/s41586-018-0787-6, <http://www.nature.com/articles/s41586-018-0787-6>.
- Piironen J. and Vehtari A. (2017). *Comparison of Bayesian predictive methods for model selection*. *Statistics and Computing*, 27, DOI: 10.1007/s11222-016-9649-y.
- Poitevin C., Wöppelmann G., Raucoules D., Cozannet G. L., Marcos M., and Testut L. (2019). *Vertical land motion and relative sea level changes along the coastline of Brest (France) from combined space-borne geodetic methods*. *Remote Sensing of Environment*, 222:275–285, ISSN: 0034–4257, DOI: 10.1016/j.rse.2018.12.035, <http://www.sciencedirect.com/science/article/pii/S0034425718305960>.
- Pugh D. and Woodworth P. (2014). *Sea-Level Science: Understanding Tides, Surges, Tsunamis and Mean Sea-Level Changes*. Cambridge University Press, DOI: 10.1017/CBO9781139235778.
- Rabus B., Eineder M., Roth A., and Bamler R. (2003). *The shuttle radar topography mission—a new class of digital elevation models acquired by spaceborne radar*. *ISPRS Journal of Photogrammetry and Remote Sensing*, 57(4):241–262, DOI: 10.1016/S0924-2716(02)00124-7.
- Raucoules D., Le G., Wöppelmann G., Michele M. D., Gravelle M., Daag A., and Marcos M. (2013). *Remote Sensing of Environment High nonlinear urban ground motion in Manila (Philippines) from 1993 to 2010 observed by DInSAR: Implications for sea-level measurement*. *Remote Sensing of Environment*, 139:386–397, ISSN: 0034–4257, DOI: 10.1016/j.rse.2013.08.021, <http://dx.doi.org/10.1016/j.rse.2013.08.021>.
- Ray R., Loomis B., and Zlotnicki V. (2021). *The mean seasonal cycle in relative sea level from satellite altimetry and gravimetry*. *Journal of Geodesy*, 95, DOI: 10.1007/s00190-021-01529-1.
- Riddell A. R., King M. A., and Watson C. S. (2020). *Present-Day Vertical Land Motion of Australia From GPS Observations and Geophysical Models*. *J. Geophys. Res. Solid Earth*, 125(2), ISSN: 2169–9313, 2169–9356, DOI: 10.1029/2019JB018034, <https://onlinelibrary.wiley.com/doi/abs/10.1029/2019JB018034>.
- Royston S., Watson C. S., Legrésy B., King M. A., Church J. A., and Bos M. S. (2018). *Sea-Level Trend Uncertainty With Pacific Climatic Variability and Temporally-Correlated Noise*. *Journal of Geophysical Research: Oceans*, 123(3):1978–1993, DOI: 10.1002/2017JC013655, <https://agupubs.onlinelibrary.wiley.com/doi/abs/10.1002/2017JC013655>.
- Rudenko S., Dettmering D., Zeitlhöfler J., Alkhal R., Upadhyay D., and Bloßfeld M. (2023). *Radial Orbit Errors of Contemporary Altimetry Satellite Orbits*. *Surveys in Geophysics*, 44(3):705–737, ISSN: 1573–0956, DOI: 10.1007/s10712-022-09758-5, <https://doi.org/10.1007/s10712-022-09758-5>.
- Sanli D. and Blewitt G. (2001). *Geocentric sea level trend using GPS and >100-year tide gauge record on a post-glacial rebound nodal line*. *Journal of Geophysical Research*, 106:713–720, DOI: 10.1029/2000JB900348.

- Santamaría-Gómez A., Gravelle M., Dangendorf S., Marcos M., Spada G., and Wöppelmann G. (2017). *Uncertainty of the 20th century sea-level rise due to vertical land motion errors*. *Earth and Planetary Science Letters*, 473:24–32, ISSN: 0012-821X, DOI: 10.1016/j.epsl.2017.05.038, <http://dx.doi.org/10.1016/j.epsl.2017.05.038>.
- Santamaría-Gómez A., Gravelle M., and Wöppelmann G. (2014). *Long-term vertical land motion from double-differenced tide gauge and satellite altimetry data*. *Journal of Geodesy*, 88(3):207–222, DOI: 10.1007/s00190-013-0677-5.
- Santamaría-Gómez A., Bouin M.-N., Collilieux X., and Wöppelmann G. (2011). *Correlated errors in GPS position time series: Implications for velocity estimates*. *Journal of Geophysical Research: Solid Earth*, 116(B1), DOI: 10.1029/2010JB007701, <https://agupubs.onlinelibrary.wiley.com/doi/abs/10.1029/2010JB007701>.
- Santamaría-Gómez A., Gravelle M., Collilieux X., Guichard M., Míguez B. M., Tiphaneau P., and Wöppelmann G. (2012). *Mitigating the effects of vertical land motion in tide gauge records using a state-of-the-art GPS velocity field*. *Global and Planetary Change*, 98-99:6 – 17, ISSN: 0921-8181, DOI: 10.1016/j.gloplacha.2012.07.007, <http://www.sciencedirect.com/science/article/pii/S0921818112001476>.
- Santamaría-Gómez A., Gravelle M., and Wöppelmann G. (2016). *GPS Solution ULR6*. SONEL Data Center, DOI: 10.26166/sonel_ulr6a, <https://www.sonel.org/-Vertical-land-movement-estimate-.html?lang=en>.
- Scharroo R., Leuliette E., Lillibridge J., Byrne D., Naeije M., and Mitchum G. (2012). *RADS: Consistent multi-mission products*. 20 Years of Progress in Radar Altimetry, held 24-29 September, 2012 in Venice, Italy, 20:59–60, ISBN: 978-92-9221-274-2.
- Schwarz G. (1978). *Estimating the Dimension of a Model*. *Ann. Statist.*, 6(2):461–464, DOI: 10.1214/aos/1176344136.
- Seitz M., Bloßfeld M., Angermann D., and Seitz F. (2021). *DTRF2014: DGFI-TUM's ITRS realization 2014*. *Advances in Space Research*, ISSN: 0273-1177, DOI: 10.1016/j.asr.2021.12.037, <https://www.sciencedirect.com/science/article/pii/S0273117721009479>.
- Serpelloni E., Faccenna C., Spada G., Dong D., and Williams S. D. P. (2013). *Vertical GPS ground motion rates in the Euro-Mediterranean region: New evidence of velocity gradients at different spatial scales along the Nubia-Eurasia plate boundary: GPS VERTICAL DEFORMATION IN EUROPE*. *J. Geophys. Res. Solid Earth*, 118(11):6003–6024, ISSN: 21699313, DOI: 10.1002/2013JB010102, <http://doi.wiley.com/10.1002/2013JB010102>.
- Shirzaei M., Freymueller J., Törnqvist T. E., Galloway D. L., Dura T., and Minderhoud P. S. J. (2021). *Measuring, modelling and projecting coastal land subsidence*. *Nature Reviews Earth & Environment*, 2(1):40–58, ISSN: 2662-138X, DOI: 10.1038/s43017-020-00115-x, <https://doi.org/10.1038/s43017-020-00115-x>.

- Slangen A. B., Palmer M. D., Camargo C. M., Church J. A., Edwards T. L., Hermans T. H., Hewitt H. T., Garner G. G., Gregory J. M., Kopp R. E., and et al. (2023). *The evolution of 21st century sea-level projections from IPCC AR5 to AR6 and beyond*. Cambridge Prisms: Coastal Futures, 1:e7, DOI: 10.1017/cft.2022.8.
- Slangen A. B. A., Carson M., Katsman C. A., van de Wal R. S. W., Köhl A., Vermeersen L. L. A., and Stammer D. (2014). *Projecting twenty-first century regional sea-level changes*. Climatic Change, 124(1):317–332, ISSN: 1573–1480, DOI: 10.1007/s10584-014-1080-9, 10.1007/s10584-014-1080-9.
- Snay R., Cline M., Dillinger W., Foote R., Hilla S., Kass W., Ray J., Rohde J., Sella G., and Soler T. (2007). *Using global positioning system-derived crustal velocities to estimate rates of absolute sea level change from North American tide gauge records*. Journal of Geophysical Research: Solid Earth, 112(B4), DOI: 10.1029/2006JB004606, <https://agupubs.onlinelibrary.wiley.com/doi/abs/10.1029/2006JB004606>.
- Stammer D. and Cazenave A. (2017). *Satellite Altimetry over Oceans and Land Surfaces*. CRC Press, Boca Raton, FL : Taylor & Francis, 2017., 1 edition, ISBN: 978-1-315-15177-9, DOI: 10.1201/9781315151779, <https://www.taylorfrancis.com/books/9781498743464>.
- Stammer D., Cazenave A., Ponte R. M., and Tamisiea M. E. (2013). *Causes for Contemporary Regional Sea Level Changes*. Annual Review of Marine Science, 5(1):21–46, DOI: 10.1146/annurev-marine-121211-172406, <https://doi.org/10.1146/annurev-marine-121211-172406>. PMID: 22809188.
- Storch H. v. and Zwiers F. W. (1999). *Statistical Analysis in Climate Research*. Cambridge University Press, DOI: 10.1017/CB09780511612336.
- Sweet W., Hamlington B., Kopp R., Weaver C., Barnard P., Bekaert D., Brooks W., Craghan M., Dusek G., Frederikse T., Garner G., Genz A., Krasting J., Larour E., Marcy D., Marra J., Obeysekera J., Osler, Pendleton M. M., Roman D., Schmied L., Veatch W., White K., and Zuzak C. (2022). *Global and Regional Sea Level Rise Scenarios for the United States: Updated Mean Projections and Extreme Water Level Probabilities Along U.S. Coastlines*. NOAA Technical Report NOS 01. National Oceanic and Atmospheric Administration, National Ocean Service, <https://oceanservice.noaa.gov/hazards/sealevelrise/noaa-nos-techrpt01-global-regional-SLR-scenarios-US.pdf>.
- Syvitski J. P. M., Kettner A. J., Overeem I., Hutton E. W. H., Hannon M. T., Brakenridge G. R., Day J., Vörösmarty C., Saito Y., Giosan L., and Nicholls R. J. (2009). *Sinking deltas due to human activities*. Nature Geosci, 2(10):681–686, ISSN: 1752-0894, 1752-0908, DOI: 10.1038/ngeo629, <http://www.nature.com/articles/ngeo629>.
- Sánchez L. and Bosch W. (2009). *The role of the TIGA project in the unification of classical height systems*. In: Drewes H. (Ed.): Geodetic Reference Frames, IAG Symposia 134: 285-290, Springer, DOI: 10.1007/978-3-642-00860-3_44.
- Sánchez L., Völksen C., Sokolov A., Arenz H., and Seitz F. (2018). *Present-day surface deformation of the Alpine region inferred from geodetic techniques*. Earth Syst. Sci. Data, 10(3):1503–1526, ISSN: 1866–3516, DOI: 10.5194/essd-10-1503-2018, <https://essd.copernicus.org/articles/10/1503/2018/>.

- Taburet G., Sanchez-Roman A., Ballarotta M., Pujol M.-I., Legeais J.-F., Fournier F., Faugere Y., and Dibarboure G. (2019). *DUACS DT2018: 25 years of reprocessed sea level altimetry products*. *Ocean Science*, 15(5):1207–1224, DOI: 10.5194/os-15-1207-2019, <https://os.copernicus.org/articles/15/1207/2019/>.
- Tapley B. D., Bettadpur S., Watkins M., and Reigber C. (2004). *The gravity recovery and climate experiment: Mission overview and early results: GRACE MISSION OVERVIEW AND EARLY RESULTS*. *Geophys. Res. Lett.*, 31(9):n/a–n/a, ISSN: 00948276, DOI: 10.1029/2004GL019920, <http://doi.wiley.com/10.1029/2004GL019920>.
- Tay C., Lindsey E. O., Chin S. T., McCaughey J. W., Bekaert D., Nguyen M., Hua H., Manipon G., Karim M., Horton B. P., Li T., and Hill E. M. (2022). *Sea-level rise from land subsidence in major coastal cities*. *Nature Sustainability*, ISSN: 2398–9629, DOI: 10.1038/s41893-022-00947-z.
- Taylor S. J. and Letham B. (2018). *Forecasting at Scale*. *The American Statistician*, 72(1):37–45, DOI: 10.1080/00031305.2017.1380080, <https://doi.org/10.1080/00031305.2017.1380080>.
- Tehranchi R., Moghtased-Azar K., and Safari A. (2020). *A New Statistical Test Based on the WR for Detecting Offsets in GPS Experiment*. *Earth and Space Science*, 7(8):e2019EA000810, DOI: 10.1029/2019EA000810, <https://agupubs.onlinelibrary.wiley.com/doi/abs/10.1029/2019EA000810>, e2019EA000810 10.1029/2019EA000810.
- Toomey T., Amores A., Marcos M., Orfila A., and Romero R. (2022). *Coastal Hazards of Tropical-Like Cyclones Over the Mediterranean Sea*. *Journal of Geophysical Research: Oceans*, 127(2):e2021JC017964, DOI: 10.1029/2021JC017964, <https://agupubs.onlinelibrary.wiley.com/doi/abs/10.1029/2021JC017964>, e2021JC017964 2021JC017964.
- Törnqvist T. E., Wallace D. J., Storms J. E. A., Wallinga J., van Dam R. L., Blaauw M., Derksen M. S., Klerks C. J. W., Meijneken C., and Snijders E. M. A. (2008). *Mississippi Delta subsidence primarily caused by compaction of Holocene strata*. *Nature Geosci*, 1(3):173–176, ISSN: 1752–0894, 1752–0908, DOI: 10.1038/ngeo129, <http://www.nature.com/articles/ngeo129>.
- Vafeidis A. T., Nicholls R. J., McFadden L., Tol R. S. J., Hinkel J., Spencer T., Grashoff P. S., Boot G., and Klein R. J. T. (2008). *A New Global Coastal Database for Impact and Vulnerability Analysis to Sea-Level Rise*. *Journal of Coastal Research*, 24(4 (244)):917–924, ISSN: 0749–0208, DOI: 10.2112/06-0725.1, <https://doi.org/10.2112/06-0725.1>.
- van Ravenzwaaij D., Cassey P., and Brown S. (2018). *A simple introduction to Markov Chain Monte-Carlo sampling*. *Psychonomic Bulletin Review*, 25(1):143–154, ISSN: 1069–9384, DOI: 10.3758/s13423-016-1015-8.
- Vehtari A., Gelman A., and Gabry J. (2017). *Practical Bayesian model evaluation using leave-one-out cross-validation and WAIC*. *Statistics and Computing*, 27:1413–1432, DOI: 10.1007/s11222-016-9696-4.
- Veit E. and Conrad C. P. (2016). *The impact of groundwater depletion on spatial variations in sea level change during the past century*. *Geophysical Research Letters*, 43(7):3351–3359, DOI: 10.1002/2016GL068118, <https://agupubs.onlinelibrary.wiley.com/doi/abs/10.1002/2016GL068118>.

- Vigny C., Socquet A., Peyrat S., Ruegg J.-C., Metois M., Madariaga R., Morvan S., Lancieri M., Lacassin R., Campos J., Carrizo D., Bejar-Pizarro M., Barrientos S., Armijo R., Aranda C., Valderas-Bermejo M.-C., Ortega I., Bondoux F., Baize S., Lyon-Caen H., Pavez A., Vilotte J. P., Bevis M., Brooks B., Smalley R., Parra H., Baez J.-C., Blanco M., Cimbaro S., and Kendrick E. (2011). *The 2010 Mw 8.8 Maule Megathrust Earthquake of Central Chile, Monitored by GPS*. *Science*, 332(6036):1417–1421, ISSN: 0036–8075, 1095–9203, DOI: 10.1126/science.1204132, <https://www.sciencemag.org/lookup/doi/10.1126/science.1204132>.
- Vitti A. (2012). *SIGSEG: A tool for the detection of position and velocity discontinuities in geodetic time-series*. *GPS Solutions*, 16:405–410, DOI: 10.1007/s10291-012-0257-9.
- Wada Y., van Beek L. P. H., Sperna Weiland F. C., Chao B. F., Wu Y.-H., and Bierkens M. F. P. (2012). *Past and future contribution of global groundwater depletion to sea-level rise*. *Geophysical Research Letters*, 39(9), DOI: 10.1029/2012GL051230, <https://agupubs.onlinelibrary.wiley.com/doi/abs/10.1029/2012GL051230>.
- Wang J., Church J. A., Zhang X., and Chen X. (2021). *Reconciling global mean and regional sea level change in projections and observations*. *Nat Commun*, 12(1):990, ISSN: 2041–1723, DOI: 10.1038/s41467-021-21265-6, <http://www.nature.com/articles/s41467-021-21265-6>.
- Wang X., Cheng Y., Wu S., and Zhang K. (2016). *An enhanced singular spectrum analysis method for constructing nonsecular model of GPS site movement*. *Journal of Geophysical Research: Solid Earth*, 121(3):2193–2211, DOI: 10.1002/2015JB012573, <https://agupubs.onlinelibrary.wiley.com/doi/abs/10.1002/2015JB012573>.
- Watson C., White N., Church J., King M., Burgette R., and Legresy B. (2015). *Unabated global mean sea-level rise over the satellite altimetry era*. *Nature Climate Change*, 5, DOI: 10.1038/nclimate2635.
- Williams S. D. P. (2008). *CATS : GPS coordinate time series analysis software*. *GPS Solutions*, 12:147–153, DOI: 10.1007/s10291-007-0086-4.
- Woodworth P. L., Hunter J. R., Marcos M., Caldwell P., Menéndez M., and Haigh I. (2016). *Towards a global higher-frequency sea level dataset*. *Geoscience Data Journal*, 3(2):50–59, DOI: 10.1002/gdj3.42, <https://rmets.onlinelibrary.wiley.com/doi/abs/10.1002/gdj3.42>.
- Woodworth P. L., Melet A., Marcos M., Ray R. D., Wöppelmann G., Sasaki Y. N., Cirano M., Hibbert A., Huthnance J. M., Monserrat S., and Merrifield M. A. (2019). *Forcing factors affecting sea level changes at the coast*. *Surveys in Geophysics*, 40(6):1351–1397, DOI: 10.1007/s10712-019-09531-1, <http://nora.nerc.ac.uk/id/eprint/523283/>.
- Wudong L., Jiang W.-P., Li Z., Chen H., Chen Q., Wang J., and Zhu G. (2020). *Extracting Common Mode Errors of Regional GNSS Position Time Series in the Presence of Missing Data by Variational Bayesian Principal Component Analysis*. *Sensors*, 20:2298, DOI: 10.3390/s20082298.
- Wöppelmann G., Gravelle M., Guichard M., and Prouteau E. (2019). *Fourth Progress Report on the GNSS at Tide Gauge Activities: SONEL Data Holdings & Tools to access the data, presented at the XVIth GLOSS group of experts meeting, hosted by the Korean Hydrographic and*

Oceanographic Agency, Busan (Republic of Korea), 11-13 April 2019. Online version available at: https://www.sonel.org/IMG/pdf/ge16_gnssattg_activities_sonel_report_v2.pdf.

Wöppelmann G., Le Cozannet G., de Michele M., Raucoules D., Cazenave A., Garcin M., Hanson S., Marcos M., and Santamaría-Gómez A. (2013). *Is land subsidence increasing the exposure to sea level rise in Alexandria, Egypt?* *Geophysical Research Letters*, 40(12):2953–2957, DOI: 10.1002/grl.50568, <https://agupubs.onlinelibrary.wiley.com/doi/abs/10.1002/grl.50568>.

Wöppelmann G. and Marcos M. (2016). *Vertical land motion as a key to understanding sea level change and variability.* *Reviews of Geophysics*, 54(1):64–92, DOI: 10.1002/2015RG000502, <https://agupubs.onlinelibrary.wiley.com/doi/abs/10.1002/2015RG000502>.

Wöppelmann G., Martin Miguez B., Bouin M.-N., and Altamimi Z. (2007). *Geocentric sea-level trend estimates from GPS analyses at relevant tide gauges world-wide.* *Global and Planetary Change*, 57:396–406, DOI: 10.1016/j.gloplacha.2007.02.002.

Yousefi M., Milne G. A., Love R., and Tarasov L. (2018). *Glacial isostatic adjustment along the Pacific coast of central North America.* *Quaternary Science Reviews*, 193:288–311, ISSN: 0277-3791, DOI: 10.1016/j.quascirev.2018.06.017, <https://www.sciencedirect.com/science/article/pii/S0277379117310107>.

Zanchettin D., Bruni S., Raicich F., Lionello P., Adloff F., Androsov A., Antonioli F., Artale V., Carminati E., Ferrarin C., Fofonova V., Nicholls R. J., Rubineti S., Rubino A., Sannino G., Spada G., Thiéblemont R., Tsimplis M., Umgiesser G., Vignudelli S., Wöppelmann G., and Zerbini S. (2021). *Sea-level rise in Venice: historic and future trends (review article).* *Nat. Hazards Earth Syst. Sci.*, 21(8):2643–2678, ISSN: 1684-9981, DOI: 10.5194/nhess-21-2643-2021, <https://nhess.copernicus.org/articles/21/2643/2021/>.

Zlotnicki V., Qu Z., and Willis J. (2019). *MEASUREs Gridded Sea Surface Height Anomalies Version 1812.* *PO.DAAC, CA, USA.* DOI: 10.5067/SLREF-CDRV2. Dataset accessed [2019-01-01] at , <https://doi.org/10.5067/SLREF-CDRV2>.

Acknowledgements

This work couldn't exist without the contribution and endless support of Marcello, Florian, Denise, Laura, Marta, Robert, Sönke and many others. In the preface to my thesis, I begin by asking how much of one's success is due to luck and how much is due to personal contribution. I have learnt that a lot of it is indeed luck and external factors, especially the opportunity to work with Marcello and the rest of the institute and all the other opportunities I have been given at DGFI!

I am therefore particularly grateful to Marcello for his help during this project. He has really played a key role, not only in my work but, perhaps more importantly, in my personal development by improving my independent thinking, networking and collaboration skills, as well as my ability to stay positive and never give up. His attitude and enthusiasm are truly contagious, so he has had an extremely positive influence on me. He has also introduced me to countless opportunities, e.g., to work with the ESA Baltic Seal Team, ESA CCI, the ISSI team and other colleagues such as Marta and many others, all of which have been great experiences. So I couldn't imagine a better mentor!

I am also very thankful for Florian's support, who helped me staying afloat on the ocean of information of geodesy. Florian supported me from the beginning, trusting an oceanographer to tackle the problem of vertical land motion, something I didn't know much about at the beginning. He also has a great attention to detail, which really helped me to stay focused and learn a lot about many technical challenges in geodesy. So I'm grateful for his constant support, encouragement and involvement in my work.

Many thanks also to Denise, who does not only have an incredible broad knowledge in altimetry and geodesy, but was also a massive support and discussed every idea with me. She always had time for questions, even though she wasn't not my direct supervisor. I am also very grateful to Laura, who together with Marcello initiated the project that funded me, and who has been very supportive throughout this journey. She helped me whenever I had questions about vertical land motion, GNSS, GIA, tectonics and many other things. Last but not least, she's a lot of fun to work with because she's very enthusiastic about this work and always has a smile on her face =). Marta, who I visited in Esporles, Spain, also played a key role in my work and contributed some really important ideas. She is not only a very likeable person, but also a great role model for any scientist (or maybe a time management professional), as she could miraculously allocate a lot of time to each of her students/colleagues, while being involved in countless other scientific projects and organisations. So one of the things I learned from her is that 'Sorry, I don't have time for this right now' is no excuse =). So I'm very grateful to have made contact with her. The same goes for all the great people I met at IMEDEA, like Carolina, Tim, Diego, Angel and Dario! Finally, I'm very grateful for the input of Sönke, who I got to know from the beginning of my PhD (through his inspiring papers) and then personally towards the end of my PhD (so far only online). It was really fun to discuss our work together, because Sönke is really passionate and dedicated to this work! I hope we'll continue to work together in the future!

Besides those who were directly involved in my work, I would also like to thank my lovely colleagues and friends at DGFI who have provided so much joy and hilarious moments over the past few years. One of

these lovely people is Mike, who made everyone at the Institute laugh with his South African vibes and is the guy who applies sinus'es to sea level data. I still wonder how anyone can be so technically and socially intelligent and at the same time have such an incredible sense of humour. Mike keeps you up to date better than Google scholar and is the first place to go for relaxing background music while coding. His daily text messages have made my work really enjoyable. In fact, we almost wrote a paper together once. This is the abstract: (Mike, 13.10.2022, 13:27): 'We start it: Since 2019, Oelsmann and Hart-Davis have been arguing about whether tides should be removed before making monthly estimates to produce more reliable trend estimates from tide gauge estimations. In this manuscript, the argument is settled.' Unfortunately, we never did this study because removing tides before monthly averaging doesn't have much impact on trends (please don't steal the idea without citing).

And then there was Floschl. Floschl really is one of the most determined and efficient people I have ever met. I really learned an incredible amount from him and still miss our lively conversations and discussions. As I had a fundamentally different working style to him, I was able to learn a lot from his efficient and reproducible way of programming. Floschl is the guy to think of when you are unmotivated, because he really showed what a person is capable of. Or who does a PhD, has a child and does an Ironman at the same time?

Another interesting and endearing person at DGFI is soon-to-be Nobel Prize winner Sergiy Rudenko. This rationed Russian-Ukrainian-German cosmologist and orbital enthusiast has a very big heart, probably also a photographic memory, and is up for any fun. He has a genuine interest in people and has made everyday life at DGFI very pleasant. This has also resulted in numerous photos (please search for his Instagram profile). I'm especially grateful because he has also read most of my papers and has always provided very helpful comments. I am also very grateful to have met Alex, who always has something interesting to say about any topic and has a penchant for reporting on extraordinary experiences from non-mainstream tourist destinations like Transnistria. I am very interested in his future development and wonder when he will finally discover his hidden talent (triple jump). Marie was another great colleague who made every moment beautiful with her open heart and mind. I recommend having her at every conference, it's great fun! It was also super nice to meet Hergeir, Tadea and Maria, with whom I had really funny moments! I am also very happy about the help from all the other colleagues in the altimetry group. Christian, Felix, Daniel, Maria and Michael are just great people and have always supported me when I had questions about missions, corrections, MVA, holiday requests, coding, plotting and life!

The second half of my PhD became particularly exciting after meeting many great other scientists through ISSI, my stay at IMEDEA and various conferences. I got very good ideas from them and I am very grateful to Kiko (who inspired me to try Bayesian models and was great to discuss the big questions with), Robert (who really made me think outside the box of geodesy) and all the other bright minds like Chris, Chris, Sveta, Karoline, Kristin and Anthony.

Finally, I am especially grateful for the constant and unconditional support and love from my wife Sarah and for our daughter Merle, who was born just a few days after the defense.

Appendix

1 Model initialization

Before estimating the parameters, time series are normalized, such that the same prior assumptions are valid for both SATTG and GNSS data. Compared to SATTG time series, GNSS data have much lower noise amplitudes, so without normalization the prior of, e.g., σ_w would need to be set individually. The data are normalized by the median of their 2-year running-standard-deviation, hereinafter called σ_{obs} . With this approach I avoid that extreme discontinuities (in particular present in GNSS data), which present orders of magnitudes larger than the 'true noise amplitude' influence the normalization. I also subtract the offset of the first observation from the data.

Next to the initial probability of \vec{q}_0 , which is explained in section 3.2.1 several other parameters need to be initialized. The maximum number n_{max} of possible detectable change points is set to 5. The initial AR(1) noise parameter (i.e., the lag-one autocorrelation coefficient) are set to $\sigma_\phi = 0.4$ and $\hat{\sigma}_w = 1$. The white noise standard deviation is thus consistent with the standard deviation of the normalized data. In case the PLWN model is applied I set $\hat{\sigma}_w = 0.2$, $\hat{\sigma}_{pl} = 1$. To reduce the complexity of the model, the spectral index is not estimated but prescribed to $\kappa = -0.9$, which generates a noise process close to Flicker Noise. For the trend parameters, I also use informative priors: I set σ_k and $\vec{\sigma}_h$ to 1. Note that this value corresponds to $\sim 1\sigma_{obs}/year$, and is thus in the order of mm/year to cm/year (for GNSS or SATTG time series). This is another crucial prior assumption, which is based on knowledge of typical physical magnitudes of VLM. The definition primarily avoids that large shifts in the time series would be compensated in form of large VLM rates, but rather be approximated by discontinuities. For the discontinuities I use noninformative priors with σ_o and $\vec{\sigma}_p$ of 20 (which can be translated to 20 standard deviations). The exact initial change point positions are randomly drawn from the aforementioned uniform distribution. The prior standard deviation $\vec{\sigma}$ is set to 5 years. The multi-year monthly means $\vec{\mu}_m$ are set to 0 with $\vec{\sigma}_m=1$.

For very obvious and easily detectable discontinuities in the data (in particular in GNSS time series), knowledge of such events can support the model initialization and generally speed up the computation. Therefore position and magnitudes of discontinuities $\vec{\mu}_s$ and $\vec{\mu}_p$ are incorporated in the initial conditions, which are detected when absolute consecutive differences are 15 times larger than the median of all consecutive differences. In general, such events are only recognized for some GNSS time series.

2 Model selection strategies

There are several options to compare and evaluate different Bayesian models [Gelman et al., 2013]. As an objective measure to compare different individual model realizations, I take into account the out-of-sample predictive accuracy of a model. Here, the Pareto-smoothed importance sampling leave-one-out cross-validation (PSIS-LOO) introduced by [Vehtari et al., 2017] is applied, which provides an approximation of the predictive

accuracy (loo) and a simulated estimate of the effective number of parameters (p-loo) of the model. In theory, in the cross-validation (CV) approach the data is split into training sets, on which the model is trained, as well as holdout sets from which the predictive accuracy is computed. Vehtari et al. [2017] developed an efficient method to compute LOO using the existing simulation draws in order to avoid re-fitting of the full time series. As an example, the estimates of piecewise trends and discontinuities (blue) in Fig. 3.2 stem in both cases (SATTG and GNSS) from the ensemble member with the best CV-score.

Using CV (or other criteria such as widely applicable information criterion (WAIC) or deviance information criterion (DIC)) to select a single best-performing realization, can however lead to overfitting of the data and introduce a significant selection bias [Piironen and Vehtari, 2017], even though the CV-score might indicate the best predictive accuracy among the realizations. Piironen and Vehtari [2017] show that e.g. CV-based model selection is especially vulnerable to overfitting at smaller sample sizes, which might thus also have a significant influence for this application where SATTG time series have much lower samples (resolution) than the GNSS data. They underpin that Bayesian Model Averaging yields better results and is substantially less prone to overfitting than single model selection based on CV.

Therefore, I take into account the averaged number of estimated change points \bar{n} over all model candidates, as a simplified variant of Bayesian Model Averaging. Note, that even if two realizations estimated the same number of change points, the estimated change point positions and dependent parameters might still significantly deviate. For this reason, I can not average over all parameters and only use \bar{n} as ensemble average information.

In total 3 selection options are defined, to identify which is the best solution for SATTG and GNSS time series. In the first case, $best_{loo}$, I select the model with the highest predictive accuracy. Secondly, I select the model with the highest predictive accuracy from the candidates where $n = \bar{n}$. This selection is called $\overline{best_{loo}}$ and represents a less optimistic choice than $best_{loo}$. Finally, as the most conservative selection scheme, I use the model with the lowest effective number of parameters $\overline{lowest_{p-loo}}$. Note, that this is not necessarily equivalent to the model with the lowest number of change points. The estimated effective number of parameters is also reduced, for example, when there is no significant trend change after a change point and \vec{h} becomes zero.

The comparison of SATTG and GNSS piecewise trends in section 3.2.3 reveals that the highest agreement of piecewise trends is achieved when selecting SATTG ensemble member based on $\overline{lowest_{p-loo}}$ and GNSS chains based on $\overline{best_{loo}}$. I obtain similar results when using $best_{loo}$ to select the best GNSS time series realization. The fact that the best results are obtained when the chain with the lowest number of effective parameters for SATTG ($\overline{lowest_{p-loo}}$) is chosen, indicates that using $best_{loo}$ instead might lead to overfitting of the data, as also discussed by Piironen and Vehtari [2017]. The necessity to apply different selection schemes is most likely caused by the general differences in noise properties of the different techniques, combined with the different sample sizes of the observations. SATTG data could especially be vulnerable to overfitting in cases when change points are detected due to discrepancies of SAT and TG data, which are not attributable to local VLM dynamics or equipment changes.

3 Piecewise and linear trend validation

For either synthetic or real data, I investigate how the performance of piecewise trend estimation agrees with the fit of a linear trend estimate computed using linear least square estimation. I compare the deviations of piecewise estimated trends with the deviations of a linear trend fit with respect to the known (prescribed) trends of the synthetic time series. Similarly, I analyse the deviations of piecewise SATTG trends and deviations of linear SATTG trends with respect to the piecewise GNSS trends. Note that in the latter case I consider the piecewise GNSS trends as the ground truth, which are also estimated with the Bayesian model. With the real data application, I aim to answer my research questions, i.e., to which extent variable velocities can be detected in SATTG time series and what improvements or benefits are obtained by using this approach.

Figure 3.2 exemplifies how the piecewise SATTG and the piecewise GNSS trends are compared and matched with each other. The two SATTG trend segments to be compared with GNSS are indicated by $sattg_1$ and $sattg_2$. Every piecewise SATTG trend is matched with the piecewise GNSS trend which is estimated over the same period. In case that one SATTG trend segment is compared to several piecewise GNSS trends pw_gnss_i , the latter are again averaged and weighted by the fraction of the length of the GNSS segment l_i relative to the overlap period of SATTG and GNSS segments.

Thus, for $n > 0$ I obtain several piecewise SATTG and GNSS trend differences for a single station pair. In order to derive a single trend difference estimate for a SATTG-GNSS pair, I average these absolute piecewise trend differences again by weighting them by the time of the individual overlap periods as given in eq. (1). This procedure yields absolute trend differences, which are both based on piecewise SATTG and GNSS trends and hereinafter called ΔPW .

$$\Delta PW = \frac{\sum_{i=1}^n |(pw_sattg_i - pw_gnss_i)| l_i}{\sum_{i=1}^n l_i} \quad (1)$$

In a similar way, I compute ΔLIN to analyse the differences between single linear SATTG lin_sattg_i and piecewise GNSS trend estimates, as shown in Eq. (2)

$$\Delta LIN = \frac{\sum_{i=1}^n |(lin_sattg_i - pw_gnss_i)| l_i}{\sum_{i=1}^n l_i} \quad (2)$$

The example of the real data trend comparison can also be transferred to the sensitivity experiments. Here, the piecewise SATTG fit can be thought of as the synthetic data fit and the piecewise GNSS trends are representative for the known piecewise trends of the synthetic data.

4 Comparison of InSAR and GNSS VLM data

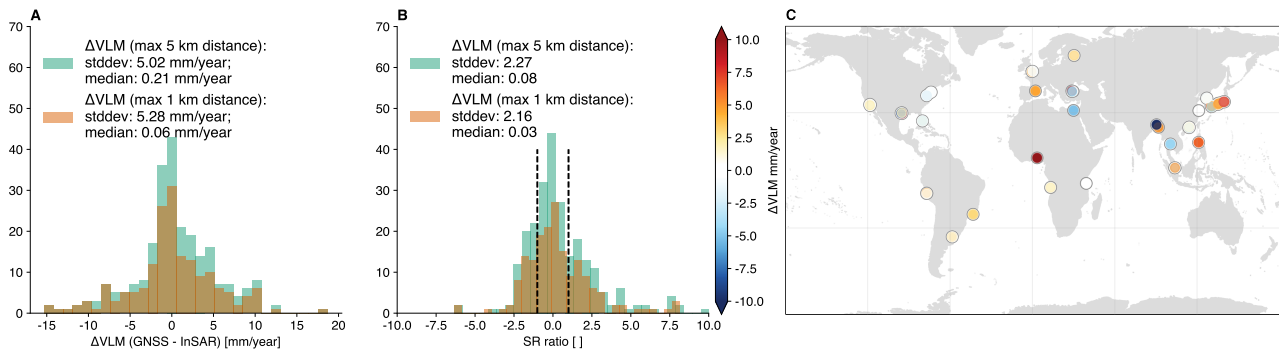


Figure 1 Comparison of GNSS [Blewitt et al., 2016] and InSAR VLM [Tay et al., 2022]. (A) displays a histogram of the trend differences for different allowed maximal distances (5 and 1 km) between a GNSS station and a data point of the InSAR data. (B) shows the significance ratio of the same quantities (i.e. the trend differences divided by the combined errors). Absolute values greater than 1 are considered significant. (C) shows the geographical distribution of these differences. Note that the differences may also be due to different observation periods.